



Provided by the author(s) and University of Galway in accordance with publisher policies. Please cite the published version when available.

Title	Micromechanical modelling of size effects in crack initiation with application to fretting fatigue and cold dwell fatigue
Author(s)	Ashton, Patrick
Publication Date	2018-12-19
Publisher	NUI Galway
Item record	http://hdl.handle.net/10379/14785

Downloaded 2024-04-20T02:40:32Z

Some rights reserved. For more information, please see the item record link above.



Micromechanical Modelling of Size Effects in Crack Initiation with Application to Fretting Fatigue and Cold Dwell Fatigue

Patrick J. Ashton B.E. (2014)

Supervisors: Prof. Sean Leen and Dr. Annette Harte



A thesis submitted to the National University of Ireland as fulfilment of the requirements for the Degree of Doctor of Philosophy

Mechanical Engineering, National University of Ireland, Galway.

2018

Contents

1	Introduction	1
1.1	General	1
1.2	Fretting	4
1.3	Fretting in Industry	6
1.4	Aims and Objectives	9
1.5	Overview of Thesis	10
1.6	References	12
2	Literature Review	15
2.1	General	15
2.2	Fatigue in Metals	15
2.2.1	General	15
2.2.2	Fatigue Crack Propagation	18
2.2.3	Fatigue Crack initiation	21
2.2.4	FCI Modelling	23
2.2.5	Life Prediction with Crystal Plasticity	26
2.3	Size Effects in Metals	28
2.4	Contact Mechanics	31
2.5	Tribology	34
2.5.1	General	34
2.5.2	Friction	34
2.5.3	Wear	35
2.6	Fretting	36

2.6.1	General	36
2.6.2	Fretting Fatigue	37
2.6.3	Microstructure Sensitive Fretting Fatigue.....	39
2.6.4	Fretting Wear	41
2.6.5	Size Effects in Fretting.....	42
2.6.6	Fretting in Marine Risers	44
2.7	Conclusions	44
2.8	References	45
3	Experimental Characterisation of Pressure Armour Steel	59
3.1	Introduction	59
3.2	Microstructure Characterisation	59
3.3	Strain-Controlled Testing	62
3.3.1	Unprocessed Rod Material.....	62
3.3.2	Processed Pressure Armour Wire Material	66
3.4	Nanoindentation Testing	69
3.5	Fretting Wear Testing.....	72
3.6	Conclusions	75
3.7	References	76
4	Micromechanical Modelling Methodology	79
4.1	Introduction	79
4.2	Large Deformation Mechanics	79
4.2.1	Deformation Gradient	79
4.3	Crystal Plasticity Theory	82
4.4	CP Material Models.....	86
4.4.1	Phenomenological Power Law Slip Rule.....	86

4.4.2	Physically-based Length-Scale Dependent Model.....	88
4.4.3	J ₂ Plasticity.....	94
4.5	Microstructure Geometry Modelling.....	95
4.5.1	General.....	95
4.5.2	2D Modelling.....	95
4.5.3	3D Microstructure Geometry Modelling.....	98
4.6	FCI Prediction.....	100
4.7	Crystallographic Orientation.....	102
4.7.1	General.....	102
4.7.2	Euler Angles and the Rotation Matrix.....	102
4.7.3	Pole Figures.....	104
4.8	Conclusion.....	106
4.9	References.....	106
5	Statistical Microstructure Effects in Fretting Crack Initiation.....	109
5.1	Introduction.....	109
5.2	Methodology.....	109
5.2.1	Constitutive Models.....	109
5.2.2	Microstructure Model.....	111
5.2.3	Fatigue Crack Initiation.....	114
5.2.4	Microstructure Sensitive Fretting Model.....	115
5.3	Results.....	119
5.3.1	Spatial Distributions.....	120
5.3.2	N _i Predictions.....	123
5.3.2	Effect of Δ	125
5.4	Conclusions.....	126

5.5	References	127
6	The Effect of the Beta Phase on the Performance of Dual-Phase Titanium Alloys 130	
6.1	Introduction	130
6.2	Material and Constitutive Model.....	131
6.3	CPFE Model Calibration	135
6.4	Alpha-Beta Colony Study	137
6.5	Application to Cold Dwell Fatigue	144
6.5.1	Methodology	144
6.5.2	Results and Discussion.....	147
6.6	Conclusions	151
6.7	References	152
7	A Strain Gradient, Crystal Plasticity Model for Microstructure-Sensitive Fretting Crack Initiation in Ferritic-Pearlitic Steel for Flexible Marine Risers.....	156
7.1	Introduction	156
7.2	Modelling Methodology and Calibration	157
7.3	Generation of Microstructure Geometries.....	158
7.4	Calibration of CP Material Parameters.....	159
7.5	Strain-Gradient Length-Scale Effects.....	161
7.6	Fatigue Prediction Model	163
7.7	Application to Fretting	166
7.7.1	Micromechanical Fretting Model.....	166
7.7.2	FCI Location and Initial Orientation.....	168
7.7.3	Strain Gradient Effects	171
7.8	Crystallographic Texture Effects.....	174
7.9	Conclusions	179

7.10	References	180
8	Conclusions and Future Work.....	183
8.1	Conclusions	183
8.2	Recommendations for Future Work	184
8.3	References	187
	Appendix A Fretting Fatigue Testing and Heat Treatment.....	189
	A1 Fretting Fatigue Testing	189
	A2 Heat Treatment	192
	Appendix B Preliminary 2D Microstructure-Sensitive Fretting Study	195
	B.1 Overview.....	195
	B.2 Unit Cell Model	195
	B.3 2D Fretting Model	196
	Appendix C Asperity Modelling.....	199
	C.1 Overview.....	199
	C.2 Methodology.....	199
	C.3 Results and Discussion	200
	Appendix D Mesh Sensitivity Studies	201
	D.1 Ti Unit Cell Model	201
8.4	D.2 Ti Dwell Model – Pure Alpha Microstructure.....	201
8.5	D.3 Ti Dwell Model –Alpha-Beta Microstructure	203
	Appendix E Python Scripts.....	204
	E.1 Overview.....	204
	E.2 2D Microstructure Model Generation.....	204

Abstract

This thesis presents the development of a micromechanical computational framework for microstructure sensitivity of crack initiation in metals, with application to fretting fatigue and cold-dwell facet fatigue. It is well-known that the mechanical and fatigue behaviour of metals is sensitive to a number of size effects, which can occur when critical component length-scales are directly comparable to key microstructural dimensions (e.g. grain size). For example, in fretting contacts, the key length-scales (e.g. contact width, relative slip) are typically of the order of micro-meters, and therefore fretting fatigue life is sensitive to size effects. This phenomenon is a concern for engineering designers across a broad range of applications as popular continuum mechanics-based mechanical analysis and fatigue prediction techniques are not representative of real material behaviour at small length-scales. However, micromechanical modelling techniques that explicitly model the material microstructure are capable of capturing size effects.

Three dimensional crystal plasticity (CP) modelling is employed to simulate the micromechanical response of three microstructurally distinct metals: CoCr alloy for biomedical applications, dual-phase alpha-beta Ti alloy for aerospace applications and ferritic-pearlitic steel for marine structural applications. A microstructure basis for a well-known contact size effect in fretting is identified through modelling of statistical and strain gradient size effects. A strain-gradient, length-scale dependent model has been successfully implemented in a crystal plasticity finite element (CPFE) fretting model. The model was thus able to demonstrate, for the first time, the beneficial effects of reducing length-scale (viz. smaller contact and microstructure length-scales) on resistance to fretting crack initiation.

A 3D cylinder-on-flat finite element fretting contact model is developed to incorporate realistic microstructure geometries and a CP material model in the fretting contact zone. The micromechanical fretting model predicts that a key consideration in the design of metallic fretting contacts is the ratio of contact semi-width to average grain size. A critical contact semi-width to average grain size ratio of approximately 1 is identified,

below which an increase in fatigue scatter and increase in average number of cycles to crack initiation is observed. It is shown that values greater than 1 should be chosen in the design of fretting contacts to reduce uncertainty in fatigue life predictions

A physically-based, length-scale dependent material model is employed to determine the role of the beta phase on the micromechanical response of a dual-phase alpha-beta Ti alloy. Beta lath width and relative orientation is shown to significantly affect the micromechanical response of the material. The role of the beta phase in cold-dwell facet fatigue is investigated; the presence of beta laths in a rogue grain combination is predicted to increase dwell fatigue resistance. The key driving force in “faceting”, the rogue grain local normal stress, is shown to reduce by as much as 12% with explicit inclusion of beta laths.

A CPFE fretting modelling framework is developed to study the role of length-scale effects and crystallographic texture in fretting crack initiation of ferritic-pearlitic steel for marine risers. A program of experimental testing has facilitated the calibration and validation of the material model and fatigue prediction model. Strain gradient length-scale effects and crystallographic texture are shown to play a key role in the predicted number of cycles to crack initiation. By decreasing the length-scale of the fretting contact by a factor of 10, an increase of up to 24% in number of cycles to crack initiation is predicted. The texture induced by cold forming of the marine riser material is shown to be beneficial in fretting crack initiation.

Acknowledgements

Firstly, I wish to thank my supervisors Prof. Sean Leen and Dr. Annette Harte for their guidance and support during this research. I would like to thank Prof. Fionn Dunne for his invitation to carry-out a research visit to Imperial College London to gain experience on strain-gradient computational modelling. Thanks to the Irish Research Council for funding this research.

I would also like to thank to the research students and staff in NUI Galway for their assistance with computational modelling and experimental work. In particular, Conor, Eimear and Dr. Barry O'Brien for microscopy advice, Caoimhe for help with CP modelling, Reyhaneh and Ronan for nanonindentation training, and Sinead for fretting and fatigue testing assistance. Thanks as well to Brian, Donncha, Enda, Spoon, Tarek, Shane and all the other postgrads for the craic.

I wish to thank the technical staff at NUI Galway for providing assistance with experimental work. A special thanks to William Kelly for his consistent help with IT issues, Boni Kennedy for manufacturing specimens and Pat Kelly for test set-up and general help. Thanks to Dr. Eadaoin Timmins at the National Centre for Biomedical Engineering Science (NCBES) for providing training in SEM operation.

Lastly, I would like to thank my parents for their support and the enjoyable weekends away in Dingle and on the Corrib.

List of Publications

Published Journal Papers

P. J. Ashton, A. M. Harte, and S. B. Leen, “Statistical grain size effects in fretting crack initiation,” *Tribol. Int.*, vol. 108, pp. 75–86, 2016.

P. J. Ashton, T. S. Jun, Z. Zhang, T. B. Britton, A. M. Harte, S. B. Leen, and F. P. E. Dunne, “The effect of the beta phase on the micromechanical response of dual-phase titanium alloys,” *Int. J. Fatigue*, vol. 100, pp. 377–387, 2017.

P. J. Ashton, A. M. Harte, and S. B. Leen, “A strain-gradient, crystal plasticity model for microstructure-sensitive fretting crack initiation in ferritic-pearlitic steel for flexible marine risers,” *Int. J. Fatigue*, vol. 111, pp. 81-92, 2018.

Acronyms

2D	Two-dimensional
3D	Three-dimensional
BCC	Body centre cubic
BOR	Burgers orientation relationship
CoCr	Cobalt Chromium
COF	Coefficient of friction
CP	Crystal Plasticity
CPFE	Crystal plasticity finite element
DDP	Discrete dislocation plasticity
DIC	Digital image correlation
DVRT	Differential variable reluctance transducer
EBSD	Electron backscatter diffraction
EDX	Energy-dispersive X-ray spectroscopy
FCC	Face centre cubic
FCI	Fatigue crack initiation
FDA	Food and Drug Association
FE	Finite Element
FIB	Focused ion beam
FIP	Fatigue indicator parameter
FS	Fatemi-Socie
GND	Geometrically necessary dislocation
HCF	High-cycle fatigue
HCP	Hexagonal close packed
IHD	Ischemic heart disease
IPF	Inverse Pole Figure

LCF	Low-cycle fatigue
LCG	Long crack growth
LEFM	Linear elastic fracture mechanics
LVDT	Linear variable differential transducer
MSCG	Microstructurally small crack growth
NLKH	Non-linear kinematic hardening
PSB	Persistent slip bands
PBCs	Periodic boundary conditions
SEM	Scanning electron microscope
SCG	Short crack growth
S-N	Stress-life
SS	Stainless steel
SWT	Smith-Watson-Topper
Ti	Titanium
UMAT	User material subroutine
UEL	User element subroutine
XFEM	Extended finite element method

1 Introduction

1.1 General

It is estimated that fatigue is the key life limiting factor for 50 to 90% of all mechanical components [1]. Any structure or component that experiences cyclic loading is likely to experience fatigue damage. In the present day, engineering components and systems are required to withstand increasingly harsh and complex environments. For example, the search for subsea oil and gas is continually extending into greater and harsher water depths. Similarly in the biomedical engineering industry, orthopaedic and cardiovascular implants are expected to perform without failure for ten years, and in the aerospace industry the search for new light-weight materials to increase fuel efficiency is on-going. Critical mechanical components implemented in the latter industries are loaded cyclically and are thus susceptible to fatigue during service. It is therefore more important than ever to understand the causes of fatigue damage in these components to avoid premature failure and the potentially catastrophic consequences.

The fatigue design processes currently employed in industry are typically on conservative prediction techniques that rely on a number of simplifying assumptions. For example, the assumption of a linear elastic, homogeneous material is often made for fatigue life prediction despite the well-known importance of localised plastic strain in fatigue. A common technique for prediction of fatigue life, which is used in the subsea oil and gas industry, is to perform computational finite element analysis of a component to identify fatigue ‘hotspots’ where stress concentrations exist and then calculate fatigue life using experimentally determined stress-life (S-N) data for the relevant material. A large factor of safety is often applied in fatigue analysis to account for assumptions made in the above, or similar, predictive techniques, such as scatter in S-N data, uncertainty in material behaviour and the presence of complex loading conditions. The uncertainty associated with using high factors of safety has a number of undesirable outcomes, including: (i) increased manufacturing costs associated with excessive use of material in order to reduce over-predicted stresses and strains (ii) the premature

replacement of in-service components due to conservative life predictions and (iii) the risk of failure due to insufficient knowledge of the material and component system. For example, a factor of safety of 10 [2] is employed for fatigue predictions in the subsea oil and gas industry to account for the uncertainty associated with a number of stochastic factors, including environmental conditions, and material behaviour under complex multi-axial loading. This results in significant additional costs with respect to the manufacture of mechanical components, where in-service components are replaced before any significant fatigue damage has occurred. It is clear that the use of more rigorous life prediction techniques (that account for microstructure, surface roughness etc.) will be beneficial, both economically and environmentally.

Fatigue life can generally be divided into three stages: crack nucleation, short crack growth, and crack propagation. The latter stage of propagation is relatively well understood and theoretical predictions using linear elastic fracture mechanics give reasonable results. Some life prediction techniques, in cardiovascular stents for example, neglect the crack initiation stage and implement fracture mechanics to calculate the number of cycles to propagate the largest pre-existing flaw in the component [3]. However, this approach is undoubtedly over conservative, as a significant portion of fatigue life for metal components can be consumed by the initiation stage [4], particularly at low applied stresses. Crack initiation in metals is still the subject of widespread research. Crack nucleation and early stage growth in metals is highly sensitive to a number of factors including material microstructure, manufacture quality and loading conditions, and thus a number of complex mechanisms can potentially drive the nucleation of cracks, and it is crucial that research is aimed at this topic.

Advances in computational infrastructure and material science over the past two decades has allowed engineers to explicitly represent microstructure in computational mechanical analysis, and hence better understand the mechanical and fatigue behaviour by identifying the physical mechanisms which drive crack initiation. The microstructure of metals typically consists of grains with differing crystallographic orientations, multiple phases, inclusions, and precipitates among other small-scale features, depending on the type of metal. The onset of fatigue damage is often related to these

microstructural features. For example, in ferritic steels, fatigue cracks have been observed to initiate where favourably oriented grains, with respect to the loading direction, occur at the surface of the component [5] and localised regions of microscale plasticity form.

An example of how micromechanical computational analysis can benefit fatigue design is seen in the aero-engine industry. Titanium alloys are used to manufacture numerous aero-engine components due to their superior properties, including high strength to weight ratios and corrosion resistance. However premature fatigue failure has been observed in a number of these alloys due to the phenomenon of cold dwell. The ability of these materials to creep at low temperatures combined with the presence of a dwell period during the in-service loading cycles results in a significant reduction in fatigue life compared to standard cyclic loading. The phenomenon of cold dwell has been known for over 40 years, but is still not fully understood. It was first brought to attention in 1972 after the failure of fan discs in Rolls-Royce RB211 engines [6]. As a result, extensive research projects were initiated to remedy the problem. In recent times, micromechanical computational analysis of such materials under dwell loading conditions has shown that the nucleation of fatigue cracks is associated with regions where a particular combination of grains exist in the microstructure [7]. However, a comprehensive understanding of the key microstructure characteristics in dwell fatigue has not yet been achieved, as a number of Ti alloys exist, with varying chemical compositions, phase volume fractions and phase distributions.

The use of micromechanical prediction techniques is especially beneficial for components with small associated length-scales. One such application is coronary stents, which are used to treat ischemic heart disease (IHD). IHD is a condition where blood flow through coronary arteries is restricted by the build-up of plaque. Stents are deployed to re-open the closing artery through non-surgical angioplasty procedure. This procedure employs a catheter to locate the blockage, and an inflatable balloon to expand and plastically deform the stent to open the plaque blockage and restore normal blood flow, as shown in Fig. 1.1a. The dimensions of metallic stent struts are of the order of microns, similar to the average grain size of the materials, such as CoCr alloy and 316L

SS. The mechanical behaviour, and therefore fatigue behaviour is governed by a small number of grains across the cross section of each strut (Fig. 1.1b), as demonstrated by Grogan et al [8]. This can potentially result in a significant statistical variation in number of cycles to fracture of nominally identical stents at the macro-scale. Over 2.5 million stents are deployed worldwide each year, and the number of reported stent fractures is increasing [9]. It is obvious that the current recommendations for fatigue analysis are insufficient given the materials employed and the available computational resources. Currently the FDA advises computational finite element analysis of stents incorporating non-linear material models; the explicit representation of material microstructure is not emphasised despite the advantages highlighted by Sweeney et al [10], whereby small grained components show superior fatigue performance.

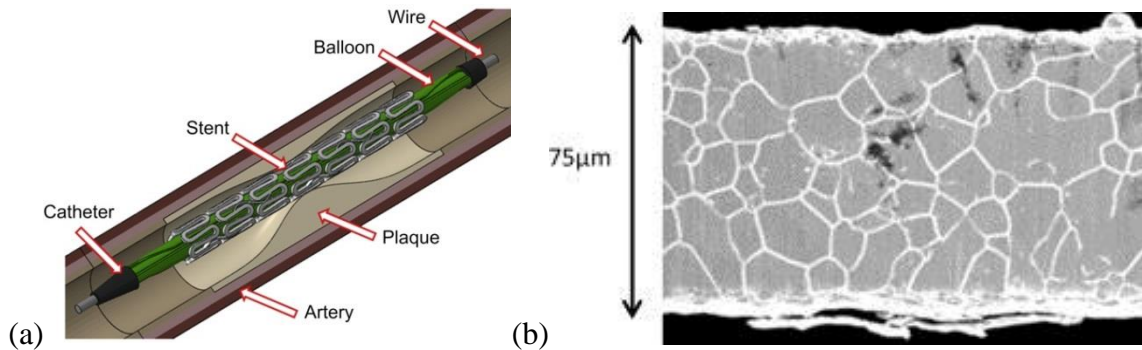


Figure 1.1. (a) A schematic of coronary stent [11] and (b) microscope image of stent strut showing small number of grains across the thickness [12].

1.2 Fretting

Fretting is a particularly detrimental form of fatigue that occurs when a small-scale (typically micro-scale) cyclic relative displacement exists between two surfaces in contact. Fretting is a concern for engineering designers as localised regions of high stresses and strains in the contact act as ideal locations for fatigue cracks to nucleate, and potentially grow under a bulk load. Extensive research has shown the detrimental effects of fretting by including fretting contacts in standard uniaxial fatigue experiments and observing a considerable reduction in life.

The small length-scales generally associated with fretting contacts suggest that microstructure can play a key role in fretting fatigue performance, as suggested in Fig 1.2. Typically the highly localised contact region is of the order of microns and may contain only a small number of metallic grains with varying crystallographic orientations, depending on contact geometry, loading conditions and materials. It would therefore appear to be important to explicitly include the effect of microstructure in fretting fatigue prediction to achieve a more accurate representation of the material, and hence, better understand the mechanisms that drive crack initiation.

An important size effect has been observed by a number of authors for a cylinder on flat contact [13], [14] whereby a critical contact size exists below which fatigue life increases dramatically. An understanding of this effect is critically important for reliable design as smaller contact sizes may have superior fretting fatigue performance. It has been suggested by Araújo and Nowell [15] that it is the combination of both contact size and microstructure which determine the significance of this effect. Therefore a detailed analysis of both microstructure and contact size would provide a better understanding of this complex phenomenon, and thus potentially transform the design of engineering components and materials against fretting damage.

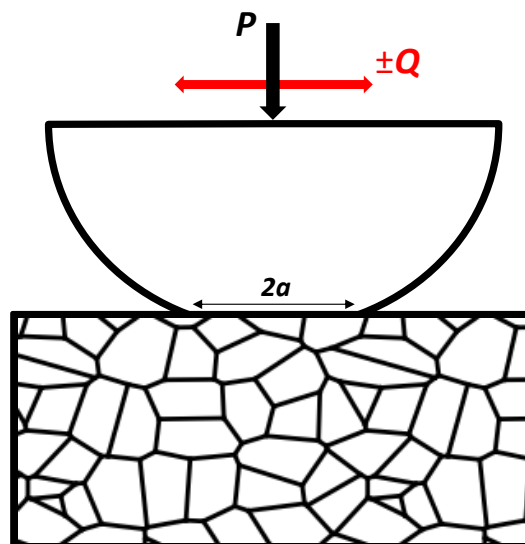


Figure 1.2. Schematic of cylinder-on flat fretting model showing material microstructure and contact width $2a$.

1.3 Fretting in Industry

The problem of fretting arises in a number of engineering industries, including aerospace, biomedical and the offshore marine industry. It is estimated that the US aerospace industry invests 20 million USD [16] on maintenance and inspection of fretting damage in turbine engine components; shaft spline couplings (Fig. 1.3) and dovetail blade-disk connections are particularly susceptible. Biomedical implants such as cardiovascular stents and orthopaedic implants are also susceptible to fretting damage. In the case of stents, fretting can occur when multiple stents are deployed in a patient with recurring lesions, for example. Regions of overlapping stents may exist in the patient, leading to fretting damage [17].

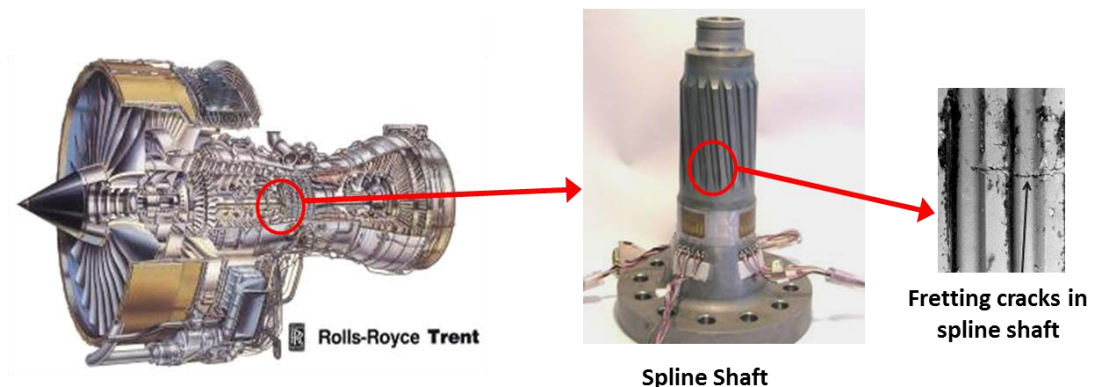


Figure 1.3. Fretting in spline shaft couplings.

A relatively recent observation is the risk of fretting in flexible marine risers [18]. Flexible marine risers serve the purpose of transporting hydrocarbons from a subsea well to a floating production vessel. Riser systems are subject to extreme dynamic loads resulting from wind, wave and current conditions. Risers are composed of a number of polymer and metallic layers, each of which serves a specific purpose to ensure safe extraction of oil and gas in harsh environments. One such layer, the pressure armour layer, is particularly susceptible to fretting [19]. This steel layer is designed to resist external pressures due to large water depths and internal hydrocarbon pressure and therefore, prevent pipe collapse and burst. For one design, the cross section of the wire has a ‘zeta’ profile, which is wound helically to form a pipe with an interlocking nub-groove region, as shown in Fig. 1.4. This design provides bending flexibility to

compensate for vessel motions. However, the interlocking of the zeta profile leads to potential fretting damage, as the nub and groove move relative to each other during pipe bending. Current design procedures do not account for fretting of the pressure armour wire in fatigue life predictions of marine risers.

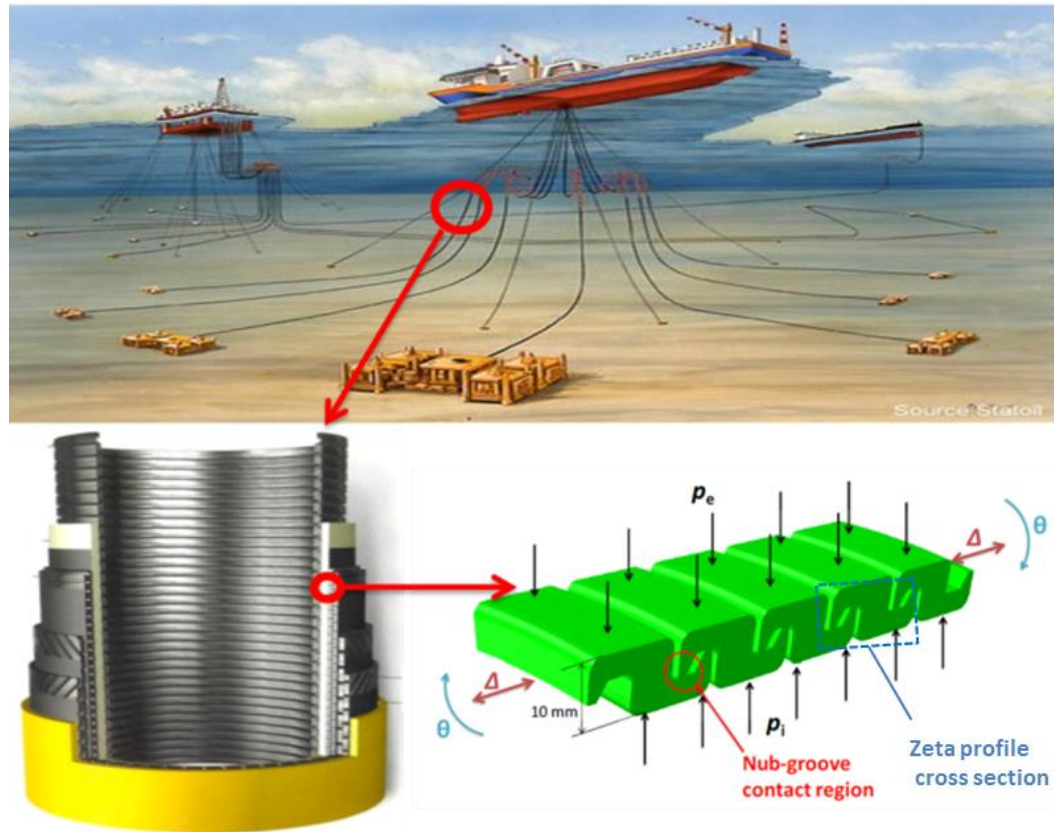


Figure 1.4. The pressure armour layer in flexible marine risers.

It is critical that all potential failure mechanisms of these pipes are clearly understood to prevent catastrophic environmental damage and ensure economic extraction of hydrocarbons, especially given the current slump in oil prices. In recent times in-service risers have been removed on reaching the predicted fatigue life, and replaced with new risers costing approximately 1.3 million euro per riser plus installation costs. Upon inspection, no significant fatigue damage was observed in a number of these retrieved pipes. This shows that current prediction techniques are overly conservative, as a result of the large factors of safety used to account for the significant design assumptions. On the other hand, if the factors of safety are reduced without a scientific basis, the risk of

pipe failure is dramatically increased. The potential results of such a subsea failure can be seen in the Deepwater Horizon disaster of 2010, where the spillage of oil caused catastrophic environmental damage and a clean-up operation costing approximately 55 billion euros.

In light of the above, industry corporations are interested in improving their fatigue prediction techniques by studying all potential failure mechanisms, and developing better understanding of the fatigue behaviour of these complex components. One area which has recently been assessed is the significance of fretting in the pressure armour wire, as studied by O'Halloran [20]. This work has shown that riser systems are susceptible to fretting fatigue, depending on loading conditions. An outcome of this work was the benefit of large relative displacements in the nub-groove contact region, which reduce the possibility of fretting crack initiation due to gross slip ear effects. However, the role of some key parameters, such as material microstructure, in fretting of the pressure armour wire has not yet been quantified.

The design codes for dynamic riser fatigue analysis [21] currently require that stress concentration factors are determined, via local FE analysis for example, and applied to S-N data to determine the predicted life. Another requirement is that all component stresses remain elastic under the expected environmental loading whilst in service. However, the fretting-induced contact stresses are currently neglected, so it is likely that localised plasticity occurs in the pressure armour layer, as shown by O'Halloran [20]. In addition component-level elastic stresses and strain can be large enough to induce micro-plasticity in the microstructure of the material, which can lead to crack initiation under dynamic loading. It is therefore necessary that the combined effects of microstructure and fretting in riser fatigue are investigated.

1.4 Aims and Objectives

The aim of this thesis is to develop a microstructure-sensitive methodology for fatigue and fretting, with particular application to fretting of ferritic-pearlitic steel for flexible marine risers, cold-dwell fatigue of Ti alloy for aero-engines, and fretting of CoCr for biomedical applications. It is anticipated that the findings of this research will also be relevant to a broader range of applications. The key objectives are as follows:

1. Develop 3D crystal plasticity fretting model including microstructure generation techniques, and apply to statistical size effects for fretting.
2. Develop length-scale dependent crystal plasticity model for dual-phase Ti alloys with application to effect of β phase on cold dwell fatigue.
3. Experimentally characterise the fatigue (low cycle) and fretting behaviour of ferritic-pearlitic marine riser steel for flexible armour layer contacts.
4. Develop a length-scale dependent crystal plasticity model for dual-phase ferritic-pearlitic riser steel for fatigue and fretting and implement scale-consistent fatigue indicator parameters.
5. Investigate the effects of strain gradients due to microstructure and contact size in fatigue and fretting of dual-phase ferritic-pearlitic steel for marine risers.

These objectives can be viewed as four key steps towards the development of a computational framework for studying length-scale effects in fretting, as shown in the flowchart presented in Fig. 1.5.

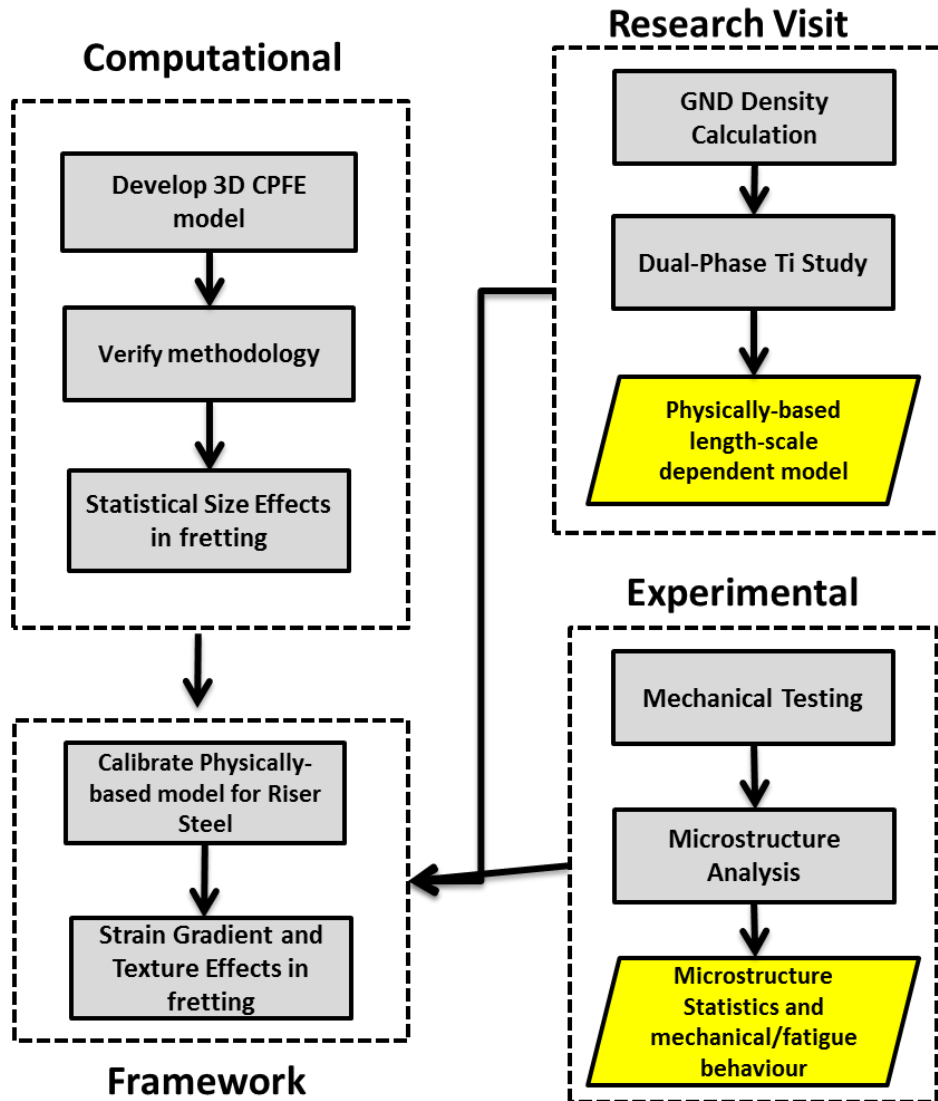


Figure 1.5. Methodology flowchart for the development of a length-scale dependent CPFE fretting model.

1.5 Overview of Thesis

Chapter 2 provides a review of the literature relevant to this work, including established fatigue prediction techniques, micromechanical modelling of fatigue crack initiation and computational modelling and experimental testing of fretting fatigue. An overview of the various computational modelling approaches for fretting and fatigue is presented.

Chapter 3 describes the experimental work carried out on the marine riser material in this thesis. This includes (i) characterisation of the fatigue behaviour of the marine riser material through a series of LCF tests (ii) preparation of microscopy samples and microstructural analysis to characterise the microstructure of the material (iii) determination of COF via plain fretting tests.

Chapter 4 is concerned with the development of a microstructure-sensitive finite element models. A description of the two crystal plasticity constitutive models implemented in this work is given. The modifications made to these models are discussed, including the calculation of length-scale effects and the introduction of kinematic hardening. The combined ABAQUS-Python scripting methodology developed to generate representative finite element geometries of material microstructures is presented. A preliminary study on microstructure sensitivity in fretting is first presented for a 2D case. The additional complexity of a 3D case is then described and implemented in the remainder of the thesis. The process of identifying material parameters for the constitutive models by calibrating the predicted cyclic mechanical response of unit cell models against measured experimental data is described. The development of a 3D microstructure sensitive cylinder-on-flat fretting model is described; the calibrated material model and representative microstructure geometries are included in the contact zone. Finally, the fatigue prediction methodology is described. A number of candidate scale-consistent fatigue indicator parameters are adapted and implemented in this work. The mechanistic basis behind each parameter is discussed here.

Chapter 5 presents a computational study of the statistical size effects in fretting crack initiation for a CoCr alloy. The microstructure sensitive fretting model described in Chapter 4 and previously published crystal plasticity material parameters and microstructure statistics for this material are employed in this study. Two potentially important fretting parameters are assessed: the ratio of contact semi-width a to average grain size d (a/d), and relative slip Δ to average grain size d (Δ/d). The former ratio is shown to have a significant influence on predicted fretting crack initiation.

Chapter 6 investigates the role of beta phase on the micro-mechanical behaviour of dual-phase titanium alloys, with particular emphasis on the phenomenon of cold dwell

fatigue, which occurs in such alloys under room temperature conditions. The length-scale dependent crystal plasticity model described in Chapter 4 is calibrated against micro-pillar compression test data for a dual-phase alpha-beta specimen. The effects of key microstructural variables, such as relative beta lath orientation and lath spacing, on the micromechanical response of idealised alpha-beta colony microstructures is investigated. A study on the effects of beta laths on the local micromechanical variables controlling cold dwell fatigue is also presented.

Chapter 7 is concerned with the prediction of microstructure-sensitive length-scale effects and crystallographic texture in crack initiation, under fatigue and fretting fatigue conditions, for the ferritic-pearlitic steel material used in flexible marine risers. Length-scale effects arising from the presence of plastic strain gradients potentially play a significant role in fretting fatigue due to the small length-scales associated with the contact region and microstructure. Prediction of the effects of length-scale on fretting crack initiation is based on the three-dimensional, crystal plasticity, frictional contact model described in Chapter 4. In addition, a critical plane micro-scale fatigue indicator parameter is employed to predict fretting crack location and initial growth path, accounting for the effects of crystallographic orientation. The crystallographic texture induced by cold-drawing is also shown to significantly affect crack initiation.

Chapter 8 states the conclusions of this thesis, and provides a discussion on the key findings. Finally, recommendations are made with regards to future work.

1.6 References

- [1] H.O. Fuchs and R.I. Stephens, *Metal Fatigue Engineering*. New York: John Wiley & Sons, 1980.
- [2] API, "Recommended practices for flexible marine risers," 17J, (Journal Article), *Am. Pet. Ind.*, 2009.

-
- [3] R. V. Marrey, R. Burgermeister, R. B. Grishaber, and R. O. Ritchie, “Fatigue and life prediction for cobalt-chromium stents: A fracture mechanics analysis,” *Biomaterials*, vol. 27, no. 9, pp. 1988–2000, 2006.
- [4] D. L. McDowell and F. P. E. Dunne, “Microstructure-sensitive computational modeling of fatigue crack formation,” *Int. J. Fatigue*, vol. 32, no. 9, pp. 1521–1542, 2010.
- [5] V. S. Sarma and K. A. Padmanabhan, “Low cycle fatigue behaviour of a medium carbon microalloyed steel,” *Int. J. Fatigue*, vol. 19, no. 2, pp. 135–140, 1997.
- [6] M. R. Bache, “A review of dwell sensitive fatigue in titanium alloys: The role of microstructure, texture and operating conditions,” *Int. J. Fatigue*, vol. 25, no. 9–11, pp. 1079–1087, 2003.
- [7] F. P. E. Dunne, D. Rugg, and a. Walker, “Lengthscale-dependent, elastically anisotropic, physically-based hcp crystal plasticity: Application to cold-dwell fatigue in Ti alloys,” *Int. J. Plast.*, vol. 23, no. 6, pp. 1061–1083, 2007.
- [8] J. A. Grogan, S. B. Leen, and P. E. McHugh, “Influence of statistical size effects on the plastic deformation of coronary stents,” *J. Mech. Behav. Biomed. Mater.*, vol. 20, pp. 61–76, 2013.
- [9] R. N. Nair and K. Quadros, “Coronary Stent Fracture: A Review of the Literature,” *Card. Cath Lab Dir.*, vol. 1, no. 1, pp. 32–38, 2011.
- [10] C. A. Sweeney, “Micromechanics of fatigue with application to stents,” PhD Thesis, National University of Ireland Galway, 2014.
- [11] J. A. Grogan, S. B. Leen, and P. E. McHugh, “Optimizing the design of a bioabsorbable metal stent using computer simulation methods,” *Biomaterials*, vol. 34, no. 33, pp. 8049–8060, 2013.
- [12] P. Savage, B. P. O’Donnell, P. E. McHugh, B. P. Murphy, and D. F. Quinn, “Coronary Stent Strut Size Dependent Stress-Strain Response Investigated Using

Micromechanical Finite Element Models,” *Ann. Biomed. Eng.*, vol. 32, no. 2, pp. 202–211, Feb. 2004.

[13] R. Bramhall, “Studies in fretting fatigue,” PhD Thesis, University of Oxford, 1973.

[14] D. Nowell, “An analysis of fretting fatigue,” PhD Thesis, University of Oxford, 1988.

[15] J. A. Araújo and D. Nowell, “The effect of rapidly varying contact stress fields on fretting fatigue,” *Int. J. Fatigue*, vol. 24, no. 7, pp. 763–775, 2002.

[16] T. N. Farris, M. P. Szolwinski, and G. Harish, “Fretting in Aerospace Structures and Materials,” ASTM STP 1367, 2000.

[17] K. K. Kapnisis, D. O. Halwani, B. C. Brott, P. G. Anderson, J. E. Lemons, and A. S. Anayiotos, “Stent overlapping and geometric curvature influence the structural integrity and surface characteristics of coronary nitinol stents,” *J. Mech. Behav. Biomed. Mater.*, vol. 20, pp. 227–236, 2013.

[18] S. A. Lotveit and R. Bjaerum, Second generation analysis tool for flexible pipes, in: *Proceedings of the Second European Conference on Flexible Pipes, Umbilicals and Marine Cables-Structural Mechanics and Testing*. London: Bentham, 1994.

[19] R. Perera, S.D.R., Fernando, U.S., Sheldrake, T., Clements, “An investigation into fretting behaviour in pressure armor wires of unbonded flexible pipes,” in *Volume 3: Pipeline and Riser Technology; CFD and VIV*. San Diego, California, USA, 2007, pp. 363–370.

[20] Sinead O’Halloran, “Experimental Characterisation, Computational Modelling and Design Tool Development for Fretting Fatigue and Wear in Flexible Marine Risers,” PhD Thesis, NUI Galway, 2017.

[21] Det Norske Veritas, “DNV-OS-F201 Dynamic Risers,” no. October, p. 91, 2010.

2 Literature Review

2.1 General

Fatigue in metals has been the focus of extensive research due to its prevalence across a wide range of industries. The complex multi-scale nature of fatigue has resulted in a depth of scientific discovery across a range of materials and length-scales. In this thesis, fatigue crack initiation, particularly fretting crack initiation, is the focus. Therefore, key findings regarding fatigue crack initiation in metals are discussed in this chapter, with emphasis on microstructure sensitive modelling and fretting. A number of areas have been identified where further work is required. These areas will be addressed in this thesis.

2.2 Fatigue in Metals

2.2.1 General

The fatigue process is typically divided into two regimes, depending on the presence of macroscopic plastic deformation resulting from the cyclically applied load. The high-cycle fatigue regime (HCF) corresponds to nominally elastic loading conditions, resulting from low stress or strain amplitudes. The low-cycle fatigue (LCF) regime results from macroscopically plastic loading conditions. Fatigue of a metal component can generally be attributed to one of these two distinct regimes so that the S-N behaviour can be represented as bi-linear, as shown schematically in Fig. 2.1. Traditionally, fatigue life is estimated using empirical relations for each regime. The Basquin equation [1] estimates number of cycles to failure N_f for a given applied stress range $\Delta\sigma$:

$$\frac{\Delta\sigma}{2} = \sigma_f' (2N_f)^b \quad (2.1)$$

where σ'_f is the fatigue strength coefficient and b is the fatigue strength exponent, which are determined from experimentally measured S-N data. Similarly the fatigue life in the low-cycle fatigue regime can be calculated using the empirical Coffin-Manson relationship. In low-cycle fatigue, the plastic strain range $\Delta\varepsilon_p$ is a more appropriate measure than stress, as the stress range becomes unsuitable in the presence of macroscopic plasticity (due to the presence of softening and hardening). The number of cycles to failure can therefore be estimated by:

$$\frac{\Delta\varepsilon_p}{2} = \varepsilon'_f (2N_f)^c \quad (2.2)$$

where ε'_f and c are the fatigue ductility coefficient and exponent, respectively, for a given material.

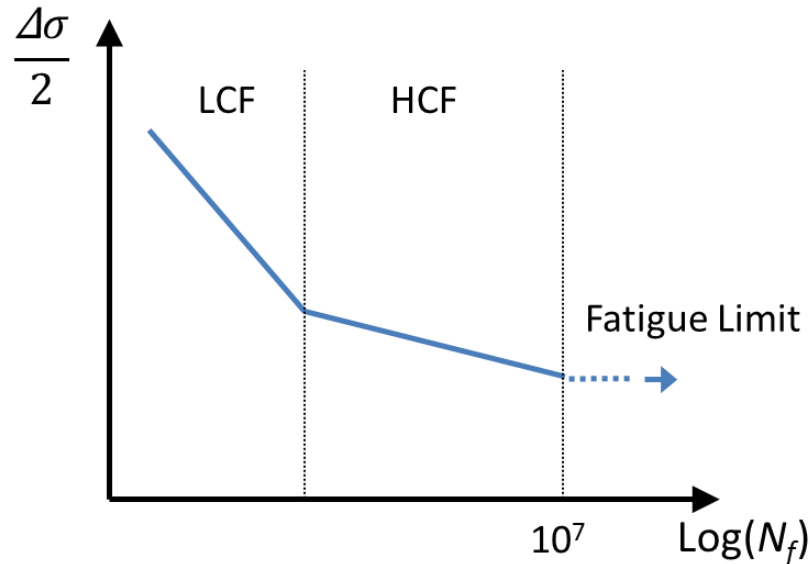


Figure 2.1. A schematic of fatigue regimes in terms of the stress-life relationship.

Complex loading conditions often exist in real-life applications, and therefore the simple approaches described above, for predicting fatigue life are often inadequate. Alternative methods have been developed to account for the additional parameters which have been shown to affect fatigue performance. For example, a more robust Smith-Watson-Topper [2] approach has been developed to cover a wide range of loading conditions and

account for the effect of mean stress. The SWT parameter combines the Basquin and Coffin-Manson equations, where total strain range is used:

$$SWT = \sigma_{max} \frac{\Delta\varepsilon}{2} = \frac{(\sigma'_f)^2}{E} (2N_f)^{2b} + \sigma'_f \varepsilon'_f (2N_f)^{b+c} \quad (2.3)$$

where σ_{max} is the maximum normal stress and E is the elastic modulus. The SWT is an example of a fatigue indicator parameter (FIP). FIPs are commonly used to measure fatigue damage. They are particularly useful in the context of finite element modelling, where the cyclic accumulation of a chosen FIP at each material point can be calculated to identify critical locations and estimate N_f .

Fatigue loading is often multi-axial, and therefore assessment of the three dimensional stress-strain state is required. For this purpose, a critical plane approach is commonly used, where an incremental process identifies the material plane with the highest value of a FIP. Some FIPs often used in this context are; (i) Brown and Miller [3], which combines normal and shear strain, (ii) Fatemi Socie [4], which considers shear strain and normal stress and (iii) a modified SWT parameter, which combines the effect of maximum normal stress and normal strain amplitude in tensile cracking modes and maximum normal stress and shear strain amplitude in shear cracking modes.

Figure 2.1 also shows a region where the applied stress range results in N_f greater than 10^7 cycles, which is considered to be the fatigue limit, where stresses below this stress do not pose a threat in terms of fatigue failure. However, in recent times, this limit has become a problem for designers in the biomedical industry [5]. Experimental fatigue tests for coronary stent materials are stopped after 10^8 cycles, as the recommended practice requires stents to only reach this limit. However, after installation, stents can experience significantly more than 10^8 cycles. Consequently, there is uncertainty associated with this method of life prediction, which poses a risk to the safety of the patient. It has been observed that a third fatigue regime exists, termed the ultra-high cycle fatigue (UHCF) [6].

The above approach describes classical techniques for predicting total fatigue life. However, as mentioned in Chapter 1, fatigue life consists of initiation and propagation

stages. A more thorough description of fatigue life is the following decomposition of N_f into:

$$N_f = N_i + N_{msc} + N_{psc} + N_{lc} \quad (2.4)$$

where N_i is crack initiation life, N_{msc} , is microstructurally small crack growth life, N_{psc} is physically small crack growth life and N_{lc} is long crack growth life.

2.2.2 Fatigue Crack Propagation

Linear elastic fracture mechanics (LEFM) is employed for predicting long crack growth. The localised plastic deformation at the crack tip is small when compared to the crack length, allowing the assumption of linear elastic material behaviour to be made. The Paris law [7] is a popular and effective method for predicting long crack growth, where the growth rate of an existing small crack a , in a dynamic stress field at the crack tip is calculated as follows:

$$\frac{da}{dN} = C(\Delta K)^m \quad (2.5)$$

where $\frac{da}{dN}$ is the increase in crack length per cycle, C and m are material constants, and ΔK is the stress intensity factor. The magnitude of ΔK depends on geometry and loading conditions and is typically calculated as follows:

$$\Delta K = \Delta\sigma Y \sqrt{\pi a} \quad (2.6)$$

where $\Delta\sigma$ is the cyclic stress range and Y is a geometrical factor.

Crack growth is generally divided into three regimes; short crack growth, long crack growth, and an unstable regime until fracture, as shown in Fig. 2.2. The power law relationship described by the Paris equation can successfully predict the long crack growth behaviour. However as ΔK is reduced, a threshold value ΔK_{th} is reached and the predicted crack growth rate tends to zero, as shown in Fig. 2.2. This small-scale behaviour cannot be captured by the Paris model.

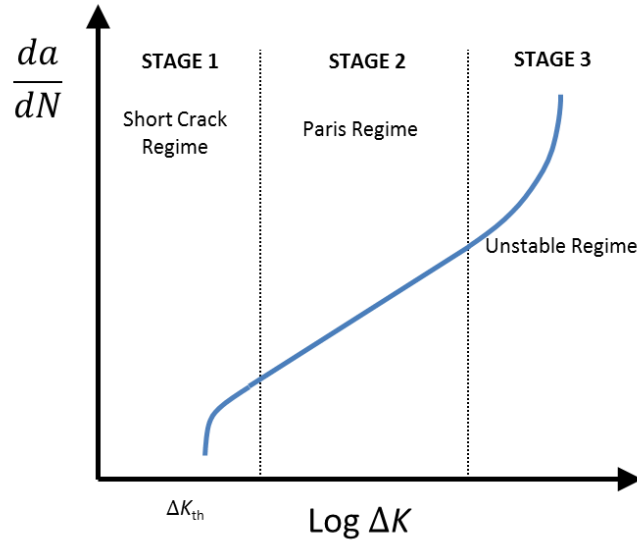


Figure 2.2. A schematic of crack growth regimes.

El-Haddad [8] introduced an additional term for calculating stress intensity factor to account for the growth of small cracks, which is not captured by the Paris law. A threshold crack length a_{th} , is included in the calculation of ΔK , which represents the change of regime from short crack growth to long crack growth:

$$\Delta K = \Delta\sigma Y \sqrt{\pi(a + a_{th})} \quad (2.7)$$

where a_{th} is related to the threshold stress intensity factor and the fatigue endurance limit σ_e :

$$a_{th} = \frac{1}{\pi} \left(\frac{\Delta K_{th}}{\sigma_e} \right)^2 \quad (2.8)$$

The change in crack growth regime at this threshold crack size has been shown by Kitagawa and Takahashi [9], who experimentally measured the growth of small cracks at low stress ranges, and noticed the relatively low rate of growth when $a < a_{th}$. The Kitagawa –Takahashi diagram, shown in Fig. 2.3, illustrated this change in regime from short crack growth to long crack growth.

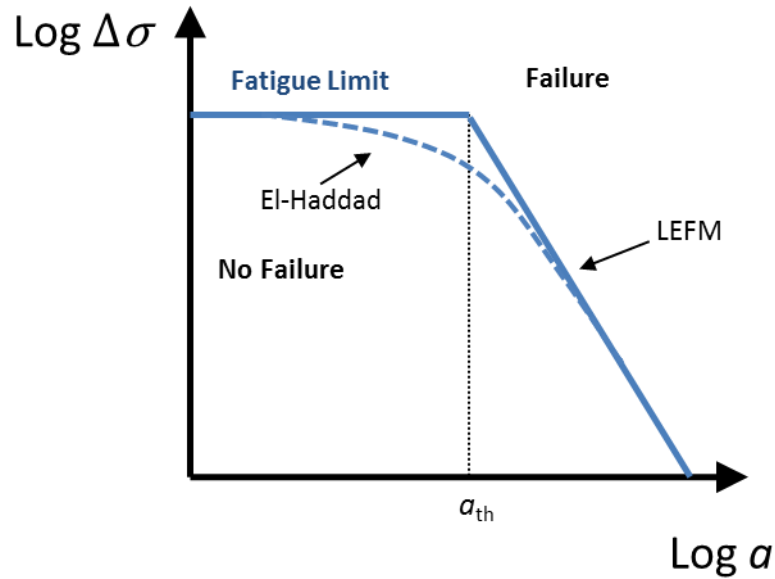


Figure 2.3. Kitagawa and Takahashi diagram for short crack growth [9].

Elastic-plastic fracture mechanics is implemented when the crack length is similar in size to the plastic strain field around the crack tip. The J -integral technique developed by Rice [10] can be used to analyse crack behaviour in these conditions, where J represents the strain energy release rate. The calculation of the J -integral, involves integrating along an arbitrary closed path around a crack tip, as shown in Fig. 2.4, and is calculated as follows:

$$J = \int_{\Gamma} \left(W dy - \mathbf{T} \cdot \frac{\partial \mathbf{u}}{\partial x} ds \right) \quad (2.9)$$

where Γ is any closed curve around the crack tip, W is the strain energy density, u is the displacement vector, ds is an increment on the curve Γ and T is the traction vector determined from the stress tensor σ_{ij} and normal vector n along Γ :

$$\mathbf{T}_i = \sigma_{ij} n_j. \quad (2.10)$$

A crack is predicted to grow when J is greater than a critical value J_c , which can be determined experimentally.

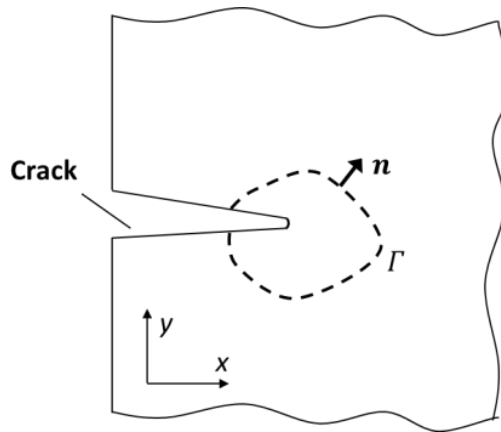


Figure 2.4. A schematic of the J-integral method.

The methods described above concerned with crack growth can neglect the effect of material microstructure with reasonable results. However, as the length-scale associated with cracks is reduced, the role of material microstructure becomes more significant. In particular, fatigue crack initiation and microstructurally small crack growth in metals can be attributed to a number of mechanisms, depending on the constituents of material microstructure and loading conditions, which is discussed in the next section.

2.2.3 Fatigue Crack initiation

A number of definitions exist for crack initiation, as it is difficult to physically observe where the initiation stage ends and the propagation stage begins. It is often assumed that the smallest crack that can be detected experimentally, is considered to be a nucleated crack, and that any further growth belongs to the propagation regime. However, a more succinct distinction, which was proposed by Lukáš [11] and Mughrabi [12], states that the initiation stage terminates when fracture mechanics methods can be employed to predict any further growth behaviour.

The importance of cycle slip irreversibility has been shown to play a key role in the fatigue behaviour of a number of materials, as described by Mughrabi et al. [13], [14]. For example, pure α - iron polycrystals [15] and α - brass single crystals [16] have been tested to fatigue failure across a range of applied plastic strain amplitudes, and a log-linear relationship between measured cyclic slip irreversibility and N_f was observed for both materials. Since fatigue crack initiation often occurs at the surface of a material,

slip irreversibility can generally be described as the emergence of a dislocation at a free surface, causing the formation of a slip step which does not annihilate upon reverse loading. As this process repeats with cyclic loading, a number of extrusions and intrusions form on the surface of the material, leading to local stress concentrations, and act as ideal locations for cracks to nucleate. These are associated with persistent slip bands (PSBs), regions of localised strain resulting from the accumulation of dislocation density, which are strongly related to material microstructure. The phenomenon of PSBs was first established by Ewing and Humphrey [17], who performed fatigue experiments on polycrystalline iron specimens. The work concluded that slip bands would first appear in favourably oriented crystals in the microstructure, and the band width would increase with number of cycles, and eventually lead to the nucleation of cracks. A schematic diagram of PSB formation and surface intrusions and extrusions is provided in Fig. 2.5.

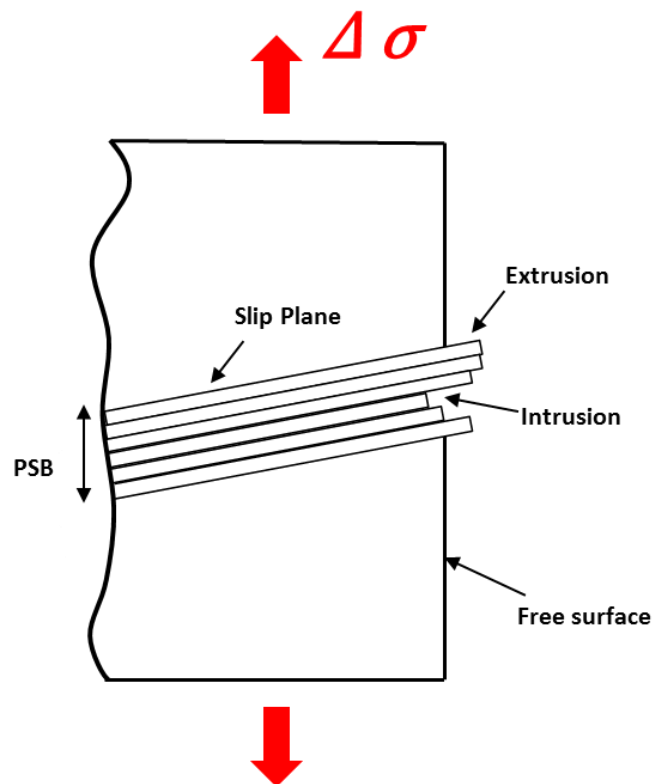


Figure 2.4. A schematic of a persistent slip band along a slip plane in a material under a cyclic stress.

A number of authors [18] [19] [20] have shown the important role that microstructure plays in localised strain accumulation, and thus fatigue crack initiation. For example, in the work of Abuzaid et al. [19], the microstructure and strain fields of polycrystal specimens were measured using electron backscatter diffraction (EBSD) and digital image correlation (DIC) measurement techniques before and after uniaxial loading and unloading. A heterogeneous distribution of strain was observed, with concentrations at twin and grain boundaries.

Although the emergence of PSBs at free surfaces explains the mechanistic basis for crack initiation in a variety of ductile materials and loading conditions, a number of mechanisms exist which result in crack initiation, and eventually fatigue failure. PSBs, which form subsurface in polycrystals, can be obstructed by grain boundaries, leading to high stress concentrations and potential locations for FCI. However a number of factors influence the interaction of PSBs and grain boundaries, including crystallographic misorientation and grain boundary angles. PSBs can pass through low angle grain boundaries [21], where a small misorientation (approximately 15°) exists between the crystal lattice of adjacent grains. Conversely, high angle grain boundaries obstruct the flow of dislocations, resulting in pile-ups and stress concentrations [22].

2.2.4 FCI Modelling

The continuum mechanics-based fatigue criteria described in Section 2.2 are often adopted to predict crack initiation, where the material parameters are based on the number of cycles to crack initiation instead of failure. This typically involves an additional calculation in order to estimate the number of cycles required to initiate a crack of specific size, based on experimental data and a damage evolution law [23]. Although this is a useful approach, in light of the above review on crack initiation, it is becoming increasingly accepted that large-scale component level fatigue criteria are inappropriate given the significance of micro-scale features.

Dunne [24] presents a review of mechanistic modelling of crack initiation across length-scales ranging from the microstructure level to the molecular level. Perhaps the first theoretical crack initiation model to introduce the concept of PSBs was that of Stroh

[25], which considers a single PSB in an elastic medium formed by a line of dislocations. The development of a crack was based on the number of dislocations in the slip band. This model is not commonly used for crack initiation prediction due to the detailed microstructural information required for the fatigue nucleation criteria. However, a number of small-scale modelling techniques have been implemented for FCI, namely molecular dynamics, discrete dislocation, and crystal plasticity.

Molecular dynamics methods simulate arrays of atoms, where the motion of atoms and molecules is determined by solving Newton's laws. Sangid et al. [26] showed the potential of this method in terms of FCI; however, this method is not yet widely used due to computational resources required, with regard to model size and time increment size. Discrete dislocation-based techniques, which operate at the micron scale, are more popular small scale methods for modelling crack initiation. Discrete dislocation plasticity (DDP) explicitly models the motion of individual dislocations. Van der Giessen and Needleman [27] developed a classical 2D DDP model, where dislocations are represented as line defects in a linear elastic solid. In this model dislocations are allowed to nucleate at a Frank-Read source, glide along slip planes based on a constitutive model, and interact with other dislocations via annihilation and pinning. An advantage of DDP is the ability to identify dislocation arrangements such as PSBs and pile-ups, and thus predict likely locations of FCI [28]. Recently, a DDP formulation, with the inclusion of thermal activation events, has been successfully implemented to provide a more thorough understanding of cold dwell fatigue in Ti alloys [29], highlighting the importance of material rate sensitivity.

In terms of practicality, crystal plasticity finite element modelling (CPFEM) is arguably the most appropriate method for modelling crack initiation. The length-scale associated with CPFEM is small enough to capture the material microstructure, but large enough to model a reasonable portion of material without excessive computational run-times. CPFEM explicitly represents individual grains in the microstructure, each with a specific crystallographic orientation and crystal type (FCC, BCC, HCP etc.). The crystallographic slip (glide of dislocations) is represented as a shear strain in the finite element formulations. Crystal plasticity theory follows Schmid's law, where the rate of

slip is dependent on resolved shear stress on a slip system (Fig. 2.5). Generally, formulations are based on the assumption that slip occurs once a critical value of resolved shear stress is reached. Early CP models, such as that of Huang [30], implement phenomenological equations to calculate slip rate and hardening rate on each slip system in a crystal (grain). Physically-based CP [31] [32] models now exist, where micro-scale quantities such as dislocation density are included in formulations, and therefore provide more accurate description of microscale material deformation. The incorporation of non-local gradient formulations [33] [34] has resulted in a significant advance in CP capability, where the effects of plastic strain gradients [35], to be discussed in Section 2.3, can be captured.

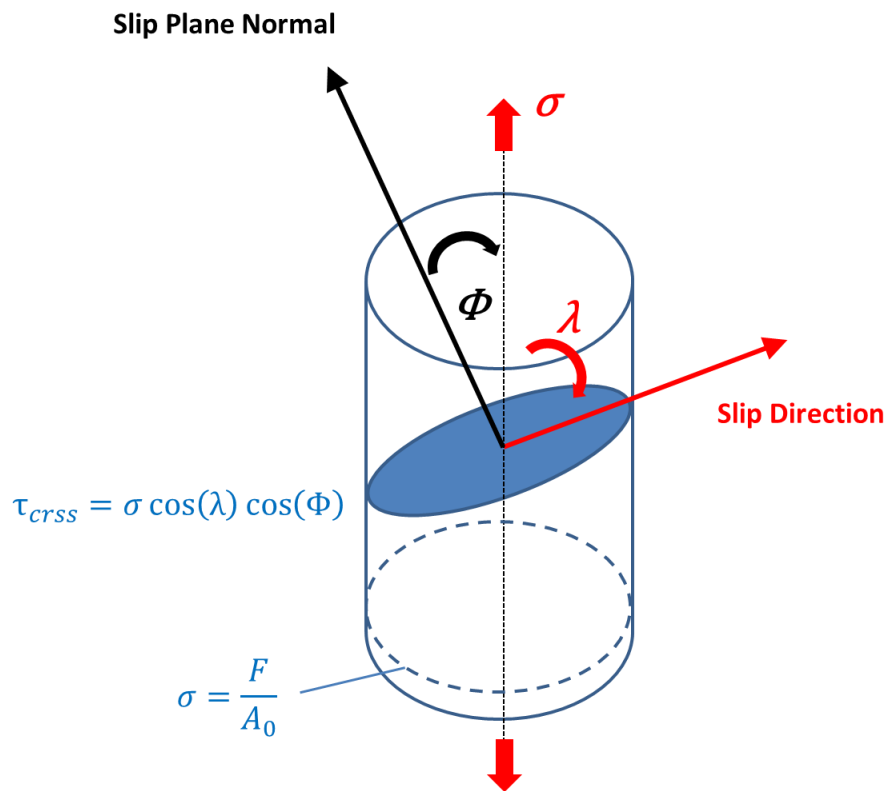


Figure 2.5. Resolved shear stress on a slip plane.

CP models have been successfully implemented to predict locations of crack initiation by identifying the localised accumulation of key quantities. For example, Sweeney et al. [36] compared observed crack locations in four point bend fatigue specimens with an

equivalent CPFE model, and showed that the location of cracking occurred at predicted concentrations of localised accumulated equivalent plastic strain.

As stated by Dunne [24], a key challenge in modelling FCI is determining the key microstructural features and length-scales for a material. An example of this is the phenomenon of dwell fatigue of titanium alloys, where the key microstructural features have been identified to be microstructural regions with specific crystallographic orientation. Crystal plasticity modelling of these Ti alloys, along with experimental studies, has shown that strain accumulation due to cold creep during the load-holding dwell period leads to load shedding from a favourably oriented grain to an adjacent unfavourably oriented grain with respect to the loading direction [37]–[39].

A number of microstructural features have been shown to act as favourable locations for FCI, as reviewed by Chan [40]. For example, Gell and Leverant [41] have shown that for Ni-based superalloys, fatigue cracks can form at a variety of locations (e.g. pores, grain boundaries slip bands etc.) with respect to microstructure, depending on loading and environmental conditions. The presence of hard second-phase particles, precipitates, and inclusions [42] are also key microstructural features with respect to FCI. Chan [43] utilised a micromechanical modelling framework to investigate the role of hard particles in this context for a two phase α - β Ti alloy. This work has shown that the presence of the hard β phase accentuates localised plastic strains in adjacent soft α phases, thus reducing FCI resistance.

2.2.5 Life Prediction with Crystal Plasticity

As described in Section 2.2, a variety of FIPs are commonly used with continuum mechanics to quantify fatigue damage and predict numbers of cycles to failure or initiation. Similar methods have been implemented for CP based models, where micro-scale quantities are generally employed for calculation of an FIP, and are therefore more suited to FCI prediction due to scale consistency. McDowell and Dunne [44] provide a thorough review of FIPs and crystal plasticity modelling of FCI. As discussed previously, localised regions of plastic strain (specifically, the formation persistent slip bands) are key locations for crack initiation in a number of metals. As a result, much

work on FCI life prediction with CPFE is based on the accumulation of plastic strain (or irreversible plastic slip) per cycle. An accumulated crystallographic slip parameter p proposed by Manonakul and Dunne [45], which sums the slip quantities on each slip system, has been shown to successfully predict N_i in a nickel alloy across both LCF and HCF regimes. Crack initiation is predicted to occur when p reaches a critical value p_{crit} . In this work p_{crit} is considered to be a material property, which can be identified using experimental LCF data. Fatemi and Socie- type parameters have been adopted to quantify fatigue damage in fretting of a titanium alloy by Neu and co-workers [46].

A number of energy-based parameters also exist for fatigue prediction with CPFE, based on the premise that a fraction of the dissipated energy over one stabilised cycle is necessary for the formation of a fatigue crack. Korsunsky et al. [47] developed an energy dissipation parameter, which sums resolved shear stress and slip on a slip system. Cruzado et al. [48] demonstrated the capability of this parameter by successfully predicting the low cycle fatigue behaviour of a nickel alloy across a wide range of applied strains.

In recent years, realistic CPFE microstructure models have been constructed using EBSD data. This significant advance CPFE modelling capability has allowed a number of variables to be probed in order to identify the key drivers in FCI. For example, Signor et al. [49] developed a reconstructed CPFE model (Fig. 2.6) of a microstructure region of 316LN stainless steel containing a fatigue crack. It was shown that the crack occurred in the grain with the most predicted slip activity. Similarly, Zhang et al. [50] combined CPFE modelling techniques with high resolution DIC and EBSD measurements to investigate fatigue crack nucleation in a nickel superalloy containing a non-metallic inclusion. The representative CPFE model facilitated a number of fatigue indicators to be explored including residual elastic strain fields and accumulated plastic slip.

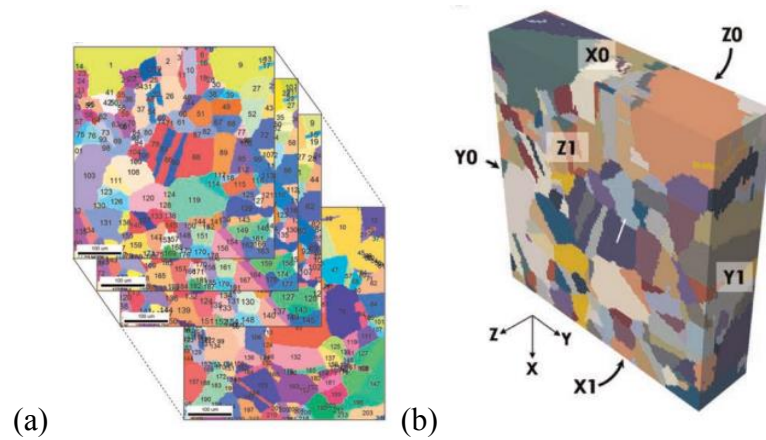


Figure 2.6. Representative CPFE model of 316LN stainless steel developed by Signor *et al.* [49].

2.3 Size Effects in Metals

The mechanical, and hence fatigue, performance of metals is known to be sensitive to a number of size effects. As described by Geer *et al* [51] size effects can be divided into strain gradient effects, statistical size effects, intrinsic size effects and surface constraint effects. Strain gradient effects and statistical effects are focused on in the thesis.

Strain gradient effects [52],[53],[35] in metals are associated with the occurrence of non-uniform plastic strain. Extra dislocations in the material are necessary to accommodate lattice curvature resulting from such plastic strain gradients. These dislocations, termed geometrically necessary dislocations (GNDs), are sessile in nature and act as obstacles to mobile dislocations (e.g. statistically stored dislocations [52]), resulting in localised slip system hardening.

Fleck *et al.* [35] performed torsional tests on copper wires and found that a pronounced size effect occurs where effective lengths (or diameters) are $10\ \mu\text{m}$ or lower. The high plastic strain gradients in smaller diameter wires resulted in a significantly harder response

The formation of GNDs can be explained by considering a beam in bending under plastic deformation, as shown schematically in Fig. 2.6. A gradient in plastic strain exists between the centroidal axis and the surface of the bent beam, resulting in curvature of the crystal lattice. Additional dislocations are then necessary to accommodate this curvature. These effects are also seen in materials with small average grain sizes, inclusions and dual phase microstructures, where the small intrinsic length-scales result in high plastic strain gradients [54],[33]. As the characteristic length (e.g. grain size) is reduced, higher gradients of plastic strain arise, resulting in a harder material response.

Fleck et al. also developed a phenomenological plasticity law to capture these effects, where stress is a function of both strain and strain gradient. Non-local strain gradient plasticity was incorporated into CPFEE models by Acharya and Bassani [55] and Shu and Fleck [56] using two different formulations, as described by Segurado et al. [57]. Acharya and Bassani introduced a lower order formulation that can be implemented in CPFEE codes with relative ease. Shu and Fleck introduced a higher order formulation for CPFEE codes, where some internal variables are considered as kinematic variables, resulting in additional higher order boundary conditions. These higher order formulations [58] are therefore significantly more complex than lower order formulations. As a result, most physically based strain gradients CPFEE models are based on low-order formulations [33], [59],[31], [60], where the density of GNDs is usually related to gradients of plastic slip. GND density is incorporated into hardening models to simulate the size effect.

Although GND density cannot be determined directly from experimental data, it can be estimated using lattice curvature maps, which can be generated from high angular resolution, cross correlation based EBSD [61]. This technique has been implemented to study GND evolution in Ti alloys [62] and copper [63]. CPFEE predictions of GNDs have also been compared to these high resolution EBSD determined GND densities and distributions as a form of validation. Zhang et al. [50] showed good quantitative and qualitative agreement between CPFEE predicted and experimentally determined GND densities.

Dunne et al. [31] implemented a lower order strain-gradient crystal plasticity modelling approach to study the effect of length-scales on stress and plastic strain across grain interfaces. A considerable increase in stress and decrease in accumulated plastic strain at grain boundaries was observed when the average grain size was reduced from 20 μm to 2 μm . Dunne et al. [64] also successfully predicted the experimentally determined distribution of GND density in near- α Ti and single crystal nickel alloy with this strain-gradient crystal plasticity finite element model. Sweeney et al. [54] implemented a similar modelling methodology to predict the effect of measured grain size on stabilized cyclic stress-strain hysteresis loops for CoCr alloy.

Intrinsic size effects arise when small intrinsic length-scales affect dislocation motion. A number of microstructural attributes can cause these effects, including grain boundaries, precipitates, laths, which can cause a pile-up of dislocation and lead to increased strength. A famous example of this is the work of Hall [65] and Petch [66], who observed an increase in material strength with decreasing grain size, commonly known as the Hall-Petch effect.

Although most work on this topic focuses on monotonic loading, it has been shown both experimentally and theoretically [67],[68] that the presence of GNDs also leads to a Bauschinger effect upon reverse loading.

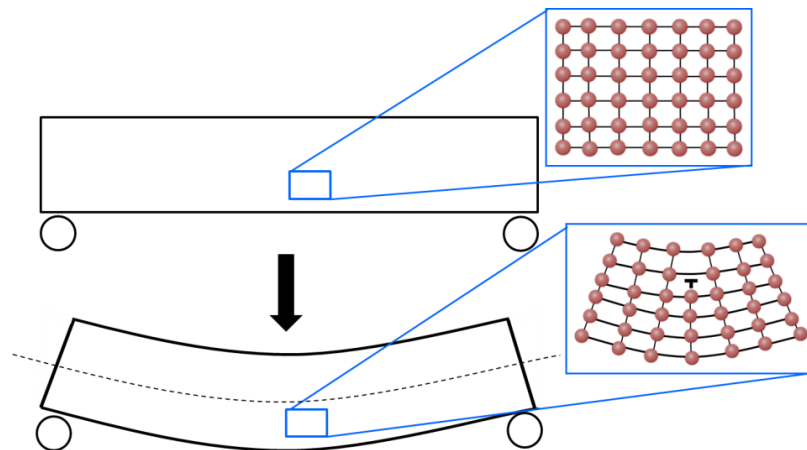


Figure 2.6. Schematic of GNDs arising in beam bending, where a gradient of plastic strain exists.

Statistical size effects arise when component dimensions are similar to those of the metallic grains. Grogan et al. [69] performed a systematic study on the statistical size effects in coronary stent struts under bending and tension. In Grogan's study, strain to failure was predicted to increase as the number of grains across the strut thickness increased. Similarly, Cuddihy et al. [70] studied grain size effects (termed relative geometry effects in this case) in a titanium alloy using a polycrystal model under uniaxial loading. As the ratio of grain size to ligament width (width of polycrystal) decreased, peak grain boundary stresses were predicted to become increasingly sensitive to material microstructure. Such effects may arise in a fretting situation as the ratio of contact semi-width to average grain size increases.

Components with a high ratio of surface area to volume, in biomedical cardiovascular stents for example, can experience surface constraint effects. Raulea et al. [71] studied the effect of reducing the thickness, and thus increasing the ratio of surface area to volume, on the yield strength of thin metal sheets. It was concluded that reduced thickness resulted in a decrease in yield strength. This was attributed to the larger grain area at free surfaces, and thus, the increased probability of surface extrusions and intrusions due to crystallographic slip.

2.4 Contact Mechanics

The size effects described in the previous section can considerably affect the mechanical and fatigue behaviour of components with small associated length-scales. In fretting, the highly localised contact region contains steep gradients of stress and strain, and therefore crack initiation is sensitive to size effects. Contact mechanics can be used to describe the deformation of solids in a fretting contact.

Hertz [72] developed the first analytical solutions for stresses at the contact of two elastic bodies under a normal load. As described by Johnson [73], a number of assumptions are made in these solutions, namely frictionless contact, plane strain conditions (infinite half space), small strains and surfaces are continuous and non-conforming. These trusted solutions are still widely used today for a number of applications, including experimental test design, and finite element model validation.

The theoretical solution for Hertzian contact pressure distribution for a cylinder-on-flat case (shown schematically in Fig. 2.7) is given as:

$$p(x) = p_0 \sqrt{1 - \left(\frac{x}{a}\right)^2} \quad (2.11)$$

where x is the distance from the centre of contact, p_0 is the peak pressure, and a is the contact semi-width calculated as follows:

$$a = \sqrt{\frac{4PR}{\pi E^*}} \quad (2.12)$$

The peak pressure p_0 is given by

$$p_0 = \sqrt{\frac{PE^*}{\pi R}} \quad (2.13)$$

where R is the radius of the cylinder and E^* is the composite elastic modulus of the two bodies defined as:

$$E^* = \left(\frac{1 - (v^f)^2}{E^f} + \frac{1 - (v^c)^2}{E^c} \right) \quad (2.14)$$

where E^f , v^f and E^c , v^c are the elastic moduli and Poisson's ratio for the flat and cylindrical body, respectively.

If a tangential load Q is applied to the cylinder-on-flat case described above, a surface shear traction will be introduced. The tangential load required to produce full sliding between the two bodies is calculated by

$$Q = \mu P \quad (2.15)$$

where μ is the coefficient of friction. When $Q \geq \mu P$ the shear traction distribution is simply:

$$q(x) = \mu p(x) \quad (2.16)$$

If $Q < \mu P$, full sliding will not occur, and instead partial slip arises, whereby a stick region will exist at the centre of contact, with slip regions towards the edge of contact. Cattaneo [74] and Mindlin [75] developed analytical solutions for such a partial slip case where a combination of normal and tangential loads is applied. The semi-width of the central stick region c is calculated as follows:

$$\frac{c}{a} = \sqrt{1 - \frac{Q}{\mu P}} \quad (2.17)$$

The shear traction distribution in the slip regions near the edge of contact $q'(x)$ given as

$$q'(x) = \mu p_0 \sqrt{1 - \frac{x^2}{a^2}} \quad (2.19)$$

where $c \geq |x| \leq a$. The shear traction throughout the stick region, represented as $q''(x)$, is given as

$$q''(x) = -\frac{c}{a} \mu p_0 \sqrt{1 - \frac{x^2}{c^2}} \quad (2.18)$$

where $-c \geq x \leq c$.

The total shear traction distribution is achieved by simply adding $q'(x)$ and $q''(x)$:

$$q(x) = q'(x) + q''(x) \quad (2.20)$$

The schematic shown in Fig 2.7 illustrates the contact shear distribution across a cylinder on flat contact for a partial slip case.

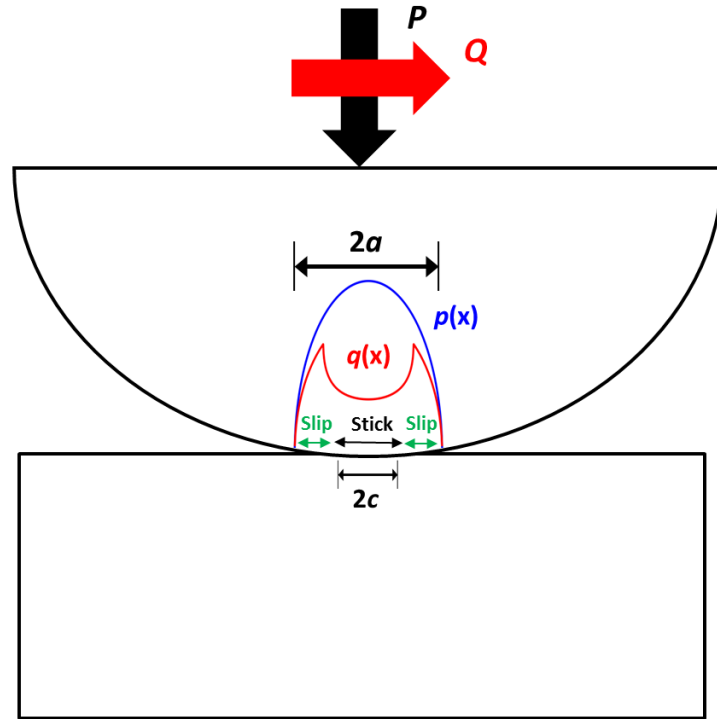


Figure 2.7. A schematic of a 2D cylinder on flat contact with applied normal and tangential loads. The Hertz and Cattaneo and Mindlin solutions for contact pressure and contact shear are given for a partial slip condition.

2.5 Tribology

2.5.1 General

Tribology is the science of how contact surfaces interact under relative motion. The three key areas of interest in tribology are friction, lubrication, and wear.

2.5.2 Friction

Friction is a resisting force to relative motion between surfaces in contact. Leonardo da Vinci first described the laws of friction, which were later credited to Guillaume Amontons. These empirical laws are stated as follows [76]:

1. The friction force is proportional to the normal load.
2. The friction force is independent of the apparent area of contact.

The frictional force F , which acts parallel to the surface, is described by:

$$F = \mu P \quad (2.21)$$

where P is the force normal to the surface and μ is the coefficient of friction. The value of μ generally varies from 0.1 to 1.0 for common engineering applications with metal-on-metal contact.

It is well known that metallic surfaces are composed of a number of peaks and troughs at the micro-scale. The frictional contact behaviour between metal surfaces is a result of the interaction of these microscale asperities. Bowdon and Tabor [77] developed a model for frictional force between metal surfaces surfaces. The total frictional force is decomposed into an adhesion force contribution and a deformation force contribution:

$$F = F_{adh} + F_{def} \quad (2.22)$$

The adhesion force F_{adh} arises from cold welding at asperity contacts. This is particularly prominent in ductile metals. The deformation force F_{def} represents the force required to plastically deform individual asperities. This model is a rather simple description of friction and, in reality, other factors are known to affect the frictional force, including surface film generation and thermal work dissipation.

2.5.3 Wear

Surfaces are damaged when relative motion is applied between contacting bodies, resulting in the loss of material. Wear can be divided into a number of categories [78] including abrasive, adhesive, fatigue, erosion, corrosion and electrical arc. Typically a combination of wear types occurs in metals under frictional contact. Adhesive wear is again related to the bonding of individual asperities, which under relative motion can result in material removal. This, in turn, results in abrasive wear, where the worn debris can become oxidised to form hard particles that remain in the contact and cause further surface damage. This process is common in the presence of a small oscillating relative displacement, such as fretting, where worn material may be trapped in the contact region, resulting in significant material removal.

Archard [79] developed an empirical law for sliding wear for a wide range of materials and loading conditions. This commonly employed law shows that the volume of worn material V is related to material hardness H , contact pressure P and sliding distance S :

$$\frac{V}{S} = K \frac{P}{H} \quad (2.23)$$

where K is a wear coefficient.

2.6 Fretting

2.6.1 General

As stated in Chapter 1, fretting is a small oscillating relative motion between contact surfaces. The relative displacement, or stroke, is typically in the range of 5 to 100 μm for macroscale applications such as splined couplings [80], bolted connections [81] and biomedical hip implants [82]. The presence of fretting in engineering applications can lead to crack initiation or wear, depending on the fretting regime. The combination of relative displacement, coefficient of friction (COF) and normal load determines the fretting regime, which can be classified as gross slip, partial slip, and mixed slip regimes. Gross slip causes significant wear and material removal, and is generally considered the least detrimental fretting regime, since nucleated cracks are either ‘ground away’ during the wear process or propagation rates diminish due to wear-induced contact evolution and stress redistribution [83],[84]. The partial slip regime causes a stick zone with slip zones near the edges of contact, where the shear traction is large enough to overcome the resisting frictional force, as shown in Fig 2.7. This fretting regime is of most concern in the context of fatigue crack initiation due to the absence of significant wear. Vingsbo and Soderberg [85] constructed a fretting map, where the effect of slip amplitude on wear rate and fatigue life is plotted, as shown in Fig 2.8. It can be seen that the partial slip regime generally results in the lowest fatigue life and wear rate. As the slip amplitude is increased, the wear rate increases, leading to longer fatigue lives. There are two forms of damage in fretting; fretting fatigue and fretting wear. Fretting fatigue is generally associated with partial slip, where crack

initiation occurs, leading to failure. Fretting wear is associated with the gross slip regime where material removal exists. Fretting fatigue and fretting wear are not mutually exclusive in real-life applications, due to the presence of irregular loading conditions and the cyclic evolution of contact parameters. For example, during the early stage of fretting in metals, the COF generally increases [86] over the first several thousand cycles, leading to a reduced relative slip, and the possibility of evolution of slip regime from gross slip into partial slip.

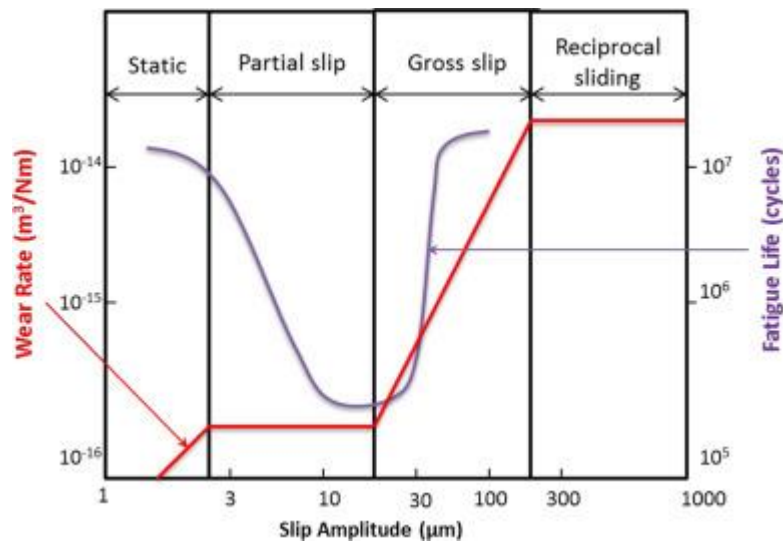


Figure 2.8. The effect of slip amplitude on wear rate and fatigue life in metals [87].

2.6.2 Fretting Fatigue

Fretting fatigue failure can typically be divided into three stages; crack nucleation, short crack growth within the fretting contact region and long crack growth through the component in the presence of a bulk load. Crack nucleation is dominated by the fretting-induced stresses and strains in the slip regions, or at the trailing edge of contact. As nucleated cracks propagate, a bulk fatigue loading begins to control propagation, as the tip crack moves away from the contact stress field. The long crack propagation process can be treated like a plain fatigue problem outside the contact-induced stress fields,

where the methods described in section 2.2 have been employed for predictive purposes [88]. In contrast, the mechanisms that drive the fretting-dominated crack initiation and microstructurally small crack growth, are not fully understood. For example, Nevarro et al. [89] performed a series of fretting fatigue tests and measured the initial growth paths of cracks. It was shown that cracks could nucleate anywhere in the slip region of contact and at the contact edge, and initially grow at a wide range of angles with respect to the surface.

Lamacq et al. [90] used a simple dislocation model to identify two mechanisms of crack initiation: (i) brittle tensile fracture due to high traction stresses, where cracks initially grow approximately normal to the surface, and (ii) a slip mechanism, where cracks nucleate at surface intrusions and extrusions due to the formation of crystallographic slip bands and initially grow at a shallow angle, along the plane of maximum shear stress.

Finite element modelling is commonly used to predict crack initiation in fretting fatigue, where stress and strain based parameters, such as Fatemi-Socie (FS) [4], Smith-Watson-Topper (SWT) [2] and Ruiz [91] parameters, are employed to indicate crack location. For example, Araujo and Nowell [92] compared theoretical results with experimentally observed fretting fatigue cracks. The FS and SWT parameters both predicted cracks to initiate at the edge of contact, which was in contrast to experiments, where cracks were also observed to occur within the slip zones. Similarly, the Ruiz [91] parameter predicts cracks at the edge of contact where a sharp peak in tangential stress occurs. Indeed, the majority of commonly used continuum mechanics based parameters for fretting crack initiation predict cracks at this same location.

Numerous factors have been shown to significantly affect the fretting fatigue behaviour, including relative slip, normal load, COF, material type, temperature, and environmental conditions [93]. O'Halloran et al [94] studied the effect of COF on predicted fatigue life using a critical plane SWT parameter. It was shown that N_i was highly sensitive to COF, particularly at low values of COF (< 0.6). The effect of relative slip (introduced in Section 2.6.1) has been studied extensively. For example the work of Jin and Mall [95] has shown that a competition between cracking and material removal exists in the gross slip regime. The effect of contact force on fretting was studied by Lee and Mall for Ti-

6AL-4V [96] with fretting fatigue tests. In this work, fretting damage was observed to decrease with increasing contact force, due to the resulting reduction in relative slip amplitude. In terms of overall fretting fatigue life, this work showed that high contact loads were detrimental at high applied fatigue specimen bulk stresses, and beneficial at low applied bulk stresses. This work highlights that some key fretting variables (e.g. relative slip) are dependent on each other. Abbassi and Majzoubi [97] experimentally observed a decrease of up to 46% in fretting fatigue life for stainless steel as the testing temperature was increased from RT to 200 °C. The material microstructure and contact size are also important variables, as discussed in Section 2.6.3 and Section 2.6.5.

More recently, Pereira et al. [98] introduced a cohesive zone modelling methodology with XFEM as an alternative to the critical plane approach. Two stress-based damage criteria were implemented in this work; quadratic traction separation and maximum normal stress. Both parameters were shown to successfully predict locations of crack initiation, when compared to experiments and critical plane approaches. The quadratic traction parameter also successfully predicted crack orientations. The potential of the relatively new computational tool XFEM for predicting short crack propagation in fretting has also been explored by Martinez et al. [99]. In this case a shear stress range criteria predicted crack paths with reasonable results, compared to experimentally measured crack paths.

2.6.3 Microstructure Sensitive Fretting Fatigue

A limitation of previous computational work on fretting crack initiation prediction is the omission of microstructural effects, which is discussed in a number of publications [90],[100],[89]. It is well known that, at the small length-scales associated with fretting fatigue, metals are not homogeneous, and consequently are not accurately represented by isotropic elastic material models, even in macroscopically elastic strain fields. It is therefore important to consider microstructure in fretting models to achieve a more accurate representation of the material, and hence, better understand the mechanisms that drive crack initiation. In addition, as discussed in Section 2.2, crack initiation is highly sensitive to microstructure, which suggests that microstructure is especially important in fretting crack initiation.

Research in this area is almost exclusively through computational modelling; however, some limited work has investigated the effect of grain size on fretting fatigue life. Jayaprakash [101], performed fretting fatigue tests on a stainless steel specimens with two different average grain sizes, where no clear trend was observed. Conversely, Mall et al. [102] showed a beneficial effect of small grains on fretting fatigue resistance for a nickel-based super alloy. In this study, two average grain sizes of 3 μm and 7 μm were analysed. The finer grained microstructure showed increased FCI resistance and longer total fatigue lives. However, the coarser microstructure showed superior fatigue crack propagation resistance. This observation is in general agreement with plain fatigue, where small grains are considered desirable for crack initiation resistance, whereas large grains are considered more desirable for propagation resistance.

For modelling the influence of microstructure in fretting fatigue, crystal plasticity finite element (CPFE) frameworks have typically been employed. The first published work in this field was that of Goh et al. [103], who incorporated a crystal plasticity model and square-shaped grains into the contact zone of a 2D fretting fatigue model for a Ti alloy. Using a cyclically accumulated equivalent plastic strain-based parameter, this study predicted similar crack locations to equivalent fretting fatigue experiments, where cracks were observed to form at the edges of contact and within the slip zones. A key finding of this study was the importance of ratchetting on crack initiation. Similar work by Mayuer et al. [104] further explored the effects of microstructure by including more realistic microstructure geometries and the α - β phase in a Ti alloy fretting model. It was shown that the presence of two microstructural phases significantly influenced the ratchetting behaviour of the material, thus highlighting the need for explicit representation of material microstructure for studying fretting fatigue crack formation.

Some authors have performed simulations with 3D microstructure geometries in fretting [105], [106], [46]. Zhang [46] and implemented a Fatemi-Socie parameter to assess the microstructure sensitivity of fretting fatigue resistance in Ti alloys. This work predicted, for the highly anisotropic microstructures in Ti alloys, that crystallographic texture is an important factor in fretting crack initiation. Zhang [106] also investigated the effect of average grain size. Fretting resistance was predicted to increase as average grain size

was reduced due to the inclusion of an empirical Hall-Petch term in the material model. However, a limited number of microstructures were considered in this work.

The work above has been qualitative, where a number of stress or strain-based parameters are implemented to study fatigue resistance, rather than calculating fatigue life. Recently, more quantitative fatigue life prediction methods have been included in microstructure sensitive fretting modelling. McCarthy [107] implemented the accumulated crystallographic slip FIP [45] to predict scatter in fretting fatigue life due to grain orientation. This work however has some limitations, including the use of a 3D CPFE model with 2D microstructure geometry, the absence of kinematic hardening in simulating material constitutive behaviour and the use of relatively simple microstructure geometries.

Recent work by Han et al. [108] has investigated the importance of crystallographic slip in the formation of fretting fatigue cracks. Fretting fatigue tests were conducted in-situ with an EBSD in order to observe the active crystal slip systems and slip traces during fretting fatigue. The key findings of this work suggest that cracks follow the path of the active slip systems at the edge of contact.

2.6.4 Fretting Wear

Fretting wear occurs when cyclic gross sliding occurs between contact surfaces. As shown in Fig. 2.7, the gross sliding regime is beneficial in fretting due to the removal of initiated fatigue cracks during the wear process. This behaviour has been observed experimentally, i.e. fatigue life increases as relative displacement increases [109], [110]. For this phenomenon to be captured in computational models, the wear process must be accounted for. The Archard equation described in Section 2.4 is often incorporated into finite element models to capture wear. For example, McColl et al. [111] implemented an Archard wear approach and an adaptive meshing technique to simulate material removal due to wear, and thus, the wear-induced evolution of contact pressure and sub-surface stresses.

Ding et al. [84] developed an efficient method for capturing the ‘pick-up’ in life due to wear without the need for computationally expensive adaptive meshing. A D_{fret}

parameter was incorporated in an SWT fatigue prediction methodology to successfully predict the experimentally observed [95] effect of relative displacement on life across the partial slip and gross slip regimes. McCarthy et al. [112] proposed the use of the microscale accumulated crystallographic slip parameter p for predicting fretting wear using CPFEM, where material removal is considered to occur when a critical value of p was reached. The benefit of this approach is the potential to predict more realistic wear scars due to the presence of microstructure.

Alternatives to finite element modelling exist for simulating wear [113], [114], [115]. Nowell [114] developed an efficient quadratic programming method for predicting fretting wear, and showed good agreement with corresponding finite element analysis results [116].

2.6.5 Size Effects in Fretting

A number of important length-scales exist in fretting, as described by Nowell et al. [117], including material microstructural dimensions, nominal contact size, individual asperity contact sizes and spacing, relative slip amplitude and size of the fretting induced stress fields. All of these lengths are typically on the scale of microns, and are therefore considered to play an important role in the crack initiation process. Particular combinations of the parameters listed above can lead to favourable or detrimental conditions for fretting crack initiation, depending on the contact conditions and material. A famous example of this is the contact size effect.

As mentioned in Chapter 1, a number of authors [118],[119],[120] have observed a contact size effect in fretting fatigue whereby a critical contact size is observed below which fatigue life increases dramatically. This effect has been attributed to the different stress fields associated with varying contact size. It is argued that larger stress fields are more likely to encompass key microstructurally weak features (e.g ‘weak’ grain combination, existing flaw) in the critically stressed region. As contact size is reduced, the smaller stress fields are less likely to contain such critical features, and thus average life increases. Nominally, classical macro-scale elastic-plastic finite element fretting models are unable to predict this effect due to the absence of explicit microstructural

representation, and size dependent material models. However, some authors have introduced length- or volume-averaging procedures in fretting fatigue calculations to account for such size effects. An averaging dimension similar to that of key microstructural dimensions has been argued to give acceptable results [92],[84]. Araujo and Nowell [92] averaged SWT and FS FIPs over (i) a critical depth along the critical plane, and (ii) over a critical volume of material to predict fretting fatigue life. In both cases, the averaging dimensions which agreed with experimental results were similar to the average grain size and grain volume of the material analysed. For example, the critical depth of 5-20 μm showed reasonable agreement with experiments for a Ti alloy with average grain size of 5 μm . Fouvry et al. [121] accounted for the steep stress gradient effect by averaging stresses over a critical volume, which is not necessarily related to a microstructural dimension.

Another hypothesis for this contact size effect is concerned primarily with crack propagation and stress gradients. For example, the rapidly decreasing stress field associated with small contacts may lead to the inability of propagating cracks to overcome microstructural barriers (e.g. grain boundaries.), leading to crack arrest. Short crack arrest methodologies have been explored by a number of authors [119], [122], [123] with similar results to those achieved with averaging procedures.

Hills et al. [124] applied Kitagawa and Takahashi methods to an asymptotic description of slip and stress at the edges incomplete contacts and predicted a boundary between propagation, leading to failure, and crack arrest, leading to infinite life. The predicted trends, which did not require averaging procedures, were in agreement with the experimentally observed contact size effect. Nowell and Dini [125] explored a notch analogy between the stress fields at crack tips and the stress fields at the edge of punch-on-flat contact This work showed the potential of tensile tests on notched specimens for studying the stress gradient effect without the additional surface damage effects seen in fretting.

2.6.6 Fretting in Marine Risers

As described in chapter 1, the interlocking nub-groove contact region in the pressure armour layer of marine risers is prone to fretting fatigue [126]. Perera et al. [127] were the first authors to experimentally observe and characterise the fretting behaviour of pressure armour wire. The experimental set-up consisted of two interlocking sections of pressure armour wire subjected to a controlled normal pressure and relative tangential displacement. It was shown that cracks initiated at the edge of contact and significant wear could occur, depending on loading conditions. O'Halloran [128] characterised the fatigue and fretting behaviour of pressure armour steel. The experimentally obtained properties were then employed to perform a detailed computational study on fretting of the pressure armour wire. A multiscale approach was developed to determine the in-service contact and fretting conditions (i.e slip amplitude contact width and contact pressure) based on global dynamic riser analysis in representative sea states. It was shown that a wide range of fretting conditions exist, of which, partial slip conditions were the most detrimental. Relative contact slips with a magnitude greater than the contact width were shown to be beneficial, as this ensured that effective lubrication occurs.

2.7 Conclusions

In conclusion, the increase in computational power, micro- and nano-scale experimental techniques, and physically-based micromechanical material models has resulted in key findings with regard to the mechanisms that drive fatigue. The majority of this work focused on uniaxial fatigue loading conditions. However, some recent research has concentrated on the role of microstructure in fretting fatigue. Fretting fatigue in metals is a highly complex problem with a number of influencing contact parameters, loading parameters, and length-scales. The crack initiation process in fretting fatigue is particularly sensitive to length-scales.

The roles of crystallographic texture, grain size and phase distribution have only been studied to a limited extent using computational crystal plasticity modelling. There is a clear need to further study the role of microstructure in fretting, including the assessment

of multiple microstructure geometries in order to analysis the statistical effects of microstructure on fretting.

The contact size effect seen in fretting fatigue is still not fully understood. Averaging techniques are currently necessary in homogeneous computational models to capture the contact-induced stress gradient effect. By explicitly representing microstructure in computational models it may be possible to capture this effect without the need for averaging procedures.

Until recently fretting in marine riser pressure armour material has been the subject of limited research. The work of O'Halloran has highlighted some of the key contact conditions necessary to ensure that fretting is not the most detrimental form of fatigue in marine risers. However, the micromechanical behaviour of the material has not yet been studied.

2.8 References

- [1] S. Suresh, *Fatigue of materials*. Cambridge University Press, 1998.
- [2] T. T. K Smith, P Watson, "Stress-strain function for the fatigue of metals," *J. Mater.*, vol. 5, pp. 767–778, 1970.
- [3] M. W. Brown and K. J. Miller, "A theory for fatigue failure under multiaxial stress–strain conditions," *ARCHIVE: Proceedings of the Institution of Mechanical Engineers 1847-1982 (vols 1-196)*, vol. 187, no. 1973. pp. 745–755, 2006.
- [4] A. Fatemi and D. F. Socie, "A critical plane approach to multiaxial fatigue damage including out-of-phase loading," *Fatigue Fract. Eng. Mater. Struct.*, vol. 11, no. 3, pp. 149–165, 1988.
- [5] R. V. Marrey, R. Burgermeister, R. B. Grishaber, and R. O. Ritchie, "Fatigue and life prediction for cobalt-chromium stents: A fracture mechanics analysis," *Biomaterials*, vol. 27, no. 9, pp. 1988–2000, 2006.
- [6] Bathias, "There is no infinite fatigue life in metallic materials," *Fatigue Fract. Eng. Mater. Struct.*, vol. 22, no. 7, pp. 559–565, 1999.

-
- [7] P. Paris and F. Erdogan, "A Critical Analysis of Crack Propagation Laws," *J. Basic Eng.*, vol. 85, no. 4, pp. 528–533, Dec. 1963.
- [8] M. H. El Haddad, T. H. Topper, and K. N. Smith, "Prediction of non propagating cracks," *Eng. Fract. Mech.*, vol. 11, no. 3, pp. 573–584, 1979.
- [9] T. S. Kitagawa. H, "Applicability of fracture mechanics to very small cracks or the cracks in the early stage," in *Proc 2nd Int. Conf. on Mech. Behavior of Materials*. ASM, 1976, pp. 627–631.
- [10] J. R. Rice, "A Path Independent Integral and the Approximate Analysis of Strain Concentration by Notches and Cracks," *J. Appl. Mech.*, vol. 35, no. 2, p. 379, 1968.
- [11] Lukas. P, "Fatigue crack nucleation and microstructure," in *ASM handbook. Fatigue and fracture*, 1996, pp. 96–109.
- [12] H. Mughrabi, "Specific features and mechanisms of fatigue in the ultrahigh-cycle regime," *Int. J. Fatigue*, vol. 28, no. 11, pp. 1501–1508, 2006.
- [13] H. Mughrabi, "Microstructural fatigue mechanisms: Cyclic slip irreversibility, crack initiation, non-linear elastic damage analysis," *Int. J. Fatigue*, vol. 57, pp. 2–8, 2013.
- [14] H. Mughrabi, "Cyclic slip irreversibilities and the evolution of fatigue damage," *Metall. Mater. Trans. B Process Metall. Mater. Process. Sci.*, vol. 40, no. 4, pp. 431–453, 2009.
- [15] H. Mughrabi and C. Wüthrich, "Asymmetry of slip and shape changes during cyclic deformation of α -iron single crystals," *Philos. Mag. A J. Theor. Exp. Appl. Phys.*, vol. 33, no. 6, pp. 963–984, Jun. 1976.
- [16] P. Lukáš and M. Klesnil, "Dislocation structures in fatigued single crystals of Cu–Zn system," *Phys. status solidi*, vol. 5, no. 1, pp. 247–258, 1971.

-
- [17] J. A. Ewing and H. JCW., “The fracture of metals under repeated alternations of stress,” *Philos. Trans. R. Soc. London. Ser. A, Contain. Pap. a Math. or Phys. Character*, vol. 200, no. 321–330, p. 241 LP-250, Jan. 1903.
- [18] S. H. Daly, “Digital Image Correlation in Experimental Mechanics for Aerospace Materials and Structures,” in *Encyclopedia of Aerospace Engineering*, John Wiley & Sons, Ltd, 2010.
- [19] W. Z. Abuzaid, M. D. Sangid, J. D. Carroll, H. Sehitoglu, and J. Lambros, “Slip transfer and plastic strain accumulation across grain boundaries in Hastelloy X,” *J. Mech. Phys. Solids*, vol. 60, no. 6, pp. 1201–1220, 2012.
- [20] M. A. Tschopp, B. B. Bartha, W. J. Porter, P. T. Murray, and S. B. Fairchild, “Microstructure-Dependent Local Strain Behavior in Polycrystals through In-Situ Scanning Electron Microscope Tensile Experiments,” *Metall. Mater. Trans. A*, vol. 40, no. 10, pp. 2363–2368, Oct. 2009.
- [21] Z. F. Zhang, Z. G. Wang, and H. H. Su, “Observations on persistent slip bands transferring through a grain boundary in a copper bicrystal by the electron channelling contrast in scanning electron microscopy technique,” *Philos. Mag. Lett.*, vol. 79, no. 5, pp. 233–240, May 1999.
- [22] T. Benjamin Britton and A. J. Wilkinson, “Stress fields and geometrically necessary dislocation density distributions near the head of a blocked slip band,” *Acta Mater.*, vol. 60, no. 16, pp. 5773–5782, 2012.
- [23] A. Fatemi and L. Yang, “Cumulative fatigue damage and life prediction theories: a survey of the state of the art for homogeneous materials,” *Int. J. Fatigue*, vol. 20, no. 1, pp. 9–34, 1998.
- [24] F. P. E. Dunne, “Fatigue crack nucleation: Mechanistic modelling across the length scales,” *Curr. Opin. Solid State Mater. Sci.*, vol. 18, no. 4, pp. 170–179, 2014.
- [25] A. N. Stroh, “The formation of cracks as a result of plastic flow,” *Proc. R. Soc. London. Ser. A. Math. Phys. Sci.*, vol. 223, no. 1154, p. 404 LP-414, May 1954.

-
- [26] M. D. Sangid, H. J. Maier, and H. Sehitoglu, “A physically based fatigue model for prediction of crack initiation from persistent slip bands in polycrystals,” *Acta Mater.*, vol. 59, no. 1, pp. 328–341, 2011.
- [27] E. Van der Giessen and A. Needleman, “Discrete dislocation plasticity: a simple planar model,” *Model. Simul. Mater. Sci. Eng.*, vol. 3, no. 5, 1995.
- [28] S. Brinckmann and E. Van der Giessen, “A discrete dislocation dynamics study aiming at understanding fatigue crack initiation,” *Mater. Sci. Eng. A*, vol. 387–389, no. 1–2 SPEC. ISS., pp. 461–464, 2004.
- [29] Z. Zheng, D. S. Balint, and F. P. E. Dunne, “Discrete dislocation and crystal plasticity analyses of load shedding in polycrystalline titanium alloys,” *Int. J. Plast.*, vol. 87, pp. 15–31, 2016.
- [30] Y. Huang, “A User-Material Subroutine Incorporating Single Crystal Plasticity In the ABAQUS Finite Element Program, Mech Report 178,” Division of Applied Sciences, Harvard University, 1991.
- [31] F. P. E. Dunne, D. Rugg, and A. Walker, “Lengthscale-dependent, elastically anisotropic, physically-based hcp crystal plasticity: Application to cold-dwell fatigue in Ti alloys,” *Int. J. Plast.*, vol. 23, no. 6, pp. 1061–1083, 2007.
- [32] D.-F. Li, B. J. Golden, and N. P. O’Dowd, “Multiscale modelling of mechanical response in a martensitic steel: A micromechanical and length-scale-dependent framework for precipitate hardening,” *Acta Mater.*, vol. 80, pp. 445–456, 2014.
- [33] E. P. Busso, F. T. Meissonnier, and N. P. O’Dowd, “Gradient-dependent deformation of two-phase single crystals,” *J. Mech. Phys. Solids*, vol. 48, no. 11, pp. 2333–2361, 2000.
- [34] K. S. Cheong, E. P. Busso, and a. Arsenlis, “A study of microstructural length scale effects on the behaviour of FCC polycrystals using strain gradient concepts,” *Int. J. Plast.*, vol. 21, no. 9, pp. 1797–1814, 2005.

-
- [35] N. A. Fleck, G. M. Muller, M. F. Ashby, and J. W. Hutchinson, “Strain gradient plasticity: Theory and experiment,” *Acta Metall. Mater.*, vol. 42, no. 2, pp. 475–487, 1994.
- [36] C. A. Sweeney, W. Vorster, S. B. Leen, E. Sakurada, P. E. McHugh, and F. P. E. Dunne, “The role of elastic anisotropy, length scale and crystallographic slip in fatigue crack nucleation,” *J. Mech. Phys. Solids*, vol. 61, no. 5, pp. 1224–1240, 2013.
- [37] M. R. Bache, “A review of dwell sensitive fatigue in titanium alloys: The role of microstructure, texture and operating conditions,” *Int. J. Fatigue*, vol. 25, no. 9–11, pp. 1079–1087, 2003.
- [38] V. Hasija, S. Ghosh, M. J. Mills, and D. S. Joseph, “Deformation and creep modeling in polycrystalline Ti–6Al alloys,” *Acta Mater.*, vol. 51, no. 15, pp. 4533–4549, 2003.
- [39] F. P. E. Dunne and D. Rugg, “On the mechanisms of fatigue facet nucleation in titanium alloys,” *Fatigue Fract. Eng. Mater. Struct.*, vol. 31, no. 11, pp. 949–958, 2008.
- [40] K. S. Chan, “Roles of microstructure in fatigue crack initiation,” *Int. J. Fatigue*, vol. 32, no. 9, pp. 1428–1447, 2010.
- [41] M. Gell and G. Leverant, “Mechanisms of High-Temperature Fatigue BT - Mechanisms of High-Temperature Fatigue,” 1973.
- [42] K. Tanaka and T. Mura, “A theory of fatigue crack initiation at inclusions,” *Metall. Trans. A*, vol. 13, no. 1, pp. 117–123, 1982.
- [43] K. S. Chan, “Changes in fatigue life mechanism due to soft grains and hard particles,” *Int. J. Fatigue*, vol. 32, no. 3, pp. 526–534, 2010.
- [44] D. L. McDowell and F. P. E. Dunne, “Microstructure-sensitive computational modeling of fatigue crack formation,” *Int. J. Fatigue*, vol. 32, no. 9, pp. 1521–1542, 2010.

-
- [45] F. P. E. Dunne, A. Manonukul, “High- and low- cycle fatigue crack initiation using polycrystal plasticity,” *Proc. R. Soc. A Math. Phys. Eng. Sci.*, vol. 460, pp. 1881–1903, 2004.
- [46] M. Zhang, R. W. Neu, and D. L. McDowell, “Microstructure-sensitive modeling: Application to fretting contacts,” *Int. J. Fatigue*, vol. 31, no. 8–9, pp. 1397–1406, 2009.
- [47] A. M. Korsunsky, D. Dini, F. P. E. Dunne, and M. J. Walsh, “Comparative assessment of dissipated energy and other fatigue criteria,” *Int. J. Fatigue*, vol. 29, no. 9–11, pp. 1990–1995, 2007.
- [48] A. Cruzado, S. Lucarini, J. LLorca, and J. Segurado, “Microstructure-based fatigue life model of metallic alloys with bilinear Coffin-Manson behavior,” pp. 1–25, 2017.
- [49] L. Signor, P. Villechaise, T. Ghidossi, E. Lacoste, M. Gueguen, and S. Courtin, “Influence of local crystallographic configuration on microcrack initiation in fatigued 316LN stainless steel: Experiments and crystal plasticity finite elements simulations,” *Mater. Sci. Eng. A*, vol. 649, pp. 239–249, 2016.
- [50] T. Zhang, D. M. Collins, F. P. E. Dunne, and B. A. Shollock, “Crystal plasticity and high-resolution electron backscatter diffraction analysis of full-field polycrystal Ni superalloy strains and rotations under thermal loading,” *Acta Mater.*, vol. 80, pp. 25–38, 2014.
- [51] M. G. D. Geers, W. a M. Brekelmans, and P. J. M. Janssen, “Size effects in miniaturized polycrystalline FCC samples: Strengthening versus weakening,” *Int. J. Solids Struct.*, vol. 43, no. 24, pp. 7304–7321, 2006.
- [52] M. F. Ashby, “The deformation of plastically non-homogeneous materials,” *Philos. Mag.*, vol. 21, no. 170, pp. 399–424, 1970.
- [53] H. Gao and Y. Huang, “Geometrically necessary dislocation and size-dependent plasticity,” *Scr. Mater.*, vol. 48, no. 2, pp. 113–118, 2003.

-
- [54] C. A. Sweeney, B. O'Brien, F. P. E. Dunne, P. E. McHugh, and S. B. Leen, "Strain-gradient modelling of grain size effects on fatigue of CoCr alloy," *Acta Mater.*, vol. 78, pp. 341–353, Oct. 2014.
- [55] J. L. Acharya, A. Bassani, "Incompatible lattice deformations and crystal plasticity," in *ASME Proceedings*, 1995, no. 57, pp. 75–80.
- [56] J. Y. Shu and N. A. Fleck, "Strain gradient crystal plasticity: size-dependent deformation of bicrystals," *J. Mech. Phys. Solids*, vol. 47, no. 2, pp. 297–324, 1999.
- [57] J. Segurado, R. A. Lebensohn, and J. LLorca, "Chapter One - Computational Homogenization of Polycrystals," in *Advances in Crystals and Elastic Metamaterials, Part 1*, vol. 51, M. I. B. T.-A. in A. M. Hussein, Ed. Elsevier, 2018, pp. 1–114.
- [58] M. E. Gurtin, "A gradient theory of single-crystal viscoplasticity that accounts for geometrically necessary dislocations," *J. Mech. Phys. Solids*, vol. 50, no. 1, pp. 5–32, 2002.
- [59] A. Acharya and J. L. Bassani, "Lattice incompatibility and a gradient theory of crystal plasticity," *J. Mech. Phys. Solids*, vol. 48, no. 8, pp. 1565–1595, 2000.
- [60] C.-S. Han, H. Gao, Y. Huang, and W. D. Nix, "Mechanism-based strain gradient crystal plasticity—I. Theory," *J. Mech. Phys. Solids*, vol. 53, no. 5, pp. 1188–1203, 2005.
- [61] P. S. Karamched and A. J. Wilkinson, "High resolution electron back-scatter diffraction analysis of thermally and mechanically induced strains near carbide inclusions in a superalloy," *Acta Mater.*, vol. 59, no. 1, pp. 263–272, 2011.
- [62] P. D. Littlewood, T. B. Britton, and A. J. Wilkinson, "Geometrically necessary dislocation density distributions in Ti–6Al–4V deformed in tension," *Acta Mater.*, vol. 59, no. 16, pp. 6489–6500, 2011.

-
- [63] J. Jiang, T. B. Britton, and A. J. Wilkinson, "Evolution of dislocation density distributions in copper during tensile deformation," *Acta Mater.*, vol. 61, no. 19, pp. 7227–7239, 2013.
- [64] F. P. E. Dunne, R. Kiwanuka, and a. J. Wilkinson, "Crystal plasticity analysis of micro-deformation, lattice rotation and geometrically necessary dislocation density," *Proc. R. Soc. A Math. Phys. Eng. Sci.*, vol. 468, no. 2145, pp. 2509–2531, 2012.
- [65] E. O. Hall, "The Deformation and Ageing of Mild Steel: III Discussion of Results," *Proc. Phys. Soc. Sect. B*, vol. 64, no. 9, p. 747, 1951.
- [66] N. J. Petch, "The cleavage strength of polycrystals," *J. Iron Steel Inst.*, vol. 174, pp. 25–28, 1953.
- [67] C. F. Niordson and B. N. Legarth, "Strain gradient effects on cyclic plasticity," *J. Mech. Phys. Solids*, vol. 58, no. 4, pp. 542–557, 2010.
- [68] D. Liu, Y. He, L. Shen, J. Lei, S. Guo, and K. Peng, "Accounting for the recoverable plasticity and size effect in the cyclic torsion of thin metallic wires using strain gradient plasticity," *Mater. Sci. Eng. A*, vol. 647, pp. 84–90, 2015.
- [69] J. A. Grogan, S. B. Leen, and P. E. McHugh, "Influence of statistical size effects on the plastic deformation of coronary stents," *J. Mech. Behav. Biomed. Mater.*, vol. 20, pp. 61–76, 2013.
- [70] M. A. Cuddihy, Z. Zheng, J. Gong, T. B. Britton, A. J. Wilkinson, and F. P. E. Dunne, "Grain size effects in hcp polycrystals : from GNDs to blocky alpha," pp. 1–28.
- [71] L. V Raulea, A. M. Goijaerts, L. E. Govaert, and F. P. T. Baaijens, "Size effects in the processing of thin metal sheets," *J. Mater. Process. Technol.*, vol. 115, no. 1, pp. 44–48, 2001.
- [72] H. Hertz, "Über die Berührung fester elastischer Körper," *J. fur die Reine und Angew. Math.*, pp. 156–171, 1882.
- [73] K. L. Johnson, *Contact Mechanics*. 1985.

-
- [74] C. C., “Sul contatto di due corpi elastici: distribuzione locale degli sforzi,” *Rend. Accad. Naz.*, vol. Lincei 27, pp. 342–348.
- [75] R. D. Mindlin, “Compliance of elastic bodies in contact,” *J. Appl. Mech.*, vol. 16, pp. 259–268, 1949.
- [76] I. M. Hutchings, *Tribology: Friction and Wear of Engineering Materials*. Cambridge: Arnold, 1992.
- [77] D. Bowden, F. P. , Tabor, *Friction and lubrication of solids*. Oxford University Press. Oxford University Press, 1950.
- [78] B. K. Bhushan, B., Gupta, *Handbook of tribology: Materials, coatings, and surface treatments*. New York: McGraw-Hill, 1991.
- [79] J. F. Archard, “Contact and Rubbing of Flat Surfaces,” *J. Appl. Phys.*, vol. 24, no. 8, pp. 981–988, Aug. 1953.
- [80] J. Ding, I. R. McColl, and S. B. Leen, “The application of fretting wear modelling to a spline coupling,” *Wear*, vol. 262, no. 9–10, pp. 1205–1216, 2007.
- [81] A. Benhamena, A. Amrouche, A. Talha, and N. Benseddiq, “Effect of contact forces on fretting fatigue behavior of bolted plates: Numerical and experimental analysis,” *Tribol. Int.*, vol. 48, pp. 237–245, 2012.
- [82] T. Zhang, N. M. Harrison, P. F. McDonnell, P. E. McHugh, and S. B. Leen, “A finite element methodology for wear-fatigue analysis for modular hip implants,” *Tribol. Int.*, vol. 65, pp. 113–127, 2013.
- [83] J. J. Madge, S. B. Leen, and P. H. Shipway, “A combined wear and crack nucleation-propagation methodology for fretting fatigue prediction,” *Int. J. Fatigue*, vol. 30, no. 9, pp. 1509–1528, 2008.
- [84] J. Ding, D. Houghton, E. J. Williams, and S. B. Leen, “Simple parameters to predict effect of surface damage on fretting fatigue,” *Int. J. Fatigue*, vol. 33, no. 3, pp. 332–342, 2011.

-
- [85] S. Vingsbo, O., Söderberg, “On Fretting Maps,” *Wear*, vol. 126, no. 2, pp. 131–147, 1988.
- [86] S. M. O’Halloran, A. M. Harte, P. H. Shipway, and S. B. Leen, “An experimental study on the key fretting variables for flexible marine risers,” *Tribol. Int.*, vol. 117, pp. 141–151, 2018.
- [87] S. M. O’Halloran, P. H. Shipway, A. D. Connaire, S. B. Leen, and A. M. Harte, “A combined wear-fatigue design methodology for fretting in the pressure armour layer of flexible marine risers,” *Tribol. Int.*, vol. 108, pp. 7–15, 2017.
- [88] J. A. Araújo, L. Susmel, D. Taylor, J. C. T. Ferro, and J. L. A Ferreira, “On the prediction of high-cycle fretting fatigue strength: Theory of critical distances vs. hot-spot approach,” *Eng. Fract. Mech.*, vol. 75, no. 7, pp. 1763–1778, 2008.
- [89] C. Navarro, J. Vázquez, and J. Domínguez, “Nucleation and early crack path in fretting fatigue,” *Int. J. Fatigue*, vol. 100, pp. 602–610, 2017.
- [90] V. Lamacq, M.-C. Dubourg, and L. Vincent, “A theoretical model for the prediction of initial growth angles and sites of fretting fatigue cracks,” *Tribol. Int.*, vol. 30, no. 6, pp. 391–400, 1997.
- [91] C. Ruiz, P. H. B. Boddington, and K. C. Chen, “An investigation of fatigue and fretting in a dovetail joint,” *Exp. Mech.*, vol. 24, no. 3, pp. 208–217, Sep. 1984.
- [92] J. A. Araújo and D. Nowell, “The effect of rapidly varying contact stress fields on fretting fatigue,” *Int. J. Fatigue*, vol. 24, no. 7, pp. 763–775, 2002.
- [93] R. B. Waterhouse, “Fretting fatigue,” *Int. Mater. Rev.*, vol. 37, no. 1, pp. 77–98, Jan. 1992.
- [94] S. M. O’Halloran, A. D. Connaire, A. M. Harte, and S. B. Leen, “Modelling of fretting in the pressure armour layer of flexible marine risers,” *Tribol. Int.*, vol. 100, pp. 306–316, 2015.

-
- [95] O. Jin and S. Mall, “Effects of slip on fretting behavior: experiments and analyses,” *Wear*, vol. 256, no. 7, pp. 671–684, 2004.
- [96] H. Lee and S. Mall, “Effect of dissimilar mating materials and contact force on fretting fatigue behavior of Ti–6Al–4V,” *Tribol. Int.*, vol. 37, no. 1, pp. 35–44, 2004.
- [97] F. Abbasi and G. H. Majzoobi, “An investigation into the effect of elevated temperatures on fretting fatigue response under cyclic normal contact loading,” *Theor. Appl. Fract. Mech.*, vol. 93, pp. 144–154, 2018.
- [98] K. Pereira, N. Bhatti, and M. Abdel Wahab, “Prediction of fretting fatigue crack initiation location and direction using cohesive zone model,” *Tribol. Int.*, vol. 127, pp. 245–254, 2018.
- [99] J. C. Martínez, L. V. Vanegas Useche, and M. A. Wahab, “Numerical prediction of fretting fatigue crack trajectory in a railway axle using XFEM,” *Int. J. Fatigue*, vol. 100, pp. 32–49, 2017.
- [100] J. A. Araújo, G. M. J. Almeida, J. L. A. Ferreira, C. R. M. da Silva, and F. C. Castro, “Early cracking orientation under high stress gradients: The fretting case,” *Int. J. Fatigue*, vol. 100, pp. 611–618, 2017.
- [101] M. Jayaprakash, J. S. Kumar, S. Katakam, and S. Ganesh Sundara Raman, “Effect of grain size on fretting fatigue behaviour of aisi 304 stainless steel,” in *International Symposium of Research Students on Materials Science and Engineering*, 2004.
- [102] S. Mall, H. K. Kim, E. C. Saladin, and W. J. Porter, “Effects of microstructure on fretting fatigue behavior of IN100,” *Mater. Sci. Eng. A*, vol. 527, no. 6, pp. 1453–1460, 2010.
- [103] C.-H. Goh, J. M. Wallace, R. W. Neu, and D. L. McDowell, “Polycrystal plasticity simulations of fretting fatigue,” *Int. J. Fatigue*, vol. 23, pp. 423–435, 2001.

- [104] J. R. Mayeur, D. L. McDowell, and R. W. Neu, “Crystal plasticity simulations of fretting of Ti-6Al-4V in partial slip regime considering effects of texture,” *Comput. Mater. Sci.*, vol. 41, no. 3, pp. 356–365, 2008.
- [105] T. Dick and G. Cailletaud, “Fretting modelling with a crystal plasticity model of Ti6Al4V,” *Comput. Mater. Sci.*, vol. 38, no. 1, pp. 113–125, 2006.
- [106] M. Zhang, D. L. McDowell, and R. W. Neu, “Microstructure sensitivity of fretting fatigue based on computational crystal plasticity,” *Tribol. Int.*, vol. 42, no. 9, pp. 1286–1296, 2009.
- [107] O. J. McCarthy, J. P. McGarry, and S. B. Leen, “The effect of grain orientation on fretting fatigue plasticity and life prediction,” *Tribol. Int.*, vol. 76, pp. 100–115, 2013.
- [108] Q.-N. Han, W. Qiu, Z. He, Y. Su, X. Ma, and H.-J. Shi, “The effect of crystal orientation on fretting fatigue crack formation in Ni-based single-crystal superalloys: In-situ SEM observation and crystal plasticity finite element simulation,” *Tribol. Int.*, 2018.
- [109] Z. R. Zhou and L. Vincent, “Mixed fretting regime,” *Wear*, vol. 181–183, pp. 531–536, 1995.
- [110] D. J. Gaul and D. J. Duquette, “The effect of fretting and environment on fatigue crack initiation and early propagation in a quenched and tempered 4130 Steel,” *Metall. Trans. A*, vol. 11, no. 9, pp. 1555–1561, Sep. 1980.
- [111] I. R. McColl, J. Ding, and S. B. Leen, “Finite element simulation and experimental validation of fretting wear,” *Wear*, vol. 256, no. 11–12, pp. 1114–1127, 2004.
- [112] O. J. McCarthy, J. P. McGarry, and S. B. Leen, “Micro-mechanical modelling of fretting fatigue crack initiation and wear in Ti-6Al-4V,” *Int. J. Fatigue*, 2013.
- [113] D. A. Hills, A. Sackfield, and R. J. H. Paynter, “Simulation of Fretting Wear in Halfplane Geometries: Part 1—The Solution for Long Term Wear,” *J. Tribol.*, vol. 131, no. 3, pp. 31401–31404, May 2009.

-
- [114] D. Nowell, “Simulation of Fretting Wear in Half-Plane Geometries—Part II: Analysis of the Transient Wear Problem Using Quadratic Programming,” *J. Tribol.*, vol. 132, no. 2, pp. 21402–21408, Mar. 2010.
- [115] A. V Dimaki, A. I. Dmitriev, Y. S. Chai, and V. L. Popov, “Rapid simulation procedure for fretting wear on the basis of the method of dimensionality reduction,” *Int. J. Solids Struct.*, vol. 51, no. 25, pp. 4215–4220, 2014.
- [116] J. Ding, S. B. Leen, and I. R. McColl, “The effect of slip regime on fretting wear-induced stress evolution,” *Int. J. Fatigue*, vol. 26, no. 5, pp. 521–531, 2004.
- [117] D. Nowell, D. Hills, and R. Moobola, “Length Scale Considerations in Fretting Fatigue BT - Length Scale Considerations in Fretting Fatigue,” 2000.
- [118] D. Nowell, “An analysis of fretting fatigue,” , PhD Thesis, University of Oxford, 1988.
- [119] J. A. Araújo and D. Nowell, “Analysis of pad size effects in fretting fatigue using short crack arrest methodologies,” *Int. J. Fatigue*, vol. 21, no. 9, pp. 947–956, 1999.
- [120] R. Bramhall, “Studies in fretting fatigue,” , PhD Thesis, University of Oxford, 1973.
- [121] S. Fouvry, P. Duó, and P. Perruchaut, “A quantitative approach of Ti-6Al-4V fretting damage: Friction, wear and crack nucleation,” *Wear*, vol. 257, no. 9–10, pp. 916–929, 2004.
- [122] S. Fouvry, D. Nowell, K. Kubiak, and D. A. Hills, “Prediction of fretting crack propagation based on a short crack methodology,” *Eng. Fract. Mech.*, vol. 75, no. 6, pp. 1605–1622, 2008.
- [123] K. S. Chan, Y. Lee, D. L. Davidson, and S. J. Hudak, “A fracture mechanics approach to high cycle fretting fatigue based on the worst case fret concept – I. Model development,” *Int. J. Fract.*, vol. 112, no. 4, pp. 299–330, 2001.

- [124] D. A. Hills, A. Thaitirarot, J. R. Barber, and D. Dini, “Correlation of fretting fatigue experimental results using an asymptotic approach,” *Int. J. Fatigue*, vol. 43, pp. 62–75, 2012.
- [125] D. Nowell and D. Dini, “Stress gradient effects in fretting fatigue,” *Tribol. Int.*, vol. 36, no. 2, pp. 71–78, 2003.
- [126] S. A. Lotveit and R. Bjaerum, Second generation analysis tool for flexible pipes, in: *Proceedings of the Second European Conference on Flexible Pipes, Umbilicals and Marine Cables-Structural Mechanics and Testing*. London: Bentham, 1994.
- [127] R. Perera, S.D.R., Fernando, U.S., Sheldrake, T., Clements, “An investigation into fretting behaviour in pressure armor wires of unbonded flexible pipes,” in *Volume 3: Pipeline and Riser Technology; CFD and VIV*. San Diego, California, USA, 2007, pp. 363–370.
- [128] Sinead O’Halloran, “Experimental Characterisation, Computational Modelling and Design Tool Development for Fretting Fatigue and Wear in Flexible Marine Risers,” PhD Thesis, NUI Galway, 2017.

3 Experimental Characterisation of Pressure Armour Steel

3.1 Introduction

The experimental methods implemented in this work are described in this chapter. This includes the characterisation process for the marine riser material via microscopy techniques and low cycle fatigue testing and fretting-wear testing. The measured data is implemented to calibrate and validate a CP material model in later chapters. In addition, the microstructure, mechanical behaviour and fatigue behaviour of processed and unprocessed marine riser material are compared.

3.2 Microstructure Characterisation

Two forms of the marine riser pressure armour layer material were obtained from industrial suppliers. The first is an ex-service length of flexible riser, as shown in Fig. 3.1, allowing lengths of pressure armour wire to be extracted with careful dissection of the individual layers, as described by O'Halloran [1]. This material has undergone extensive cold forming to produce the zeta profile described in Chapter 1. The second form is in 21 mm diameter rods of unprocessed riser material that have not undergone the cold wire drawing process.

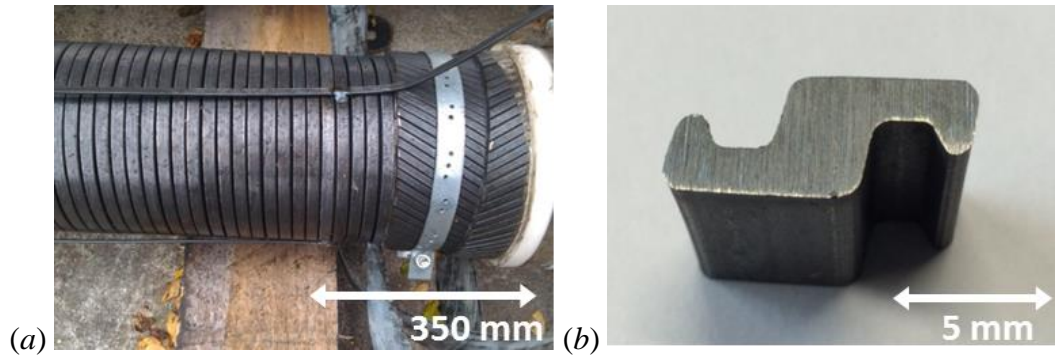


Figure 3.1. (a) Dissected portion of ex-service marine riser and, (b) photograph of pressure armour wire cross section showing zeta profile.

Microscopy specimens were extracted from both materials, mounted in epoxy resin and the surfaces were prepared for analysis on a Beuhler EcoMet 250 Grinder-Polisher. The surfaces were first ground with three grades of silicon carbide paper ranging from a coarse P300 grade to a fine P1200 grade. Samples were then polished with 9 μm and 3 μm diamond suspension and finished with a 0.05 μm fumed silica solution. After each polishing stage, samples were submerged in ethanol and cleaned in an ultrasonic bath. Finally, the surfaces were etched with a 3 % Nitol solution for 30 seconds to expose the microstructure.

Optical microscopy and scanning electron microscopy (SEM) were performed to characterise the microstructure of the material. The microstructure of the unprocessed rod material was observed to contain ferrite and pearlite phases. The pearlite phase consists of a thin lamellar structure of brittle cementite and ductile ferrite. SEM images of the unprocessed material microstructure are shown in Fig. 3.2, where the two distinct phases of ferrite (dark phase) and pearlite (light phase) phases can be seen. Figure 3.2b clearly shows the cementite (light) lamellae embedded in ferrite to collectively form a pearlite colony.

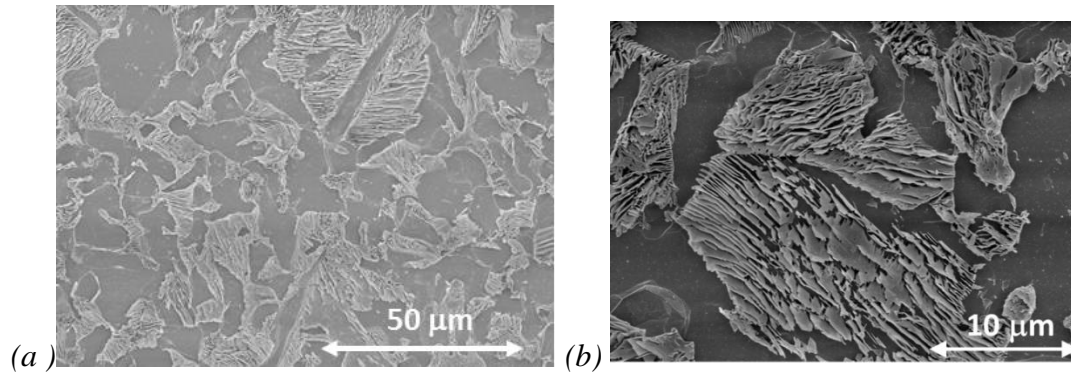


Figure 3.2. (a) SEM image of the flexible riser pressure armour material microstructure showing the light-coloured pearlite phase and darker ferrite phase and, (b) SEM image of a pearlite colony, showing the lamellar ferrite-cementite structure.

Figure 3.3 shows a comparison of optical microscopy images for the unprocessed and processed microstructure. The consequence of cold forming is seen here, as individual grains and phases in the processed sample are not as distinct as in the unprocessed sample. The grains have become elongated during the cold drawing process. This is typical for a heavily cold drawn material [2]. The clear lamellar structure of cementite and ferrite in the pearlite colonies is not observed in the processed material. This is due to fracture of the cementite under the high deformations induced by processing.

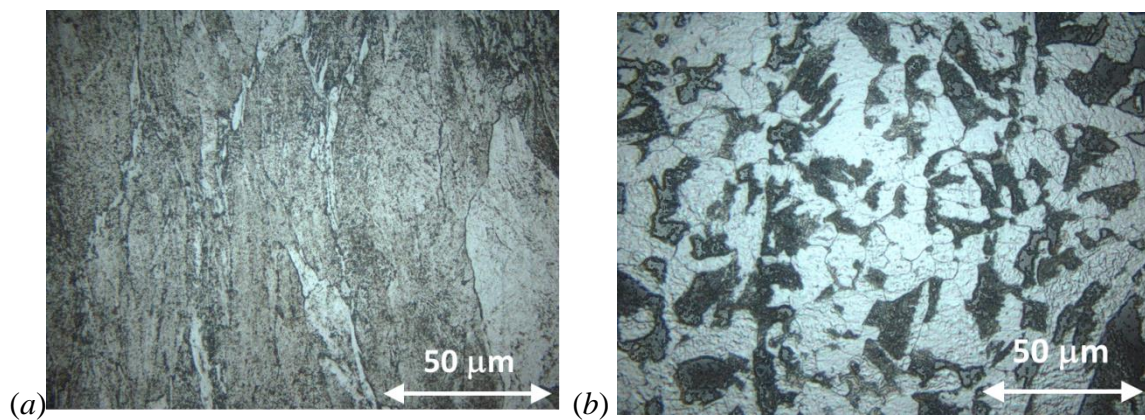


Figure 3.3. Optical microscope images of (a) cold drawn riser material and (b) unprocessed material.

A Python scripting code was written to compute microstructure statistics by implementing Gaussian filtering, thresholding and pixel counting techniques. The

microstructural analysis has identified a volume fraction of 51% ferrite and 49% pearlite, with an average ferrite grain size of 11 μm . The average grain size is calculated by representing a grain as a hexagon of equal area to the measured grain area, as shown schematically in Fig 3.4. The width of the corresponding hexagon is the grain size d , calculated as follows [3]:

$$d = \sqrt{\frac{2 * A_{\text{grain}}}{\sqrt{3}}}. \quad (3.1)$$

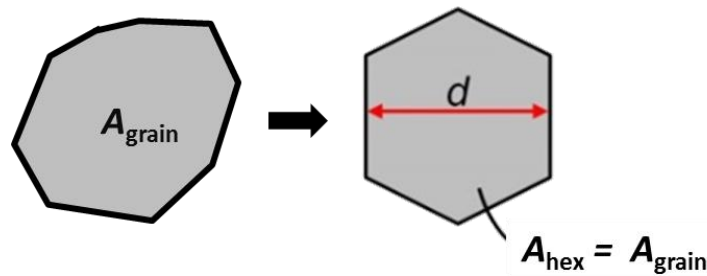


Figure 3.4. Representing an arbitrary polygonal grain as a hexagon in order to determine grain size d .

Energy-dispersive X-ray (EDX) analysis has established a carbon content of 0.4% for this material. This carbon content is expected for a near-equal volume fraction of ferrite and pearlite phases, as seen in hypo-eutectoid steels.

3.3 Strain-Controlled Testing

3.3.1 Unprocessed Rod Material

A program of strain-controlled low cycle fatigue (LCF) tests was conducted to characterise the cyclic plasticity and fatigue behaviour of the material and to facilitate calibration of the CPFGE and fatigue prediction model in subsequent chapters. Specimens were manufactured according to the American Society for Testing and Materials (ASTM) standards [4] and tested using an Instron 8500 servo hydraulic system. An

extensometer with knife-edge probes was used to measure, and hence control via Bluehill closed loop feedback, the applied strain range, using a constant rate of 0.1% per second. The fatigue specimen geometry is given in Fig. 3.5.

Figure 3.6 shows the measured evolutions of stress range for applied strain ranges of 0.8%, 1.0%, 1.6% and 2.0%. For all but the highest strain range case, the material is seen to cyclically soften during the first 20 cycles. Gradual hardening is thereafter observed over a large fraction of the life in each test before failure, which is represented by the sudden drop in stress range. Subramanya et al. [5] observed a similar stress evolution during LCF tests of a ferritic-pearlitic steel, particularly at lower strain ranges. The slight hardening observed for the highest applied strain range has also been observed by Sankaran et al. [6] and is attributed to the formation of sub-grains and dislocation accumulation at grain and phase boundaries, as a result of high plastic strains. The rapid decay in stress near failure suggests that crack propagation phase is negligible. Hence, the total life can be assumed to correspond to number of cycles to crack initiation also.

Figure 3.7 shows the cyclic stress-strain response of the material at half-life (essentially stabilised) for each strain range considered. A significant amount of kinematic hardening can be seen in each case. For example, reverse yield occurs in tension for the applied strain range of $\pm 1\%$. The number of cycles to failure is plotted in Fig. 3.8 for two (repeat) tests at each strain range. Fatigue scatter is seen to be more significant at the lower strain ranges; this is potentially due to the absence of bulk plasticity and greater dependency of crack initiation on microstructural features [7].

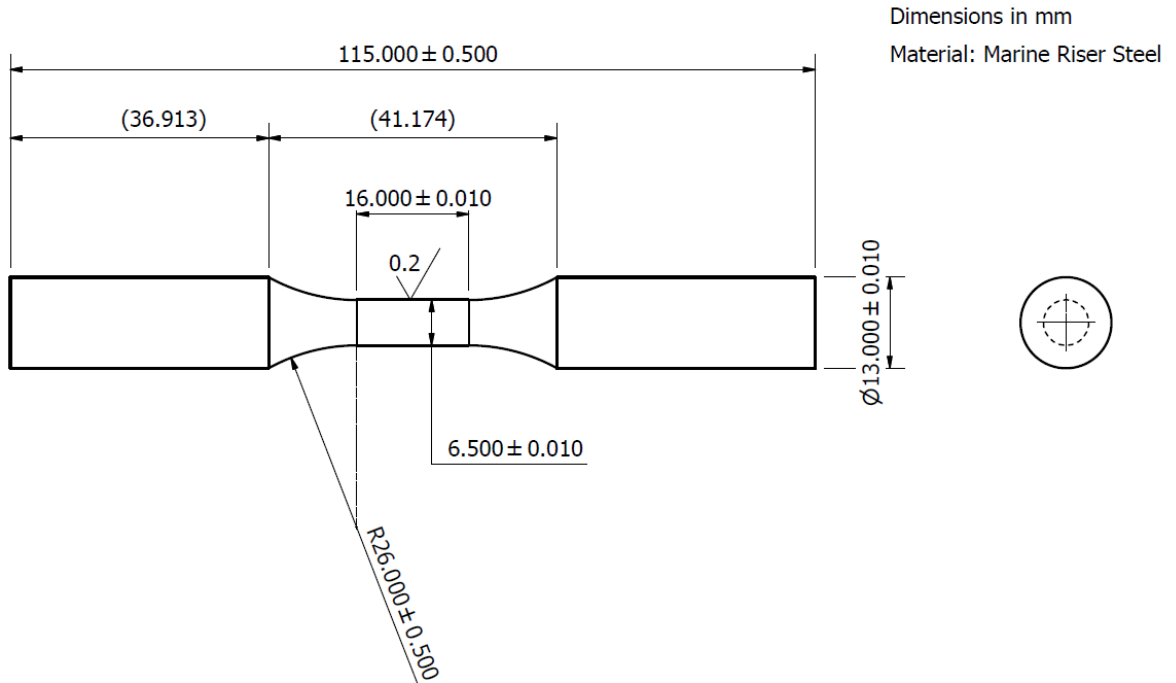


Figure 3.5. Fatigue specimen geometry for LCF testing (Dimensions in mm).

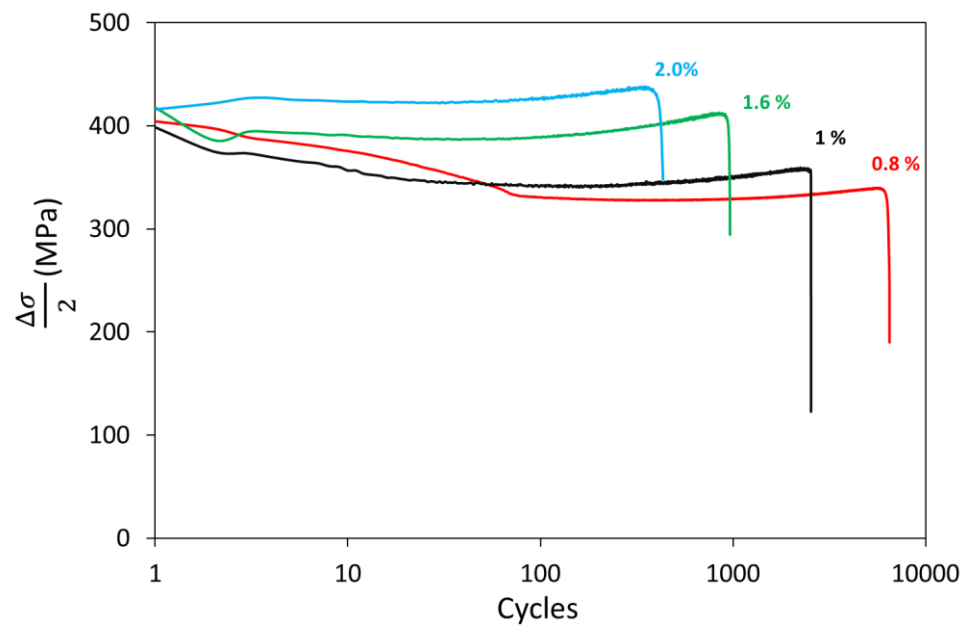


Figure 3.6. Experimentally-measured evolutions of stress range during strain-controlled LCF tests for different strain ranges.

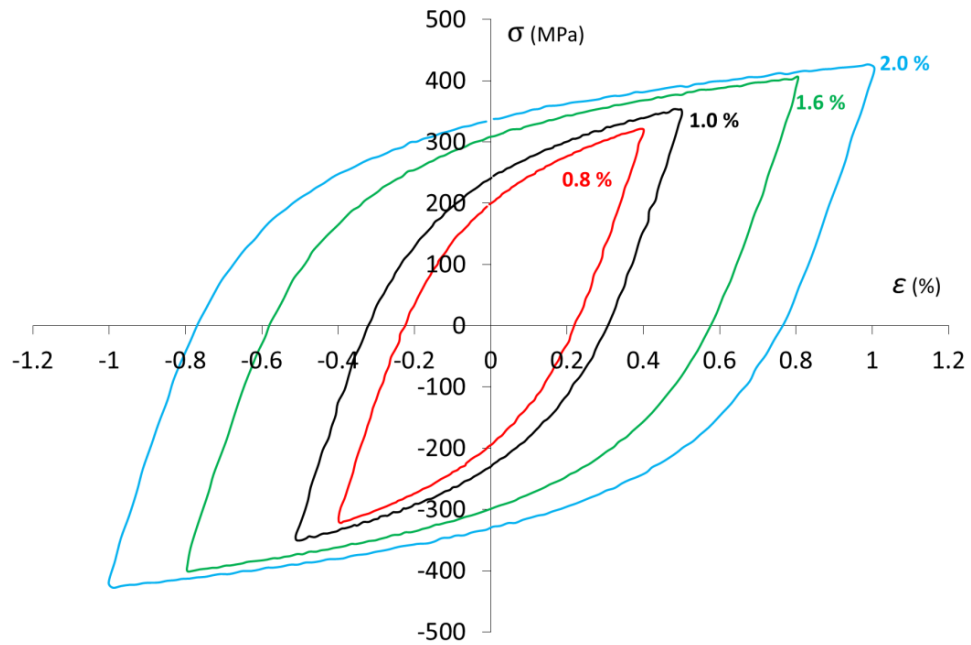


Figure 3.7. Experimentally-measured (half-life) cyclic stress-strain response for strain-controlled LCF tests at different strain ranges.

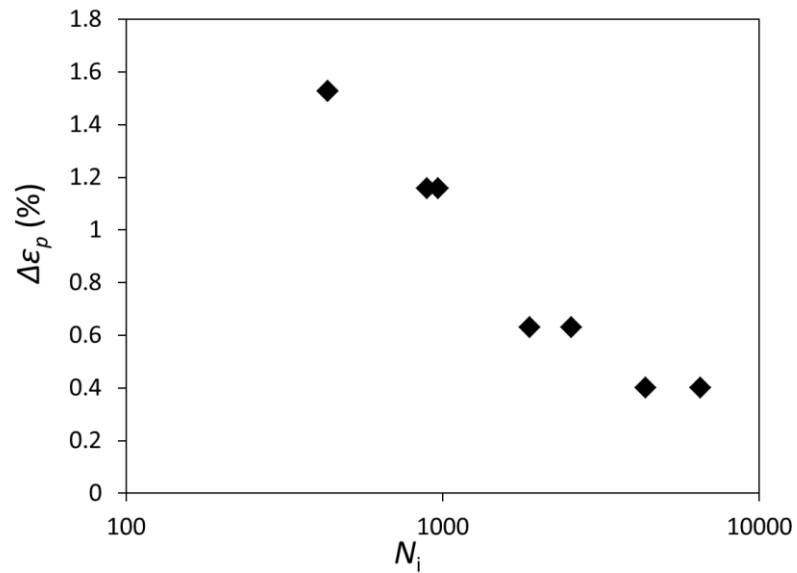


Figure 3.8. Experimentally-measured relationship between plastic strain range and numbers of cycles to failure, with repeat tests at each applied strain range.

Figure 3.9 shows an SEM image of the fracture surface of a 1% SR specimen. A region of crack growth, with striations, is observed near the edge of the specimen. The small area fraction of the striation region again indicates that the fatigue propagation regime consumes a relatively small portion of the fatigue life, and hence the majority is consumed by the crack initiation process.

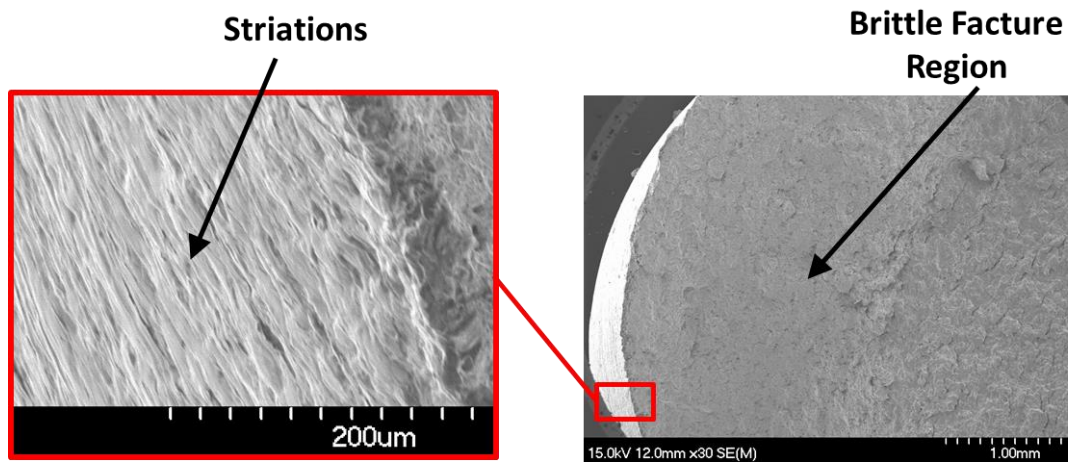


Figure 3.9. SEM image of a fracture surface, showing relatively small region of crack growth region.

3.3.2 Processed Pressure Armour Wire Material

The processed cold formed wire was tested in LCF by O'Halloran [1] using the same testing apparatus and procedure as described in Section 3.3.1. However, the geometry of the processed wire restricted the manufacture of specimens conforming to the ASTM standards. The specimens were thus designed to be a dog bone shape with a cylindrical gauge section. An image of this specimen design is given in Fig 3.10. A comparison of the mechanical behaviour of both materials is presented in Fig. 3.11, showing the monotonic response, cyclic stress strain response at half-life, and LCF behaviour. The rod material shows a yield plateau, with negligible strain hardening observed after initial yielding. This occurs when dislocations become unpinned on initial loading, causing them to become mobile, which leads to a rapid accumulation of macroscopic strain. The yield stress and work hardening in the processed material is significantly greater than the rod material. For a similar material the strengthening mechanisms have been attributed to (i) boundary strengthening, (ii) dislocation strengthening and (iii) solid solution

hardening [8]. During cold forming, the dislocation density increases significantly, leading to dislocation-dislocations interactions, whereby gliding dislocations are obstructed by sessile dislocations. Cementite laths also act as barriers to dislocation motion. No yield plateau is observed for the processed material. The characteristics of a yield plateau is not an intrinsic material property and can be attributed to a large number of variable including grain size, prior processing, heat treatment and test conditions [9].

The evolution of stress with number of cycles is plotted in Fig. 3.11c for a 1% strain range test. It is clear that cold formed material cyclically softens throughout the test. The drop in stress is significantly greater than for the unprocessed rod material. This result is expected, as cold worked materials are generally seen to cyclically soften due to dynamic recovery, where the high dislocation density induced by cold-working, combined with an applied stress, leads to dislocation annihilation. The overall decrease in dislocation density results in a reduction in the number of barriers to dislocation motion, and thus, increased crystallographic slip, leading to softening. Another potential factor here is the absence of the lamellar pearlite structure, which has been broken during the cold working process (See Fig. 3.12). This is thought to allow for easier dislocation motion, and accentuates the softening behaviour, compared to the unprocessed rod, where the cementite laths restrict dislocation motion on particular slip systems, depending on crystallographic orientation and relative lath orientations.

The low cycle fatigue behaviour is compared in Fig. 3.11d. The cold drawn riser material has shorter life in all cases. It is thought that the extensive cold working process here has induced a large amount of damage to the material prior to the fatigue tests. In addition, a number of authors have reported high residual tensile stresses at the surface of post-drawn ferritic [10] and pearlitic [11] steel rods. It is well known that tensile residual stresses are detrimental for fatigue resistance.

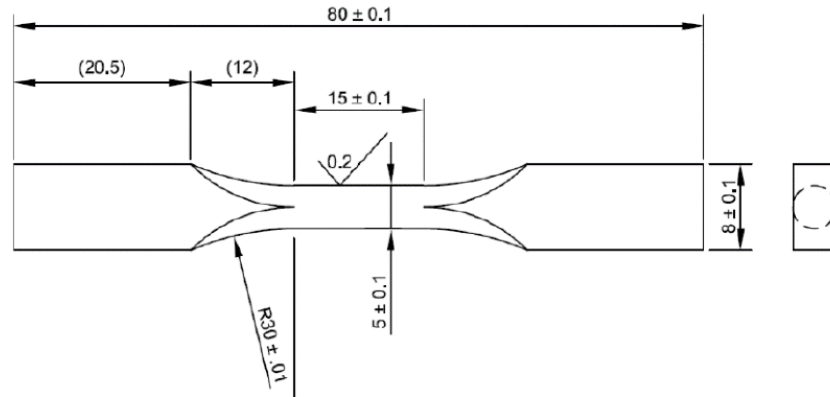


Figure 3.10. Image of fatigue specimen manufactured from marine riser pressure armour wire.

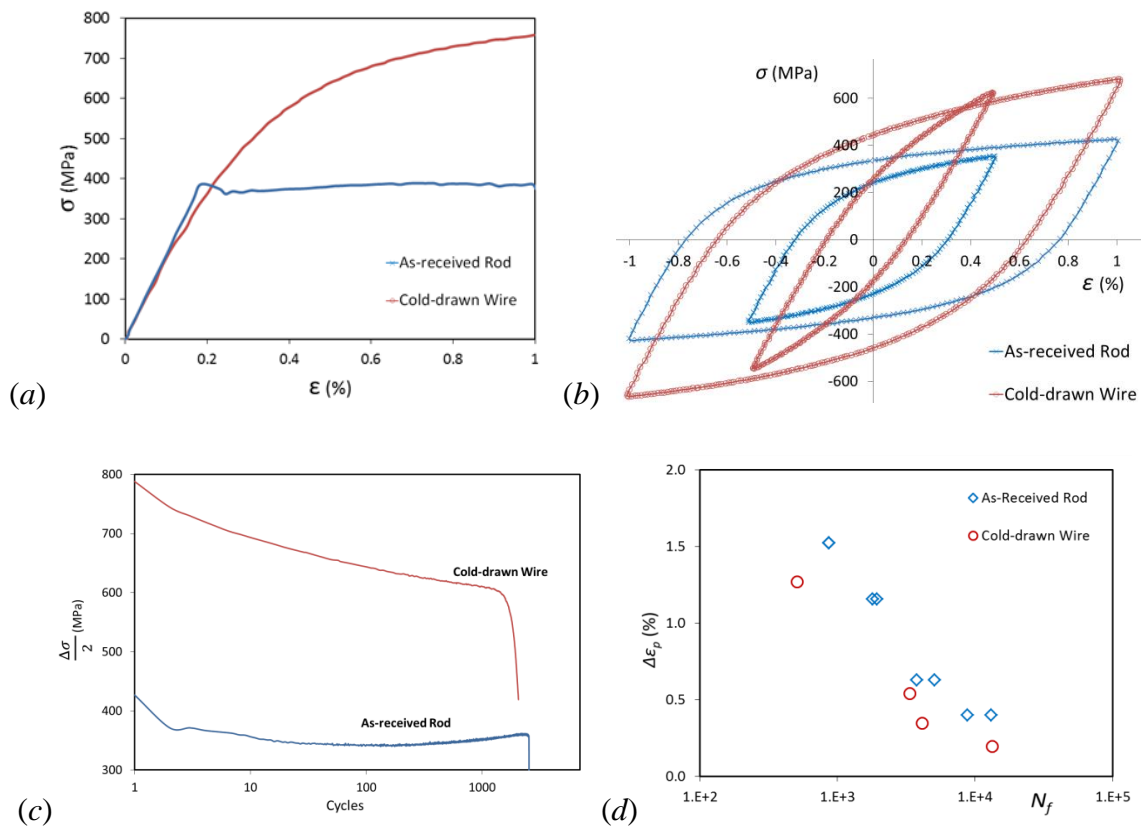


Figure 3.11. Comparison of the mechanical behaviour of cold worked riser [1] and unprocessed rod material showing (a) monotonic stress strain response, (b) cyclic stress-strain response at half-life, (c) evolution of stress with no. of cycles and (d) Coffin-Manson type strain-life data.

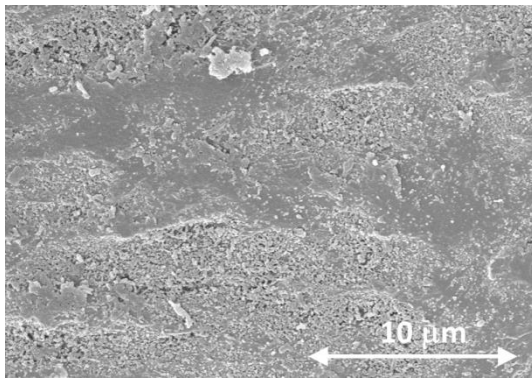


Figure 3.12. SEM image of cold drawn riser material showing a broken and less pronounced pearlite structure compared to the unprocessed material shown in fig. 3.2.

3.4 Nanoindentation Testing

Nanoindentation is a relatively new technique for microscale indentation to help obtain material properties in multiphase materials. Where large-scale test methods provide the component level material response, nanoindentation can potentially provide a distinction between the mechanical behaviour of each phase at the micro scale. Depending on the specific material and indentation control capability, individual grains and phases in the microstructure can potentially be indented to provide load versus depth response curves. Mechanical properties such as hardness and Young's modulus can be extracted using empirical relationships. However, these relationships are generally based on larger scale indents that span multiple grains [12]

In this work, nanoindentation was employed to attempt to distinguish between the pearlite and ferrite phases of the material for possible input into CPFEM models (e.g. critical resolved shear stress for the ferrite and pearlite phases) introduced in Chapter 4. Specimens were polished and etched as per the description in Section 3.2. The etching procedure is necessary for the individual phases to be targeted by the indenter. However, the surface corrosion introduced by the etching may affect the material response in tests. Testing was performed by a diamond tip pyramidal Berkovich indenter in load control mode. The maximum load was chosen to be 100 mN, applied at a rate of 40 mN/min with a dwell time of 10 seconds before unloading.

Fig. 3.13 shows images of single indents in the ferrite and pearlite phases. In some cases the edge of the indent crosses a grain boundary. This problem arises due to the small grain size relative to the indent, limited control capability and small error associated with the targeting microscope.

Figure 3.14 shows load versus indentation depth curves for indentations on four ferrite grains and four pearlite grains. It can be seen that these results do not show any significant trend in material response for each phase. This result is attributed to a number of factors including (i) differing crystal orientations of each grain, which have a considerable influence nanoindentation response of metals [13] (ii) cementite lath orientation, and (iii) the effects of etching the surface of the material.

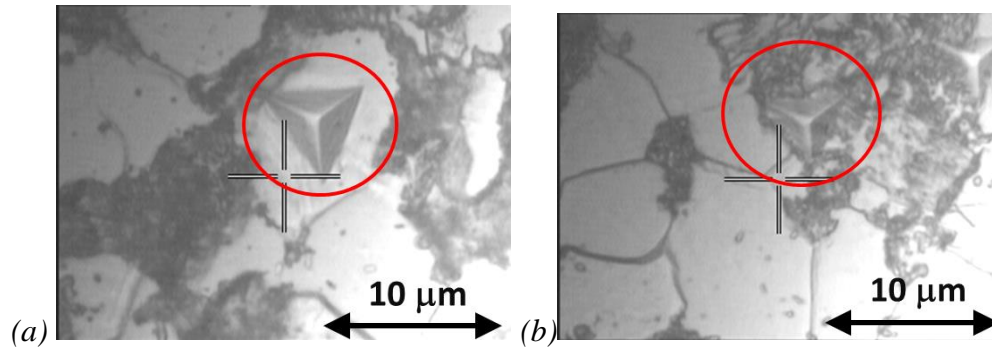


Figure 3.13. Indent of (a) ferrite and (b) pearlite phases.

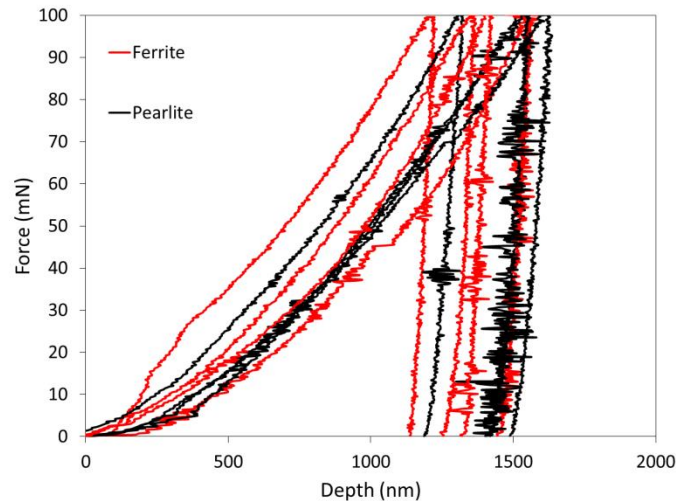


Figure 3.14. Load versus depth nanoindentation curves for 4 ferrite and 4 pearlite phases.

The indentation hardness H_{Π} for each test is calculated using the Oliver and Pharr [14] method as follows:

$$H_{\Pi} = \frac{P_{max}}{A(h_c)} \quad (3.1)$$

where P_{max} is the maximum applied load and $A(h_c)$ is the contact area. $A(h_c)$ is determined using the following tip shape function:

$$A(h_c) = 24.5h_c^2 + C_1h_c + C_2h_c^{0.5} + \dots \quad (3.2)$$

where h_c is the contact depth and C_1 and C_2 are constants determined via a calibration process by indenting fused silica [15]. The indentation hardness H_{Π} is converted to Vickers by $H_V = 0.0945(H_{\Pi})$. The Vickers hardness H_V calculated for each test is presented in Table 3.1.

Table 3.1. Comparison of Vickers hardness values for four pearlite and four ferrite grains.

Pearlite		Ferrite	
Test	Hv	Test	Hv
1	192.89	1	256.98
2	157.39	2	202.11
3	205.26	3	171.93
4	143.08	4	190.69
AVERAGE	174.655	AVERAGE	205.4275

The macro-scale hardness for this material is approximately $H_V = 170$, in general agreement with the measured results. However, the results presented in Table 3.1 echo those presented in Fig. 3.14, where no clear trend is observed between the hardness of the ferrite and pearlite phases. The average hardness value over the four tests is higher for the ferrite phase. Prior to the tests, it was anticipated that the pearlite phase would exhibit higher hardness values due to the presence of cementite laths. It is possible that the effects of crystal orientation and cementite lath orientation are dominant here. Therefore the current methodology for measuring individual phase hardness is considered to be insufficient without more detailed knowledge of the crystallographic orientations of each grain.

Seok et al. [16] also performed nanoindentation on a similar ferritic-pearlitic steel and showed that the pearlite phase displayed a harder force-depth response. However in [16], only a single indent for each phase was compared, making it difficult to compare with the results presented here, as the potential sensitivity to grain orientation has not been quantified.

3.5 Fretting Wear Testing

A fretting-wear rig has recently been developed at NUI Galway by O'Halloran [17] to characterise the fretting wear behaviour of the material and identify coefficient of friction. An annotated photograph of the rig is given in Figure 3.15. A piezoelectric actuator applies a reciprocating micro-scale displacement of the order of $1 \times 10^1 \mu\text{m}$ or so, representative conditions of those in the pressure armour wire of marine risers,. A DVRT (Differential Variable Resistance Transducer) and dynamic force sensor are used to measure tangential displacement and force, respectively, via a developed Labview data acquisition program. This allows for the calculation of coefficient of friction and observation of fretting loops (tangential force versus displacement response), which was studied by O'Halloran.

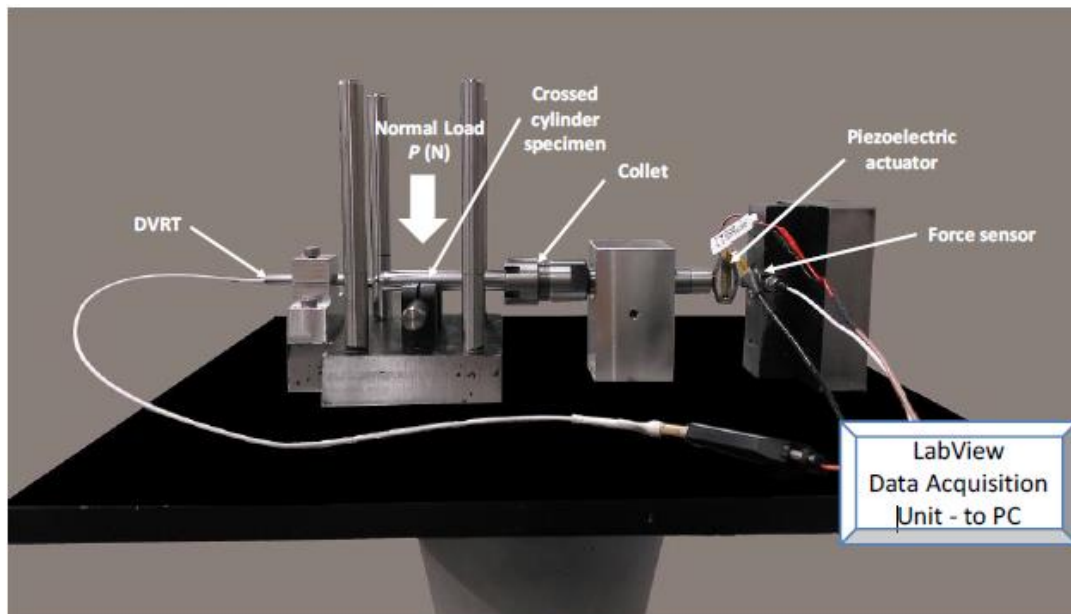


Figure 3.15. Annotated photograph of fretting-wear rig at NUI Galway (Top cylinder removed for visibility).

The fretting rig is employed in this work to observe fretting-induced surface damage and possible cracks in the marine riser material. A number of plain fretting tests were performed for up to one million cycles with the aim of observing fatigue cracks. To aid the observation of fretting-induced cracks, a cylinder-on-flat contact arrangement was designed, as shown Fig. 3.16a. This set-up is intended to develop a fretting scar across the thickness of the flat specimen, as compared to a single point contact in the crossed cylinder arrangement used by O'Halloran [17]. This in turn facilitates a cross-section to be cut and observed through a microscope to help identify cracking and damage. However, this also significantly reduces the magnitude of the associated maximum contact pressure.

Figure 3.16b shows a sample of measured fretting loops for a partial slip fretting test (where the tangential force does not exceed the resisting frictional force and full sliding does not occur). A 5th order Butterworth low pass frequency filter was implemented in Python to remove unwanted frequencies in the force displacement response of the test. This response is typical for a partial slip fretting case [18], where the area of the fretting loop represents the dissipated energy due to a number of factors, including heat loss and localised asperity plasticity.

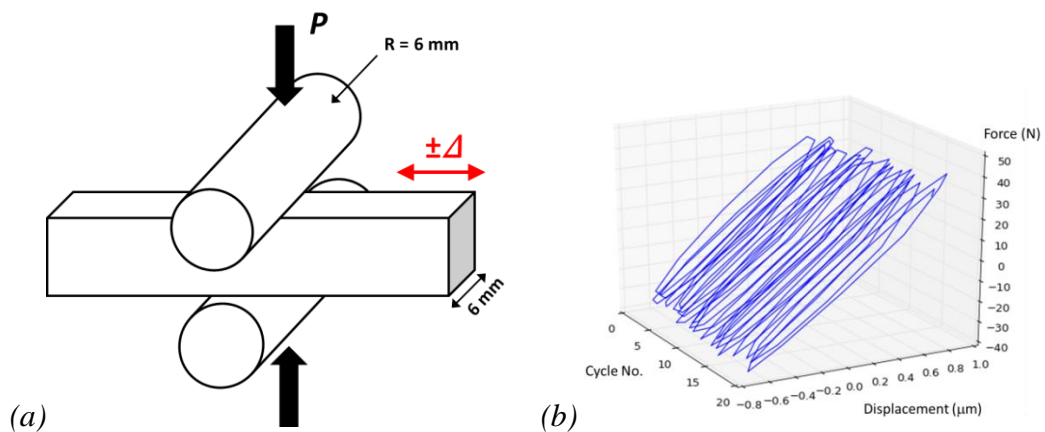


Figure 3.16. (a) Cylinder-on-flat set-up used for fretting tests, where P and Δ are applied normal load and tangential displacement range, respectively, and (b) fretting loops extracted from measured force and displacement data over 20 fretting cycles.

The highest possible normal load, P , of 92 N (corresponding to a peak contact pressure of 300 MPa) and largest possible applied tangential displacement Δ of $\pm 0.7\mu\text{m}$ (the test remained in the partial slip regime) were chosen to achieve high stresses at the edge of contact and in the slip zones and thus, provide the most detrimental conditions to increase the probability of cracking. Despite these test conditions, the localised cyclic stresses in the contact region were not large enough to generate observable fretting fatigue cracks. A CPFE model with equivalent geometry predicts a plastic strain field of less than $10\mu\text{m}$ in depth at the slip zones under the same applied loads, as shown in Fig 3.17. This highlights the very small length-scales associated with the test conditions adopted here to observe cracking.

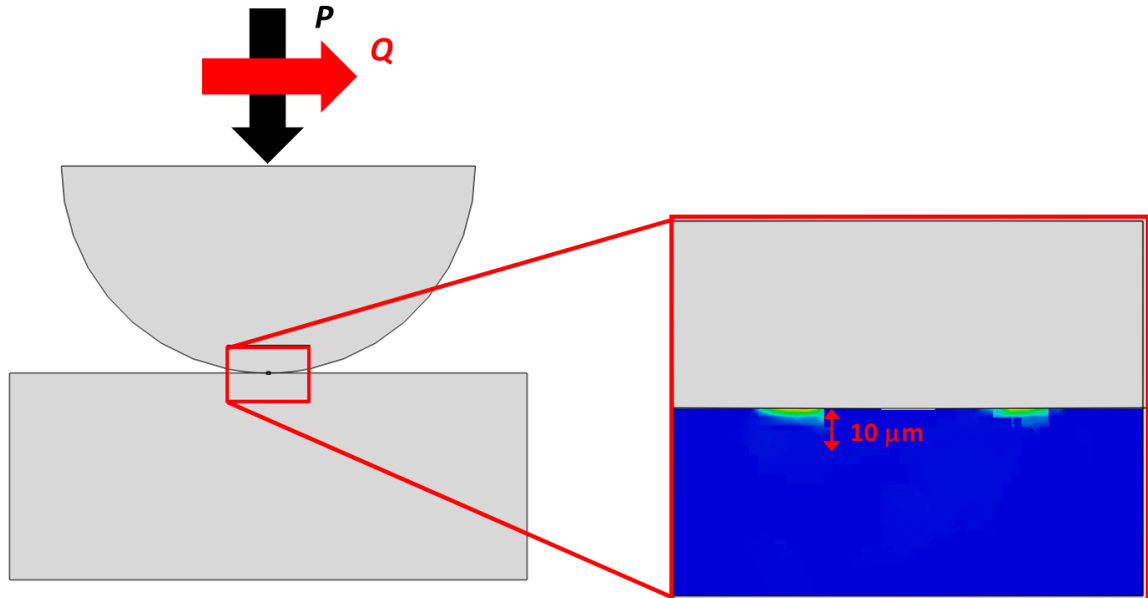


Figure 3.17. Cross section view of equivalent CPFE model showing small regions of plasticity. The blue region indicates elastic stresses and strains only.

The fretting scar in Fig. 3.18, suggests that the contact pressure was not completely uniform across the flat specimen surface. Cross sectioned views were observed through the microscope, although no distinct signs of cracking were identified, as shown in Fig. 3.18. The red circle in Fig. 3.18 shows an unconfirmed crack in the fretted specimen. However, similar features, such as grain boundaries were also observed outside the contact region.

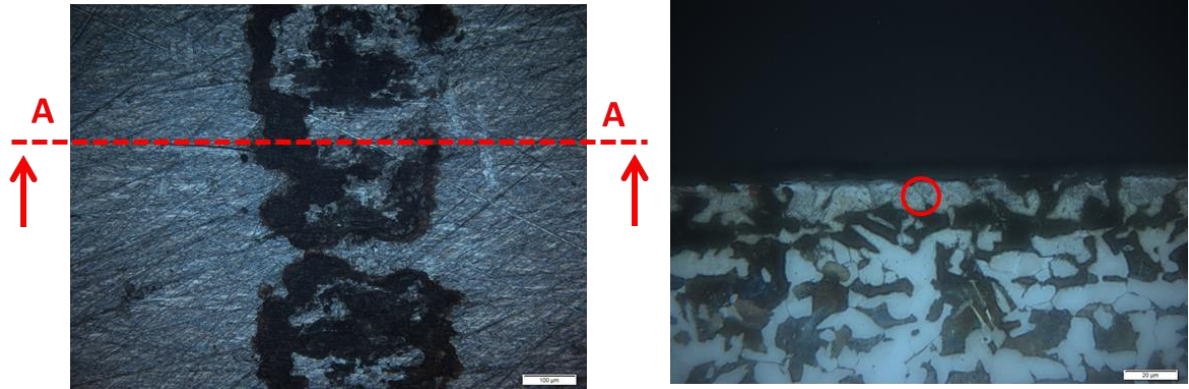


Figure 3.18. Fretting wear results showing (a) fretting scar on flat specimen and (b) cross section view along AA with unconfirmed cracks highlighted.

For these reasons, it was decided that fretting fatigue tests would be a more suitable method for observing cracks, where the additional substrate stress ensures crack propagation, allowing the material to be studied further. The additional advantage of fretting fatigue testing is the provision of a total fretting fatigue life, and thus allows some quantitative assessment studies to be performed. The fretting fatigue testing methodology developed by McCarthy is adopted in this work, and is presented in Appendix A. However due to rig availability problems, this was not further pursued. An aim of this work was to implement the previously developed methodology and apparatus to study the effect of grain size on fretting fatigue. This included the development of a heat treatment procedure to increase the grain size of the material. This procedure is also detailed in Appendix A. Due to technical issues with fatigue testing machine, this fretting fatigue grain size study could not be performed within the timeframe of this thesis. However, the specimens have been manufactured and it is anticipated that this testing will be conducted in future research.

3.6 Conclusions

The experimental methods developed and employed in this work have been described in this chapter. The mechanical behaviour, low cycle fatigue behaviour and microstructure of processed and unprocessed forms of marine riser material have been characterised. The cold-forming process for manufacturing zeta-shape wire has been shown to significantly change the material behaviour and microstructure. In particular, the

processed wire exhibits a harder uniaxial stress-strain response and significantly lower low cycle fatigue life when compared to the unprocessed material. The results from this characterisation process will be employed in subsequent chapters to calibrate the crystal plasticity material model and fatigue prediction models for the as-received rod material.

3.7 References

- [1] Sinead O'Halloran, "Experimental Characterisation, Computational Modelling and Design Tool Development for Fretting Fatigue and Wear in Flexible Marine Risers," PhD Thesis, NUI Galway, 2017.
- [2] M. Zidani, S. Messaoudi, T. Baudin, D. Solas, and M. H. Mathon, "Deformation textures in wire drawn perlitic steel," *Int. J. Mater. Form.*, vol. 3, no. 1, pp. 7–11, 2010.
- [3] C. A. Sweeney, "Micromechanics of fatigue with application to stents," PhD Thesis, National University of Ireland Galway, 2014.
- [4] L. F. Testing, "Standard Practice for Statistical Analysis of Linear or Linearized Stress-Life ($S-N$) and Strain-Life ($\epsilon-N$) Fatigue Data 1," *Annu. B. ASTM Stand.*, vol. i, pp. 1–7, 2012.
- [5] V. S. Sarma and K. A. Padmanabhan, "Low cycle fatigue behaviour of a medium carbon microalloyed steel," *Int. J. Fatigue*, vol. 19, no. 2, pp. 135–140, 1997.
- [6] S. Sankaran, V. S. Sarma, and K. a. Padmanabhan, "Low cycle fatigue behavior of a multiphase microalloyed medium carbon steel: comparison between ferrite + pearlite and quenched and tempered microstructures," *Mater. Sci. Eng. A*, vol. 345, pp. 328–335, 2003.
- [7] D. L. McDowell and F. P. E. Dunne, "Microstructure-sensitive computational modeling of fatigue crack formation," *Int. J. Fatigue*, vol. 32, no. 9, pp. 1521–1542, 2010.
- [8] X. Zhang, A. Godfrey, X. Huang, N. Hansen, and Q. Liu, "Microstructure and strengthening mechanisms in cold-drawn pearlitic steel wire," *Acta Mater.*, vol. 59, no. 9, pp. 3422–3430, 2011.

-
- [9] E. O. Hall, *Yield point phenomena in metals and alloys*. London : Macmillan, 1970.
- [10] J. M. Atienza, M. L. Martinez-Perez, J. Ruiz-Hervias, F. Mompean, M. Garcia-Hernandez, and M. Elices, “Residual stresses in cold drawn ferritic rods,” *Scr. Mater.*, vol. 52, no. 4, pp. 305–309, 2005.
- [11] J. M. Atienza, J. Ruiz-Hervias, M. L. Martinez-Perez, F. J. Mompean, M. Garcia-Hernandez, and M. Elices, “Residual stresses in cold drawn pearlitic rods,” *Scr. Mater.*, vol. 52, no. 12, pp. 1223–1228, 2005.
- [12] A. E. Giannakopoulos and S. Suresh, “Determination of elastoplastic properties by instrumented sharp indentation,” *Scr. Mater.*, vol. 40, no. 10, pp. 1191–1198, 1999.
- [13] T. B. Britton, H. Liang, F. P. E. Dunne, and A. J. Wilkinson, “The effect of crystal orientation on the indentation response of commercially pure titanium: experiments and simulations,” *Proc. R. Soc. A Math. Phys. Eng. Sci.*, vol. 466, no. 2115, p. 695 LP-719, Mar. 2010.
- [14] W. C. Oliver and G. M. Pharr, “Measurement of hardness and elastic modulus by instrumented indentation: Advances in understanding and refinements to methodology,” *J. Mater. Res.*, vol. 19, no. 01, pp. 3–20, 2004.
- [15] R. N. Shirazi, F. Aldabbagh, A. Erxleben, Y. Rochev, and P. McHugh, “Nanomechanical properties of poly(lactic-co-glycolic) acid film during degradation,” *Acta Biomater.*, vol. 10, no. 11, pp. 4695–4703, 2014.
- [16] M. Y. Seok, I. C. Choi, J. Moon, S. Kim, U. Ramamurty, and J. Il Jang, “Estimation of the Hall-Petch strengthening coefficient of steels through nanoindentation,” *Scr. Mater.*, vol. 87, pp. 49–52, 2014.
- [17] S. M. O’Halloran, A. M. Harte, and S. B. Leen, “Development of a piezoelectrically-actuated fretting wear test rig for pressure armour layer nub-groove contact,” *Rev.*, 2017.

- [18] S. Fouvry and B. Berthel, “Prediction of Fretting-fatigue Crack Nucleation Using a Surface Shear - Sliding Size Crack Analog Parameter,” *Procedia Eng.*, vol. 133, no. 0, pp. 179–191, 2015.

4 Micromechanical Modelling Methodology

4.1 Introduction

This chapter describes the framework developed to study the microstructure sensitivity of mechanical behaviour, fatigue and fretting fatigue behaviour of metals. The theoretical of crystal plasticity modelling is first described, followed by a description of the material models used in this thesis. Modifications are made to existing material models to better represent the mechanical behaviour of the materials investigated. In particular, strain gradients effects due to the presence of geometrically necessary dislocations, and kinematic hardening are included in the CPFEE models. The Python scripting methodologies developed to generate finite element geometries of material microstructure and represent crystallographic texture are also described in the chapter.

4.2 Large Deformation Mechanics

4.2.1 Deformation Gradient

Crystal plasticity material models are formulated using large deformation mechanics. Large deformation mechanics considers the deformation of a body from a reference configuration to a deformed, current configuration [1]. The deformation gradient \mathbf{F} describes the transformation of any vector in a body from the reference configuration to the current configuration. For example, consider the deformation of the arbitrary body shown in Fig. 4.1. The position of point P in the undeformed body is given by the vector \mathbf{X} with respect to the global material coordinate system. The body undergoes deformation and P is translated to P' by a displacement vector \mathbf{u} . The position of P' is given by the vector \mathbf{x} where

$$\mathbf{x} = \mathbf{X} + \mathbf{u} \quad (4.1)$$

Similarly, the vector between point P and Q , $d\mathbf{X}$ is transformed to $d\mathbf{x}$ in the deformed body. The deformation gradient \mathbf{F} is used to describe this transformation:

$$dx = FdX \quad (4.2)$$

and can be written more explicitly in component form as

$$\begin{pmatrix} dx \\ dy \\ dz \end{pmatrix} = \begin{pmatrix} \frac{\partial x}{\partial X} & \frac{\partial x}{\partial Y} & \frac{\partial x}{\partial Z} \\ \frac{\partial y}{\partial X} & \frac{\partial y}{\partial Y} & \frac{\partial y}{\partial Z} \\ \frac{\partial z}{\partial X} & \frac{\partial z}{\partial Y} & \frac{\partial z}{\partial Z} \end{pmatrix} \begin{pmatrix} dX \\ dY \\ dZ \end{pmatrix} \quad (4.3)$$

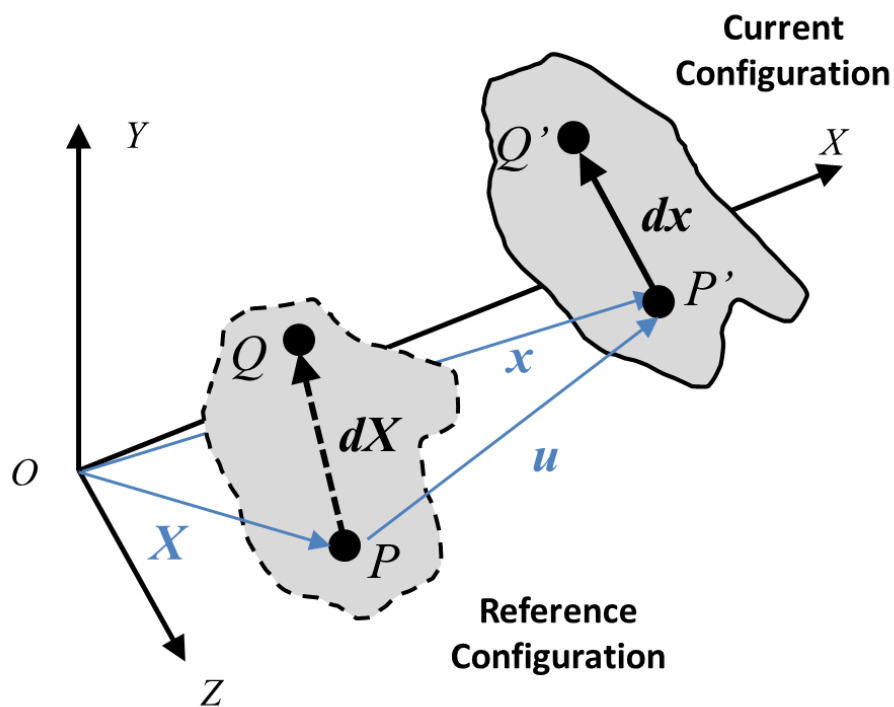


Figure 4.1. The deformation of a body from the reference configuration to the current configuration.

The deformation gradient describes the combined stretch and rigid body rotation of the body, excluding translation. The stretch and rigid body rotation contributions of F can be separated as follows:

$$F = RU \quad (4.4)$$

where \mathbf{R} and \mathbf{U} are the rotation and stretch matrices, respectively. The deformation gradient can be implemented to determine strain tensors quantities for use in mechanical analysis. For example the Almansi tensor, which is a measure of true strain, is defined as:

$$\mathbf{e} = \frac{1}{2}(\mathbf{I} - (\mathbf{F}^{-1})^T \mathbf{F}^{-1}) \quad (4.5)$$

and the Green Lagrangian strain tensor \mathbf{E} is defined as:

$$\mathbf{E} = \frac{1}{2}(\mathbf{F}^T \mathbf{F} - \mathbf{I}) \quad (4.6)$$

where \mathbf{I} is the identity matrix.

In crystal plasticity formulations, stresses and strains are generally calculated in rate form, and therefore it is useful to express the deformation gradient as a rate dependent quantity:

$$\dot{\mathbf{F}} = \frac{\partial}{\partial t} \left(\frac{\partial \mathbf{x}}{\partial \mathbf{X}} \right) = \frac{\partial \mathbf{v}}{\partial \mathbf{X}} = \mathbf{L} \mathbf{F} \quad (4.7)$$

where \mathbf{L} is the velocity gradient, which represents the spatial rate of change of velocity, and can be related to the rate of change of deformation gradient:

$$\mathbf{L} = \frac{d\mathbf{v}}{d\mathbf{x}} = \dot{\mathbf{F}} \cdot \mathbf{F}^{-1}. \quad (4.8)$$

\mathbf{L} can be decomposed into symmetric and asymmetric parts \mathbf{D} and \mathbf{W} , which correspond to rate of deformation and continuum spin, respectively:

$$\mathbf{D} = \frac{1}{2}(\mathbf{L} + \mathbf{L}^T) \quad (4.9)$$

$$\mathbf{W} = \frac{1}{2}(\mathbf{L} - \mathbf{L}^T) \quad (4.10)$$

The stress state of a material point may be determined with this large deformation mechanics description. The second Piola-Kirchoff stress \mathbf{S} , which is used in large deformation problems, is calculated by:

$$\mathbf{S} = \det(\mathbf{F}) \mathbf{F}^{-1} \boldsymbol{\sigma} \mathbf{F}^{-T}. \quad (4.11)$$

where $\boldsymbol{\sigma}$ is the Cauchy stress tensor which relates a stress vector \boldsymbol{t} acting on a surface to a normal vector \boldsymbol{n} :

$$\boldsymbol{t} = \boldsymbol{\sigma}\boldsymbol{n}. \quad (4.12)$$

As stated above, CP formulations are often expressed in rate form, which requires the calculation of a stress rate. The commonly used Jaumann stress rate is introduced in Section 4.4.2.

4.3 Crystal Plasticity Theory

In crystal plasticity models, plastic deformation is described by crystallographic slip due to the flow of dislocations along crystal slip systems. A dislocation is an imperfection in the alignment of atoms in a crystal lattice. Dislocations can basically be characterised as edge type, where the direction of motion is parallel to the direction of applied stress, or screw type, which glides perpendicular to the applied stress. In reality most dislocations are a combination of screw and edge type. Figure 4.2 shows the motion of an edge dislocation in a crystal lattice under an applied shear stress. Slip occurs on the closest packed planes of atoms in the crystal lattice in the closest packed directions. A number of different crystal structures exist in metals, each of which contains a unique set of possible slip directions or slip systems. The three most common crystal types are face centre cubic (FCC), body centre cubic (BCC), and hexagonal close packed (HCP). FCC materials have 12 slip systems (possible directions for slip), BCC have 48 and HCP have 24. All three crystal types are encountered in this thesis (FCC – CoCr alloy, BCC – marine riser steel and HCP – Ti alloy). An example of a slip system in a BCC unit cell is given in Fig. 4.3. A full description of all possible slip systems for each material type will be included in subsequent chapters.

Crystal plasticity theory is based on the relationship between crystallographic slip, or dislocation motion, and resolved shear stress on a crystal slip system. It is generally accepted that crystallographic slip will occur when the shear stress acting on a slip system reaches the critical resolved shear stress, the value of which depends on a number of factors including material type and dislocation density. Dislocations can be

mobile or sessile in nature. Mobile dislocations facilitate crystallographic slip, whereas sessile dislocations act as obstacles to slip by pinning mobile dislocations.

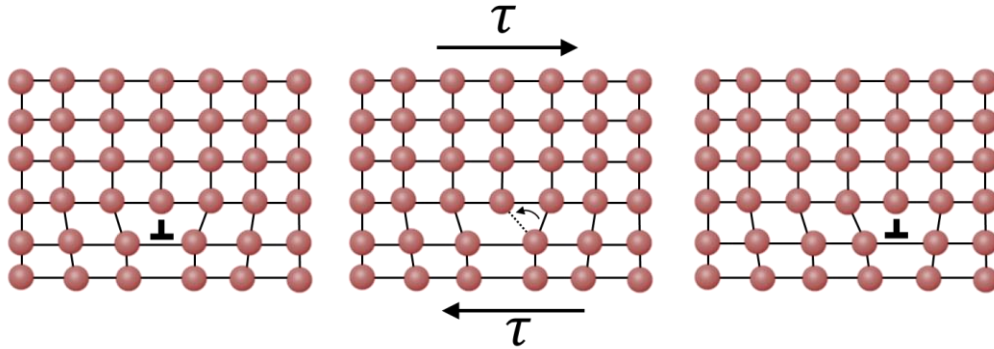


Figure 4.2. The motion of an edge dislocation through a crystal lattice under an applied shear stress.

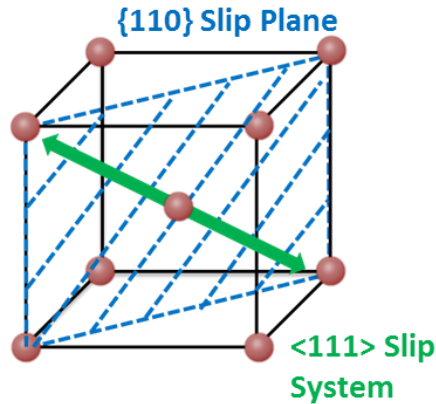


Figure 4.3. An example of a slip system in a BCC unit cell crystal.

The relationship between slip and resolved shear stress in crystal plasticity formulations is known as the slip rule, which describes the rate of crystallographic slip as a function of resolved shear stress and other microscale variables, depending on the particular model. The resolved shear stress, on a slip system α is calculated as follows:

$$\tau^\alpha = (\mathbf{n}^{*\alpha} \otimes \mathbf{s}^{*\alpha}) : \boldsymbol{\sigma} \quad (4.13)$$

where $\boldsymbol{\sigma}$ is the stress tensor, $\mathbf{n}^{*\alpha}$ is the normal vector to the slip plane, and $\mathbf{s}^{*\alpha}$ is the slip direction of the slip system α in the deformed configuration.

Additional terms are included to represent the hardening behaviour of the material, such as back stress and a drag stress. Physically-based slip rules include additional microscale quantities for a more explicit description of the material. For example, this can include modelling material hardening based on the evolution of sessile dislocation density.

Crystal plasticity models are formulated based on the knowledge of the deformation gradient \mathbf{F} described earlier. \mathbf{F} can be separated into elastic and plastic parts using multiplicative decomposition:

$$\mathbf{F} = \mathbf{F}^e \cdot \mathbf{F}^p \quad (4.14)$$

where \mathbf{F}^e represents rigid body rotation and elastic stretch and \mathbf{F}^p represents permanent plastic deformation. This decomposition can be derived from considering the body in Fig. 4.4. An intermediate configuration is introduced where the body undergoes plastic deformation only. In transformation from the reference to the deformed configuration, the line vector $d\mathbf{X}$ undergoes elastic and plastic deformation. In transformation to the intermediate configuration $d\mathbf{X}$ undergoes plastic deformation only to give $d\mathbf{p}$. The plastic deformation gradient \mathbf{F}^p describes this mapping:

$$d\mathbf{p} = \mathbf{F}^p d\mathbf{X} \quad (4.15)$$

so that

$$\mathbf{F}^p = \frac{d\mathbf{p}}{d\mathbf{X}} \quad (4.16)$$

$d\mathbf{p}$ is transformed to $d\mathbf{x}$ in the current configuration by the elastic deformation gradient \mathbf{F}^e :

$$d\mathbf{x} = \mathbf{F}^e d\mathbf{p} \quad (4.17)$$

so that

$$\mathbf{F}^e = \frac{d\mathbf{x}}{d\mathbf{p}} \quad (4.18)$$

We can then substitute Eq.4.15 into Eq.4.17 to give the following expression:

$$d\mathbf{x} = \mathbf{F}^e d\mathbf{p} = \mathbf{F}^e \mathbf{F}^p d\mathbf{X} \quad (4.19)$$

and therefore,

$$\mathbf{F} = \mathbf{F}^e \cdot \mathbf{F}^p \quad (4.20)$$

The plastic velocity gradient can be determined by

$$\mathbf{L}^p = \dot{\mathbf{F}}^p \cdot \mathbf{F}^{p-1} \quad (4.21)$$

and can be decomposed into rate of plastic deformation \mathbf{D}^p and lattice rotation \mathbf{W}^p :

$$\mathbf{L}^p = \mathbf{D}^p + \mathbf{W}^p. \quad (4.22)$$

\mathbf{D}^p and \mathbf{W}^p are derived from the below additive decompositions of the rate of deformation rates and spin, based on the assumption of small elastic strains:

$$\mathbf{D} = \mathbf{D}^e + \mathbf{D}^p \quad (4.23)$$

$$\mathbf{W} = \mathbf{W}^e + \mathbf{W}^p. \quad (4.24)$$

This is a commonly used assumption for implementation of plasticity models into finite element codes, allowing the rate of plastic deformation \mathbf{D}^p to be specified by a constitutive law. The total deformation is provided at the start of the time increment, and thus \mathbf{D}^e can be determined using eq. 4.17 and the stress rate can be calculated using Hookes Law [1].

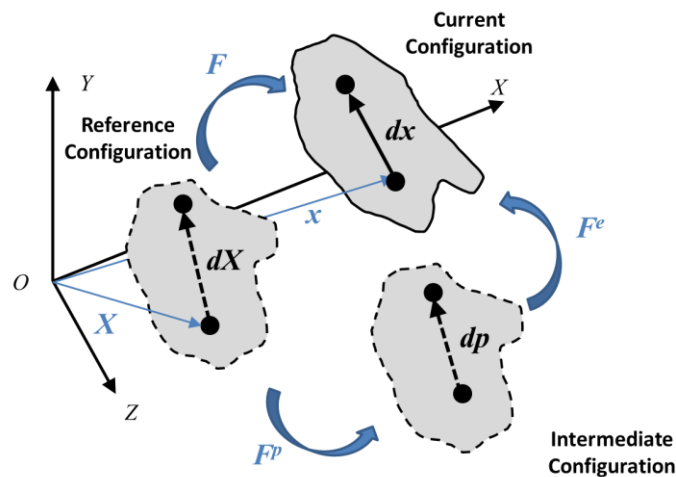


Figure 4.4. Schematic diagram showing a body in reference, intermediate and current configurations.

In this work, plastic deformation is caused only by crystallographic slip, so we can write

$$\mathbf{L}^p = \sum_{\alpha} \dot{\gamma}^{\alpha} \mathbf{s}^{\alpha} \mathbf{n}^{\alpha} \quad (4.25)$$

where $\dot{\gamma}^{\alpha}$ is the rate of slip on slip system α .

This is the mechanistic basis of the two CP constitutive models implemented in this work. CP formulations are implemented in ABAQUS finite element analysis software using a user defined material (UMAT) subroutine. The function of a UMAT is to update the stress, and provide the material Jacobian after every time increment in the analysis. The Jacobian is necessary in order to determine an implicit solution for the force balance equations in ABAQUS.

4.4 CP Material Models

4.4.1 Phenomenological Power Law Slip Rule

The phenomenological power law flow rule used here is based on that of Huang [2], which relates the rate of crystallographic slip $\dot{\gamma}^{\alpha}$ to shear stress on a slip system τ^{α} as follows.

$$\dot{\gamma}^{\alpha} = \dot{a} \text{sgn}(\tau^{\alpha} - x^{\alpha}) \left\{ \frac{|\tau^{\alpha} - x^{\alpha}|}{|g^{\alpha}|} \right\}^n \quad (4.26)$$

where \dot{a} is the reference strain rate component, n is a rate sensitivity exponent, g^{α} is the slip system strain hardness. The inclusion of x^{α} as the back-stress on the slip system implemented by Sweeney et al. [3] to simulate kinematic hardening following the Armstrong-Frederick rule. In order to capture the complex non-linear hardening behaviour of a material over large strain ranges, a linear combination of two back-stresses was proposed by Sweeney following the method of Chaboche [4] and others:

$$x^{\alpha} = x_1^{\alpha} + x_2^{\alpha} \quad (4.27)$$

$$\dot{x}_i^{\alpha} = C_i \dot{\gamma}^{\alpha} - D_i x_i^{\alpha} |\dot{\gamma}^{\alpha}| \quad (4.28)$$

where C_i is the initial hardening modulus, D_i is the rate of decay and $i = 1, 2$.

The evolution of slip system strain hardness is defined as:

$$\dot{g}^\alpha = \sum_{\beta} h^{\alpha\beta} \dot{\gamma}^\beta \quad (4.29)$$

where $h^{\alpha\beta}$ are the hardening moduli and α and β represent particular slip systems. When $\alpha = \alpha$, $h^{\alpha\beta}$ represents self-hardening modulus and when $\alpha \neq \beta$, $h^{\alpha\beta}$ represents latent hardening modulus. Self and latent moduli are considered to be equal in this work. This means that the hardening rate on all slip systems is equal at a given material point.

The isotropic strain hardening function is based on that of Asaro and co-workers [5] :

$$g(\gamma^\alpha) = g_0 + (g_\infty - g_0) \tanh \left| \frac{h_0 \gamma^\alpha}{g_\infty - g_0} \right| \quad (4.30)$$

where g_0 is the critical resolved shear stress for a slip system, g_∞ is the saturated stress value, and h_0 is the initial hardening modulus. The hardening moduli are calculated by differentiating Eq. 4.24 above to give:

$$h^{\alpha\alpha} = h^{\alpha\beta} = h(\gamma^\alpha) = h_0 \operatorname{sech}^2 \left| \frac{h_0 \gamma^\alpha}{g_\infty - g_0} \right| \quad (4.31)$$

The accumulated slip γ^α is determined by integrating the slip rate with respect to time t :

$$\gamma^\alpha = \sum_{\alpha} \int_0^t |\dot{\gamma}^\alpha| dt \quad (4.32)$$

The stress is updated incrementally using the Jaumann rate of Cauchy stress $\dot{\sigma}_j$ on the material axes:

$$\dot{\sigma}_j = \dot{\sigma}_j^* - (\mathbf{W} - \mathbf{W}^e) \boldsymbol{\sigma} + \boldsymbol{\sigma} (\mathbf{W} - \mathbf{W}^e). \quad (4.33)$$

$\dot{\sigma}_j^*$ is the Jaumann stress rate evaluated based on the rotated crystal lattice, which is defined by the elastic relationship:

$$\dot{\sigma}_j^* + \boldsymbol{\sigma} (\mathbf{I} : \mathbf{D}^e) = \mathbf{C} : \mathbf{D}^e \quad (4.34)$$

where \mathbf{C} is the tensor of elastic moduli and \mathbf{I} is the identity tensor. The following tensors

$$\boldsymbol{\mu}^\alpha = \frac{1}{2} [\mathbf{s}^{*\alpha} \otimes \mathbf{n}^{*\alpha} + \mathbf{n}^{*\alpha} \otimes \mathbf{s}^{*\alpha}] \quad (4.35)$$

$$\boldsymbol{\omega}^\alpha = \frac{1}{2}[\mathbf{s}^{*\alpha} \otimes \mathbf{n}^{*\alpha} - \mathbf{n}^{*\alpha} \otimes \mathbf{s}^{*\alpha}] \quad (4.36)$$

are used to define the plastic components of rate of stretch and continuum spin:

$$\mathbf{D}^p = \sum_{\alpha} \boldsymbol{\mu}^\alpha \dot{\gamma}^\alpha \quad (4.37)$$

$$\mathbf{W}^p = \sum_{\alpha} \boldsymbol{\omega}^\alpha \dot{\gamma}^\alpha. \quad (4.38)$$

With the knowledge of the additive decomposition described in Equations 4.17 and 4.18, Equation 4.28 can be adapted and substituted into Equation 4.27 to give stress rate given in Equation can be expressed as

$$\dot{\boldsymbol{\sigma}}_j = \mathbf{C}:\mathbf{D} - \mathbf{C}:\mathbf{D}^p - \boldsymbol{\sigma}(\mathbf{I}:\mathbf{D}) + \boldsymbol{\sigma}(\mathbf{I}:\mathbf{D}^p) - \mathbf{W}^p\boldsymbol{\sigma} + \boldsymbol{\sigma}\mathbf{W}^p \quad (4.39)$$

Equations 4.37 and 4.38 can be substituted into the expression above to give:

$$\dot{\boldsymbol{\sigma}}_j = \mathbf{C}:\mathbf{D} - \boldsymbol{\sigma}(\mathbf{I}:\mathbf{D}) - \sum_{\alpha} \dot{\gamma}^\alpha [\mathbf{C}:\boldsymbol{\mu}^\alpha + \boldsymbol{\omega}^\alpha\boldsymbol{\sigma} - \boldsymbol{\sigma}\boldsymbol{\omega}^\alpha] \quad (4.40)$$

The stress increment can therefore be calculated by integrating $\dot{\boldsymbol{\sigma}}_j$ with respect to time. The formulation discussed above is implemented in finite element simulations via a user material subroutine (UMAT) in ABAQUS for the computational study described in Chapter 5.

4.4.2 Physically-based Length-Scale Dependent Model

A modified version of the crystal plasticity formulation of Dunne et al. [6] is implemented in Chapters 6 and 7 of this work. One of the modifications of the present implementation is the inclusion of Armstrong-Frederick kinematic hardening. A second modification is the development of a more robust calculation of GND density to capture strain gradient effects in micromechanical models. These changes are described below.

This physically-based slip rule relates slip rate to shear stress based on the strain rate equation by Gibbs [7], where the glide of dislocations is controlled by pinning at obstacles (e.g. immobile dislocation and precipitates). The slip rate $\dot{\gamma}^\alpha$ is related to shear stress τ^α on a slip system α by

$$\dot{\gamma}^{\alpha} = \rho_{SSD}^m \nu b^{\alpha 2} \exp\left(\frac{\Delta H}{-kT}\right) \sinh\left(\frac{(\tau^{\alpha} - x^{\alpha} - \tau_c^{\alpha})\gamma_0 \Delta V^{\alpha}}{kT}\right) \quad (4.41)$$

where ρ_{SSD}^m is the density of statistically stored mobile dislocations, ν is the frequency of attempts (successful or otherwise) by dislocations to jump the energy barrier, b^{α} is Burgers vector, ΔH is Helmholtz free energy, k is the Boltzman constant, T is temperature, τ_c^{α} is the critical resolved shear stress on a particular slip system, x^{α} is a back-stress on the slip system, and γ_0 is a reference slip. The activation volume ΔV on a slip system α is defined by

$$\Delta V^{\alpha} = l b^{\alpha 2} \quad (4.42)$$

where l is the pinning distance between dislocations, which is related to the density of sessile SSDs, ρ_{SSD}^s as follows:

$$l = \frac{1}{\sqrt{\rho_{SSD}^s}} \quad (4.43)$$

Taylor hardening [8] is chosen to describe the evolution of critical resolved shear stress, which is dependent on sessile dislocation density:

$$\tau_c^{\alpha} = \tau_{c0}^{\alpha} + M G b^{\alpha} \sqrt{\rho_{GND} + \rho_{SSD}^s} \quad (4.44)$$

where τ_{c0}^{α} is the initial critical resolved shear stress for a slip system α , G is material shear modulus, M is the Taylor factor and ρ_{GND} is the geometrically necessary dislocation density. The backstress on each slip system is calculated using an Armstrong-Frederick type equation:

$$\dot{x}^{\alpha} = C \dot{\gamma}^{\alpha} - D x^{\alpha} |\dot{\gamma}^{\alpha}| \quad (4.45)$$

where C is the initial hardening modulus and D is the rate of decay.

The length-scale dependency of the model arises from the inclusion of GND density. As described in Chapter 2, GNDs in the crystal lattice accommodate plastic strain gradients. These gradients become steeper as length-scale decreases, leading to a higher GND density.

An expression for GND density is obtained by first relating closure failure of a circuit on a plane per unit area due to the presence of dislocations, as described by Nye [9], to the

plastic deformation gradient \mathbf{F}^p . If we consider the portion of undeformed crystal lattice shown in Fig 4.5a, and integrate the plastic deformation around a closed path Γ in the lattice, the result is zero since there is no deformation:

$$\oint_{\Gamma} \mathbf{F} dx = 0. \quad (4.46)$$

If the crystal experiences non-uniform plastic deformation, as in Fig 4.5b, a GND arises in the lattice, leading to closure failure of the path Γ , and an open Burger's circuit \mathbf{B} , leading to the expression:

$$\oint_{\Gamma} \mathbf{F}^p dx = \mathbf{B} \quad (4.47)$$

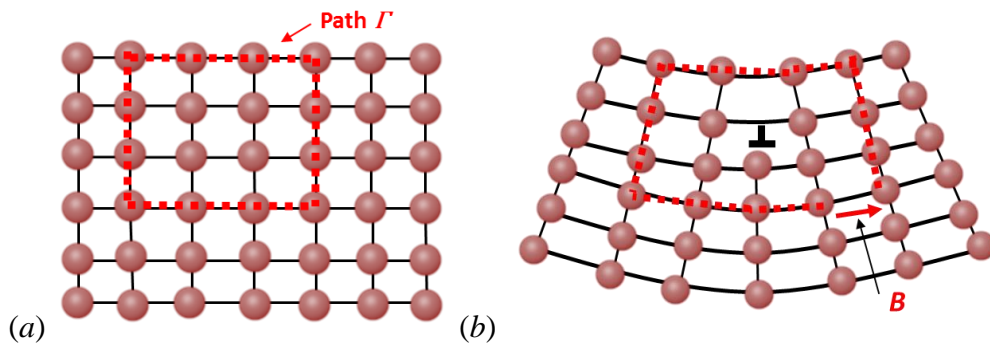


Figure 4.5. Schematic of (a) an undeformed crystal lattice with a closed path, and (b) closure failure due to the presence of a GND in a lattice under non-uniform plastic deformation.

Stokes' theorem is employed to express the latter line integral as a surface integral

$$\mathbf{B} = \oint_{\Gamma} \mathbf{F}^p dx = \iint_S \text{curl}(\mathbf{F}^p) \mathbf{r} dS \quad (4.48)$$

where S is an arbitrary surface bounded by Γ and \mathbf{r} is the unit normal vector. \mathbf{B} can also be expressed in terms of dislocation density [10] as follows

$$\mathbf{B} = \iint_S \left(\sum_{\alpha=1}^{nslip} (\mathbf{b}^{\alpha} \otimes \boldsymbol{\rho}_{GND}^{\alpha}) \right) \mathbf{r} dS \quad (4.49)$$

where $\boldsymbol{\rho}_{GND}$ is the net GND density and \mathbf{b}_{GND} is the net GND Burgers direction. Equation 4.49 can be expressed in terms of the sum $\boldsymbol{\rho}_{GND}$ on each slip system and equated to Eq. 4.48 to obtain

$$\sum_{\alpha=1}^{nslip} \mathbf{b}^{\alpha} \otimes \boldsymbol{\rho}_{GND}^{\alpha} = \text{curl}(\mathbf{F}^p) \quad (4.50)$$

Dislocations can be of edge or screw type, and therefore $\boldsymbol{\rho}_{GND}^{\alpha}$ can be decomposed into three components (two edge and one screw):

$$\sum_{\alpha=1}^{nslip} (\boldsymbol{\rho}_s^{\alpha} \mathbf{b}^{\alpha} \otimes \mathbf{s}^{\alpha} + \boldsymbol{\rho}_{et}^{\alpha} \mathbf{b}^{\alpha} \otimes \mathbf{n}^{\alpha} + \boldsymbol{\rho}_{en}^{\alpha} \mathbf{b}^{\alpha} \otimes \mathbf{t}^{\alpha}) = \text{curl}(\mathbf{F}^p) \quad (4.51)$$

where \mathbf{s}^{α} is the slip direction, \mathbf{n}^{α} is slip normal, and $\mathbf{t}^{\alpha} = \mathbf{s}^{\alpha} \times \mathbf{n}^{\alpha}$. A matrix of dyadic products \mathbf{A} can be constructed to give

$$\mathbf{A} \boldsymbol{\rho}_{GND} = \text{curl}(\mathbf{F}^p). \quad (4.52)$$

A maximum of 12 potentially active slip systems are considered to contribute to $\boldsymbol{\rho}_{GND}$ for the materials studied in this work, which will be discussed in Chapters 6 and 7. As a result, a unique solution for $\boldsymbol{\rho}_{GND}$ may not exist, as there may be fewer gradient terms than active slip systems, and therefore fewer equations than unknowns. The least squares minimization procedure, as described by Arsenlis and Parks [11], is implemented here to calculate $\boldsymbol{\rho}$. A singular value decomposition technique is employed to determine the pseudo-inverse of \mathbf{A} using the LAPACK Fortran library. The GND density used in Eq. (4.44) is the sum of the squares of dislocation density on all 12 potentially active slip systems.

The calculation of $\text{curl}(\mathbf{F}^p)$ can be described by first considering the curl of a vector as follows:

$$\text{curl}(\mathbf{X}) = \nabla \times \begin{pmatrix} X_1 \\ X_2 \\ X_3 \end{pmatrix} = \begin{vmatrix} i & j & k \\ \partial & \partial & \partial \\ \partial x & \partial y & \partial z \\ X_1 & X_2 & X_3 \end{vmatrix} \quad (4.53)$$

The curl of \mathbf{F}^p , which is a 3 x 3 tensor, and can be written more explicitly as

$$\text{curl}(\mathbf{F}^p) = \text{curl} \begin{pmatrix} F_{xx}^p & F_{xy}^p & F_{xz}^p \\ F_{yx}^p & F_{yy}^p & F_{yz}^p \\ F_{zx}^p & F_{zy}^p & F_{zz}^p \end{pmatrix} \quad (4.54)$$

is calculated by determining the curl of each individual column in the tensor:

$$\text{curl}(\mathbf{F}^p) = \begin{pmatrix} \text{curl}(\mathbf{F}_x^p) \\ \text{curl}(\mathbf{F}_y^p) \\ \text{curl}(\mathbf{F}_z^p) \end{pmatrix}. \quad (4.55)$$

Knowledge of the plastic deformation gradient at each integration point within an element is required to determine the gradients of \mathbf{F}^p within a finite element. For this reason, the above constitutive model was initially implemented as a User Element (UEL) Subroutine in ABAQUS for a 20-noded reduced integration element. For UEL implementation the user is required to define the entire element in a UEL, as compared to the relatively simpler task of updating the stress and tangent stiffness at each material point as for a UMAT. This includes the specification of internal and external force vectors for element integration. As the user is defining the entire element in a UEL, the knowledge of the solution dependent variables at each integration point in the element is known, allowing gradients of \mathbf{F}^p to be calculated. Recently, however, the compatibility of common blocks in Fortran subroutines has allowed the \mathbf{F}^p variable to be stored for each integration point during the analysis, allowing $\text{curl}(\mathbf{F}^p)$ to be calculated. The original UEL version of the CP model has been converted to a UMAT subroutine by Ed Tarleton at Oxford University and is implemented in [12] with common blocks to store the required non-local information. The spatial coordinates and \mathbf{F}^p values for each integration point are stored in a common block for each time increment to allow the spatial gradients of \mathbf{F}^p , and thus GND density, to be calculated. This UMAT implementation reduces the computational time as the additional computations required in the UEL subroutine are no longer necessary.

Element shape functions are used to determine the spatial gradient of components of \mathbf{F}^p , and hence calculate $\text{curl}(\mathbf{F}^p)$. Consider the 2D situation in Fig. 4.6 with an 8 noded full integration element. The value of \mathbf{F}^p at each gauss point is known and therefore an internal linear element is defined, with nodal coordinates corresponding to the Gauss

points of the external element. The spatial derivatives of \mathbf{F}^p are then calculated with the linear shape functions \mathbf{n} of the internal element [6] as follows:

$$\frac{\partial \mathbf{F}^p}{\partial \mathbf{x}} = \frac{\partial}{\partial \mathbf{x}} (\mathbf{n} \mathbf{F}_i^p) = \frac{\partial \mathbf{n}}{\partial \mathbf{x}} (\mathbf{F}_i^p) = \frac{\partial \mathbf{n}}{\partial \boldsymbol{\beta}} \mathbf{J}^{-1} \mathbf{F}_i^p \quad (4.56)$$

where \mathbf{F}_i^p are the Gauss point deformation gradients, \mathbf{J} is the Jacobian transformation mapping from the external to internal elements and $\frac{\partial}{\partial \mathbf{x}}$ and $\frac{\partial}{\partial \boldsymbol{\alpha}}$ represent partial derivatives with respect to the global coordinate system and the parent shape coordinate system of the inner element, respectively. Further details on this methodology for calculating spatial gradients of \mathbf{F}^p is described in detail by Kiwanuka [10].

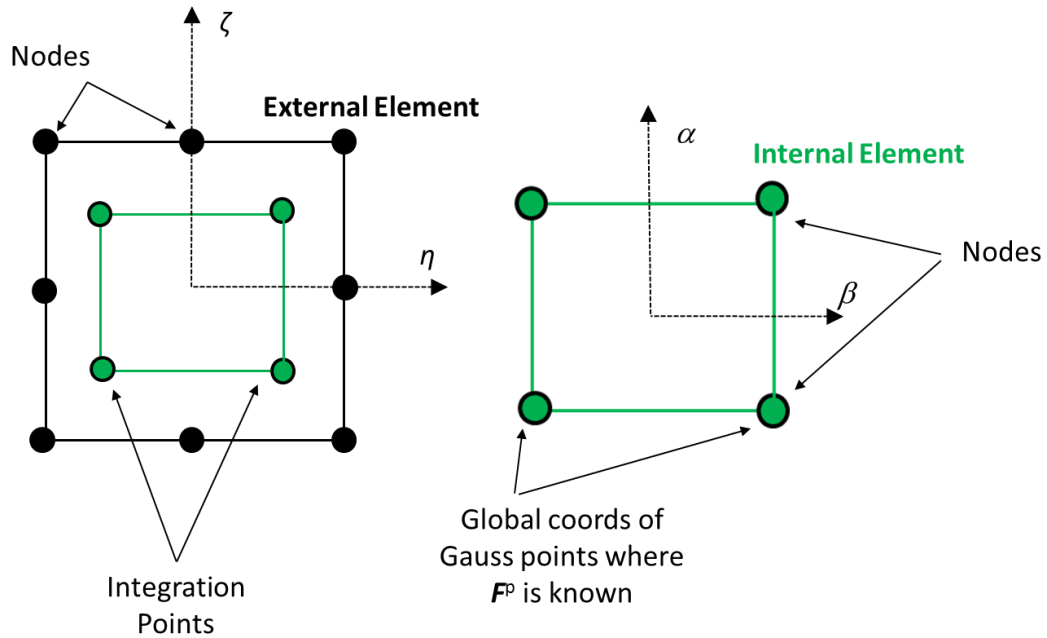


Figure 4.6. 2D representation of internal linear element defined to determine the spatial gradients of \mathbf{F}^p .

Newton iteration is employed to incrementally determine the stress at the end of each time step in the analysis. A trial stress $\boldsymbol{\sigma}^{\text{tr}}$ and a plastic corrector term are used to determine the stress as follows:

$$\boldsymbol{\sigma} = \mathbf{C}_g \boldsymbol{\varepsilon}^e = \mathbf{C}_g (\boldsymbol{\varepsilon}_t^e + \Delta \boldsymbol{\varepsilon}^e) = \mathbf{C}_g (\boldsymbol{\varepsilon}_t^e + \Delta \boldsymbol{\varepsilon}) - \mathbf{C}_g \Delta \boldsymbol{\varepsilon}^p = \boldsymbol{\sigma}^{\text{tr}} - \mathbf{C}_g \Delta \boldsymbol{\varepsilon}^p \quad (4.57)$$

where \mathbf{C}_g is the global elastic stiffness matrix and $\Delta\boldsymbol{\varepsilon}^e$ and $\Delta\boldsymbol{\varepsilon}^p$ are elastic and plastic strain increment tensors, respectively. A residual stress vector can be specified for the Newton iteration scheme

$$\boldsymbol{\psi} = \boldsymbol{\sigma} - \boldsymbol{\sigma}^{\text{tr}} - \mathbf{C}_g \Delta\boldsymbol{\varepsilon}^p \quad (4.58)$$

and the differential operator can be applied to the above to yield

$$\delta\boldsymbol{\psi} = \delta\boldsymbol{\sigma} - \delta\boldsymbol{\sigma}^{\text{tr}} - \mathbf{C}_g \delta\Delta\boldsymbol{\varepsilon}^p = 0. \quad (4.59)$$

This leads to the Taylor expansion expression for $\boldsymbol{\psi}$

$$\boldsymbol{\psi} + \frac{\partial\boldsymbol{\psi}}{\partial\boldsymbol{\sigma}} \delta\boldsymbol{\sigma} = 0. \quad (4.60)$$

where $\partial\boldsymbol{\psi}$ can be calculated and is updated iteratively until the magnitude of the residual $\boldsymbol{\psi}$ is below the specified tolerance ($<10^{-8}$ MPa):

$$\boldsymbol{\sigma}^{n+1} = \boldsymbol{\sigma}^n + \delta\boldsymbol{\sigma} \quad (4.61)$$

$$|\boldsymbol{\psi}| = |\boldsymbol{\sigma}^{n+1} - \boldsymbol{\sigma}^{\text{tr}} - \mathbf{C}_g \Delta\boldsymbol{\varepsilon}^p| < 10^{-8} \text{ MPa} \quad (4.62)$$

4.4.3 J₂ Plasticity

In addition to CP modelling, a continuum J₂ plasticity model [1] is implemented for reference in Chapter 5. This material model also includes both kinematic and isotropic hardening. The yield function is expressed as:

$$f = \left(\frac{3}{2} (\boldsymbol{\sigma}' - \boldsymbol{x}') : (\boldsymbol{\sigma}' - \boldsymbol{x}') \right)^{\frac{1}{2}} - k - r(p) \quad (4.63)$$

where $\boldsymbol{\sigma}'$ is the deviatoric stress tensor, \boldsymbol{x}' is the deviatoric back-stress tensor, k is the yield strength, and $r(p)$ is the isotropic hardening function. The Armstrong-Frederick rule is again adopted to describe non-linear kinematic hardening. A linear combination of three back stresses is used here to capture the non-linear hardening behaviour of the material:

$$\boldsymbol{x} = \boldsymbol{x}_1 + \boldsymbol{x}_2 + \boldsymbol{x}_3 \quad (4.64)$$

$$d\mathbf{x}_i = \frac{2}{3} c_i d\boldsymbol{\varepsilon}_p - \gamma_i \mathbf{x}_i dp \quad (4.65)$$

where c_i and γ_i represent initial hardening modulus and rate of decay, respectively, and $i = 1, 3$. $d\boldsymbol{\varepsilon}_p$ is the plastic strain increment tensor and dp is the effective plastic strain increment. The isotropic hardening function is defined as:

$$dr(p) = b(r_\infty - r)dp \quad (4.66)$$

where b is the rate of stabilization and r_∞ is the asymptotic value of stress.

4.5 Microstructure Geometry Modelling

4.5.1 General

A methodology has been developed for modelling material microstructure using a combination of Python and ABAQUS software. The following sections describe the processes for generating representative 2D and 3D finite element models for simulating micromechanical fatigue.

4.5.2 2D Modelling

A Python script was written to automatically generate a representative periodic repeating unit cell finite element model of material microstructure with the same average grain size and grain area distributions as the experimentally gathered microscopy data for a material. This methodology is divided into three steps: (1) specify microstructure geometry, (2) create a corresponding ABAQUS mesh with grain partitions and (3) apply periodic boundary conditions to simulate a repeating unit cell of material. In Step 1 a unit cell of desired length is divided into a number of polygons, which represent microstructural grains, using a Voronoi tessellation algorithm. The Python function implemented here uses a Delaunay Triangulation method, whereby a number of nuclei are specified in the unit cell, corresponding to the number of desired grains. The cell is divided into triangles using the specified nuclei as vertices and a circle is circumscribed around each triangle, as shown in Fig. 4.7. Finally the centres of each circumcircle are joined to define the edges of each polygon, and thus, grain boundaries. To achieve a periodic unit cell, a 3x3 cell matrix is created before the Voronoi tessellation is

performed, as shown in Fig. 4.8. The vertices of each grain boundary are written to a file to be read by an ABAQUS Python script.

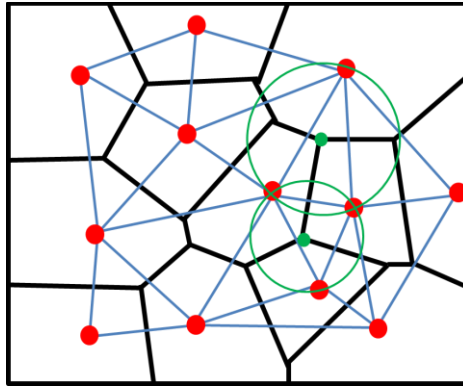


Figure 4.7. The Delaunay triangulation method, where the red points represent the nuclei, the blue lines represent the triangulation, the green lines represent the circumcircles, and the black lines represent the edges of each grain.

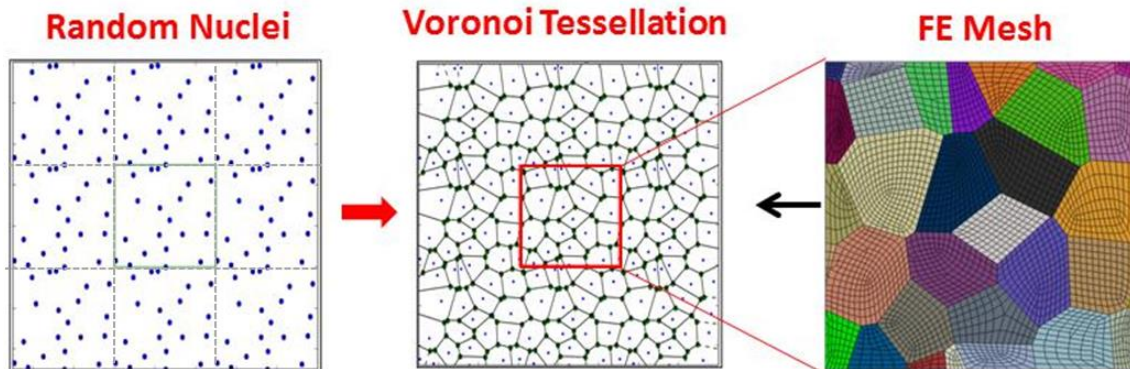


Figure 4.8. Automated Unit Cell Modelling Methodology

The coordinates of the vertices are used to partition an ABAQUS part in order to create an element set for each grain in the microstructure, as shown in Fig 4.8. Mesh constraints are applied to each free edge of the model to facilitate the application of periodic boundary conditions (PBCs). Opposing edges must contain an equal number of nodes for application of PBCs. Following the node and edge labelling convention shown in Fig. 4.9a, linear constraint equations are applied to the model according to the following equations:

$$\begin{aligned}
U_{SW}(x, y, z) &= 0 \\
U_{SE}(y) &= 0 \\
U_{NW}(x) &= 0 \\
\mathbf{U}_{East}(x) - \mathbf{U}_{West}(x) &= U_{SE}(x) \\
\mathbf{U}_{North}(y) - \mathbf{U}_{South}(y) &= U_{NW}(y) \\
\mathbf{U}_{East}(y) &= \mathbf{U}_{West}(y) \\
\mathbf{U}_{North}(x) &= \mathbf{U}_{South}(x)
\end{aligned} \tag{4.67}$$

Where scalars U_{SE} , U_{NW} , U_{SW} , U_{NE} correspond to the nodal displacements of the corner nodes and vectors \mathbf{U}_{North} , \mathbf{U}_{East} , \mathbf{U}_{West} , \mathbf{U}_{South} correspond to the nodal displacements of the nodes along the free edges of the cell. A cyclic displacement is applied to node NE to simulate the cyclic mechanical behaviour of the material. All of the above steps have been automated in an ABAQUS-Python script, given in Appendix A. An example of the deformation of a unit cell is given in Fig 4.9b, where the effect of applying periodic boundary conditions can be seen.

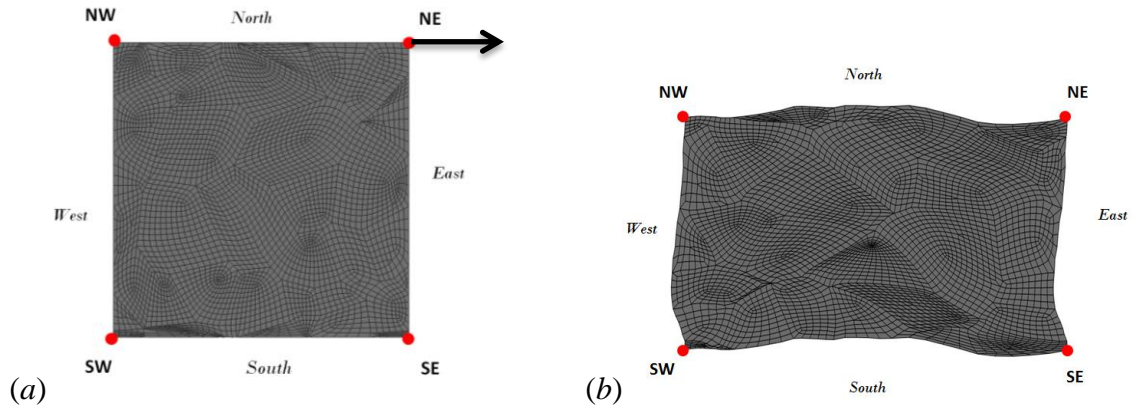


Figure 4.9. Unit cell model (a) before and (b) after deformation with the applied periodic boundary conditions.

Each grain in the model must be assigned material properties (e.g critical resolved shear stress, hardening parameters) and a crystallographic orientation for UMAT implementation. This requires a user-defined material to be specified in the ABAQUS input file for each grain. Python is again implemented to automate this process by

modifying the input file according to the desired material properties and number of grains in the model.

4.5.3 3D Microstructure Geometry Modelling

Similar to the development of the 2D microstructure geometries, a Voronoi tessellation methodology is developed to generate a periodic 3D microstructure geometry. The tessellation is then superimposed onto a finite element voxel mesh to generate an FE microstructure geometry, where each element is assigned to a particular grain. A unit cell model is shown in Fig. 4.10a.

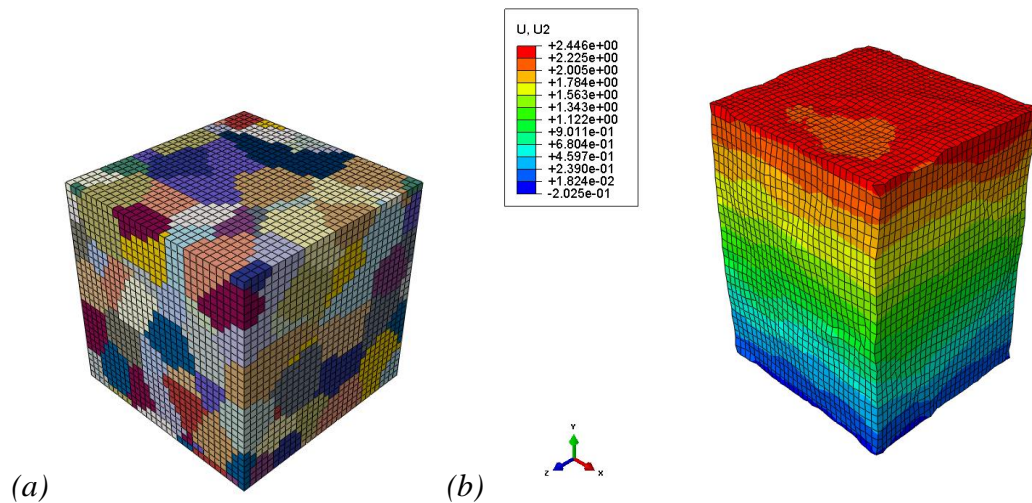


Figure 4.10. (a) 3D unit cell microstructure model and (b) an example of microscopic deformation of the periodic unit cell model under uniaxial strain.

Periodic boundary conditions are assigned to each free face. The linear constraint equations given in Eq. 4.67 are expanded into three dimensions. Figure 4.10b shows an example of a 3D unit cell with PBCs under an applied strain. A flowchart for generating microstructure unit cell models is given in Fig 4.11 to summarise these steps.

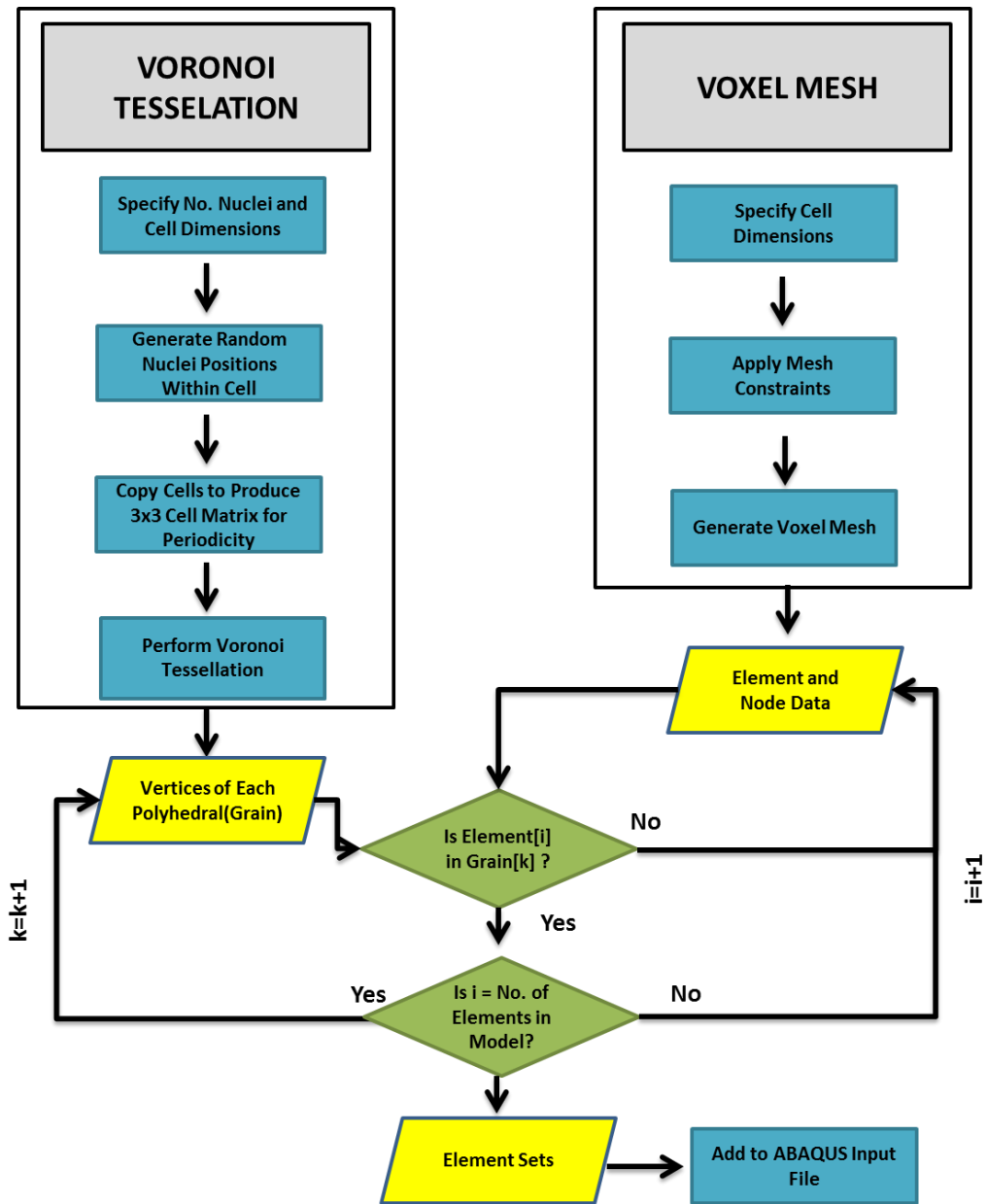


Figure 4.11. Flowchart describing the Python scripting methodology for generating finite element models of microstructure.

A voxel mesh was chosen to generate microstructure models in this thesis due to the advantages of using a structure mesh in fretting contact problems. However, it is known that grain boundaries in voxel meshes are stepped surfaces, which leads to concentrations of stresses and strains. For example, Choi et al.[13] compared a multi-grain CPFEE model with stepped grain boundaries and hexahedral elements to a nominally equivalent model with smooth grain boundaries and hexahedral elements. The

global stress-strain response of the model was shown to be identical. Localised stresses and strains near grain boundaries were predicted to fluctuate significantly for stepped boundaries in voxel meshes. Choi et al. therefore suggest that the use of voxel meshes can result in an over- and under-prediction of localised variables near grain boundaries. However, in order to fully represent the microstructures of the materials in this work with smooth grain boundaries, it is anticipated that a combination of hexahedral and tetrahedral elements would be required. Consequently, this would require significant modifications to the constitutive model code for calculating gradients on plastic strain. Hence, this is considered to be beyond the scope of the current work.

4.6 FCI Prediction

In this work, scale-consistent FIPs are adopted for FCI prediction based on the crystal plasticity modelling results. These parameters are based on micro-scale mechanical variables, such as crystallographic slip, to predict crack location and number of cycles to initiation.

Three such scale-consistent FIPs are employed in this thesis: the first, based on the work of Dunne and Manonukul [14] is the accumulated crystallographic slip parameter, designated here as p ; the second is an energy dissipation parameter W with slip and shear stress contributions, and the third is a Fatemi-Socie (FS) [15] type parameter which is comprised of crystallographic slip and normal stress on corresponding crystallographic planes. The accumulated crystallographic slip parameter p is calculated using the rate of plastic deformation tensor \mathbf{D}^p :

$$\dot{p} = \left(\frac{2}{3} \mathbf{D}^p : \mathbf{D}^p\right)^{\frac{1}{2}} \quad (4.68)$$

$$p = \int_0^t \dot{p} dt. \quad (4.69)$$

This parameter has been shown to identify persistent crystallographic slip bands [14], which are known crack initiation sites in fatigue of ferrite-pearlite steels [16] amongst other materials, as described in Chapter 2 .

The second scale-consistent FIP adopted in this thesis is accumulated crystallographic energy dissipation W . W sums the crystallographic work done on each crystal slip system:

$$W = \sum_{\alpha} \int_0^t \tau^{\alpha} \dot{\gamma}^{\alpha} dt \quad (4.70)$$

Korsunsky et al. [17] observed good correlation between experimentally-measured fatigue lives and CP-predicted lives using this microscale FIP. Li et al. [18] showed the capability of this parameter to predict crack initiation sites in austenitic steel. Sweeney et al. also successfully employed this parameter for predicting FCI in both the high [19] and low [20] cycle fatigue behaviour of a CoCr alloy across multiple grain sizes.

The third FIP, based on the macro-scale Fatemi-Socie parameter [15], considers the contribution of normal stress and slip on each crystal plane, as shown schematically in Fig. 4.12. It has recently been implemented successfully by Sharaf et al. [21] for predicting fatigue life of ferritic–pearlitic steel in fatigue. This parameter first considers the accumulation of slip and normal stress on each non-parallel slip plane i .

$$P_{fs_i} = \int_0^t \left(1 + k' \frac{\sigma_n}{\sigma_y}\right) \sum_{x=1}^N |\dot{\gamma}_i^x| dt \quad (4.71)$$

where x is the number of slip systems on a slip plane i . Here, only the six (110) slip planes are considered, and hence $x = 2$ and $i = 6$ (two slip systems on each plane). σ_n is the stress normal to the plane, σ_y is the macroscopic yield strength of the material, and k' is a constant which determines the contribution of normal stress to crack initiation (chosen here to be 0.5 [21]).

An advantage of this parameter is the potential to predict initial crack growth paths by identifying critical crystallographic planes on which cracks are predicted to initiate and initially propagate. This will be investigated in the context of fretting in Chapter 6.

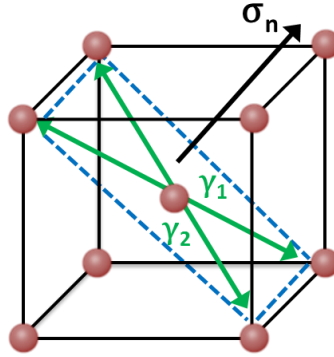


Figure 4.12. Schematic of BCC crystal indicating the slip and normal stress values used for the calculation of Fatemi-Socie parameter on a crystallographic plane.

4.7 Crystallographic Orientation

4.7.1 General

Every grain in the crystal plasticity material model is assigned a crystallographic orientation. This is a key aspect of crystal plasticity modelling, as it is the varying orientation of the grains which results in the heterogeneous deformation of the model. A study of the effects of crystallographic orientation on mechanical behaviour, fatigue, and fretting crack imitation is presented in Chapter 7 of this thesis. The processes involved in specifying and graphically presenting crystallographic orientation are described here.

4.7.2 Euler Angles and the Rotation Matrix

The orientation of a rotated crystal can be defined using Bunge Euler notation. The three angles ϕ_1 , Φ and ϕ_2 define the orientation of the crystal with respect to the reference orientation, where each angle corresponds to a rotation about a crystal axis. The process of rotating a crystal using the Euler angles is described by considering the crystal shown in Fig 4.13. The crystal is first rotated ϕ_1 about the Z axis, as shown in Fig. 4.13b. It is then rotated by the angle Φ about the new X axis, X' (Fig. 4.13c). Finally the crystal is rotated ϕ_2 about the new Z axis, Z''(Fig. 4.12d).

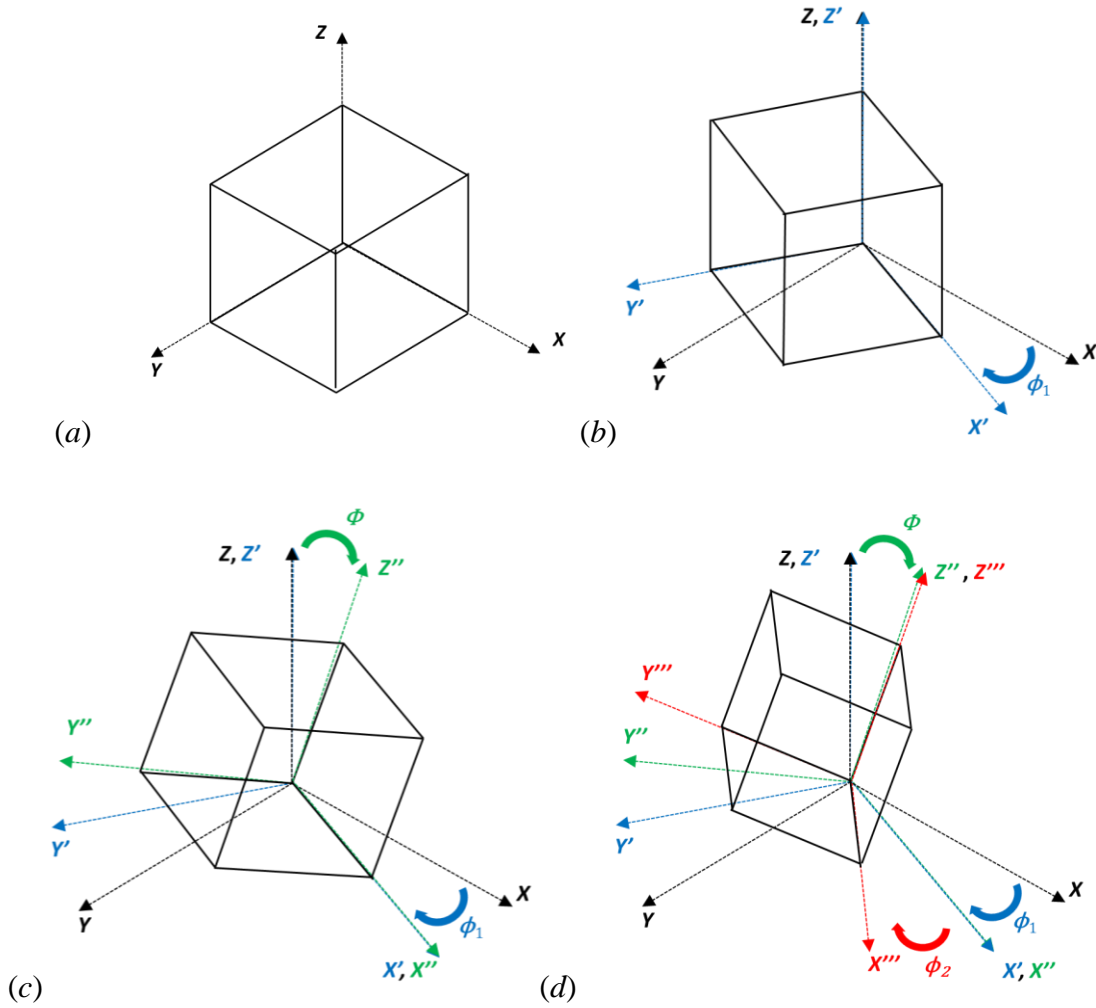


Figure 4.13. The process of defining a crystal rotation with Bunge Euler notation.

The Euler angles are used to compose a rotation matrix \mathbf{R} , which is used for determining the slip directions and normal in the UMAT subroutine. For example, the reference $\langle 100 \rangle$ direction \mathbf{s} can be multiplied by \mathbf{R} to determine the rotated direction \mathbf{s}^* .

$$\mathbf{s}^* = \mathbf{s}\mathbf{R} \quad (4.72)$$

where the rotation matrix is explicitly defined as:

$$= \begin{pmatrix} c\phi_2 c\phi_1 - c\Phi s\phi_1 s\phi_2 & c\phi_2 c\phi_1 - c\Phi s\phi_1 s\phi_2 & s\phi_2 s\Phi \\ -s\phi_2 c\phi_1 - c\Phi s\phi_1 c\phi_2 & -s\phi_2 s\phi_1 + c\Phi c\phi_1 c\phi_2 & c\phi_2 s\Phi \\ s\Phi s\phi_1 & -s\Phi c\phi_1 & c\Phi \end{pmatrix} \quad (4.73)$$

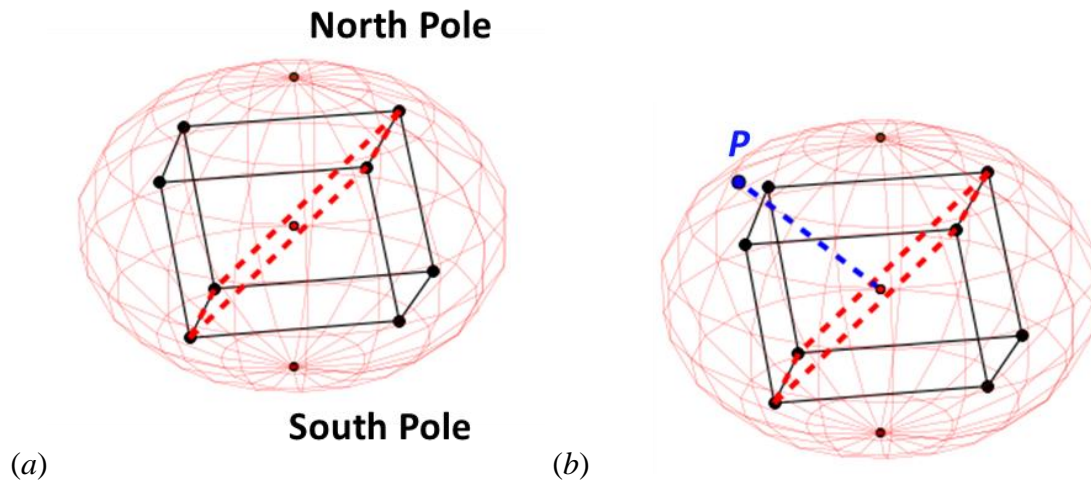
where s and c represent the *sin* and *cosine* functions, respectively.

4.7.3 Pole Figures

Pole figures are commonly used as a graphical representation of the crystallographic texture in a microstructure. The pole figure shows the normal direction of a chosen slip plane for each crystal relative to a reference axis. This three-dimensional vector is represented as a point on a plane by means of stereographic projection. For example, to plot a projection of the (110) crystal plane of a crystal on a pole figure, the following steps are taken:

- The unit cell of a rotated crystal is placed inside a unit sphere.
- The normal direction to the (110) plane in the rotated configuration is projected until it intersects the boundary of the sphere at a point P .
- A line is drawn from the south pole of the sphere to the point P and continued until it intersects with the flat plane which lies on the north pole of the sphere (stereographic projection plane).
- The point then lies on a single plane, and only two coordinates are needed to describe the orientation of the crystal.

A Python script has been developed to draw a pole figure based on the above process, as shown in Fig. 4.14, based on user-specified Euler angles. Fig. 4.14d shows the 2D pole figure plot, where RD, ND, and TD represent the reference rolling, normal and tangential directions, respectively.



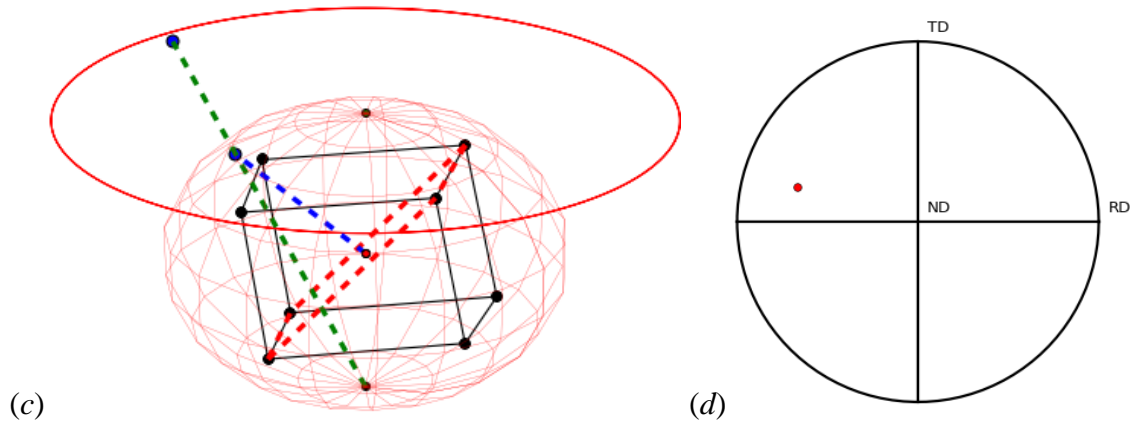


Figure 4.13. The process of defining a crystal rotation with Bunge Euler notation.

Figure 4.15 shows sample (110) pole figures for (a) an untextured microstructure, where grains are randomly orientated, and (b) a textured microstructure, where the (110) planes of each grain are aligned with the reference rolling direction, and thus the plane normals are aligned with the reference normal direction.

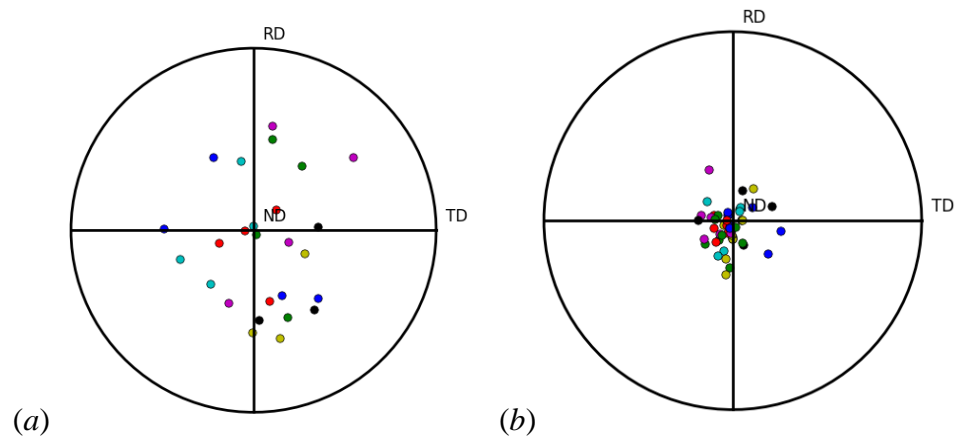


Figure 4.15. The process of defining a crystal rotation with Bunge Euler notation for (a) an untextured microstructure and (b) a (110) fibre texture in BCC materials.

4.8 Conclusion

The micromechanical modelling methodology implemented in this thesis has been outlined in this chapter. Phenomenological and physically-based crystal plasticity material models have been described. The methodology developed to generate representative microstructure finite element geometries is also detailed. These methods are employed in the subsequent chapters in this thesis to study the microstructure sensitivity in fatigue crack initiation, with focus on fretting fatigue. The input data for this micromechanical modelling analysis is obtained from a calibration process using the experimental results presented in Chapter 3 and available literature data, as will be discussed in the following chapters.

4.9 References

- [1] F. P. E. Dunne and N. Petrinic, *Introduction to Computational Plasticity*. Oxford: Oxford University Press, 2005.
- [2] Y. Huang, “A User-Material Subroutine Incorporating Single Crystal Plasticity In the ABAQUS Finite Element Program, Mech Report 178,” Division of Applied Sciences, Harvard University,. 1991.
- [3] C. A. Sweeney, P. E. McHugh, J. P. McGarry, and S. B. Leen, “Micromechanical methodology for fatigue in cardiovascular stents,” *Int. J. Fatigue*, vol. 44, pp. 202–216, 2012.
- [4] J. L. Chaboche, “Time-independent constitutive theories for cyclic plasticity,” *Int. J. Plast.*, vol. 2, no. 2, pp. 149–188, 1986.
- [5] R. J. Asaro and A. Needleman, “Overview no. 42 Texture development and strain hardening in rate dependent polycrystals,” *Acta Metall.*, vol. 33, no. 6, pp. 923–953, Jun. 1985.

-
- [6] F. P. E. Dunne, D. Rugg, and A. Walker, “Lengthscale-dependent, elastically anisotropic, physically-based hcp crystal plasticity: Application to cold-dwell fatigue in Ti alloys,” *Int. J. Plast.*, vol. 23, no. 6, pp. 1061–1083, 2007.
- [7] G. B. Gibbs, “Thermodynamic analysis of dislocation glide controlled by dispersed local obstacles,” *Mater. Sci. Eng.*, vol. 4, no. 6, pp. 313–328, Sep. 1969.
- [8] G. I. Taylor, “The Mechanism of Plastic Deformation of Crystals. Part I. Theoretical,” *Proc. R. Soc. A Math. Phys. Eng. Sci.*, vol. 145, pp. 3625–387, 1934.
- [9] J. F. Nye, “Some geometrical relations in dislocated crystals,” *Acta Mater.*, no. 1, pp. 153–162, 1953.
- [10] R. Kiwanuka, “Micro-deformation and Texture in Engineering Materials,” PhD Thesis, 2013.
- [11] A. Arsenlis and D. M. Parks, “Crystallographic aspects of geometrically-necessary and statistically-stored dislocation density,” *Acta Mater.*, vol. 47, no. 5, pp. 1597–1611, 1999.
- [12] S. Das, F. Hofmann, and E. Tarleton, “Consistent determination of geometrically necessary dislocation density from simulations and experiments,” *Int. J. Plast.*, 2018.
- [13] Y. S. Choi, M. A. Groeber, T. J. Turner, D. M. Dimiduk, C. Woodward, M. D. Uchic, and T. A. Parthasarathy, “A crystal-plasticity FEM study on effects of simplified grain representation and mesh types on mesoscopic plasticity heterogeneities,” *Mater. Sci. Eng. A*, vol. 553, pp. 37–44, 2012.
- [14] F. P. E. Dunne, A. Manonukul, “High- and low- cycle fatigue crack initiation using polycrystal plasticity,” *Proc. R. Soc. A Math. Phys. Eng. Sci.*, vol. 460, pp. 1881–1903, 2004.
- [15] A. Fatemi and D. F. Socie, “A critical plane approach to multiaxial fatigue damage including out-of-phase loading,” *Fatigue Fract. Eng. Mater. Struct.*, vol. 11, no. 3, pp. 149–165, 1988.

-
- [16] V. S. Sarma and K. A. Padmanabhan, "Low cycle fatigue behaviour of a medium carbon microalloyed steel," *Int. J. Fatigue*, vol. 19, no. 2, pp. 135–140, 1997.
- [17] A. M. Korsunsky, D. Dini, F. P. E. Dunne, and M. J. Walsh, "Comparative assessment of dissipated energy and other fatigue criteria," *Int. J. Fatigue*, vol. 29, no. 9–11, pp. 1990–1995, 2007.
- [18] Y. Li, V. Aubin, C. Rey, and P. Bompard, "Microstructural modeling of fatigue crack initiation in austenitic steel 304L," *Procedia Eng.*, vol. 31, pp. 541–549, 2012.
- [19] C. A. Sweeney, B. O'Brien, F. P. E. Dunne, P. E. McHugh, and S. B. Leen, "Micro-scale testing and micromechanical modelling for high cycle fatigue of CoCr stent material," *J. Mech. Behav. Biomed. Mater.*, vol. 46, pp. 244–260, 2015.
- [20] C. A. Sweeney, B. O'Brien, F. P. E. Dunne, P. E. McHugh, and S. B. Leen, "Strain-gradient modelling of grain size effects on fatigue of CoCr alloy," *Acta Mater.*, vol. 78, pp. 341–353, 2014.
- [21] M. Sharaf, P. Kucharczyk, N. Vajragupta, S. Munstermann, A. Hartmaier, and W. Bleck, "Modeling the microstructure influence on fatigue life variability in structural steels," *Comput. Mater. Sci.*, vol. 94, no. C, pp. 258–272, 2014.

5 Statistical Microstructure Effects in Fretting Crack Initiation

5.1 Introduction

In this chapter, a microstructure-sensitive CPFE study is presented for a cobalt chromium alloy in fretting. Cobalt chromium is commonly used to manufacture many components which are prone to fretting, including artificial hip joints [3] and cardiovascular stents [16]. As discussed in Chapter 2, the small number of grains present in typical fretting contacts suggests that microstructure can have a significant effect fretting fatigue and fretting crack initiation. As a result, two potentially important parameters for fretting crack initiation are investigated in this chapter: contact semi-width to grain size a/d and relative slip to grain size Δ/d . A 3-D finite element fretting model is developed to incorporate realistic microstructure morphologies and a crystal plasticity material model at contact zones. A preliminary 2D fretting study has been conducted to show the microstructure-dependence of fretting crack initiation, as presented in Appendix B.

5.2 Methodology

5.2.1 Constitutive Models

The phenomenological power law UMAT described in Chapter 2 is implemented here to simulate the CoCr alloy. CoCr has a face centred cubic (FCC) lattice structure with 12 possible slip systems. The (111) slip plane is shown in Fig. 5.1, which contains 3

potential slip directions. 3 additional equivalent planes exist, each with 3 potential slip directions, which make up the 12 possible slip systems.

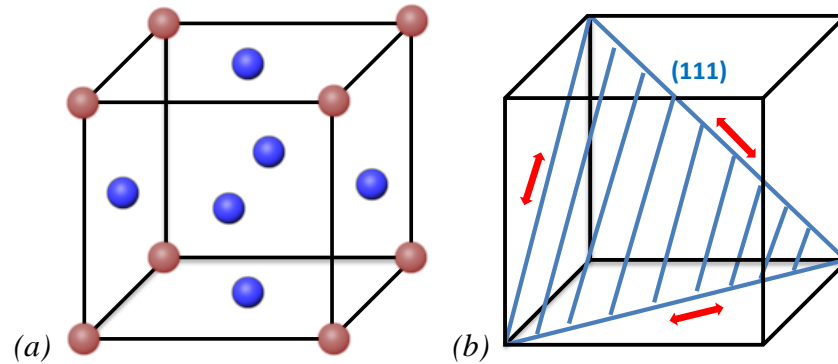


Figure 5.1. (a) An FCC unit cell with atoms at each corner and the centre of each face. (b) The (111) slip plane with red arrows indicating slip direction.

In addition to CP modelling, a continuum J_2 plasticity model is implemented for comparative purposes. Properties for the CP and J_2 material models were calibrated previously by Sweeney et al. [1], and are listed in Tables 5.1 & 5.2 respectively.

Table 5.1. Material parameters used in crystal plasticity material model [1]. Values of $\dot{\alpha}$ and n are chosen to reflect the rate insensitivity of CoCr at room temperature.

Parameter	Value
$\dot{\alpha}$	0.002 s^{-1}
n	50
g_0	100 MPa
g_∞	130 MPa
h_0	100 MPa
C_1	80 GPa
D_1	750
C_2	1.25 GPa
D_2	0.001

Table 5.2. Material parameters used in J_2 material model [1].

Parameter	Value
k	230 MPa
Q	60 MPa
b	9
c_1	240 GPa
γ_1	1846
c_2	50 GPa
γ_2	250
c_3	2.7 GPa
γ_3	0.55

5.2.2 Microstructure Model

The microstructure of the L605 cobalt chromium alloy analysed in this work has been characterised by Sweeney et al. [1]. An electron backscatter diffraction (EBSD) orientation map is given in Figs. 5.2a. This EBSD map shows the lack of crystallographic texture in the material, which indicates that the metallic grains do not have a preferred crystallographic orientation. Measured grain area distributions were employed to calculate grain volumes and average grain size by idealising grains as rhombic dodecahedrons, as shown in Figs. 5.2b and c. The identified average grain size of the material is 32 μm . The material was also observed to contain a 0.52% area fraction of tungsten carbide precipitates.

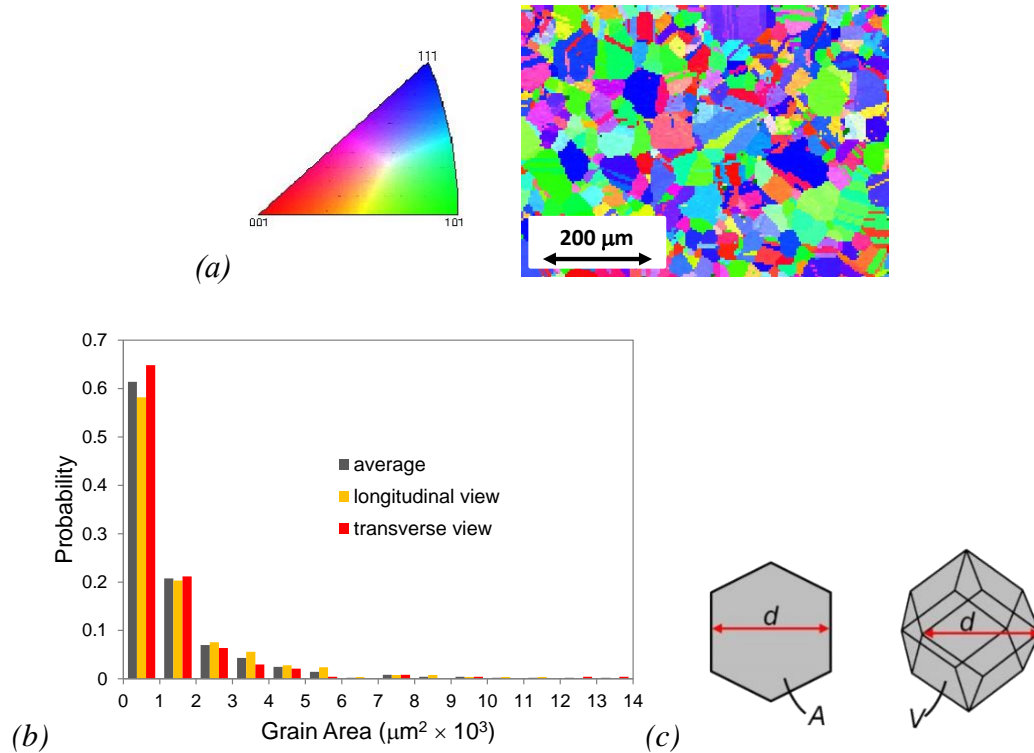


Figure 5.2. (a) EBSD orientation map showing no preferred crystallographic texture [2]. (b) Grain area distributions for a longitudinal and transverse view of the as-received rod specimens [1]. (c) Idealised geometry used to calculate average grain size and grain volumes based on measure grain area data [1].

A representative unit cell microstructure model is developed here using the CPFE constants identified by Sweeney et al. [1] and compared to experimental results to ensure the current computational framework provides results which are representative of the real material. The controlled Voronoi tessellation methodology described in Chapter 4 is employed to generate a periodic 3D microstructure geometry. A unit cell model is shown in Figure 5.3a, where each colour represents a metallic grain. Grain volume distributions of the real material are compared to a corresponding finite element microstructure model, as shown in Fig 5.3b. Grains are assigned random crystallographic orientations as the real material was observed to have no texture in EBSD maps.

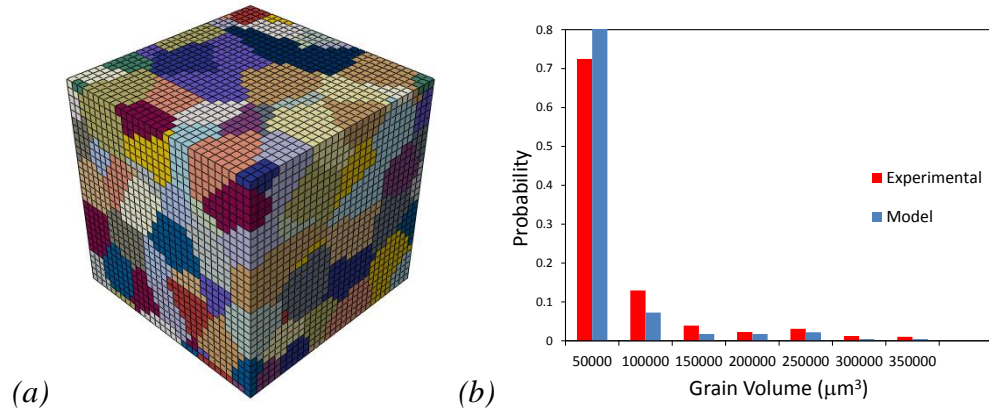


Figure 5.3. (a) 3D unit cell microstructure model, where each colour represents a metallic grain. (b) Comparison of grain volume distributions.

Periodic boundary conditions are assigned to each free face and a cyclic strain is then applied to the model to simulate the microscopic deformation of a repeating volume cell in the material, as shown in Fig 5.4a. Experimentally measured and CPFEM predicted stabilised hysteresis loops are shown in Fig. 5.4b for strain ranges of $\pm 1\%$ and $\pm 0.5\%$. It can be seen from Figs. 5.3b and 5.4b that the generated grain volume distributions and predicted cyclic stress-strain behaviour are representative of the material. This methodology is therefore employed for the subsequent microstructure-sensitive fretting analysis.

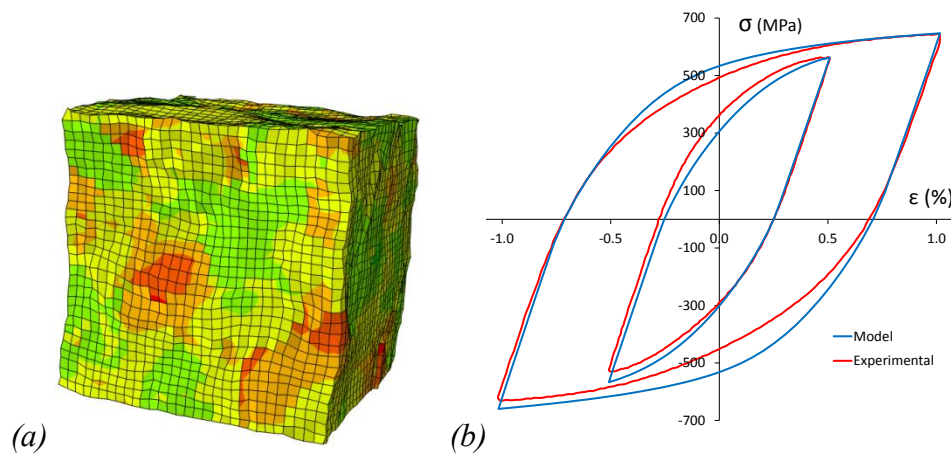


Figure 5.4. (a) Microscopic deformation of the unit cell model and (b) Comparison of computational predicted and experimentally measured stabilised cyclic stress/strain behaviour for two strain ranges.

5.2.3 Fatigue Crack Initiation

A key challenge in the modelling of fretting fatigue is the establishment of scale-consistent FIPs to predict numbers of cycles to crack initiation. One FIP implemented here is the accumulated crystallographic slip parameter p which has been introduced in Chapter 4. In the context of fretting, McCarthy et al. [3] found good agreement between experimentally measured fretting fatigue lives and computationally predicted lives using p . The accumulated crystallographic energy dissipation W of Korsunsky et al. [4], which is also described in Chapter 4, is also employed here.

As described by Manonukul and Dunne [5], the number of cycles to crack initiation N_i is calculated by dividing an identified critical FIP value by a stabilized cyclic value, as follows:

$$N_{i,w} = \frac{p_{\text{crit}}}{p_{\text{cyc}}} \quad (5.1)$$

$$N_{i,w} = \frac{W_{\text{crit}}}{W_{\text{cyc}}} \quad (5.2)$$

where

$$p_{\text{cyc}} = p(t) - p(t - \Delta t_{\text{cyc}}) \quad (5.3)$$

and

$$W_{\text{cyc}} = W(t) - W(t - \Delta t_{\text{cyc}}) \quad (5.4)$$

where Δt_{cyc} is the time taken to complete one fretting cycle. Critical values for each FIP have also been identified previously by Sweeney et al. [1] for this CoCr alloy by calibrating a unit cell polycrystal model against low cycle fatigue crack initiation data. Again, to ensure the models developed here represent the real material, N_i predictions for a unit cell model using p_{cyc} and W_{cyc} are compared to experimentally determined N_i values, as shown in Fig. 5.5. The CPFÉ model gives good predictions of N_i using both FIPs, particularly at low strain ranges, which are most relevant for this work. However, W_{cyc} shows better correlation overall, where the predicted N_i for each strain range lies within a $\pm 30\%$ margin of error.

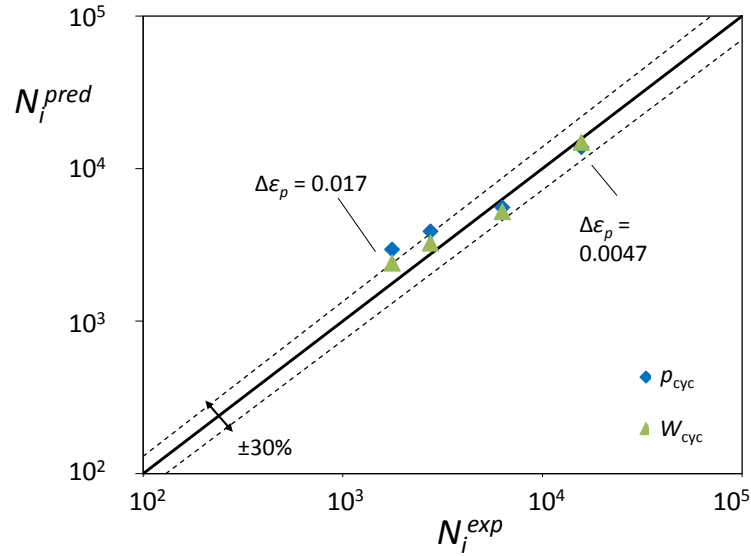


Figure 5.5. Comparison of computational predicted and experimentally determined number of cycles to crack initiation for four strain ranges, where the diagonal line represents exact agreement

5.2.4 Microstructure Sensitive Fretting Model

A 3-D cylinder-on-flat fretting model is developed to incorporate material microstructure in contact zones, as shown in Fig. 5.6. Precipitates are excluded in the fretting modelling as the aim here is to assess the effect of average grain size. The model is discretised with 20-noded reduced integration brick elements. Tied surface constraints are implemented to allow for highly localised mesh refinement towards the contact zone, as described in [6], whilst maintaining a coarse mesh away from the contact regions. An element size of $6 \mu\text{m}$ is chosen for the refined microstructure region. This results in an average of 120 elements per grain (for the smallest average grain size considered), which is in agreement with mesh refinement studies for CP simulations performed by Harewood and McHugh [7] and Sweeney et al. [8]. All other regions of the model are assigned a J_2 plasticity material model to reduce computational expense.

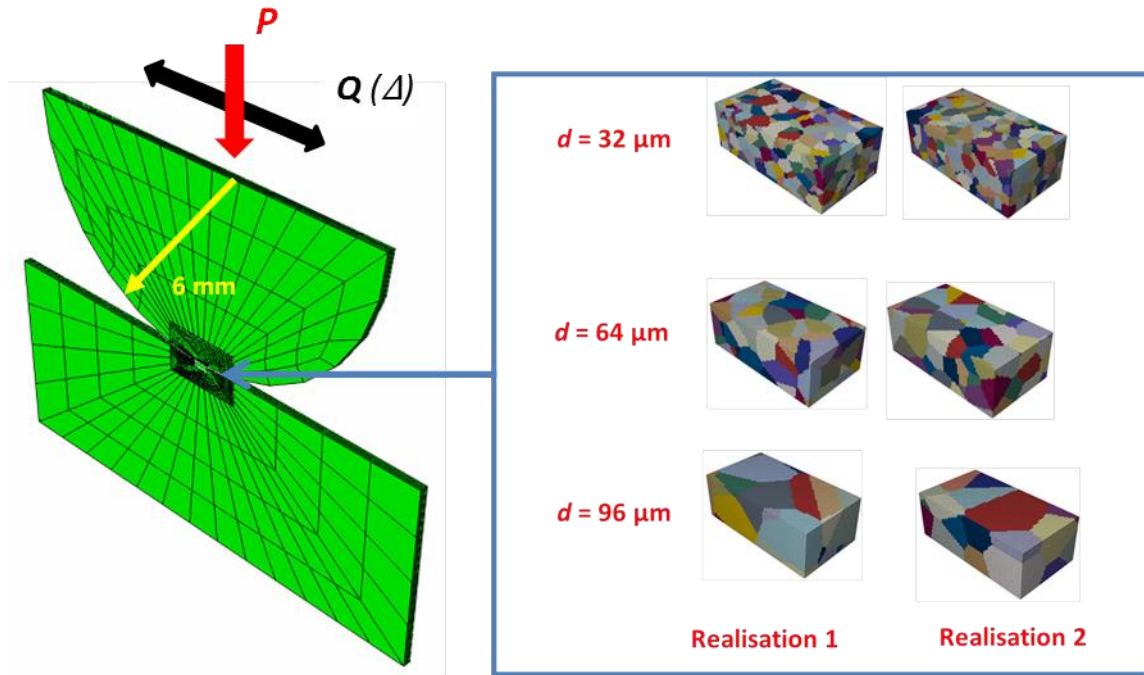


Figure 5.6. 3D cylinder-on-flat fretting model with the inclusion of microstructure in the contact region of the substrate. Two realisations are shown here for each average grain size. A total five realisations are considered for each grain size.

The simulations are restricted to partial slip fretting conditions, which is considered to be the most detrimental sliding regime in fretting fatigue, due to the absence of significant wear. The normal load P applied to the model is half the normal load necessary to cause macroscopic yielding in this material. This value P_y is calculated as follows:

$$P_y = \frac{\pi R}{E^*} (p_o)_y^2 \quad (5.6)$$

where

$$(p_o)_y = 1.8k \quad (5.7)$$

with R as the radius of the cylinder, E^* as the composite modulus [9] and k is the macroscopic yield stress of the material. The calculated normal load for a chosen 6 mm radius cylinder is 22.6 N/mm, which is kept constant for all simulations. This value of P causes a Hertzian contact semi-width a of 47 μm . A coefficient of friction (COF) has not

yet been measured for the current set-up of CoCr-on-CoCr. However, Zhang et al. [10] measured a stabilized COF of approximately 0.5 in tribological tests of titanium fretted against CoCr, which is used here. The finite sliding ABAQUS formulation with Lagrange friction is employed to ensure exact stick when the surface traction is less than the limiting frictional shear. To run simulations in the partial slip regime, tangential loads Q are chosen to be less than the limiting frictional force:

$$Q < \mu P \quad (5.8)$$

P and Q are applied to a master node on the top face of the semi-cylinder, according to the loading history illustrated in Fig 5.7a. Linear constraint equations are then employed to ensure that all remaining nodes on this surface have the same displacement as this master node. The bottom of the substrate is fixed in all three translational degrees of freedom. All faces perpendicular to the cylinder axis are constrained in the z direction to reduce edge effects.

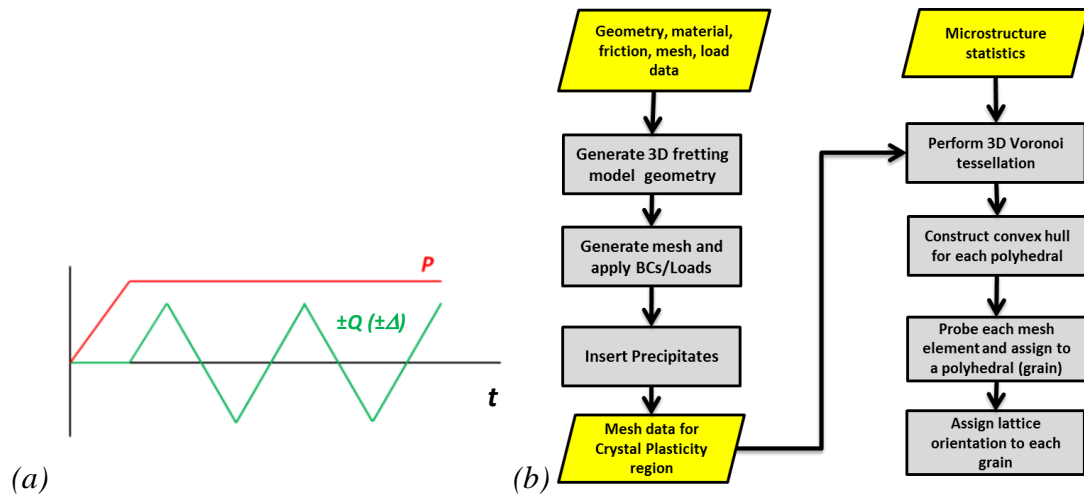


Figure 5.7. (a) Loading history showing constant normal load and cyclic tangential load and (b) Methodology flowchart for fretting model generation.

A key aim of this work is to analyse multiple microstructure realizations across a range of grain sizes. The need for efficient generation of FE models is therefore essential. An automated PythonTM scripting methodology has been developed to build models based on user-defined microstructure statistics. This process is described using the flowchart shown in Fig 5.7b.

A key non-dimensional parameter investigated is the ratio between contact semi width a and average grain size d . Three average grain sizes are investigated in this work; 32 μm , 64 μm and 96 μm , corresponding to a/d ratios of 1.38, 0.69 and 0.46, respectively. Five random microstructure realizations are analysed for each average grain size, where each realization contains random grain orientations and random geometry, whilst maintaining the same microstructure statistics. This allows for the assessment of the statistical variation in predicted fatigue life for each grain size. Microstructure geometries for two sample realizations of each average grain size are shown in Fig 5.6. Applied tangential load Q (or stroke Δ) is also analysed here in the partial slip regime. The three Q/P ratios investigated here are 0.375, 0.25 and 0.125, corresponding to relative slip values of 0.326 μm , 0.216 μm and 0.125 μm , respectively.

An initial study has been performed to establish the loading cycle where p_{cyc} and W_{cyc} have reached stabilized values. This is an essential step to reduce computational cost. Figure 5.8 shows the evolution of maximum FIPs, which are seen to reach effectively stabilised values after three cycles. In addition, Fig. 5.9 shows that the locations of maximum values of both FIPs have also stabilized by cycle 3. It is worth noting that the stabilized maximum value for p and W is predicted to occur at different locations in the model. Simulations for each microstructure realization are therefore run for three fretting cycles. These results are consistent with the CPFE predictions of Goh et al. [11], who observed stabilized cyclic ratchetting by the third cycle in simulations of a titanium alloy in fretting.

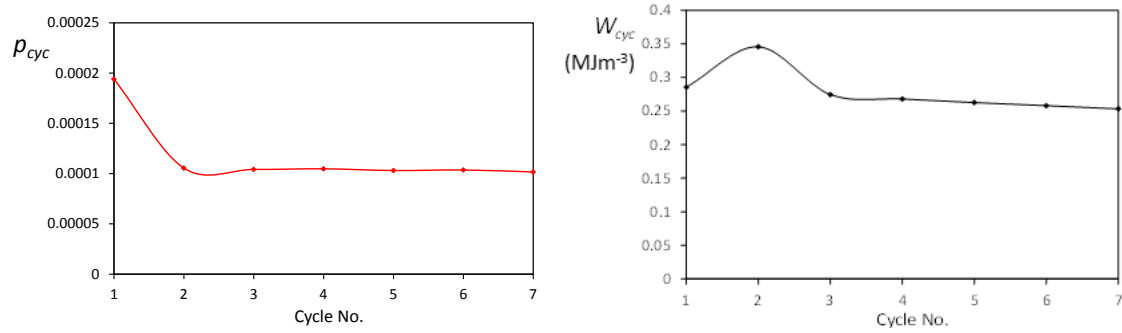


Figure 5.8. The evolution of maximum local p_{cyc} and W_{cyc} , which are both seen to stabilize after 3 fretting cycles.

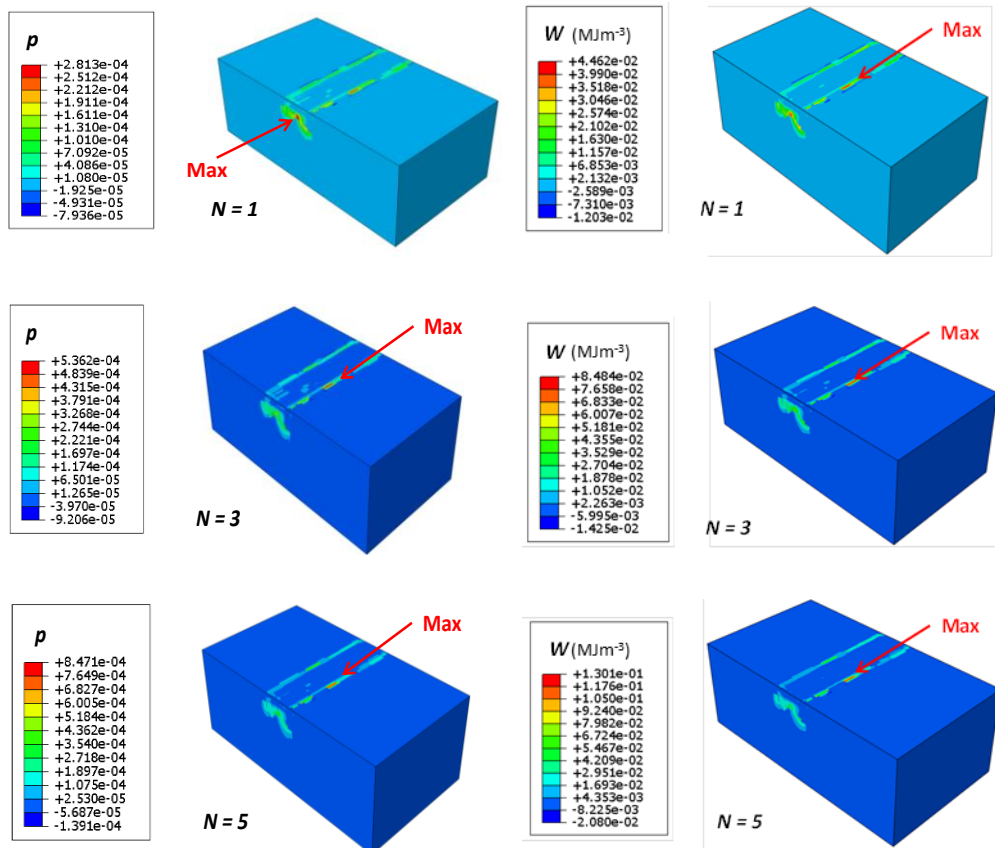


Figure 5.9. The location of maximum p and W for cycle 1, 3 and 5. Locations of maximum FIP values have effectively stabilized by the 3rd fretting cycle.

5.3 Results

5.3.1 Spatial Distributions

Initially, spatial distributions of stress and FIPs are examined to assess the sensitivity of these important variables to microstructure. The geometric path shown in Fig. 5.10, which lies on the first row of integration points $3 \mu\text{m}$ below the substrate surface, is chosen for plotting these spatial distributions. In Figs. 12a and b, the predicted tangential and shear stress distributions are plotted for each realization of $d = 32 \mu\text{m}$ and for a J_2 model with an applied Q/P ratio of 0.25 . These values are taken after three fretting cycles at the time point where the maximum Δ is applied. It is useful to compare the CP response with the J_2 response as a way of validating the crystal plasticity method without the use of experiments. J_2 plasticity is commonly used in fretting modelling and has been shown to be in good agreement with experimental observations [12], [13]. It can be seen that the crystal plasticity and J_2 material model give almost identical spatial distributions of σ_{xx} and σ_{xy} for each path considered, showing the validity of the crystal plasticity method. Figures 5.11a and b also show little variation in stress distributions between each microstructure realization. This is due to the chosen loading conditions, which result in nominally elastic behaviour. For a greater applied Q/P ratio of 0.375 , more plasticity is induced, leading to marginally more scattered stress distributions, as shown in Figs. 5.11c and d. The same trends are seen in these distributions for the larger average grain sizes of $64 \mu\text{m}$ and $96 \mu\text{m}$, which are not presented here. In addition, stress distributions do not alter significantly as the position of the path is varied with respect to the z direction.

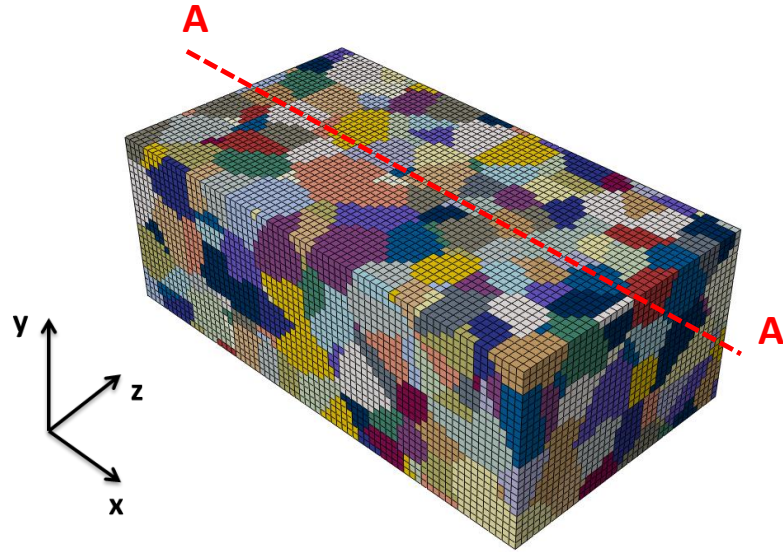


Figure 5.10. The geometric path chosen to plot spatial distributions of field variables.

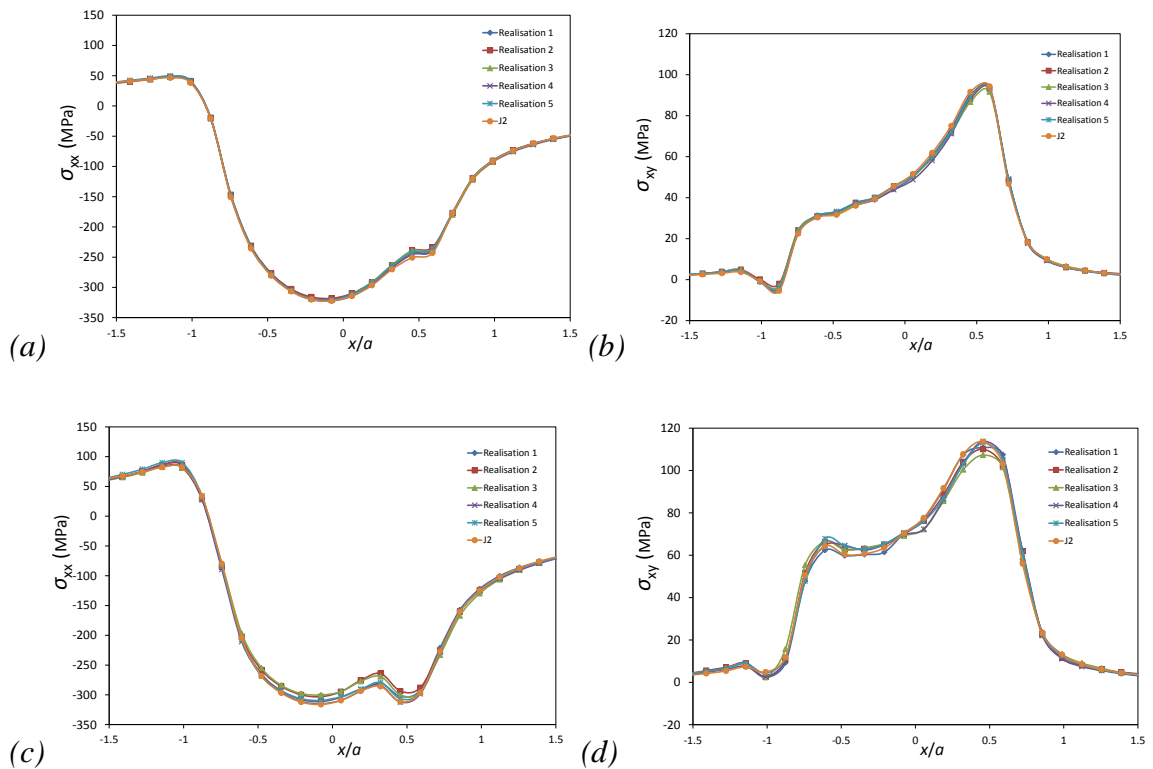


Figure 5.11. Spatial distributions of (a) tangential stress for $Q/P = 0.25$, (b) shear stress for $Q/P = 0.25$ (c), tangential stress for $Q/P = 0.375$ and (d) shear stress for $Q/P = 0.375$ for 5 microstructure realisations of $d = 32 \mu\text{m}$ and a J_2 model

A significant effect of microstructure can be seen when spatial distributions of the FIPs are plotted, as shown in Fig. 5.12, again for each realisation of $d = 32 \mu\text{m}$. For example, the maximum predicted p varies between 1.0×10^{-5} and 8.0×10^{-5} for a Q/P ratio of 0.25. This result highlights the ability of the CP model to capture highly localised regions of plastic strain within the microstructure of the material, which are known to be favourable locations for crack initiation [14]. p and W show general agreement with regard to location of maximum values and general distributions. In general, the maximum FIP is predicted to occur in the slip zones of contact, which are indicated in the peak regions of contact shear shown in Fig. 5.13. This consistent with experimental observations of crack locations in the partial slip regime [15]. In addition, maximum values are predicted to occur in the region of peak shear stress (Figs. 5.12 b and d), which is known to be the critical location for fretting crack nucleation [16].

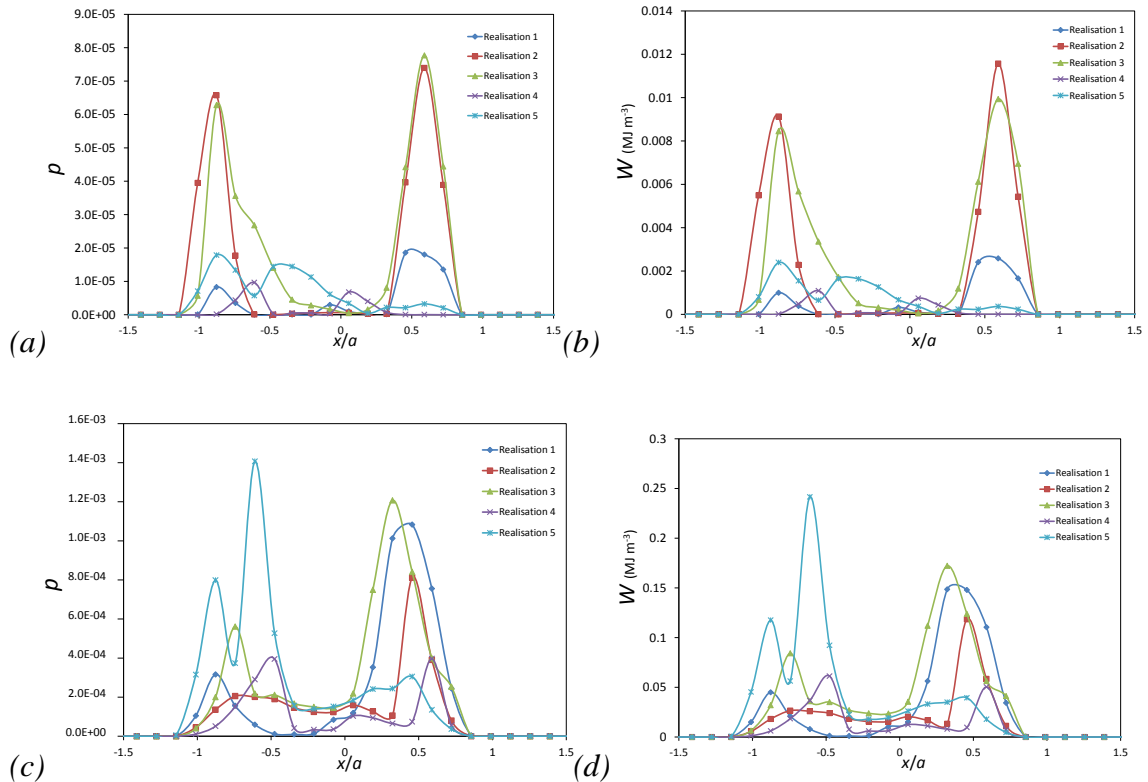


Figure 5.12. Spatial distributions of (a) p for $Q/P = 0.25$, (b) W for $Q/P = 0.25$ (c), p for $Q/P = 0.375$ and (d) W for $Q/P = 0.375$ for 5 microstructure realisations of $d = 32 \mu\text{m}$.

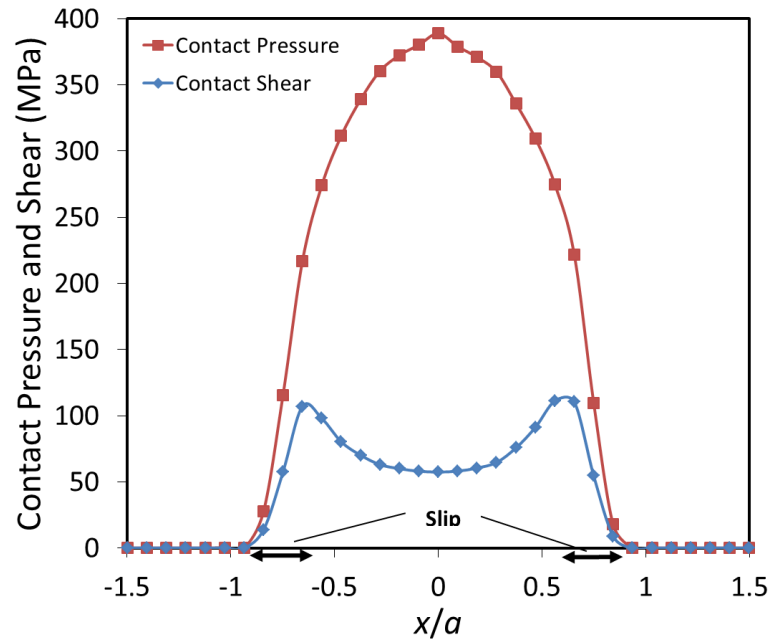


Figure 5.13. Contact pressure and shear distributions for $Q/P = 0.25$, corresponding to Fig. 12a and 12b, indicating slip zones.

5.3.2 N_i Predictions

In Fig. 5.14 the number of cycles to crack initiation N_i are plotted against a/d for both FIPs. In this case, the applied stroke is kept constant at $0.22 \mu\text{m}$ ($Q/P = 0.25$) and a is kept constant at $47 \mu\text{m}$. Each data point represents a different random realization for a given average grain size. Both FIPs predict a significant increase in scatter with decreasing a/d . Maximum N_i is predicted to increase by up to a factor of 10 as a/d is reduced from 1.38 to 0.46. The average predicted life also increases with reducing a/d . The average predicted N_i for an a/d ratio of 0.46 is 3 times higher than for an a/d ratio of 1.38. This result clearly shows a size effect. The minimum predicted N_i increases less as a/d is reduced. It should be noted that commonly-used macro-scale techniques for fretting fatigue life prediction, e.g. J_2 plasticity and Smith Watson Topper fatigue parameter [17] would not show this effect.

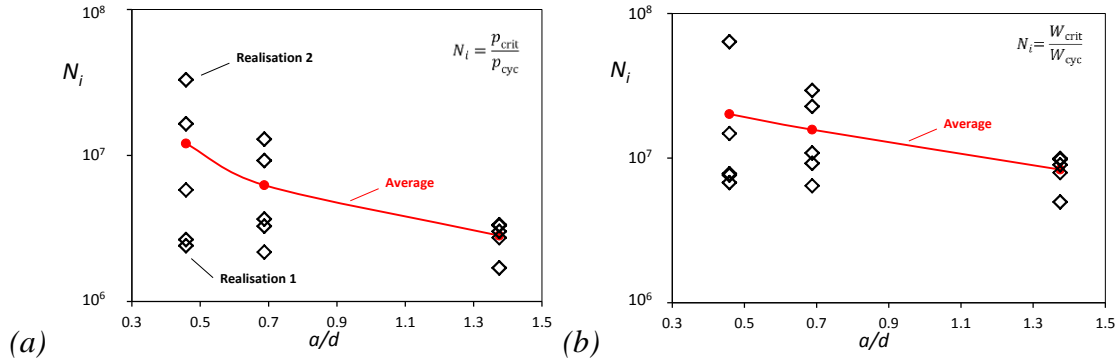


Figure 5.14. Predicted effect of contact semi-width to average grain size ratio on crack initiation life. The hollow symbols represent different microstructure realisations.

Figure 5.15 compares the location of maximum p for the two extreme cases of N_i for the lowest a/d ratio, where Realisation 1 corresponds to the lowest predicted N_i and Realisation 2 corresponds to the highest predicted N_i . It can be seen that in Realisation 1, there is a significant concentration of p at a grain boundary near the edge of the contact zone, whereas, in Realisation 2, p is more evenly distributed across the thickness of the model. The concentration of p in Realisation 1 is attributed to the presence of a particularly unfavourable combination of adjacent grains. In Realisation 2, such a grain combination does not exist, leading to a higher predicted N_i . The importance of an unfavourable grain combination in fretting has been highlighted in previous work by McCarthy et al. [18] and Mayuer et al. [19]. However, the results presented here show the statistical variation in N_i due to the possible presence of such a microstructural feature, which lead to a size effect. The probability of the presence of an unfavourable grain combination in the contact zone is reduced as a/d is reduced, resulting in a higher predicted average N_i , as shown in Fig. 5.14. It is proposed that a critical a/d ratio exists, above which, negligible statistical variation in N_i occurs. This result is consistent with the measured contact size effect of Nowell [20]. The present work provides a physical demonstration of the reason for this i.e. smaller contact sizes lead to fewer critically stressed grains or grain boundaries due to a smaller stress field, and thus, increased fatigue resistance. The present work therefore shows an explicit way to predict this for measured microstructures in the contact zone.

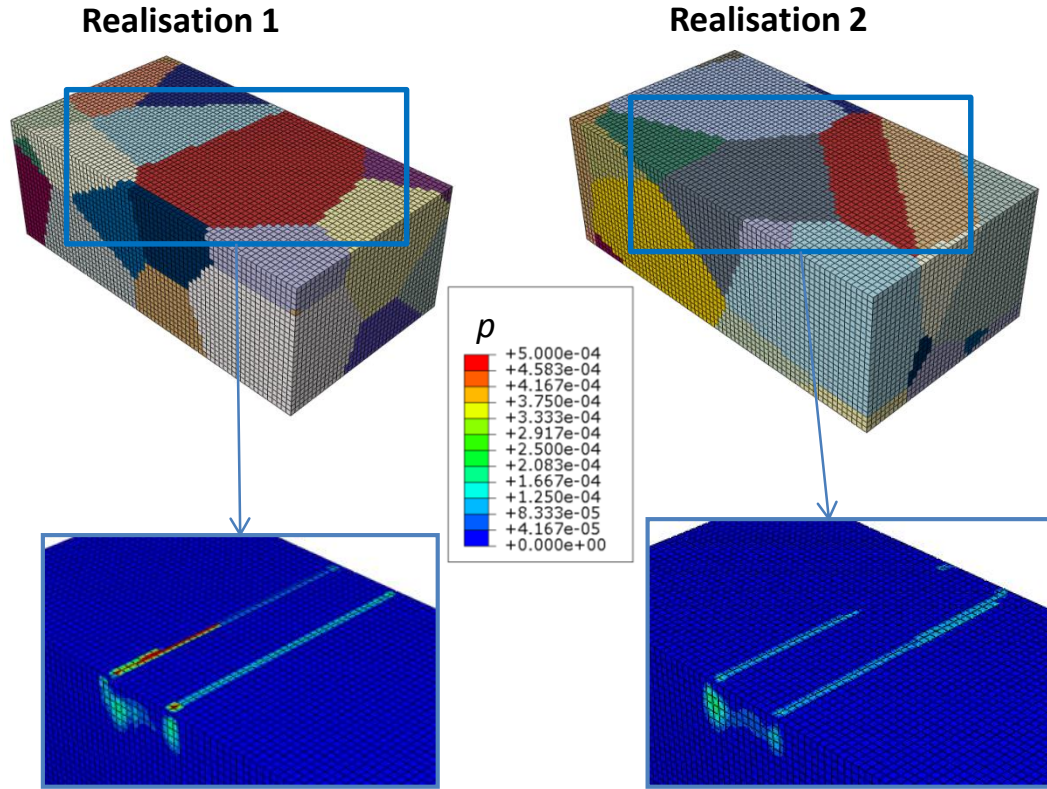


Figure 5.15. Analysis of maximum p for the two extreme N_i values seen in Fig. 5.13a where $a/d = 0.46$. A significant concentration of p exists at a grain boundary near the edge of contact in Realisation 1, resulting in the lowest resistance to crack nucleation.

5.3.2 Effect of Δ

The effect of stroke Δ is shown in Fig. 5.16. The average grain size is kept constant at $32 \mu\text{m}$ ($a/d = 1.38$) in this series of analysis, again with five realizations. A lower Δ results in a higher predicted N_i , as expected, due to the less severe loading conditions. A similarly small amount of scatter is predicted for each value of Δ . This result shows that for the partial slip regime, the microstructure considered does not have a significant influence on the effect of Δ on N_i , due to the relatively small ratio of Δ to d . Figure 5.17 shows contour plots of p for the lowest and the highest Δ . It can be seen that a high Δ results in an accumulation of p at the surface of the substrate due to a relatively large surface traction. A low Δ results in an accumulation of p below the substrate surface due to the dominance of the normal load. An intermediate Δ of $0.21 \mu\text{m}$ shows both surface and subsurface concentrations of p , depending on the grain combinations in the contact

zone, resulting in marginally more scatter than the other two cases. For this value of Δ , two data points (indicated with 'x' markers) represent microstructure realisations with maximum p at the surface and the remaining three represent realisations with subsurface maximum p .

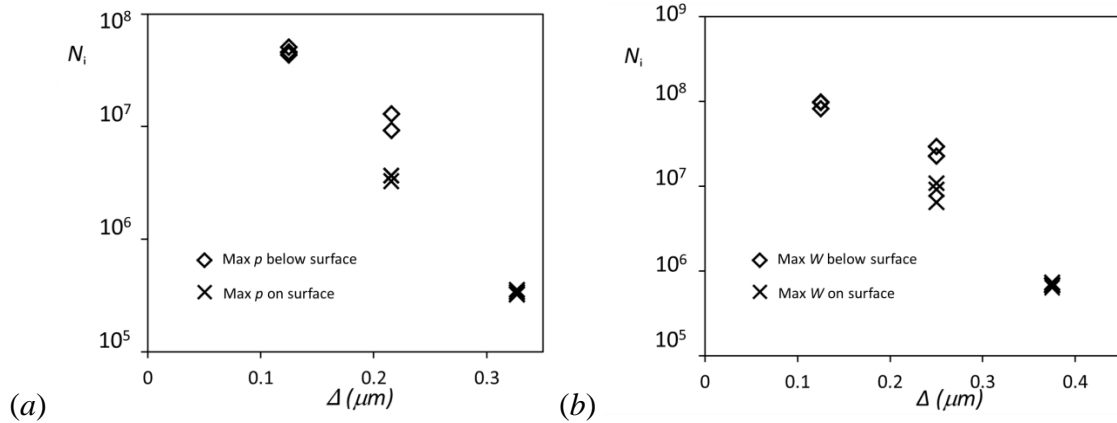


Figure 5.16. Influence of microstructure on predicted effect of stroke on N_i using (a) p and (b) W . The 'X' markers represent simulations where the maximum FIP value occurs at the surface of the substrate.

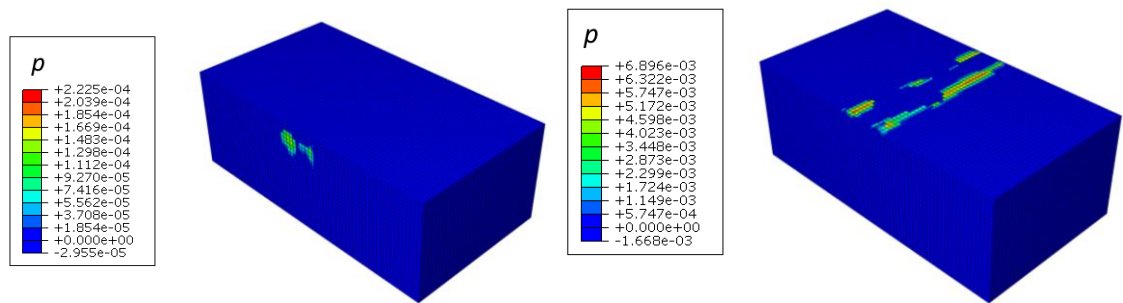


Figure 5.17. Contour plots showing concentrations of p for strokes Δ of (a) $0.1 \mu\text{m}$ and (b) $0.32 \mu\text{m}$.

5.4 Conclusions

A 3-D microstructure-sensitive CPFE fretting study has predicted a statistical grain size effect in fretting crack initiation. Both fatigue indicator parameters employed here, i.e. accumulated crystallographic slip p and crystallographic energy dissipation W , predict an increased statistical variation (scatter) in number of cycles to crack initiation N_i as the

number of grains in the fretting contact is reduced. In particular, the N_i is predicted to increase with a reducing ratio of contact width to grain size, a/d ; the average N_i is predicted to increase significantly. It is shown that the critical a/d ratio is approximately 1, with negligible scatter predicted for $a/d > 1$, i.e. when the contact semi-width is greater than the average grain size. In contrast, microstructure morphology is shown to have little influence on the effect of applied stroke in the partial slip regime due to the small ratio of applied stroke to grain size. Overall it is shown that the relative length-scales of slip, grain size and contact width need to be considered for reliable design against fretting crack initiation. It is important to note that this work does not include the effects of wear, although these may not be significant in the partial slip regime, and the effects of plastic-strain gradient-induced length-scale effects, which will be studied in following chapters. The results presented here indicate that fretting contact-material configurations need to be designed to include large numbers of grains in contact regions to minimise fatigue uncertainty.

5.5 References

- [1] C. A. Sweeney, B. O'Brien, P. E. McHugh, and S. B. Leen, "Experimental characterisation for micromechanical modelling of CoCr stent fatigue," *Biomaterials*, vol. 35, no. 1, pp. 36–48, 2014.
- [2] C. A. Sweeney, B. O'Brien, F. P. E. Dunne, P. E. McHugh, and S. B. Leen, "Strain-gradient modelling of grain size effects on fatigue of CoCr alloy," *Acta Mater.*, vol. 78, pp. 341–353, 2014.
- [3] O. J. McCarthy, J. P. McGarry, and S. B. Leen, "The effect of grain orientation on fretting fatigue plasticity and life prediction," *Tribol. Int.*, vol. 76, pp. 100–115, 2013.
- [4] A. M. Korsunsky, D. Dini, F. P. E. Dunne, and M. J. Walsh, "Comparative assessment of dissipated energy and other fatigue criteria," *Int. J. Fatigue*, vol. 29, no. 9–11, pp. 1990–1995, 2007.

-
- [5] A. Manonukul and F. P. E. Dunne, “High- and low-cycle fatigue crack initiation using polycrystal plasticity,” *Proc. R. Soc. A Math. Phys. Eng. Sci.*, vol. 460, no. 2047, pp. 1881–1903, 2004.
- [6] M. Zhang, D. L. McDowell, and R. W. Neu, “Microstructure sensitivity of fretting fatigue based on computational crystal plasticity,” *Tribol. Int.*, vol. 42, no. 9, pp. 1286–1296, 2009.
- [7] F. J. Harewood and P. E. McHugh, “Investigation of finite element mesh independence in rate dependent materials,” *Comput. Mater. Sci.*, vol. 37, no. 4, pp. 442–453, 2006.
- [8] C. A. Sweeney, “Micromechanics of fatigue with application to stents,” PhD Thesis, National University of Ireland Galway, 2014.
- [9] K. L. Johnson, “Contact Mechanics,” Cambridge University Press, Cambridge 1985.
- [10] T. Zhang, N. M. Harrison, P. F. McDonnell, P. E. McHugh, and S. B. Leen, “A finite element methodology for wear-fatigue analysis for modular hip implants,” *Tribol. Int.*, vol. 65, pp. 113–127, 2013.
- [11] C.-H. Goh, J. M. Wallace, R. W. Neu, and D. L. McDowell, “Polycrystal plasticity simulations of fretting fatigue,” *Int. J. Fatigue*, vol. 23, pp. 423–435, 2001.
- [12] D. Houghton, P. M. Wavish, E. J. Williams, and S. B. Leen, “Multiaxial fretting fatigue testing and prediction for splined couplings,” *Int. J. Fatigue*, vol. 31, no. 11–12, pp. 1805–1815, 2009.
- [13] W. S. Sum, E. J. Williams, and S. B. Leen, “Finite element, critical-plane, fatigue life prediction of simple and complex contact configurations,” *Int. J. Fatigue*, vol. 27, no. 4, pp. 403–416, 2005.
- [14] C. A. Sweeney, W. Vorster, S. B. Leen, E. Sakurada, P. E. McHugh, and F. P. E. Dunne, “The role of elastic anisotropy, length scale and crystallographic slip in fatigue crack nucleation,” *J. Mech. Phys. Solids*, vol. 61, no. 5, pp. 1224–1240, 2013.

- [15] J. Ding, G. Bandak, S. B. Leen, E. J. Williams, and P. H. Shipway, “Experimental characterisation and numerical simulation of contact evolution effect on fretting crack nucleation for Ti-6Al-4V,” *Tribol. Int.*, vol. 42, no. 11–12, pp. 1651–1662, 2009.
- [16] L. J. Fellows, D. Nowell, and D. A. Hills, “On the initiation of fretting fatigue cracks,” *Wear*, vol. 205, no. 1–2, pp. 120–129, 1997.
- [17] O. J. McCarthy, J. P. McGarry, and S. B. Leen, “A finite element study of microstructure-sensitive plasticity and crack nucleation in fretting,” *Comput. Mater. Sci.*, vol. 50, no. 8, pp. 2439–2458, 2011.
- [18] O. J. McCarthy, J. P. McGarry, and S. B. Leen, “The effect of grain orientation on fretting fatigue plasticity and life prediction,” *Tribol. Int.*, pp. 1–16, 2013.
- [19] J. R. Mayeur and D. L. McDowell, “A three-dimensional crystal plasticity model for duplex Ti-6Al-4V,” *Int. J. Plast.*, vol. 23, no. 9, pp. 1457–1485, 2007.
- [20] D. Nowell, “An analysis of fretting fatigue,” PhD Thesis, University of Oxford, 1988.

6 The Effect of the Beta Phase on the Performance of Dual-Phase Titanium Alloys

6.1 Introduction

The following chapter is the outcome of a research visit to Imperial College London, which was undertaken to develop an understanding and gain practical experience of length-scale dependent crystal plasticity material modelling.

Extensive research has been carried out on the microstructure sensitivity of titanium alloys, such as the assessment of crystallographic orientation [1], grain size [2] and morphology [3] in order to understand failure mechanisms, and hence, better predict service life of components. This chapter investigates the effect of α - β colonies on micromechanical deformation response and failure parameters in Ti-6242, a two-phase material comprised of a primary α -phase and α - β colony regions. The α - β phase has previously been modelled as a single, homogenised, microstructural unit [4]–[7] where the β phase is not explicitly modelled. The small lengths associated with α - β colonies, which is typically only several microns [8], [9], suggest that length-scale effects may be important. In this chapter, the β -phase is explicitly included in computational models, and the heterogeneous material model is calibrated against micro-pillar tests, specifically designed to elucidate the effects of the β -laths.

The computational methodology developed in this chapter is applied to the phenomenon of cold-dwell fatigue. Failure in dwell fatigue is understood to occur from the nucleation of quasi-cleavage micro-cracks of length approximately equal to grain size, known as facets. This process, known as ‘faceting’, is a key factor in the service life of several aerospace components, such as compressor rotor spools [10]. A dwell fatigue cycle includes a load holding period, which leads to a significant drop in component life in many titanium alloys compared to standard fatigue loading [11]. For example, Kassner

et al. [12] observed that the number of cycles to failure for dwell-fatigue tests were up to an order of magnitude lower than for equivalent standard low-cycle tests. This is attributed to the ability of these materials to undergo creep at low temperatures. It has been previously shown that strain accumulation due to cold creep during the load-holding dwell period leads to load shedding from a favourably oriented grain to an adjacent unfavourably oriented grain with respect to the loading direction [11], [13], [14]. This creep-induced load-shedding process is considered critical for facet nucleation.

In this chapter, a crystal plasticity computational study is performed to assess the global and local behaviour of α - β colonies in Ti-6242. A CPFEM model is developed with calibration and validation against measured micropillar tests on α - β Ti-6242. The role of α -phase ligament width, length-scale effects, and α -phase crystallographic orientation are assessed using representative models of α - β colonies. β laths are explicitly represented in these models based on previous experimental observations [8]. This work implements a physically-based approach for calculation of GND density, based on plastic strain-gradients, without the need to specify additional length terms. Hence, the length-scale is derived purely from the geometry of the model. Later in the chapter, the role of α - β colonies is assessed in the context of cold dwell. α - β colony location and orientation with respect to a rogue grain combination is analysed. This work is relevant to microstructure design of dual-phase titanium alloys for resistance to crack nucleation in cold dwell-fatigue.

6.2 Material and Constitutive Model

The primary α -phase is a hexagonal close packed (HCP) lattice system with 24 slip systems are shown in Fig 6.1. The α - β regions contain a HCP α -phase and body centre cubic (BCC) β laths. The modified physically-based length-scale dependent material model of Dunne [1] introduced in Chapter 4 is employed here to model the HCP α -phase of this material.

Previous experimental work regarding the behaviour of individual α - β colonies in dual-phase titanium alloys has shown that a key consideration when analysing these colonies is the existence of a Burgers Orientation Relationship (BOR) [15], [16] between the HCP α -phase and BCC β -phase, where the closest packed planes and directions are shared between the two phases. However, the β -phase is considered to be isotropic elastic in this work as the observations of Jun et al [8] show significantly lower slip levels in the β phase of this material under pillar compression tests. Further, since it is the α - β interfaces and their influence on plastic strain gradients and GND density which are key aspects of this study, considering the β phase to be elastic provides a worst-case scenario, or conservative approach, in consideration of the effects in cold-dwell fatigue.

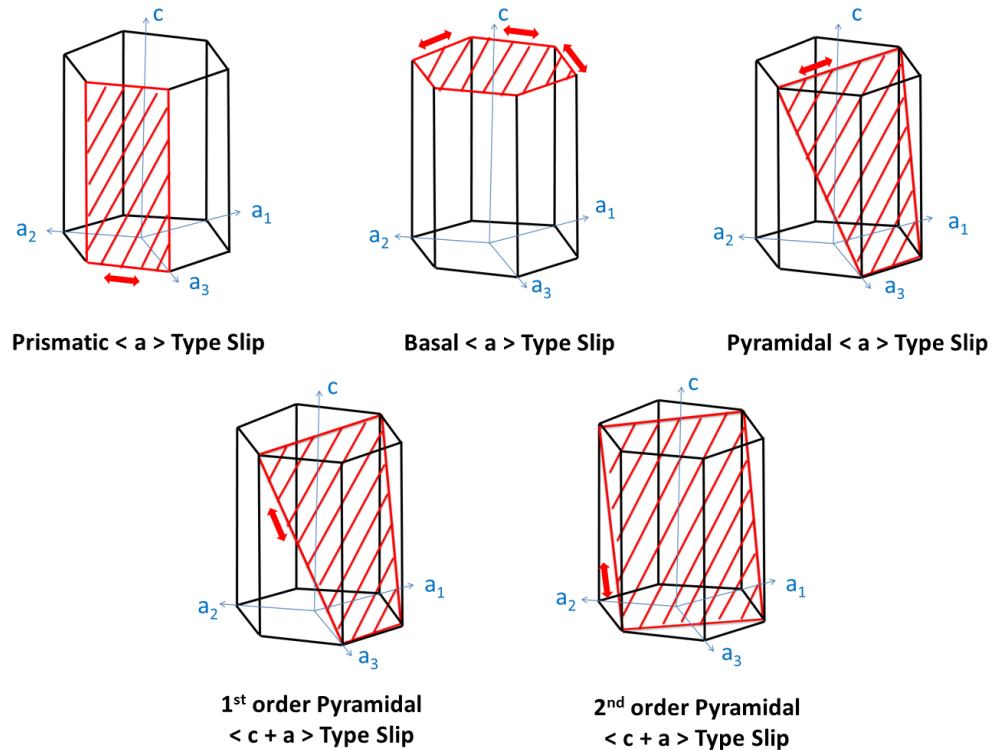


Figure 6.1. Slip systems in HCP phase of titanium alloys. The red arrows indicate slip direction.

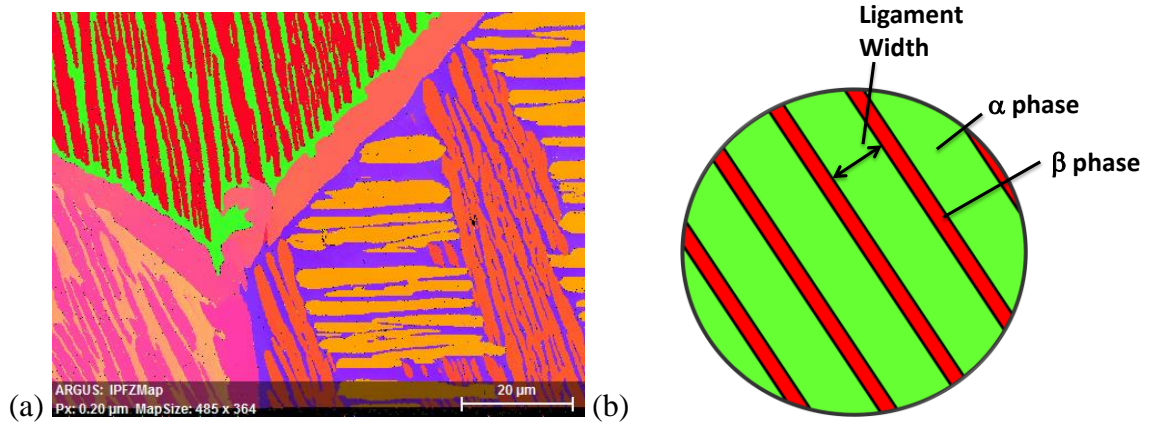


Figure 6.2. (a) IPF map of typical α - β colony structure in titanium alloys [35] (b) Idealised geometry for FE modelling of α - β colonies in Ti-6242

The elastic β -phase properties used here are those identified by Kim and Rokhlin [17]. The anisotropic elastic properties for the α -phase are taken from the experimental tests of Hasija et al. [13] on Ti-6Al. The transverse anisotropic elastic stiffness matrix C is therefore reconstructed for implementation in ABQAUUS, and is given below:

$$C = \begin{pmatrix} 134 & 76 & 65 & 0 & 0 & 0 \\ 76 & 134 & 65 & 0 & 0 & 0 \\ 65 & 65 & 160 & 0 & 0 & 0 \\ 0 & 0 & 0 & 29 & 0 & 0 \\ 0 & 0 & 0 & 0 & 40 & 0 \\ 0 & 0 & 0 & 0 & 0 & 40 \end{pmatrix} GPa. \quad (6.1)$$

The α -phase activation energy ΔH for Ti-6242 has been calibrated in previous work by Zhang et al. [18] using single phase micro-pillar compression test data. This property reflects the rate sensitivity of the material, which is important for the cold dwell problem addressed in this work. Experimental results from Jun et al. [8] are implemented to calibrate critical resolved shear stress τ_0 and Taylor hardening constant M for the CPFEM model, as discussed later. The critical resolved shear stresses for prismatic and basal slip systems are assumed to be equal, based on the negligible difference in strengths between these slip systems, as observed by Hasija et al. [13]. The $\langle c+a \rangle$ pyramidal type slip

systems are assigned slip strengths approximately three times higher than $\langle a \rangle$ type systems, in agreement with experimental results of Gong and Wilkinson [19]. Only $\langle a \rangle$ type slip systems are considered here for the calculation of GND density as Britton et al. [20] observed significantly lower densities on $\langle c+a \rangle$ type slip systems in Ti-6Al-4V. A list of material parameters used in the slip rule is given in Table 6.1. Tables 6.2 present the isotropic elastic constants for the β phase.

Fig. 6.2 shows a measured phase map for a typical α - β colony in dual-phase titanium alloys [21]. In this work, finite element models are generated using an idealised α - β lath geometry as shown in Fig. 6.2b. This assumption allows for the development of structured element meshes and mesh densities giving practical computational run-times.

Table 6.1. Material parameters used in CPFEM modelling.

Parameter	Value
$\tau_0 \langle a \rangle$	240 MPa
$\tau_0 \langle c+a \rangle$	722 MPa
M	0.3
G	29022 MPa
$b \langle a \rangle$	$2.95 \times 10^{-4} \mu\text{m}$
$b \langle c+a \rangle$	$4.68 \times 10^{-4} \mu\text{m}$
k	$1.38 \times 10^{-23} \text{ J K}^{-1}$
T	293 K
ΔH	$7.58 \times 10^{-20} \text{ J}$
ν	$1.00 \times 10^{11} \text{ Hz}$
γ_0	1.32×10^{-4}
ρ_{SSD}^m	$5.0 \mu\text{m}^{-2}$
ρ_{SSD}^s	$0.01 \mu\text{m}^{-2}$

Table 6.2. Elastic constants used for the β -phase.

Parameter	Value
E	32024 MPa
ν	0.46 MPa

6.3 CPFE Model Calibration

Jun. et al [8] performed compression tests on α - β micro-pillar specimens of Ti-6242. These experimental results have been adopted here to calibrate and validate the CPFE model. A finite element representative model of a α - β micro-pillar is developed to calibrate the critical resolved shear stress and slip system hardening by comparing global force-displacement with corresponding experimental measurements. The pillar specimen geometry is shown in Fig. 6.3. The substrate is modelled as an isotropic elastic material, based on previous simulations of pure α -phase micro-pillars [18]. Length-scale effects are included in this analysis as the presence of the β -phase is expected to result in high gradients of plastic strain near phase interfaces, and thus, significant hardening due to the presence of GNDs. The bottom face of the substrate is fixed in all directions and a compressive displacement is applied to the top face of the pillar to replicate the experimental test. A mesh sensitivity has been carried out to ensure the results presented here are mesh independent.

Fig. 6.4 shows a comparison of the calibrated CPFE predicted force-displacement response, both with and without length-scale effects, and the measured experimental response. The inclusion of length-scale effects causes a harder predicted response due to the evolution of GND density. A critical resolved shear stress τ_{c0} of 240 MPa and Taylor factor M of 0.3 are chosen for the material model as they show excellent agreement with the experimentally observed force-displacement response. These parameters are used for the subsequent analysis in this chapter.

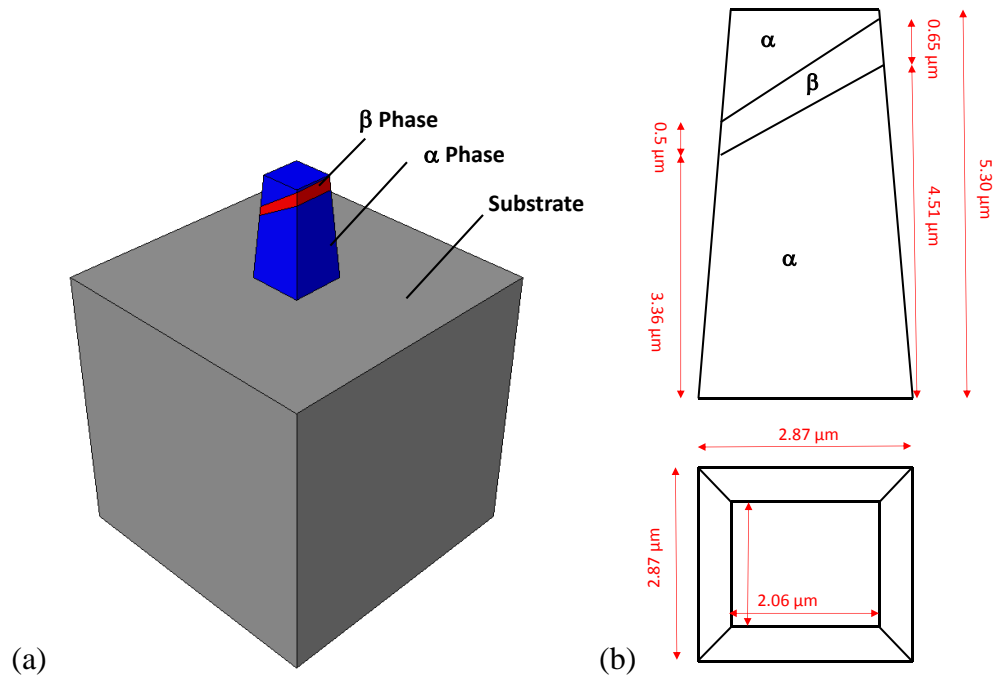


Figure 6.3. (a) Finite element model of pillar specimen and (b) α - β pillar geometry.

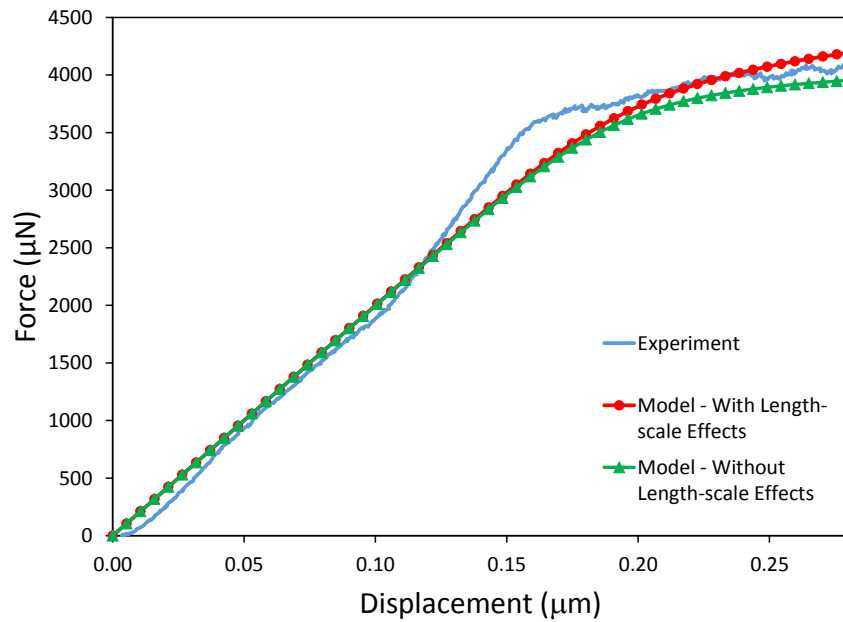


Figure 6.4. Comparison of experimental and CPFE calculated (with and without length-scale effects) force-displacement response.

6.4 Alpha-Beta Colony Study

Jun et al. [8] observed that the stress-strain behaviour of nine micropillar specimens varied significantly with respect to β -phase morphology. This experimental work suggests the need to isolate key microstructural features to gain a better understanding of the behaviour of α - β colonies. Computational modelling is attractive in this context, due to the difficulty associated with the experimental fabrication of test specimens for analysis of specific features in complicated microstructures.

This section presents a systematic study on the effects of α -phase ligament width and relative α -phase crystallographic orientation in order to further understand the deformation mechanisms in α - β colonies. Finite element unit cell models of α - β colonies are generated as discussed above. The β lath width is fixed at 0.5 μm in all analyses based on the observations of Jun et al. [8] for the as-received material. Three different α -phase ligament widths, 1 μm , 2 μm and 5 μm , are considered, as shown in Fig. 6.5.

The boundary conditions used in these compression simulations are shown in Fig. 6.6. All vertical faces of the model are unconstrained, to simulate the behaviour of a single colony under compression. A displacement is applied to the top face of the model, corresponding to 2.5% engineering strain at a strain rate of $1 \times 10^{-3} \text{ s}^{-1}$.

Fig. 6.7 shows the predicted effect of α -phase ligament width on the compressive stress-strain response, both with and without length-scale effects. The α -phase in this analysis is oriented so the primary slip direction is nearly-perpendicular to β laths as shown in Fig. 6.5c. As α -phase ligament width is reduced, a harder response is observed. This effect is attributed to the increasing number of β laths in the model microstructure, and thus, a greater volume fraction of β -phase, which is assumed to be elastic. Similarly, length-scale effects increase as ligament width decreases. The number of phase boundaries increases as ligament width decreases, resulting in a larger

proportion of the model with high strain-gradients, and therefore, increased GND hardening, as shown by the contour plots of GND density in Fig. 6.8.

In order to investigate the effect of α -phase crystallographic orientation with respect to β laths, three different α -phase orientations, as shown in Fig. 6.9, are analysed as follows: (a) primary slip direction near-perpendicular to β laths, (b) primary slip direction near-parallel to β laths, and (c) crystal c -axis parallel to loading direction. For cases (a) and (b) primary slip planes are shown with a red hatching in Fig. 6.9. Where the crystal c -axis is parallel to the loading direction, as in case (c), there are no easily activated slip systems. The unit cell model in Fig. 6.5b is implemented here in each case, applying the same boundary conditions as in Fig. 6.6. Fig. 6.10 shows the compressive stress-strain response for Cases (a) and (b). A clear difference in the elastic response of each case can be seen due to the transverse anisotropic elastic behaviour of the crystal. However, Case (a) also displays a slightly higher amount hardening and an increase length-scale effect due to GNDs. Considering first the mechanistic basis of crystal slip in α - β colonies, crystallographic slip is anticipated to be inhibited by the β laths, which act as barriers for mobile dislocations on the primary adjacent slip system. Within the crystal plasticity framework, slip transfer by dislocation transit is not explicitly captured, but is so indirectly through strain compatibility requirements. The primary slip direction in Case (b) is near-parallel to β laths, and thus, there is no barrier for mobile dislocations, leading to a significantly softer response. This is shown schematically in Fig. 6.11. Length-scale effects are more significant in Case (a) due to a higher GND density at phase α - β interfaces. It should be noted that the Schmid factors on the primary slip systems are equal.

Fig. 6.12 shows a comparison of the unit cell compressive stress-strain response for all three α -phase orientation cases, for which all $\langle a \rangle$ - and $\langle c+a \rangle$ - type slip systems are included and may potentially be activated. In case (c), where the crystal c -axis is oriented parallel to the loading direction, $\langle a \rangle$ type slip systems are difficult to activate, resulting in a significantly harder response. $\langle c+a \rangle$ type pyramidal slip systems become active at a larger macroscopic strain than the other cases.

This effect of relative α -phase orientation presented here was also observed in previous experimental work of [9], [22]. Suri et al. [22] investigated the stress-strain and creep behaviour of two individual colony samples. The α -phase of the samples was oriented for (a) $\langle a \rangle$ type slip near-parallel to the β laths and (b) $\langle a \rangle$ type slip oriented near-normal to the β laths. The latter, type (b), showed a higher macroscopic yield stress and increased hardening, attributed to the presence of misfit dislocations at α - β interfaces and relatively larger misalignment of primary slip systems between phases. Fig. 6.13 shows the stress-strain response of these two colonies extracted from Suri et al. [22]. The predicted results of Fig. 6.10 are clearly consistent with the measured responses of Fig. 6.13. For example, at a strain of 2.5%, the harder colony is shown to carry a 15% and 12% higher stress than the softer colony in Figs. 6.10 and 6.13, respectively.

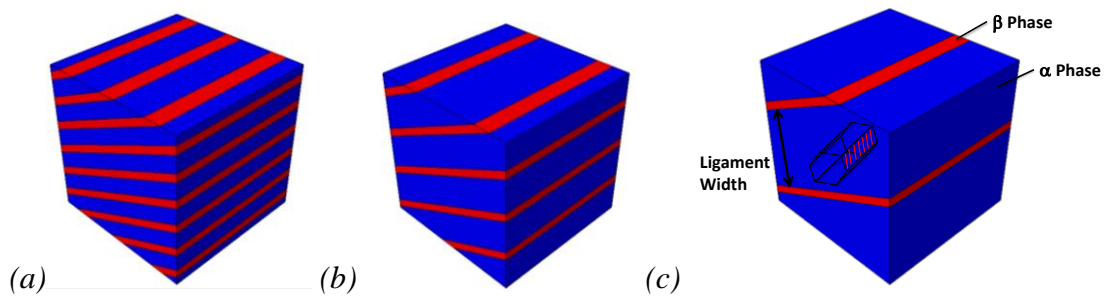


Figure 6.5. Idealised α - β colony model geometry for three α -phase ligament widths: (a) 1 μm (b) 2 μm (c) 5 μm showing the α -phase crystallographic orientation. α -phase primary slip systems are hatched in red

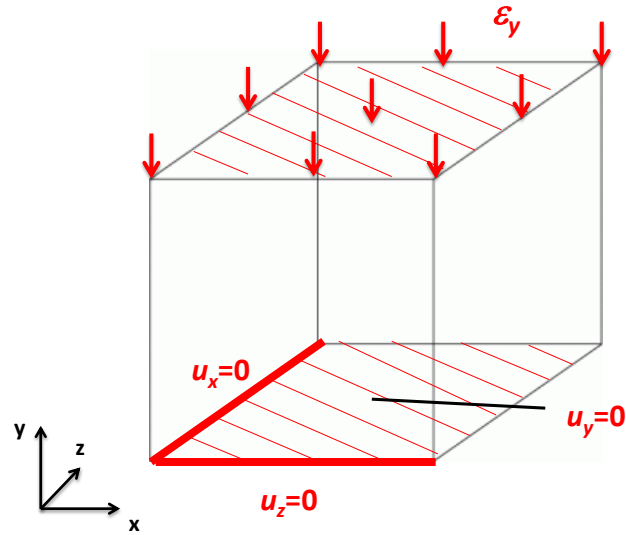


Figure 6.6. Boundary conditions used for compression simulations of α - β colony unit cell models.

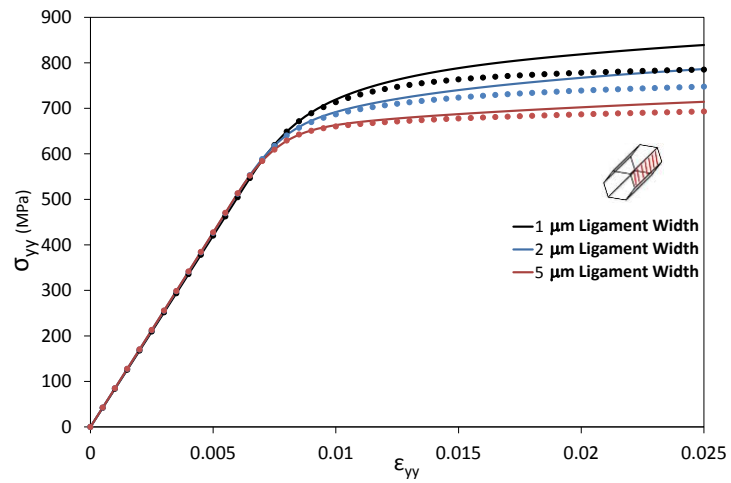


Figure 6.7. Global stress strain curves for α - β colony models. Dotted lines represent the exclusion of length-scale effects in analysis.

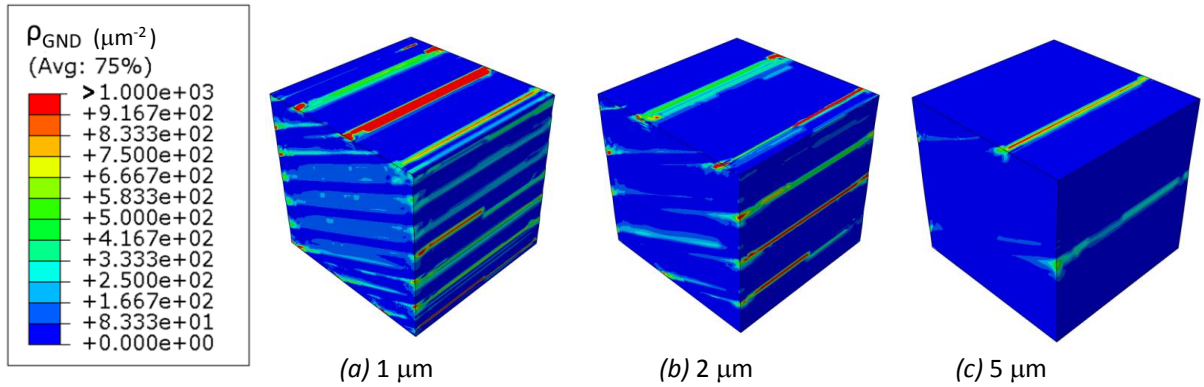


Figure 6.8. Contour plots of GND density for the 3 different ligament widths considered. A larger region of high GND density is predicted as α -phase ligament width is reduced from 5 μm to 1 μm due to the increased number of phase boundaries.

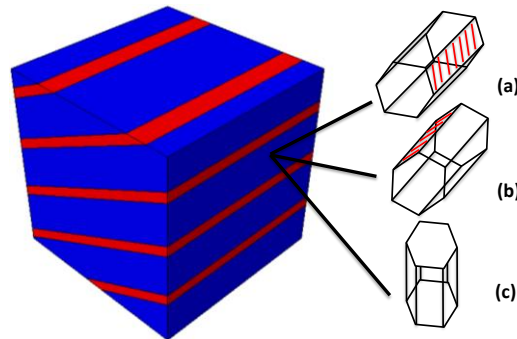


Figure 6.9. The three α -phase orientations considered (a) primary slip direction near-perpendicular to β lath (b) primary slip direction near-parallel to β lath and (c) c-axis parallel to loading direction

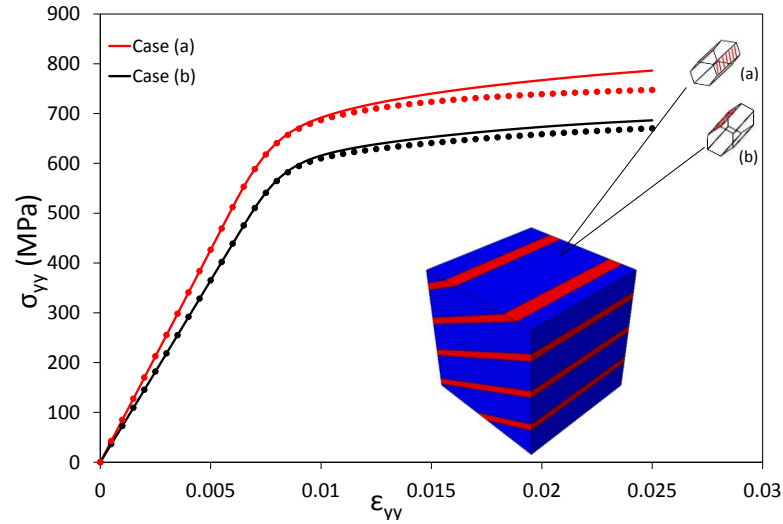


Figure 6.10. Unit cell compressive stress strain response for α -phase orientation cases (a) and (b). Ligament width = 2 μm . Dotted lines represent the exclusion of length-scale effects.

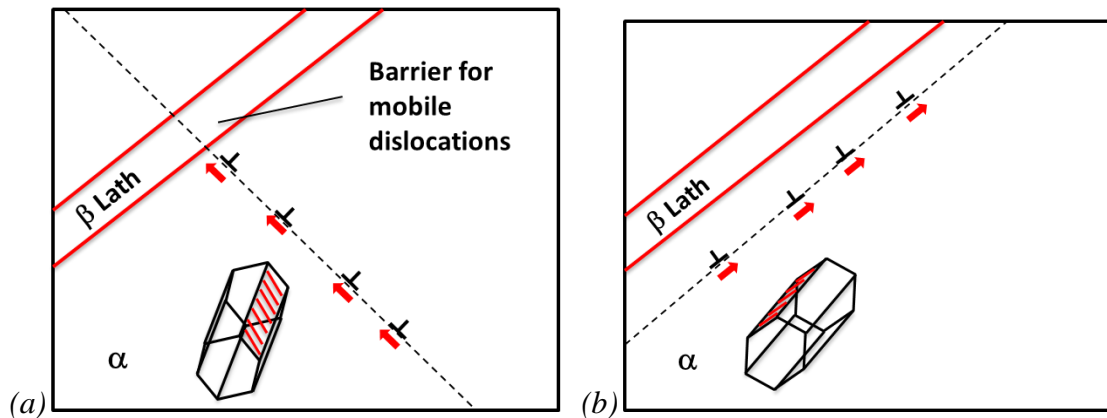


Figure 6.11. A schematic diagram of (a) β laths acting as barriers for mobile dislocations where the primary slip direction is aligned near-perpendicular to the laths and (b) the unrestricted flow of dislocations where the primary slip direction is aligned near-parallel to the laths.

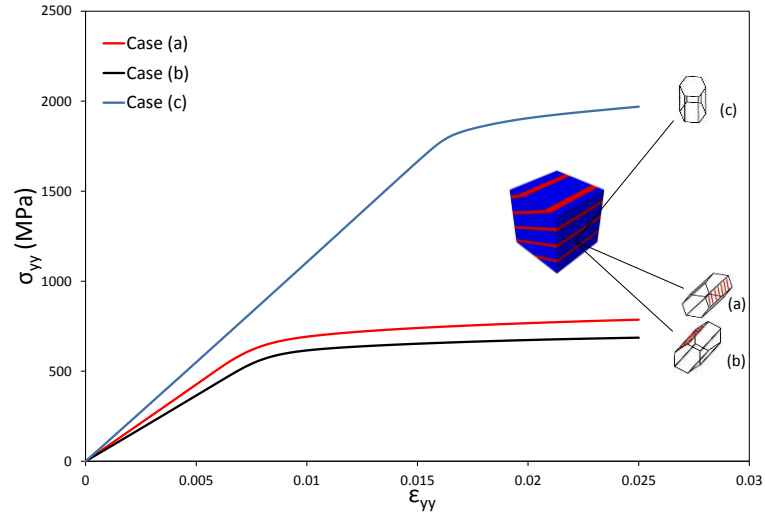


Figure 6.12. Unit cell compressive stress strain response for all three α -phase orientation cases. Ligament width = 2 μm .

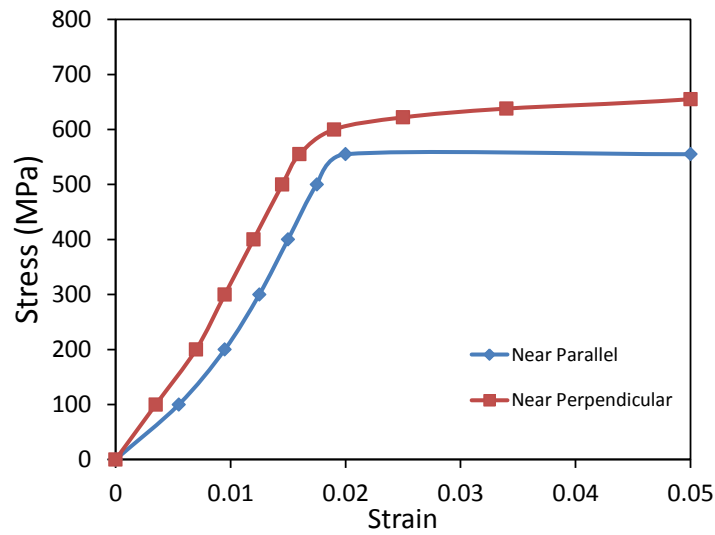


Figure 6.13. Experimental data extracted from Suri et al. [34].

6.5 Application to Cold Dwell Fatigue

6.5.1 Methodology

In this section, a polycrystal model of Ti-6242 is developed to assess the effect of α - β colonies on the key variables that control cold-dwell fatigue. As mentioned above, the presence of a rogue grain combination is an important factor for faceting, where an unfavourably oriented ‘hard’ grain lies adjacent to a favourably orientated ‘soft’ grain with respect to crystallographic slip. A load-holding dwell period causes a redistribution of stress from soft to hard grains, due to cold creep occurring in soft grains, leading to local stress relaxation. The hard grains must therefore carry a higher stress to maintain the applied load. Dunne and Rugg [14] argue that the stress component normal to the basal plane, in the hard grain, is important in faceting; a critical stress approach was adopted to identify the facet initiation near soft-hard grain boundaries, consistent with experimental observations [23].

‘Macro-zones’ are also argued to be important in dwell fatigue in titanium alloys [24]. Also referred to as micro-textured regions (MTRs), these are relatively large regions (up to mm length scales) of uniform α crystallographic orientation often containing colonies of β laths. A macro-zone, which is badly oriented for slip adjacent to a softer unit well-oriented for slip, provides the potential for load shedding from soft to hard grains during dwell and for the formation of a large basal facet across the entire α unit. This has been argued to be of particular significance in dwell fatigue and in driving the ‘dwell debit’ [25], [26], [27].

Previous work has assessed several key factors in dwell, including microstructure morphology [3], temperature [28] and material hydrogen content [29]. In relation to the α - β phase, Venkataramani et al. [30] implemented a CPFE model, with a homogenised α - β phase [7], to study the effect of various microstructural features on creep-induced load shedding in Ti-6242. The key aspect investigated here, which has not previously

been studied, is β lath location and relative orientation with respect to a particularly unfavourable combination of α -phase grains, or rogue grain combination.

A three-dimensional polycrystal model is generated with hexagonal-shaped grains. The grain size is taken to be 10 μm , giving a fine-grained representation of this material [27]. Fig. 6.14 shows (a) the geometry of the model meshed with 20-noded reduced integration elements and (b) a graphical representation of the rogue grain combination considered here, where a central hard grain is oriented so that the crystal c-axis lies parallel to the loading direction and two soft grains, favourably oriented for prismatic slip. All other grains in the model are assigned random ‘soft’ orientations. The bottom face of the polycrystal is fixed in the y-direction, the left face is fixed in the x-direction, and the back face is fixed in the z-direction. Stress holding, which is considered to be more detrimental than strain holding in dwell fatigue [14], is analysed here, by applying a stress to the top face of the model according to the loading history in Fig. 6.15. A dwell period of 24 seconds is chosen to allow a significant transfer of stress from soft grains to hard grains. The applied stress of 660 MPa ensures local slip at grain boundaries and the development of GNDs but is well below conventional macroscale yield.

Four different microstructures are considered here, as shown in Fig. 6.16, as follows:

- | | |
|-----------|--|
| Base Case | α grains only. |
| β 1 | β laths located in a soft grain (forming a colony) and oriented near-parallel to α -phase primary slip direction. |
| β 2 | β laths located in a soft grain and oriented near-perpendicular to α -phase primary slip direction. |
| β 3 | β laths located in the central hard grain. |

The path (labelled Path 1) shown in Fig. 6.16a is chosen for sample distributions of stress, to demonstrate the load shedding process during the dwell period. The α -phase crystallographic orientations of each grain are identical for all microstructures

considered. A mesh sensitivity has once again been carried out to ensure mesh independence of predicted responses (Appendix D).

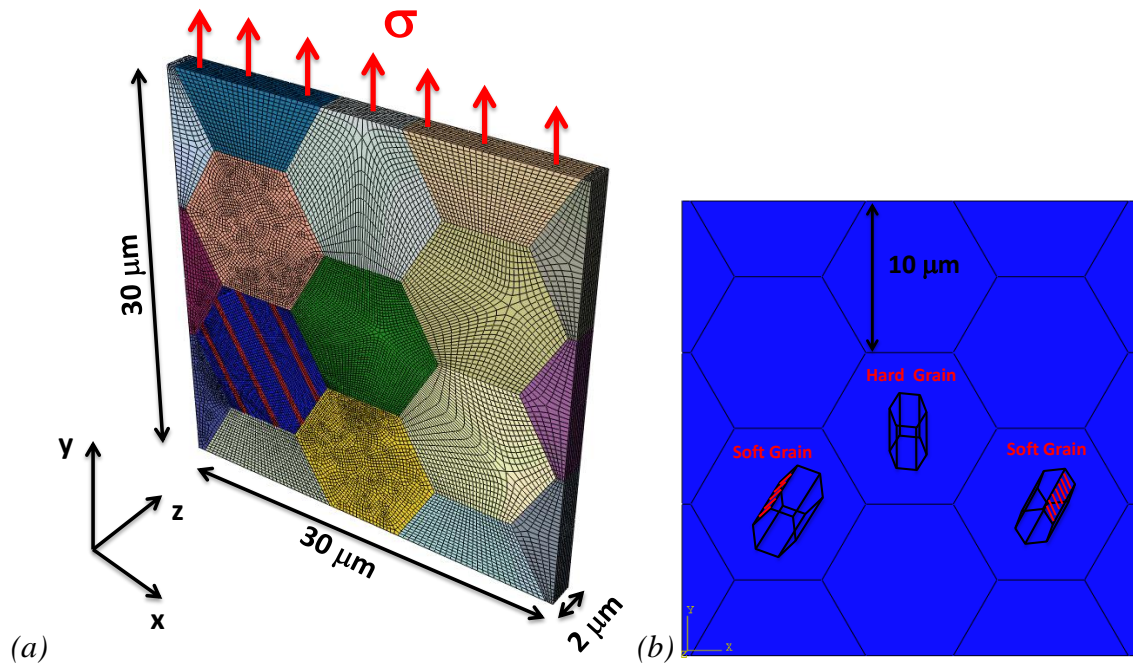


Figure 6.14. Finite element model showing (a) assumed specimen geometry with element mesh and (b) the rogue grain combination. Easily activated slip systems are hatched in red.

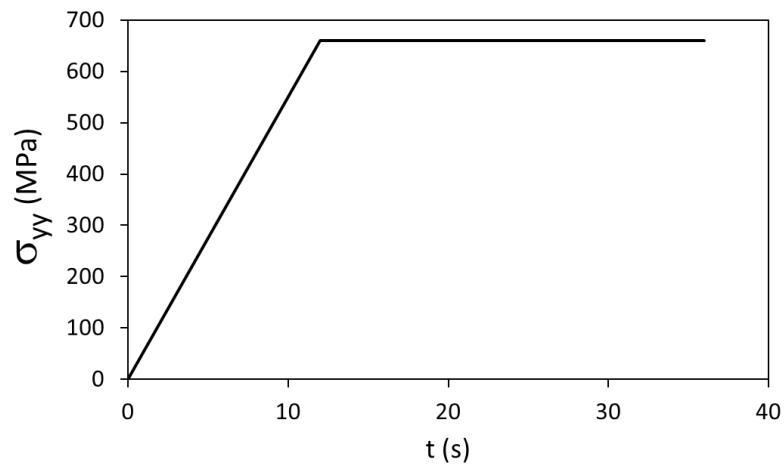


Figure 6.15. Loading history showing a dwell period of 24 seconds.

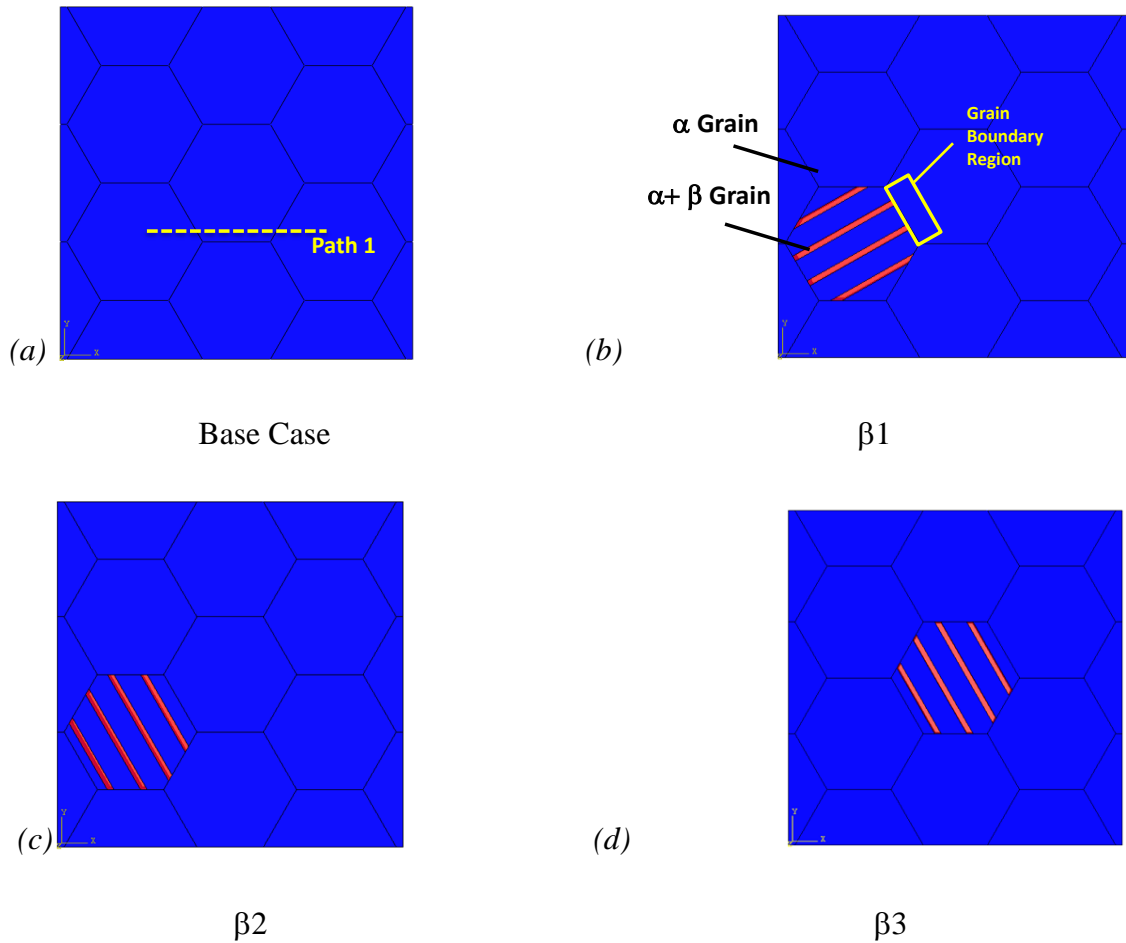


Figure 6.16. (a) Pure α -phase base case (b) β laths near-parallel to α -phase primary slip direction in soft grain (c) β laths near-perpendicular to primary slip direction in soft grain (d) β laths in hard grain.

6.5.2 Results and Discussion

In order to demonstrate the significance of the dwell period, the pre- and post-dwell σ_{yy} stress distributions are plotted in Fig. 6.17 along Path 1 for the base case (pure α -phase). As seen in previous modelling work [14], the dwell period causes a significant redistribution of stress from soft grains to hard grains, leading to large post-dwell discontinuities at soft-hard grain boundaries. The evolution of peak grain boundary stress on Path 1 is plotted in Fig. 6.18. After initial static loading, which results in a grain boundary stress of approximately 800 MPa, a steady increase in stress is observed

during the load holding period due to the occurrence of creep in the soft grains, and thus stress redistribution from the soft to the hard grains.

In order to assess the effect of the β -phase, it is necessary to analyse the effect on stresses over a more extensive region of the hard grain, adjacent to the grain boundary. Hence, the stresses are sampled from the entire rectangular region highlighted in Fig. 6.16b, to ascertain the effect of β -phase microstructure on creep dwell resistance for each of the microstructures analysed. The local maximum stress normal to the basal plane in the hard grain, has been identified as a key variable controlling facet nucleation [14]. It is therefore adopted here to quantify the effect of β laths on facet nucleation. The pre- and post-dwell value of this variable, termed σ_b^{max} here, is plotted for each microstructure in Fig. 6.19.

The pre-dwell σ_b^{max} is predicted to increase due to the presence of the β -phase, as shown in Fig. 6.19a. The $\beta 2$ microstructure shows the highest σ_b^{max} , giving a 10% increase, compared to the base case. However, for all microstructures considered, the presence of β laths reduces the post-dwell σ_b^{max} in the hard grain, as shown in Fig 6.19b. By considering the pre- and post-dwell histograms, it can be seen that the presence of the β -phase restricts load shedding from the soft grain to the hard grain, resulting in a lower predicted post-dwell σ_b^{max} . The most significant difference is seen in microstructure $\beta 3$, where σ_b^{max} is predicted to be 12% lower than the base case. This is attributed to the lower load-carrying ability of the hard grain compared to the other microstructures due to the presence of β laths. Overall, dwell fatigue resistance is predicted to increase with the inclusion of the β -phase.

This key result is consistent with previous work regarding the effect of the β -phase on dwell fatigue life in titanium alloys. Kassner et al. [12] showed experimentally the increase in dwell fatigue resistance with the increase in volume fraction of the β -phase. Previous CPFE modelling work of Venkatramani et al. [30], albeit using an homogenised α - β phase, also showed that increased β -phase volume fraction gave reduced load shedding..

The effect of excluding length-scale effects is investigated here for the pure α -phase base case microstructure.. Fig. 6.20a compares post-dwell stress distributions along Path 1, showing decreased grain boundary stresses with the exclusion of length-scale effects. σ_b^{max} is also predicted to decrease by 20% in the absence of GND density evolution. Higher stresses are predicted in the length-scale dependent model as a result of high GND density near grain boundaries, as shown in Fig. 6.20b, where the distribution of GND density is plotted along Path 1. Therefore, high strain gradients exist in the polycrystal model of Ti-6242, leading to significant GND hardening, which cannot be accounted for in a length-scale independent model.

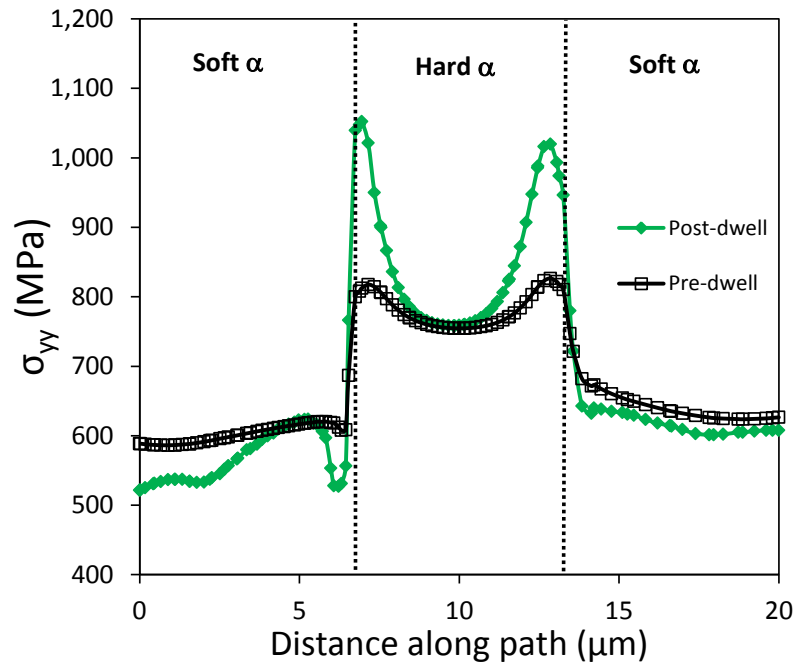


Figure 6.17. Pre- and post-dwell plots of σ_{yy} along path AA for the pure α -phase base case showing significant redistribution of stress from soft grains to hard grains.

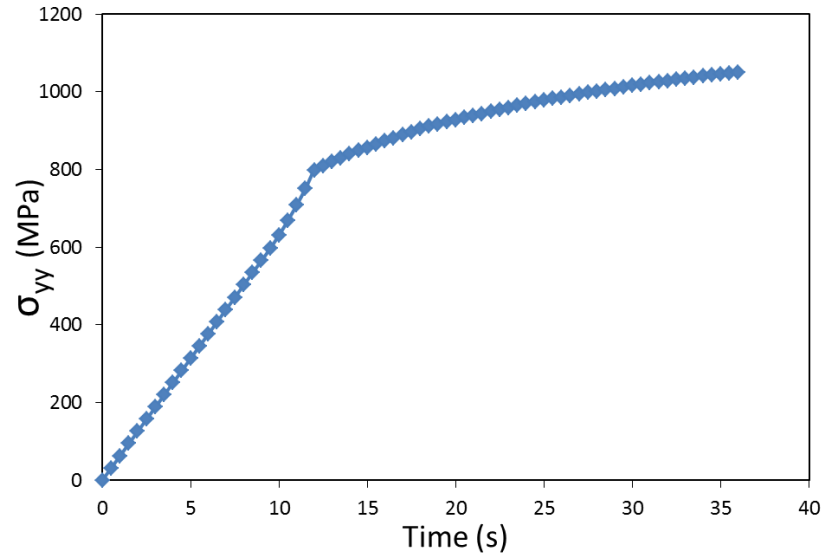


Figure 6.18. Evolution of peak grain boundary σ_{yy} from Fig. 6.17.

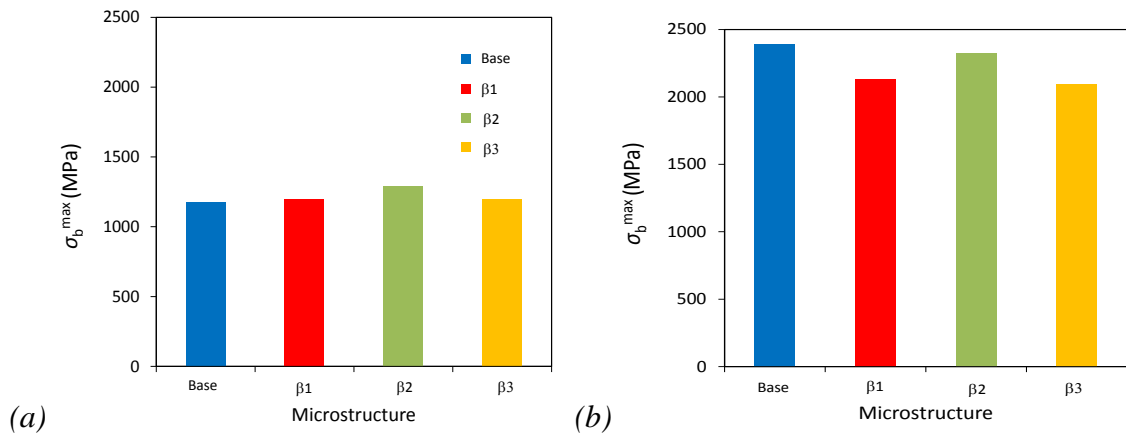


Figure 6.19. Histograms showing (a) pre- and (b) post-dwell σ_b^{\max} for each microstructure.

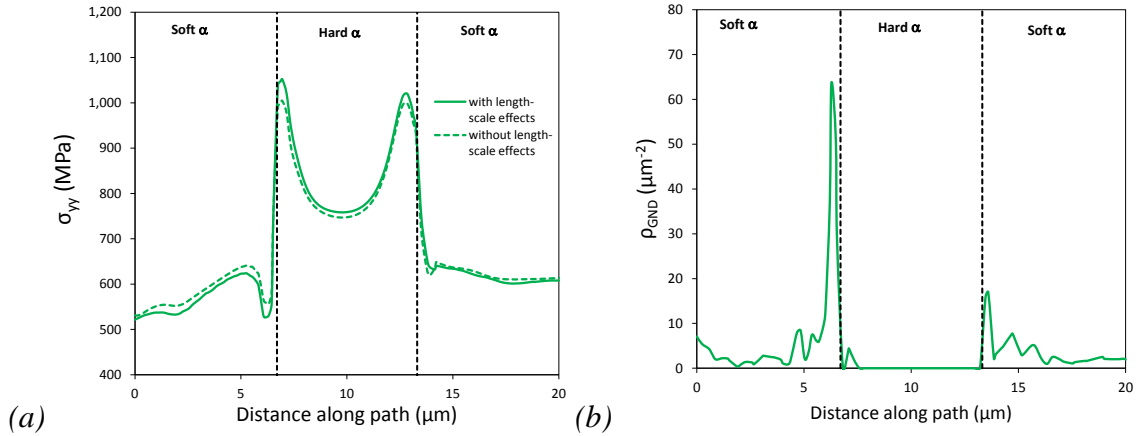


Figure 6.20. Post-dwell distributions along path AA showing (a) σ_{yy} with and without length-scale effects and (b) GND density.

6.6 Conclusions

A strain-gradient, crystal plasticity model is implemented for dual-phase titanium alloy, with explicit representation of β -phase laths, and the material model is calibrated against micro-pillar compression test data. A study of α - β colonies in Ti-6242 alloy has established increased strength as α -phase ligament width decreases, due to (i) increased β -phase volume fraction and (ii) increased GND hardening. The relative crystallographic orientation of the α -phase (with respect to β lath orientation) is found to play a key role in the stress-strain response of α - β colonies. Colonies with an α -phase primary slip direction oriented near-perpendicular to β laths show a significantly stronger stress-strain response than colonies oriented for slip near-parallel to β laths.

Analysis of a polycrystal model of Ti-6242 has shown that explicit incorporation of α - β colonies leads to restricted inter-granular load shedding during the dwell period in a fatigue cycle, resulting in lower local stresses. Dwell fatigue resistance is therefore predicted to increase due to the presence of the β -phase, consistent with previous publications.

It is shown that the very small size-scales associated with the β laths leads to important strain gradient hardening effects, which are incorporated in the present crystal plasticity

formulation via of the evolution of geometrically-necessary dislocations. It is shown that exclusion of these strain gradient effects causes a 20% under-prediction of the (critical) maximum post-dwell stress. It is therefore concluded that accurate and reliable physically-based prediction of cold dwell facet nucleation, and hence facet fatigue, requires incorporation of strain gradient effects.

The model developed and applied here, in collaboration with Prof. Fionn Dunne, for dual-phase Ti-6242 alloy, is subsequently further developed and applied in Chapter 7 for fretting crack nucleation of dual-phase ferritic-pearlitic steel for Flexible marine risers.

6.7 References

- [1] F. P. E. Dunne, D. Rugg, and A. Walker, “Lengthscale-dependent, elastically anisotropic, physically-based hcp crystal plasticity: Application to cold-dwell fatigue in Ti alloys,” *Int. J. Plast.*, vol. 23, no. 6, pp. 1061–1083, 2007.
- [2] M. A. Cuddihy, Z. Zheng, J. Gong, T. B. Britton, A. J. Wilkinson, and F. P. E. Dunne, “Grain size effects in hcp polycrystals : from GNDs to blocky alpha,” pp. 1–28.
- [3] F. P. E. Dunne, A. Walker, and D. Rugg, “A systematic study of hcp crystal orientation and morphology effects in polycrystal deformation and fatigue,” *Proc. R. Soc. A Math. Phys. Eng. Sci.*, vol. 463, no. 2082, pp. 1467–1489, 2007.
- [4] M. Zhang, J. Zhang, and D. L. McDowell, “Microstructure-based crystal plasticity modeling of cyclic deformation of Ti-6Al-4V,” *Int. J. Plast.*, vol. 23, no. 8, pp. 1328–1348, 2007.
- [5] O. J. McCarthy, J. P. McGarry, and S. B. Leen, “Micro-mechanical modelling of fretting fatigue crack initiation and wear in Ti-6Al-4V,” *Int. J. Fatigue*, vol. 62, pp. 180–193, 2013.
- [6] J. R. Mayeur and D. L. McDowell, “A three-dimensional crystal plasticity model for duplex Ti-6Al-4V,” *Int. J. Plast.*, vol. 23, no. 9, pp. 1457–1485, 2007.

-
- [7] G. Venkatramani, S. Ghosh, and M. Mills, “A size-dependent crystal plasticity finite-element model for creep and load shedding in polycrystalline titanium alloys,” *Acta Mater.*, vol. 55, no. 11, pp. 3971–3986, 2007.
- [8] T.-S. Jun, G. Sernicola, F. P. E. Dunne, and T. B. Britton, “Local deformation mechanisms of two-phase Ti alloy,” *Mater. Sci. Eng. A*, vol. 649, pp. 39–47, 2016.
- [9] K. Chan, C. Wojcik, and D. Koss, “Deformation of an alloy with a lamellar microstructure: experimental behavior of individual widmanstatten colonies of an α - β titanium alloy,” *Metall. Trans. A*, vol. 12, no. November, pp. 1899–1907, 1981.
- [10] S. Gosh, M. Mills, S. Rokhlin, V. Sinha, W. Soboyejo, and J. Williams, “The Evaluation of Cold Dwell Fatigue in Ti-6242,” *FAA Rep.*, no. January, 2007.
- [11] M. R. Bache, “A review of dwell sensitive fatigue in titanium alloys: The role of microstructure, texture and operating conditions,” *Int. J. Fatigue*, vol. 25, no. 9–11, pp. 1079–1087, 2003.
- [12] M. E. Kassner, Y. Kosaka, and J. A. Hall, “Low-cycle dwell-time fatigue in Ti-6242,” *Metall. Mater. Trans. A*, vol. 30, no. September, pp. 2383–2389, 1999.
- [13] V. Hasija, S. Ghosh, M. J. Mills, and D. S. Joseph, “Deformation and creep modeling in polycrystalline Ti–6Al alloys,” *Acta Mater.*, vol. 51, no. 15, pp. 4533–4549, 2003.
- [14] F. P. E. Dunne and D. Rugg, “On the mechanisms of fatigue facet nucleation in titanium alloys,” *Fatigue Fract. Eng. Mater. Struct.*, vol. 31, no. 11, pp. 949–958, 2008.
- [15] D. Bhattacharyya, G. . Viswanathan, R. Denkenberger, D. Furrer, and H. L. Fraser, “The role of crystallographic and geometrical relationships between α and β phases in an α/β titanium alloy,” *Acta Mater.*, vol. 51, no. 16, pp. 4679–4691, 2003.
- [16] W. G. Burgers, “On the process of transition of the cubic-body-centered modification into the hexagonal-close-packed modification of zirconium,” *Physica*, no. 7–12, pp. 561–586, 1934.

-
- [17] J.-Y. Kim and S. I. Rokhlin, “Determination of elastic constants of generally anisotropic inclined lamellar structure using line-focus acoustic microscopy,” *J. Acoust. Soc. Am.*, vol. 126, no. 6, p. 2998, 2009.
- [18] Z. Zhang, T. S. Jun, T. B. Britton, and F. P. E. Dunne, “Intrinsic anisotropy of strain rate sensitivity in single crystal alpha titanium,” *Acta Mater.*, vol. 118, pp. 317–330, 2016.
- [19] J. Gong and A. J. Wilkinson, “Anisotropy in the plastic flow properties of single-crystal α titanium determined from micro-cantilever beams,” *Acta Mater.*, vol. 57, no. 19, pp. 5693–5705, Nov. 2009.
- [20] T. Ben Britton, S. Biroasca, M. Preuss, and A. J. Wilkinson, “Electron backscatter diffraction study of dislocation content of a macrozone in hot-rolled Ti-6Al-4V alloy,” *Scr. Mater.*, vol. 62, no. 9, pp. 639–642, 2010.
- [21] T. Jun, D. E. J. Armstrong, and T. B. Britton, “A nanoindentation investigation of local strain rate sensitivity in dual-phase Ti alloys,” *J. Alloys Compd.*, vol. 672, pp. 282–291, 2016.
- [22] S. Suri, G. B. Viswanathan, T. Neeraj, D.-H. Hou, and M. J. Mills, “Room temperature deformation and mechanisms of slip transmission in oriented single-colony crystals of an α/β titanium alloy,” *Acta Mater.*, vol. 47, no. 3, pp. 1019–1034, 1999.
- [23] V. Sinha, J. E. Spowart, M. J. Mills, and J. C. Williams, “Observations on the faceted initiation site in the dwell-fatigue tested ti-6242 alloy: Crystallographic orientation and size effects,” *Metall. Mater. Trans. A*, vol. 37, no. 5, pp. 1507–1518, 2006.
- [24] D. Rugg, M. Dixon, and F. P. E. Dunne, “Effective structural unit size in titanium alloys,” *J. Strain Anal. Eng. Des.*, vol. 42, no. 4, pp. 269–279, 2007.
- [25] K. Zhang, K. V. Yang, A. Huang, X. Wu, and C. H. J. Davies, “Fatigue crack initiation in as forged Ti-6Al-4V bars with macrozones present,” *Int. J. Fatigue*, vol. 80, pp. 288–297, 2015.

-
- [26] N. Gey, P. Bocher, E. Uta, L. Germain, and M. Humbert, “Texture and microtexture variations in a near- α titanium forged disk of bimodal microstructure,” *Acta Mater.*, vol. 60, no. 6–7, pp. 2647–2655, 2012.
- [27] F. Bridier, P. Villechaise, and J. Mendez, “Slip and fatigue crack formation processes in an α/β titanium alloy in relation to crystallographic texture on different scales,” *Acta Mater.*, vol. 56, no. 15, pp. 3951–3962, 2008.
- [28] Z. Zhang, M. A. Cuddihy, and F. P. E. Dunne, “On rate-dependent polycrystal deformation: the temperature sensitivity of cold dwell fatigue,” *Proc. R. Soc. A Math. Phys. Eng. Sci.*, vol. 471, no. 2181, p. 20150214, 2015.
- [29] M. Gerland, P. Lefranc, V. Doquet, and C. Sarrazin-Baudoux, “Deformation and damage mechanisms in an α/β 6242 Ti alloy in fatigue, dwell-fatigue and creep at room temperature. Influence of internal hydrogen,” *Mater. Sci. Eng. A*, vol. 507, no. 1–2, pp. 132–143, 2009.
- [30] G. Venkataramani, K. Kirane, and S. Ghosh, “Microstructural parameters affecting creep induced load shedding in Ti-6242 by a size dependent crystal plasticity FE model,” *Int. J. Plast.*, vol. 24, no. 3, pp. 428–454, 2008.

7 A Strain Gradient, Crystal Plasticity Model for Microstructure-Sensitive Fretting Crack Initiation in Ferritic-Pearlitic Steel for Flexible Marine Risers

7.1 Introduction

The previous chapter has highlighted the importance of including length-scale effects in micromechanical modelling. These techniques are now applied to crack nucleation in fretting situation. As mentioned in Chapter 2, the steep stress gradients in fretting contacts suggest that strain-gradient induced GND hardening plays a key role in localised stresses and strains, and ultimately, fretting crack initiation.

In this work, the microstructure of a ferritic-pearlitic steel is characterised to facilitate the generation of representative finite element microstructure geometries. Crystal plasticity material parameters are identified by calibrating a unit cell microstructure model against measured experimental data. An isotropic crystallographic slip and an anisotropic combined crystallographic slip and stress parameter are investigated for prediction of number of cycles to crack initiation and validated against low cycle fatigue test data. A microstructure-sensitive fretting model is developed to study crack initiation in fretting, with particular focus on length-scale effects. The predicted location and initial growth path of fretting cracks is investigated and compared to available experimental data and commonly used continuum based approaches. The effects of length-scale due to plastic strain-gradients are assessed by comparing the fatigue performance of two fretting models with different characteristic lengths, but otherwise nominally-identical mechanical and material characteristics, viz. the same fretting stress distributions and same contact semi-width to grain size ratios. Finally, the effect of crystallographic texture is investigated.

7.2 Modelling Methodology and Calibration

The physically based material model described in Chapter 4 is implemented to simulate the micromechanical behaviour of this material. This model is the same as that implemented in Chapter 6, with the addition of a backstress term in the slip rule in order to capture the significant kinematic hardening of the material, as described in Chapter 3. The lamellar spacing of the pearlite phase is too small ($< 1\mu\text{m}$) to model geometrically, specifically with respect to the finite element mesh density required and computational overhead. As a result, the pearlite grains are homogenised and a ratio of critical resolved shear stresses is used here to distinguish between ferrite and pearlite. Ishikawa et al [37] showed experimentally that the yield strength of pure ferrite is approximately 70% that of pure pearlite. Therefore, this ratio of 0.7 is assumed here between the critical resolved shear stress τ_0 for the two phases. Although this is a relatively simple approach for modelling the pearlite phase, the ferrite phase is of most interest here, as fatigue cracks have been shown to initiate in this softer phase under fatigue loading. For example, Kucharczyk et al. [38] conducted a series of four-point bend fatigue tests on a similar material and showed that cracks always initiate in the ferrite grains.

Armstrong-Frederick type kinematic hardening is implemented to calculate the backstress x^α on a slip system α , which is related to slip rate $\dot{\gamma}^\alpha$:

$$\dot{x}^\alpha = C\dot{\gamma}^\alpha - Dx^\alpha|\dot{\gamma}^\alpha| \quad (7.1)$$

where C is the initial hardening modulus and D is the rate of decay. Although some authors have successfully implemented kinematic hardening formulations explicitly based on ρ_{GND} induced backstresses [1],[2], explicit modelling of the lamellar pearlite geometry would be required to fully capture this effect in this work. This is presently impractical for the polycrystal models considered here.

Ferrite has a body centre cubic (BCC) lattice structure with 48 possible slip systems. In this work, only the 12 $\langle 110 \rangle$ slip systems are modelled since it has been shown by Franciosi et al. [40] that these are the principal slip systems in BCC iron and similar

materials. This also helps to reduce computational complexity, and hence run-times, especially with the inclusion of length-scale effects for 3D fretting.

7.3 Generation of Microstructure Geometries

The methodology described in Chapter 4 is implemented here for generating representative unit cell microstructure finite element models for the dual-phase alloy using ABAQUS and the Python programming language based on the experimentally-measured microstructure statistics. The unit cell model, which consists of 56 grains, and is used for calibration of the material parameters, is shown in Fig. 7.1a. As stated in Chapter 3, the material contains 49% pearlite and 51% ferrite phases. These Volume fractions are incorporated in the FE model and illustrated in Fig. 7.1b. A comparison of experimentally determined and finite element grain volumes is shown in Fig. 7.2a. The microstructure is assumed to have no preferred crystallographic texture as the material has not undergone cold forming and microstructural analysis show relatively equiaxed grains. Therefore, each grain is assigned a random crystal orientation, as illustrated in the (110) pole figure given in Fig. 7.2b.

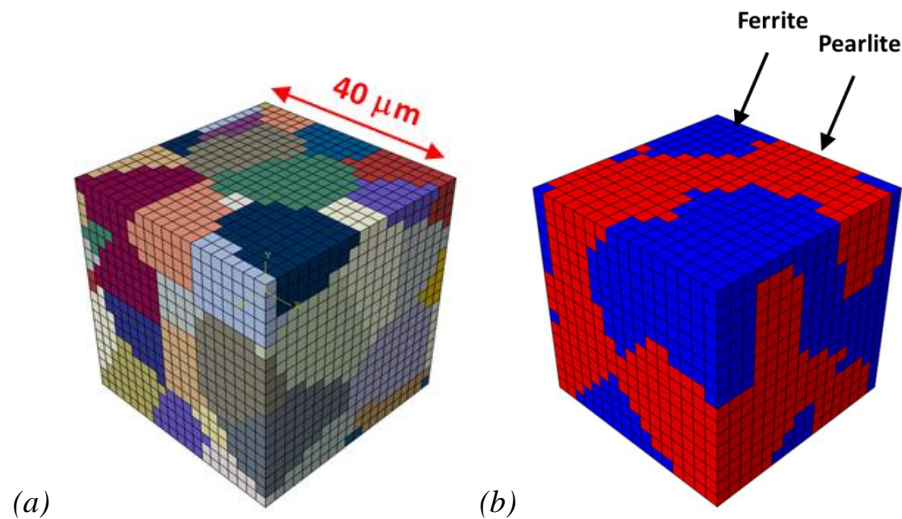


Figure 7.1. Unit cell microstructure model showing the (a) grains and (b) the ferrite (blue) and pearlite (red) phases.

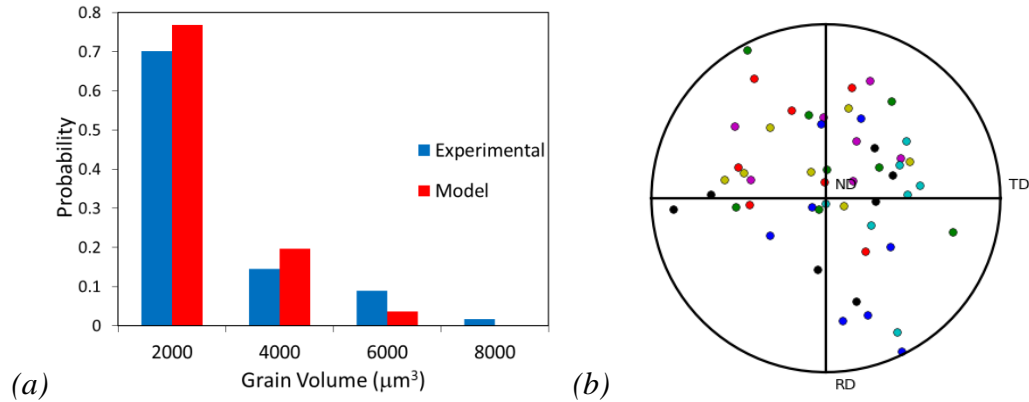


Figure 7.2. (a) Comparison of experimentally-determined and FE model grain volumes and (b) (110) pole figure showing randomly oriented grains.

7.4 Calibration of CP Material Parameters

Periodic boundary conditions are assigned to each free face of the microstructure model and a cyclic displacement is applied to simulate the microscopic deformation of a repeating unit cell in the material. A number of simulations are systematically run to calibrate the stabilised stress-strain response of the model by comparing with the experimental response, and hence, establish CPFE material parameters. The critical resolved shear stress τ_{c0}^{α} for ferrite and the kinematic hardening parameters C and D are the only parameters calibrated here. The remaining parameters b , T , and k are established physical quantities and ν , γ_0 , ρ_{SSD} and ΔH are adopted from previous published CPFE work on ferritic steel [3]. The identified material parameters for the calibrated constitutive model are given in Table 7.1. A comparison of sample final CPFE stabilised hysteresis loops with the experimentally measured loops is shown in Fig. 7.3. To ensure that the unit cell model is representative of the global response of the material, the cyclic stress-strain response is compared for three different microstructure realizations (with the same average grain size and phase volume fractions), as shown in Fig. 7.4. It can be seen that there is no significant change in response as the

microstructure is varied, and therefore, the size of the unit cell chosen is considered to be sufficiently large to represent the macroscopic deformation of the material.

Table 7.1. Identified parameters for CP material model.

Parameter	Value
$\tau_0^{pearlite}$	100 MPa
$\tau_0^{ferrite}$	70 MPa
M	0.3
G	81.15 GPa
b	$2.45 \times 10^{-4} \mu\text{m}$
k	$1.38 \times 10^{-23} \text{ J K}^{-1}$
T	293 K
ΔH	$2.605 \times 10^{-20} \text{ J}$
ν	$1.00 \times 10^{11} \text{ Hz}$
γ_0	1.0×10^{-3}
ρ_{SSD}	$0.01 \mu\text{m}^{-2}$
C	800 GPa
D	650

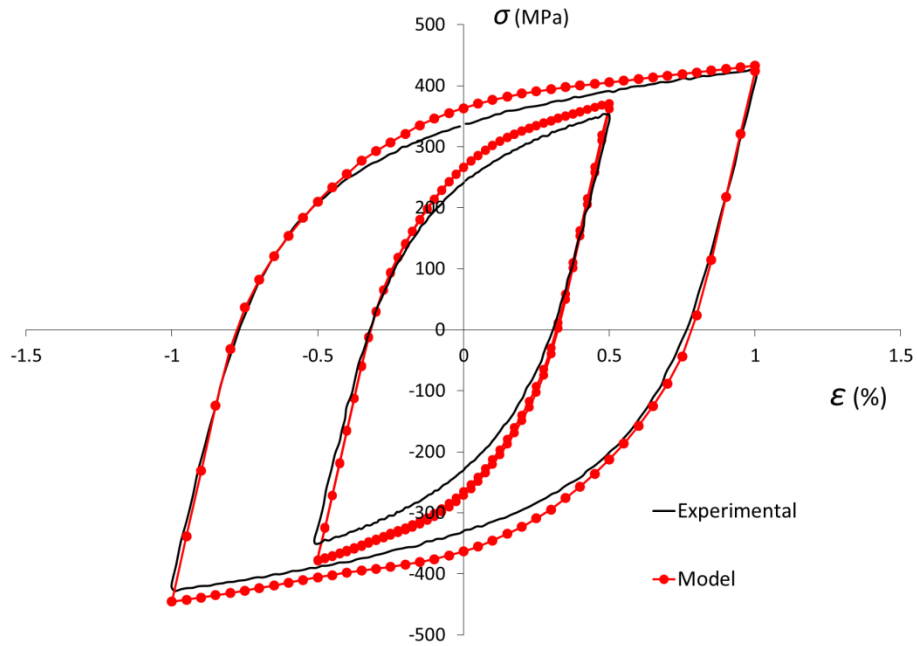


Figure 7.3. Comparison of experimentally measured and CPFE-predicted stabilised hysteresis loops.

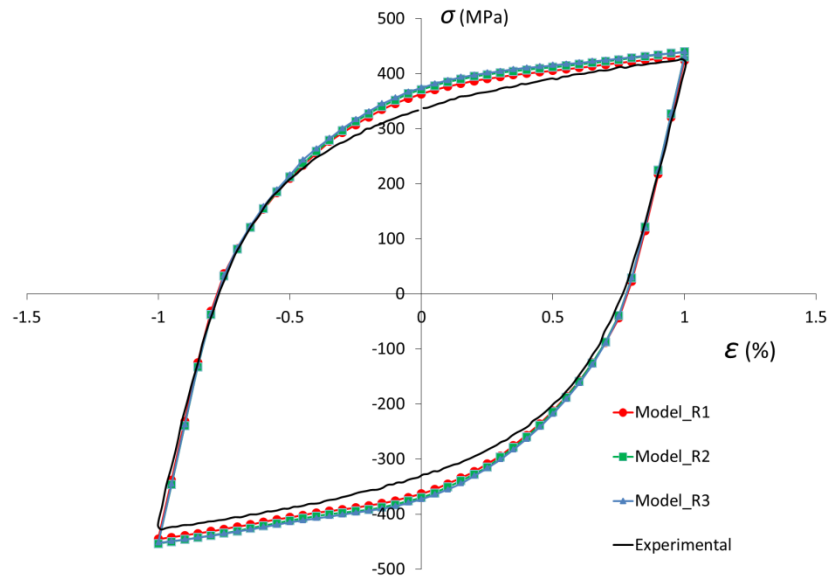


Figure 7.4. Comparison of CPFE-predicted unit cell response with measured (half-life) hysteresis response for three different microstructure realisations; this ensures insignificant statistical variability in response.

7.5 Strain-Gradient Length-Scale Effects

In order to demonstrate the ability of the model to capture length-scale effects due to the presence of plastic strain gradients in (plain) low-cycle fatigue, the cyclic stress-strain response of a 40 μm unit cell model is compared to that of a scaled-up 400 μm unit cell in Fig. 7.5 (not to scale). In this case the plastic strain gradients arise solely from the inhomogeneity (i.e the presence of grains) in the model. The smaller 40 μm model shows a 5% larger stress range for the same applied strain, resulting from higher GND densities. This effect is due to the absolute lengths over which the gradients in plastic strain exist, which are 10 times smaller in the 40 μm model, leading to more dislocations per unit volume [4], and thus, a higher GND density. Contour plots of GND density for both cases, after three strain cycles are given in Fig. 7.6, where significantly higher values can clearly be seen in the 40 μm model. The higher GND density causes increases hardening in the 40 mm unit cell, leading to the higher cyclic stress. The

responses of both models would be identical if the strain gradient formulation was omitted.

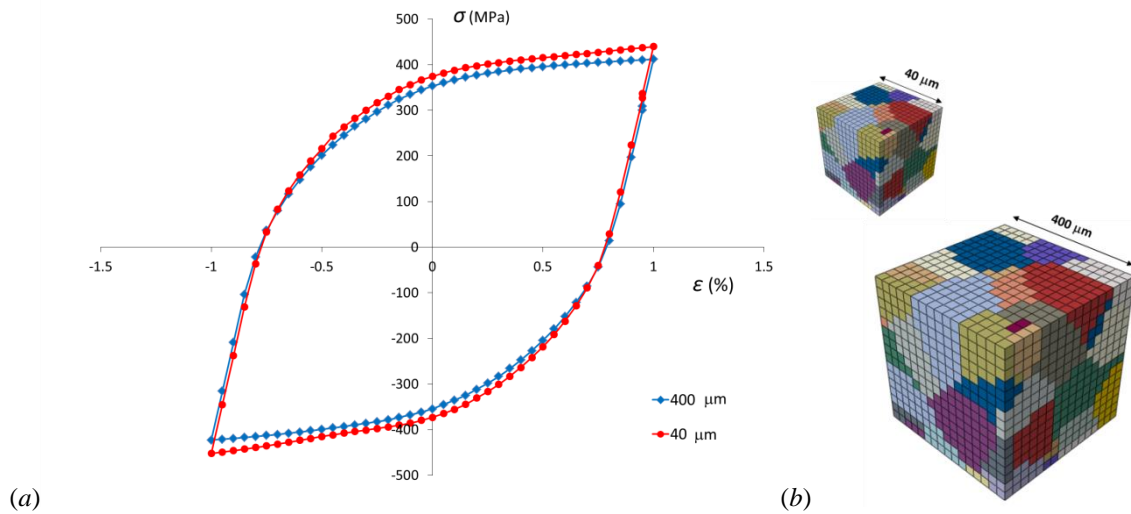


Figure 7.5. (a) Comparison of cyclic stress-strain hysteresis responses for (b) 40 μm unit cell and 400 μm unit cell microstructure model (Not to scale), thus demonstrating the length-scale effect for plain fatigue, due to inclusion of GND hardening within the strain gradient plasticity constitutive model.

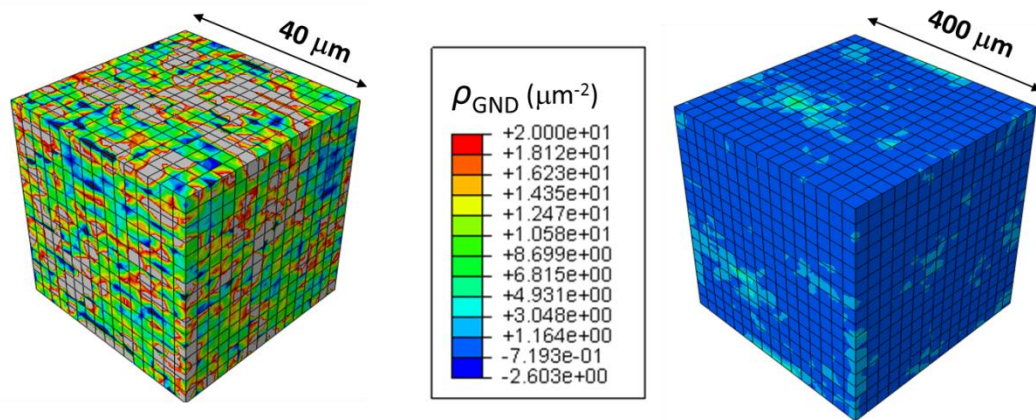


Figure 7.6. Contour plots of GND density for the 40 μm and 400 μm unit cell models after 3 cycles.

7.6 Fatigue Prediction Model

In this work, we adopt scale-consistent fatigue indicator parameters (FIPs) for use with the crystal plasticity modelling. These parameters adopt micro-scale quantities, such as crystallographic slip, to predict crack location and number of cycles to initiation.

Two such scale-consistent FIPs are implemented here: the first, is the accumulated crystallographic slip parameter, p , introduced in Chapter 4; the second is a Fatemi-Socie (FS) [5] type parameter which is based on a function of crystallographic slip and normal stress on corresponding crystallographic planes. The accumulated crystallographic slip parameter p has previously been shown to display distributions with patterns consistent persistent crystallographic slip bands [6], which are known crack initiation sites in fatigue, including ferrite-pearlite steels [7]. The number of cycles to crack initiation N_i for p is determined here using the following the power-law relationship based on the method of Cruzado et al. [8]:

$$N_i = \frac{p_{\text{crit}}}{(p_{\text{cyc}})^b} \quad (7.2)$$

where

$$p_{\text{cyc}} = p(t) - p(t - \Delta t_{\text{cyc}}). \quad (7.3)$$

Δt_{cyc} is the time taken to complete one fatigue cycle, p_{crit} is an identified critical value, and b is an exponent. This approach differs slightly from previous work using p (e.g. [4],[6]) where a linear relationship between p_{crit} and N_i was assumed. This power-law relation allows a more general fit to the data. This approach is considered to be necessary for this material as the strain to life (fig.7.8) behaviour does not follow the conventional log-linear Coffin-Manson behaviour. It is argued by Cruzado et al.[8] that this behaviour is due to increased FCI sensitivity to localised plasticity and microstructural features as the applied strain range is reduced.

The second FIP, based on the Fatemi-Socie macro-scale parameter [5], considers the contribution of normal stress and slip on each crystal plane, as shown schematically in Fig. 7.7. It has recently been implemented by Sharaf et al. [9] for predicting fatigue life of ferritic-pearlitic steel. An advantage of this parameter is the potential to predict initial

crack growth paths by identifying critical crystallographic planes on which cracks are predicted to initiate and initially propagate.

This parameter first considers the accumulation of slip and normal stress on each non-parallel slip plane i .

$$P_{fs_i} = \int_0^t \left(1 + k' \frac{\sigma_{n_i}}{\sigma_y}\right) \sum_{x=1}^N |\dot{\gamma}_i^x| dt \quad (7.4)$$

where x is the number of slip directions on a slip plane i . Here, only the 6 (110) slip planes are considered, and hence $x = 2$ and $i = 6$ (two slip systems on each plane). σ_{n_i} is the stress normal to the plane, σ_y is the macroscopic yield strength of the material, and k' is a constant which determines the contribution of normal stress to crack initiation (chosen here to be 0.5 [9]). The maximum value of P_{fs} is considered most likely to accommodate crack nucleation and therefore:

$$N_i = \frac{P_{fs_{crit}}}{(\max(P_{fs_{cyc}}))^b} \quad (7.5)$$

where $P_{fs_{crit}}$ and $P_{fs_{cyc}}$ are critical values and stabilised cyclic values, respectively. $P_{fs_{cyc}}$ is calculated as follows:

$$P_{fs_{cyc}} = P_{fs}(t) - P_{fs}(t - \Delta t_{cyc}). \quad (7.6)$$

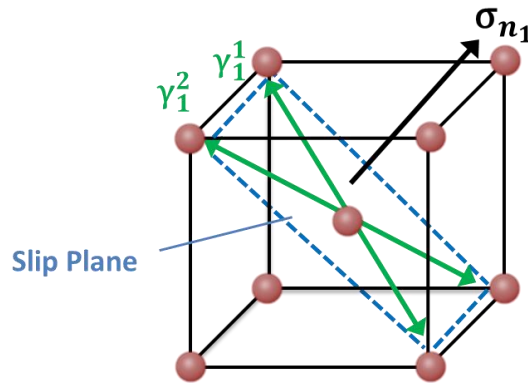


Figure 7.7. Schematic of BCC crystal indicating the slip and normal stress values used for the calculation of the P_{fs} parameter on a crystallographic plane.

The crack initiation stage is often considered to consume the majority of fatigue life, as discussed by a number of authors [10],[11]. In this work, the experimentally measured lives for the ferritic- pearlitic steel material are considered to correspond to number of cycles to crack initiation N_i , as described in Chapter 3. This allows the experimental data to be implemented for calibrating the fatigue prediction model. The unit cell model described previously is employed to identify critical FIP values FIP_{crit} and exponent b based on comparison against the corresponding measured strain-range data. Calibration is carried out for a single strain range, where a cyclic strain-controlled simulation is run until the maximum value of FIP_{cyc} has stabilised. The model is then fitted to the corresponding experimental data point to identify values of FIP_{crit} and b . Simulations are then run for the other strain ranges to validate FIP_{crit} and observe the quality of N_i prediction. A comparison of the experimentally measured and CPFE-predicted N_i values is shown in Fig. 7.8. Both FIPs show general agreement with the experimental data across all strain ranges. The identified values of FIP_{crit} and b for each parameter are given in Table 7.2.

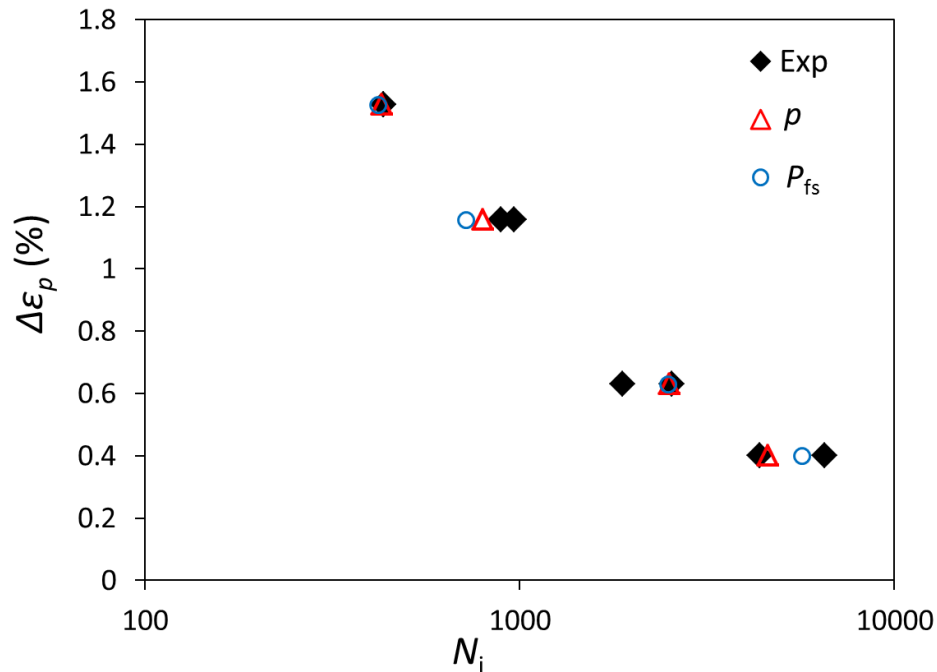


Figure 7.8. Comparison of CPFE predicted and experimentally observed numbers of cycles to crack initiation.

Table 7.2. Identified constants for fatigue prediction models.

FIP	FIP _{crit}	<i>b</i>
p	6	1.8
P_{fs}	20	1.4

7.7 Application to Fretting

7.7.1 Micromechanical Fretting Model

A 3D microstructure sensitive cylinder-on-flat fretting model is developed based on the work presented in Chapter 5. In order to reduce computational expense, only the contact region of the substrate is modelled using the calibrated CP constitutive model and representative ferrite-pearlite microstructure geometries. The surrounding regions are assigned a homogeneous isotropic elastic material model. Three distinct regions are created to allow for rapid mesh refinement. Tied surface constraints are utilised to connect these three separate ‘parts’ in the FE model, similar to the approach of Zhang et al. [12]. Coulomb friction is applied using the Lagrange multiplier technique and the assigned value appropriate to the material. The coefficient of friction of 0.6 is chosen based on the experimental fretting characterisation of O’Halloran [13], for pressure armour steel material. A 6 mm radius cylinder with an applied normal load P of 16 N/mm and tangential displacement Δ of $\pm 0.25 \mu\text{m}$ are chosen to simulate partial slip conditions. This results in a contact semi-width a of $34 \mu\text{m}$ and a peak contact pressure p_0 of approximately 310 MPa. A schematic of the model is given in Fig. 7.9, showing loading and boundary conditions. In addition to the boundary conditions in Fig. 7.9, all faces parallel to the X-Y plane are constrained in the Z direction to reduce edge effects.

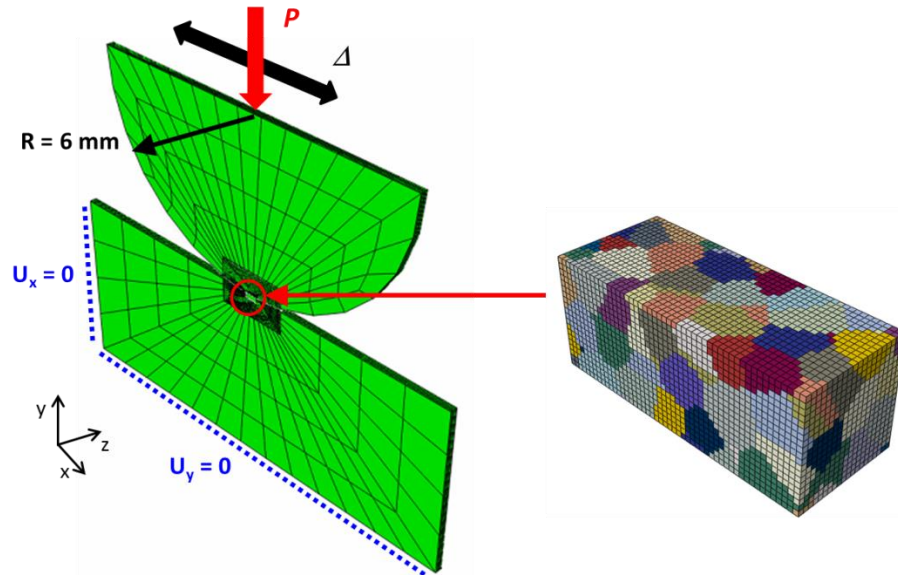


Figure 7.9. 3D fretting model ($R = 6 \text{ mm}$ case) showing key loading and boundary conditions and incorporation of ferritic-pearlitic steel microstructure in the contact region of the substrate.

The microstructure mesh consists of 20,000 twenty-noded, reduced integration brick elements with an average of 189 elements per grain. This is an extremely complex computational model due to the combination of three-dimensional frictional contact and strain gradient crystal plasticity constitutive model. As a result, it is not feasible to simulate a large numbers of fretting cycles. However previous CPFEM fretting work (see Chapter 5) has shown that plastic strain distributions and cyclic accumulation of crystallographic slip-based FIPs typically stabilize after only a few fretting cycles. The analysis is therefore run for five fretting cycles in order to investigate predicted crack location and number of cycles to crack initiation.

Figure 7.10 shows the CPFEM predicted distributions after one cycle compared with Hertz [14] and Cattaneo-Mindlin [46],[47] elastic solutions for contact pressure and shear traction distributions, respectively. Both solutions show general agreement, although a number of peaks and troughs can be seen for the CPFEM model resulting from the localised plasticity within the microstructure, as expected. The analytical solutions are based on the assumption of a homogeneous elastic material, and thus predict uniform distributions. It is worth noting that the fluctuations in contact pressure may also be a

result of the quadratic 20 noded elements employed for these simulations. The use of quadratic elements for contact problems can cause some issues in the calculation of contact forces on the mid-side nodes of the element.

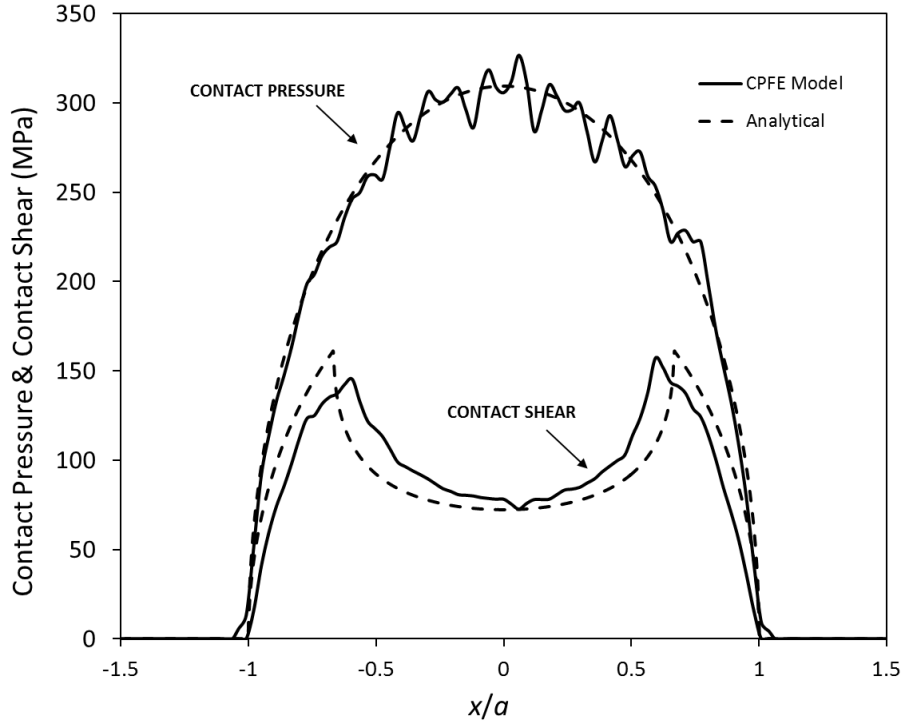


Figure 7.10. Comparison of CPFE-predicted and analytical distributions of contact pressure and shear traction across the contact.

7.7.2 FCI Location and Initial Orientation

Figure 7.11 shows the predicted distributions of p and P_{fs} after five fretting cycles, indicating the critical locations where crack initiation is predicted. As expected, crystallographic slip is concentrated in the micro-slip regions near the contact edges. The maximum FIP values are therefore predicted in these regions, as both parameters are based on the accumulation of crystallographic slip. These results are consistent with numerous experimental results available in the literature [15], [16], where fretting cracks have been found to occur within the slip zone. This is in contrast to previously-used

(continuum-based) FIPs, which consistently predict cracking at or just outside the contact edge (trailing edge), except where wear is explicitly modelled [16].

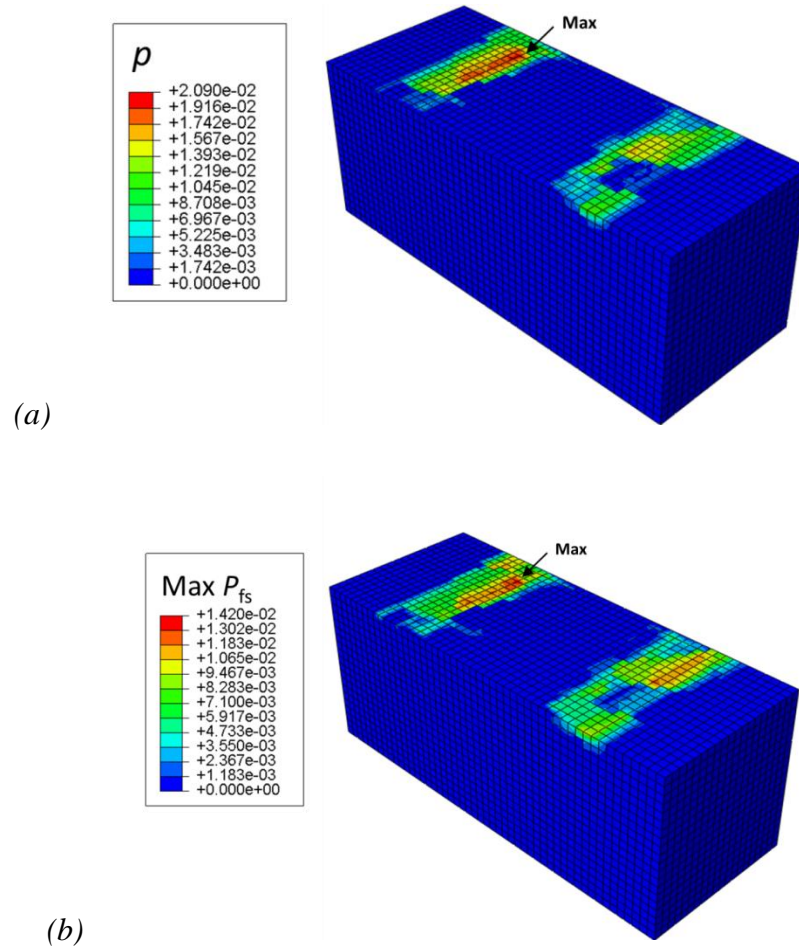


Figure 7.11. Contour plots of (a) p and (b) P_{fs} in the substrate contact region ($R = 6$ mm) of the model after 5 fretting cycles.

Figure 7.11b shows two clear regions where high values of P_{fs} accumulate, corresponding to specific instances of microstructurally ‘weak’ grains, with respect to crack initiation, in micro-slip zones. These grains are highlighted in the microstructure shown in Fig. 7.12a. The P_{fs} parameter identifies critical crystallographic planes. The initial cracking direction is assumed to follow the critical crystallographic plane in each

of these grains, that is, the crystallographic plane which accumulates the largest value of P_{fs} . These critical planes are highlighted in the BCC unit cell in Fig. 7.12b. Figure 7.12c illustrates the initial crack path based on this critical plane method, where one crack is predicted to grow at 52° to the surface towards the centre of contact and another is predicted to grow away from the contact at an angle of 84° . The 52° crack is considered to be dominated by crystallographic slip accumulation, and hence, grows at a shallow angle into the substrate. The normal stress contribution to P_{fs} is more significant for the 84° crack, as the critical plane is oriented near-perpendicular to the surface, and occurs closer to the edge of contact, where tangential stresses are more dominant. These results agree with a number of published observations regarding fretting fatigue crack location and initial orientation, e.g. [16],[17],[18]. The microstructure-based P_{fs} parameter is therefore a useful method for predicting crack initiation.

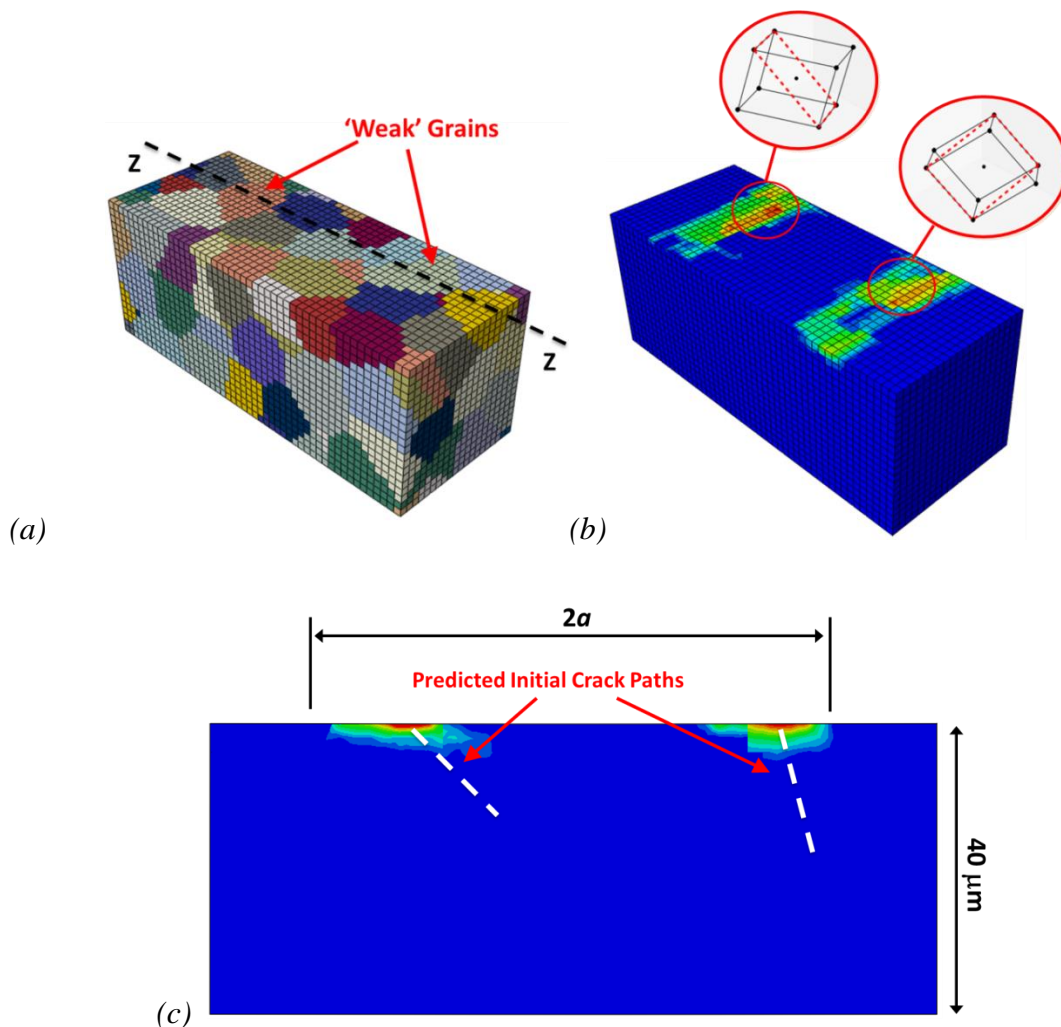


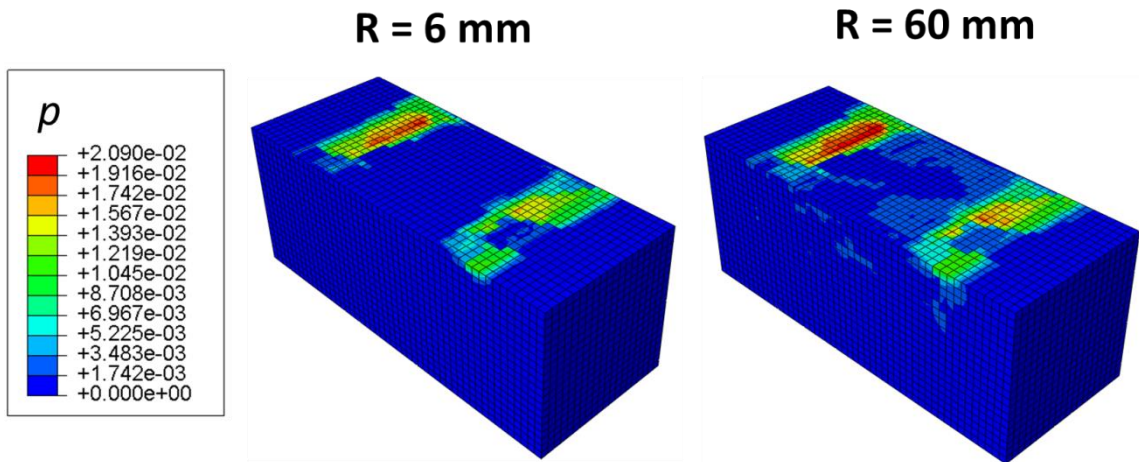
Figure 7.12. (a) The microstructure mesh, highlighting the two grains where cracking is most likely to occur, (b) the critical crystallographic plane of each grain, shown in dashed red lines and (c) a section view along the path ZZ, showing the predicted crack location and initial critical-plane (path) direction relative to the surface.

7.7.3 Strain Gradient Effects

A key novelty of the current work is the implementation of a strain-gradient, crystal plasticity model for calculating GND density in fretting. The model is therefore capable of capturing the effects of localised hardening due to the high gradients of plastic strain, which potentially arise at the contact edges. The significance of this effect is quantified here by comparing the previously described model with a larger, equivalent scaled-up model. The scaled-up model is ten times larger ($R = 60$ mm, average $d = 110$ μm , $a = 340$ μm) with the identical nominal contact stresses (peak contact pressure and shear traction), identical microstructure geometry (except for absolute length) and identical a/d ratio ($a/d = 3.1$), viz. contact to (average) grain size ratio. This excludes statistical (microstructure) effects, allowing isolation of the length-scale effects of strain gradient. In other words, the same distribution of plastic strains will occur, but over different length-scales, thus giving different strain gradients in otherwise identical fretting conditions.

Figure 7.13 shows the predicted distributions of p and GND density after five cycles for both length-scale models. It is clear that regions of concentrated (high) p are more localised in the smaller length-scale, $R = 6$ mm, model. This is due to the relatively higher GND density in the micro-slip region, as shown in Fig. 7.13b, due to the fact that the slip region covers a smaller absolute length scale but, with the same differential of plastic strain, it has a higher plastic strain gradient and hence higher GND density. The presence of these immobile GNDs results in slip system hardening, and thus, inhibits crystallographic slip. Conversely, the GND density in the micro-slip zones of the $R = 60$ mm model is negligible and insignificant GND hardening occurs. It is worth noting that when the strain gradient (GND) effects are omitted, both models show identical results e.g for p .

(a)



(b)

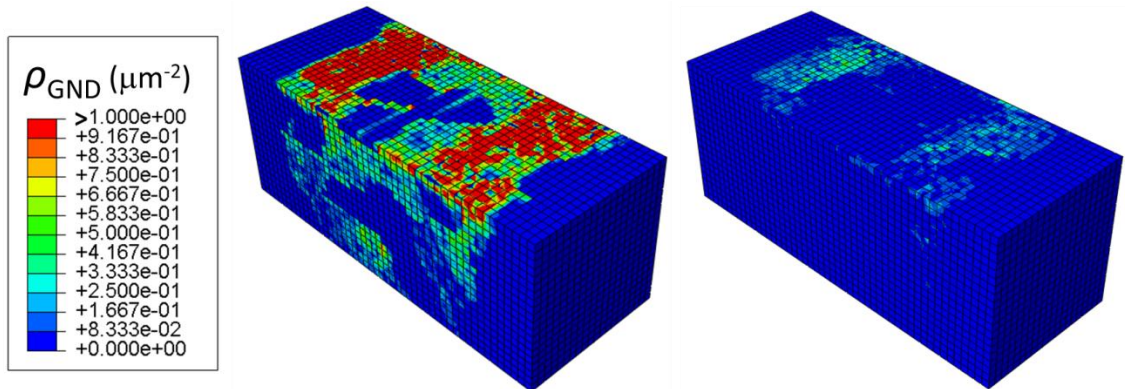


Figure 7.13. Contour plots of (a) accumulated plastic strain p and (b) GND density for a 6 mm cylinder radius model and a scaled-up 60 mm cylinder radius model.

In order to quantify this length-scale effect in fatigue, the cyclic accumulation of each FIP, p and P_{fs} is employed to predict number of cycles to crack initiation, following the methodology described in Section 7.6. Although the critical grain for crack initiation is the same for both models, the exact material point with maximum p and P_{fs} is different. This is a direct consequence of the strain gradient effects. Table 7.3 shows a comparison of the cyclic accumulation of p and P_{fs} , and corresponding predicted N_i values for the critical material point in each model over the first five fretting cycles. The predicted increase in N_i as the cylinder radius is reduced from 60 mm to 6 mm is also shown. It can be seen that the cyclic accumulation of each FIP is greater for the $R = 60$ mm model

after each cycle, with the exception of cycle 3. The most significant effect is seen after the first cycle. It is clear that the cyclic accumulation of p and P_{fs} has not yet stabilised after five cycles. If the average cyclic accumulation is considered, it can be seen that the scaled-up $R = 60$ mm model has a higher value of each FIP and lower life. Again, this is attributed to the presence of higher strain gradients in the smaller ($R = 6$ mm) model leading to higher densities of GNDs, which hinder accumulation of crystallographic slip, the primary variable for both FIPs. The considerably lower density of GNDs in the $R = 60$ mm geometry, as shown in Fig. 7.13b, results in more accumulated crystallographic slip, and therefore higher cyclic accumulation of p and P_{fs} .

Table 7.3. Cyclic accumulation of (a) p and (b) P_{fs} for $R = 6$ mm and $R = 60$ mm fretting models.

(a)

Cycle	p_{cyc}		N_i		$\frac{N_i^{6mm}}{N_i^{60mm}}$
	6 mm	60 mm	6 mm	60 mm	
1	0.0024	0.0034	304832	168058	1.81
2	0.0031	0.0039	194502	132271	1.47
3	0.0038	0.0036	138722	151931	0.91
4	0.0035	0.0041	158470	119691	1.32
5	0.0038	0.0039	134116	132958	1.01
Average	0.0033	0.0038	173038	139437	1.24

(b)

Cycle	P_{cyc}^{fs}		N_i		$\frac{N_i^{6mm}}{N_i^{60mm}}$
	6 mm	60 mm	6 mm	60 mm	
1	0.0016	0.0023	163,910	100,130	1.64
2	0.0021	0.0025	110,023	88,829	1.24
3	0.0028	0.0024	73,760	94,150	0.78
4	0.0023	0.0026	98,038	83,436	1.18
5	0.0027	0.0030	79,646	68,824	1.16
Average	0.0023	0.0025	98,065	85,858	1.14

The key aim of the present study was to isolate the effect of strain-gradients in fretting; by removing statistical size effects (see Chapter 5). This was achieved by maintaining a constant a/d ratio for the two fretting size-scales considered. The length-scale effects shown in the results of Table 7.3 are attributable to the combined effects of (i) contact slip-zone width, and (ii) grain size. The uniaxial fatigue results of Fig. 7.4 show the

effect of grain size alone; the predicted effect on LCF life of reducing grain size by a factor of 10, from 400 μm to 40 μm , was $\sim 10\%$. However, the cyclic loading in the partial slip fretting cases is multiaxial in nature and is due to slip-zone contact shear (friction), superimposed on an effectively constant contact pressure, giving mean stress-strain effects. As seen in Fig. 7.13b, the regions of high GND densities occur almost exclusively in the micro-slip region of the contact. The 6 mm case has therefore a significantly higher strain gradient effect. Table 7.3 shows the combined effects of slip-zone and grain size effects in fretting lead to between 14% and 24% average increase in life, for a factor of 10 (proportional) reduction in contact and grain size. This observed trend suggests that the high strain gradients associated with small contact widths enhance fretting fatigue performance, consistent with the previously-published size effect in fretting [19][20].

7.8 Crystallographic Texture Effects

The effect of crystallographic texture is now investigated by comparing fatigue predictions for an untextured model with a textured fretting model. The methodology for defining texture with Euler angles described in Chapter 4 is implemented here. A (110) fibre texture is focused on here, as it arises through the severe deformation caused by cold drawing BCC materials. The manufacture of marine riser pressure armour wire ‘zeta’ profile is achieved through a cold drawing process, so the effects of this process are directly relevant to fretting of the material. During the cold drawing process, the (110) planes are aligned with the drawing direction, as shown schematically in Fig. 7.14a. As a result, the normal directions to these planes are aligned to the normal direction, as depicted in the pole figure of Fig. 7.14b. These schematics are based on extreme textures and an amount of statistical variation will, in fact, exist from crystal to crystal. The severity of the texture depends on the level of plastic deformation induced by the cold drawing.

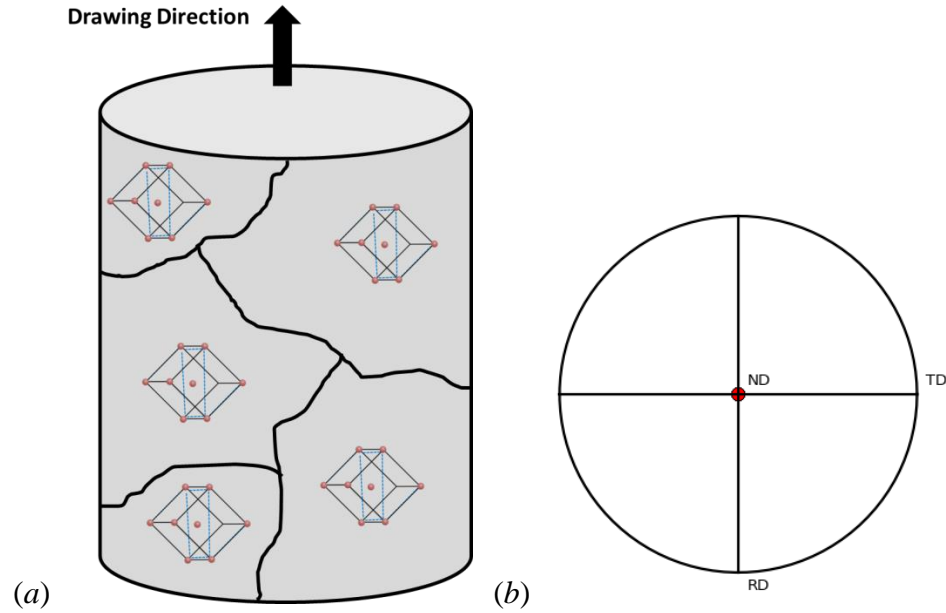


Figure 7.14.(a) Schematic of crystal rotation during cold drawing and (b) corresponding pole figure.

For this study, assumptions are made with regard to the level of texture defined in the FE models. The aim is to represent the texture that exists in the post-formed marine riser material. Without any EBSD data to provide a detailed description of each crystal orientation, the level of texture was estimated by comparing the microstructure of the riser material with available data in the literature. Zidani et al. [21] measured the texture in a similar material at various drawing strains. It can be seen from Fig. 7.15 that the processed riser microstructure is comparable to the 74% section reduction of Zidani et al. Therefore, it is assumed that the crystallographic orientations are similar and the published pole figure data of Zidani et al. is employed to specify the level of texture for the present CPFEE fretting models. Fig. 7.16a shows a (110) pole figure for the 74% section reduction material, where the (110) plane normals are highly concentrated around the centre (Normal Direction). A representative pole figure with fifty grains has been generated, as shown in Fig. 7.16b, based on the following chosen Euler angles: $\phi_1 = 0^\circ$ to 360° , $\Phi = 40^\circ$ to 50° and $\phi_2 = 45^\circ$ to 90° . The range in specified angles represents a random value within the minimum and maximum, which differs for each

grain, to allow for some statistical variation and avoid the generation of a homogeneous microstructure.

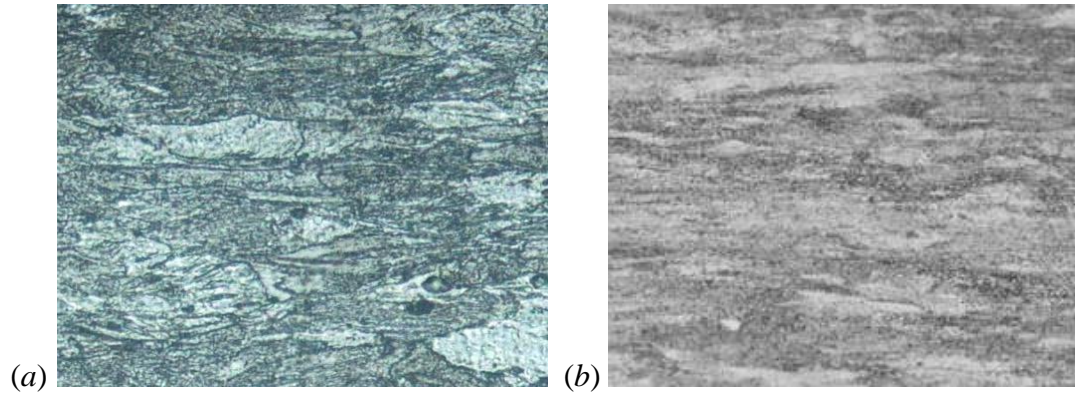


Figure 7.15. Comparison of cold drawn microstructures of (a) cold drawn pressure armour wire and (b) Zidani et al.[21].

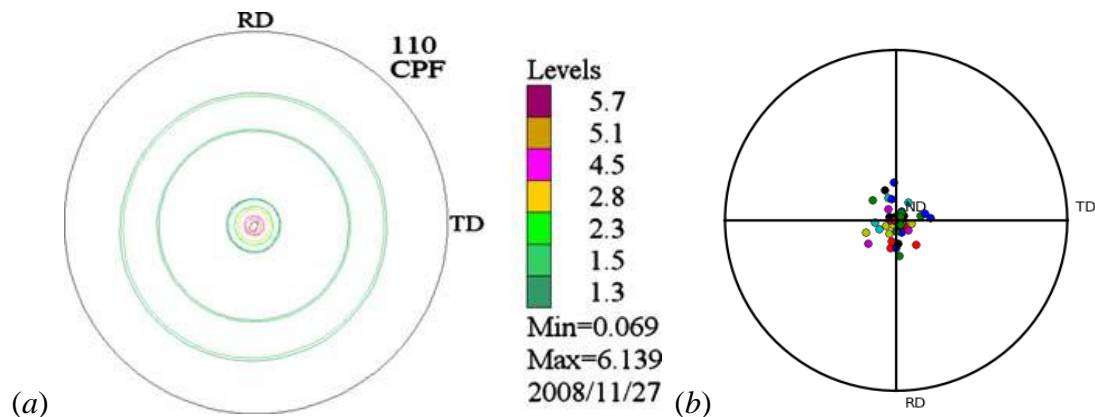


Figure 7.16 – (110) Pole figure of (a) Zidani et al. and (b) representative model.

The unit cell model used in Section 7.3 is employed to quantify the effect of this texture on the stress-strain response of the material. In this case, a simulation is run using the same microstructure model from Fig. 7.1 but with a (110) texture. The uniaxial stress-strain responses of the textured and untextured models are compared in Fig. 7.17. It can be seen that the textured case shows a significantly harder response. This effect is

attributed to a number of inactive slip systems for the textured case, which will be discussed further in the following section.

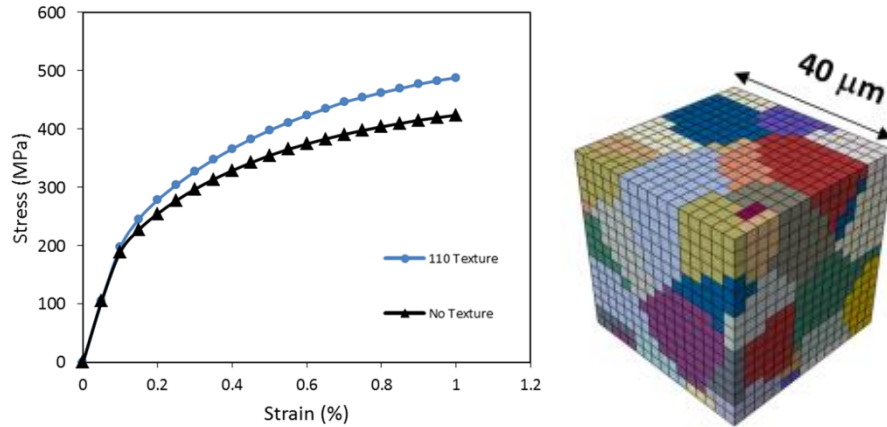


Figure 7.17. Comparison of tensile stress-strain response of unit cell microstructure model with no texture and a (110) texture.

A series of fretting simulations were run to investigate the effect of a (110) texture on fretting crack initiation. Three microstructure realisations were generated, as shown in Fig. 7.18, for this study. Each microstructure was incorporated into the fretting model and run for 6 fretting cycles with (i) an assigned random set of crystallographic orientations and (ii) a 110 fibre texture. This method allows the effect of crystallographic orientation to be isolated, without additional microstructural geometry effects. The conditions of the simulations were identical to those described above in Section 7.7, with the exception of model thickness. The thickness of the model was reduced from 40 μm to 11 μm for this study in order to reduce the large computational run-times.



Figure 7.18. The three contact region microstructure realisations generated for the texture study.

The predicted N_i values for the various untextured and textured simulations are presented in Table 7.4 for each p and P_{fs} . The textured microstructure results in a significantly higher N_i for each microstructure realisation analysed. This effect can be explained as follows: both of the FIPs implemented here are primarily based on the accumulation of plastic slip. For the (110) textured microstructures, the crystals are aligned so that the (110) plane lies parallel to the global Z direction (drawing direction). Crystallographic slip activation becomes more difficult in this orientation as slip systems on the (110) family of planes lie near-normal, or near-parallel to the surface of the substrate, resulting in low resolved shear stress on a number of (110)<111> slip systems, and thus less accumulated slip. In addition to this, the mismatch in orientation between neighbouring grains in the microstructure for different crystallographic textures can have an effect on localised plastic strain accumulation. For example, a microstructure with a strong (110) texture will be more homogeneous than a untextured microstructure, and the slip systems in neighbouring grains will be at low angles to each other, allowing for slip transfer across grains. Conversely, in untextured microstructures, the termination of slip bands at grain boundaries is more likely due to crystallographic misorientation, resulting in potential crack nucleation sites.

Table 7.4 – A comparison of predicted N_i for the untextured and (110) textured models for each realisation.

	ρ_{cyc}			ρ_{cyc}^{fs}	
	No Texture	110 Texture		No Texture	110 Texture
R1	137288	289640	R1	112934	155042
R2	931908	1027619	R2	166395	328947
(a) R3	185204	230531	(b) R3	96601	145171

Similar effects of crystallographic texture effects have been predicted by Zhang et al. [22] for a Ti alloy, where transverse textures were shown to enhance fatigue performance compared to random and basal textures due to the relatively lower accumulation of plastic strain. Texture effects are considered to be more significant for the highly anisotropic HCP crystal structures seen in Ti alloys than for the more symmetric BCC structures seen in steels.

7.9 Conclusions

A framework has been developed to model the micromechanical behaviour of a dual-phase steel used in flexible marine risers. A length-scale dependent crystal plasticity model and fatigue prediction model has been calibrated and validated against experimental data.

A microstructure-sensitive fretting study has shown that cracks can nucleate anywhere within the micro-slip zones of the contact. The implementation of an anisotropic micro-scale Fatemi-Socie type parameter shows that cracks which nucleate near the contact edge initially grow near-normal to the surface of the substrate whereas cracks that nucleate within the slip zone, away from the contact edge, grow at acute angles. The present methodology captures stochastic effects due to random crystallographic orientation of metallic grains in the contact.

The role of strain-gradient effects has been quantified by comparing two equivalent fretting models with significantly contrasting characteristic length-scales. Small contact

widths are shown to be more favourable in fretting fatigue due to increased slip system hardening as a consequence of higher density of geometrically necessary dislocations.

Crystallographic texture effects have been shown to significantly affect crack initiation in fretting of marine riser material. A strong (110) texture is shown to increase fretting fatigue resistance when compared to a textureless microstructure.

7.10 References

- [1] C. J. Bayley, W. A. M. Brekelmans, and M. G. D. Geers, “A comparison of dislocation induced back stress formulations in strain gradient crystal plasticity,” *Int. J. Solids Struct.*, vol. 43, no. 24, pp. 7268–7286, 2006.
- [2] C. F. Niordson and B. N. Legarth, “Strain gradient effects on cyclic plasticity,” *J. Mech. Phys. Solids*, vol. 58, no. 4, pp. 542–557, 2010.
- [3] C. A. Sweeney, W. Vorster, S. B. Leen, E. Sakurada, P. E. McHugh, and F. P. E. Dunne, “The role of elastic anisotropy, length scale and crystallographic slip in fatigue crack nucleation,” *J. Mech. Phys. Solids*, vol. 61, no. 5, pp. 1224–1240, 2013.
- [4] C. A. Sweeney, B. O’Brien, F. P. E. Dunne, P. E. McHugh, and S. B. Leen, “Strain-gradient modelling of grain size effects on fatigue of CoCr alloy,” *Acta Mater.*, vol. 78, pp. 341–353, Oct. 2014.
- [5] A. Fatemi and D. F. Socie, “a critical plane approach to multiaxial fatigue damage including out-of-phase loading,” *Fatigue Fract. Eng. Mater. Struct.*, vol. 11, no. 3, pp. 149–165, 1988.
- [6] A. Manonukul and F. P. E. Dunne, “High- and low-cycle fatigue crack initiation using polycrystal plasticity,” *Proc. R. Soc. A Math. Phys. Eng. Sci.*, vol. 460, no. 2047, pp. 1881–1903, 2004.
- [7] V. S. Sarma and K. a Padmanabhan, “Low cycle fatigue behaviour of a medium carbon microalloyed steel,” *Int. J. Fatigue*, vol. 19, no. 2, pp. 135–140, 1997.

-
- [8] A. Cruzado, S. Lucarini, J. LLorca, and J. Segurado, “Microstructure-based fatigue life model of metallic alloys with bilinear Coffin-Manson behavior,” pp. 1–25, 2017.
- [9] M. Sharaf, P. Kucharczyk, N. Vajragupta, S. Münstermann, A. Hartmaier, and W. Bleck, “Modeling the microstructure influence on fatigue life variability in structural steels,” *Comput. Mater. Sci.*, vol. 94, no. C, pp. 258–272, 2014.
- [10] F. P. E. Dunne, A. Manonukul, “High- and low- cycle fatigue crack initiation using polycrystal plasticity,” *Proc. R. Soc. A Math. Phys. Eng. Sci.*, vol. 460, pp. 1881–1903, 2004.
- [11] K. S. Chan, “A Microstructure-Based Fatigue-Crack-Initiation Model,” vol. 34, no. January, 2003.
- [12] M. Zhang, R. W. Neu, and D. L. McDowell, “Microstructure-sensitive modeling: Application to fretting contacts,” *Int. J. Fatigue*, vol. 31, no. 8–9, pp. 1397–1406, 2009.
- [13] Sinead O’Halloran, “Experimental Characterisation, Computational Modelling and Design Tool Development for Fretting Fatigue and Wear in Flexible Marine Risers,” NUI Galway, 2017.
- [14] H. Hertz, “Über die Berührung fester elastischer Körper,” *J. für die Reine und Angew. Math.*, pp. 156–171, 1882.
- [15] J. A. Araújo and D. Nowell, “The effect of rapidly varying contact stress fields on fretting fatigue,” *Int. J. Fatigue*, vol. 24, no. 7, pp. 763–775, 2002.
- [16] J. Ding, G. Bandak, S. B. Leen, E. J. Williams, and P. H. Shipway, “Experimental characterisation and numerical simulation of contact evolution effect on fretting crack nucleation for Ti-6Al-4V,” *Tribol. Int.*, vol. 42, no. 11–12, pp. 1651–1662, 2009.

- [17] V. Lamacq, M.-C. Dubourg, and L. Vincent, “A theoretical model for the prediction of initial growth angles and sites of fretting fatigue cracks,” *Tribol. Int.*, vol. 30, no. 6, pp. 391–400, 1997.
- [18] C. Navarro, J. Vázquez, and J. Domínguez, “Nucleation and early crack path in fretting fatigue,” *Int. J. Fatigue*, vol. 100, pp. 602–610, 2017.
- [19] R. Bramhall, “Studies in fretting fatigue,” PhD Thesis, University of Oxford, 1973.
- [20] J. A. Araújo and D. Nowell, “Analysis of pad size effects in fretting fatigue using short crack arrest methodologies,” *Int. J. Fatigue*, vol. 21, no. 9, pp. 947–956, 1999.
- [21] M. Zidani, S. Messaoudi, T. Baudin, D. Solas, and M. H. Mathon, “Deformation textures in wire drawn perlitic steel,” *Int. J. Mater. Form.*, vol. 3, no. 1, pp. 7–11, 2010.
- [22] M. Zhang, D. L. McDowell, and R. W. Neu, “Microstructure sensitivity of fretting fatigue based on computational crystal plasticity,” *Tribol. Int.*, vol. 42, no. 9, pp. 1286–1296, 2009.

8 Conclusions and Future Work

8.1 Conclusions

The primary outcome of this thesis is the development of a length-scale dependent 3D micromechanical computational framework for studying crack initiation in fatigue and fretting of metals. This has facilitated a number of microstructure-sensitive computational studies to be performed to assess the role of several key parameters in fretting crack initiation. The current model represents a significant advance in computational modelling of fretting. For the first time, a physically-based, length-scale dependent crystal plasticity finite element (CPFE) formulation has been implemented in micromechanical fretting models. This has provided a microstructure-based quantified demonstration for the physical basis of contact size effects in fretting. Two types of size effects in fretting have been demonstrated, namely, strain-gradient size effects and statistical size effects.

A study of a variety of microstructures, across a range of grain sizes, has shown the capability of 3D CPFE modelling techniques for predicting statistical size effects in fretting. A critical ratio of contact semi-width to grain size has been established. A contact semi-width to grain size ratio of below 1 leads to large uncertainty in number of cycles to crack initiation, and it is therefore suggested that a value of above 1 is chosen for safe component and system design against fretting.

It has been found, through length-scale dependent CPFE modelling, that the explicit inclusion of beta lath geometry in dual-phase Ti alloys significantly affects mechanical response and dwell fatigue resistance. The stress-strain response of individual alpha-beta colonies is dependent on the relative orientation of beta laths and beta lath spacing, where smaller spacing results in a harder response. In relation to dwell fatigue, the presence of the beta phase was predicted to increase resistance to ‘faceting’ in this

material. It was also shown that the exclusion of GND-induced length-scale effects leads to an over prediction of post-dwell grain boundary plastic strains and thus, potentially leads to an under prediction of dwell fatigue life.

The development of a representative 3D length-scale dependent CPFE fretting model and fatigue prediction model is facilitated by mechanical testing and microscopy of marine riser material. A study of strain gradient effects in fretting contacts has shown that small grain sizes and small contact widths benefit the resistance of fretting crack initiation due to increased geometrically necessary dislocation hardening, and consequently, less accumulation of crystallographic slip. A (110) fibre crystallographic texture, which is typically induced by cold drawing of marine riser steel, is shown to benefit crack initiation resistance in fretting.

Overall, this work has demonstrated that crack initiation in metals is sensitive to a number of microstructural features, namely grain size, GND density, secondary phases and crystallographic orientation. In order to optimise the design of flexible marine risers against fretting, it is recommended that small grain sizes and small contact widths are used to increase resistance to crack initiation due to strain gradient effects. In addition, large contact semi-width to grain size ratios are recommended to eliminate fatigue uncertainty that arises from statistical size effects

8.2 Recommendations for Future Work

8.2.1 Fretting Fatigue Testing

As mentioned in Chapter 3, due to issues regarding test rig availability, the planned fretting fatigue tests could not be completed. The specimen redesign and test methodology developed by McCarthy [1] is given in Appendix A. The heat treatment procedure developed to increase the grain size of the material is also described in Appendix A. Fretting fatigue specimens and pads with average grain sizes of 11 μm and 23 μm have been manufactured. A first step for future workers on this topic should be

to test the manufactured specimens and study the effect of grain size on fretting fatigue of pressure armour material.

8.2.2 Micro-pillar testing of Ferrite and Pearlite

The nanoindentation testing carried out in Chapter 3 was unsuccessful for distinguishing between the mechanical behaviour of the ferrite and pearlite phases of the pressure armour material. It is suggested that micro-pillar testing is conducted on the ferrite and pearlite phases of the material to obtain results similar to those employed in Chapter 6. This would include fabricating micro-pillars of the individual phases via a focused ion beam (FIB). The micro-pillars can then be tested in compression to generate a unique force-displacement response for each sample.

8.2.3 Material Modelling of Pressure Armour Material

The pearlite phase of the pressure armour wire material consists of a thin lamellar structure of ferrite and cementite. It is currently practically impossible to explicitly model this geometry in polycrystal FE models due to the associated computational costs. The current physically based material model employs a ratio of critical resolved shear stress to distinguish between the ferrite and pearlite phases, essentially modelling pearlite phase as a homogenised phase. This modelling approach could be improved by incorporating a drag stress term into the constitutive model to account for the effect of cementite laths on crystal slip. Mayeur and Mc Dowell [2] employed this term to account for beta laths in dual phase Ti alloys where the relative lath orientation and lath spacing were considered as additional model input parameters.

8.2.4 The Effect of Cold Drawing

Although the crystallographic texture induced by cold drawing can be beneficial in fatigue, the experimental results presented in Chapter 3 suggest that the damage and residual stresses induced by the cold drawing process outweighs this effect, in terms of total life. Therefore, it is recommended that post-forming procedures are investigated in an attempt to increase fatigue resistance. The first step would be to experimentally measure the residual stresses and dislocation density in the pre- and post- formed

material to better understand the cause of the observed post-forming drop in life. Another essential step would be to perform EBSD experiments to quantify the level of texture in the material.

8.2.5 Wear

Due to the complexity of the current work, the effects of material removal due to wear were neglected. However, it has been shown by McCarthy et al. [3] that microscale parameters, such as accumulated crystallographic slip p , are potentially useful for indicating wear in CPFEM models. The current modelling framework could be further expanded to incorporate re-meshing techniques such as those implemented by O'Halloran [4] based on a microscale wear indicator parameter, e.g. some function of p .

8.2.6 Asperity Modelling

Metallic surfaces consist of microscale asperities, and under fretting contact conditions, the interaction and plastic deformation of individual asperities can significantly affect the COF, and consequently the fretting fatigue life. Mulvihill et al. [5] have attempted to predict COF using elastic-plastic FE models of individual asperities, with good results. A short investigation was carried out, as described in Appendix C, where a similar approach to Mulvihill was employed, with the addition of a CP material model. Asperity geometry of marine riser material was measured using a profilometer, and representative CPFEM models were developed. However, computational difficulties were encountered due to the high levels of plastic deformation. In order to overcome these problems, which relate to convergence of the implicit FE solution, it is suggested that future work converts the current CPFEM material model into an explicit code.

8.2.7 Crack Propagation

Another significant advance in the capability of the current modelling methodology would be the inclusion of a crack propagation model. A relatively recent software X-FEM is now used extensively for crack propagation in FE models. For example, Wan et al. [6] have successfully predicted experimentally observed crack paths in notched beam specimens using an anisotropic elastic material model and X-FEM. X-FEM has also

been coupled with polycrystal CP material models by Farukh et al. [7] for prediction of crack growth. It is therefore possible to incorporate such methods for predicting fretting-induced crack initiation. However, this will significantly increase computational cost and simulation run-times.

8.2.8 Further Microstructure-Sensitive Studies

The complexity of the current microstructure sensitive fretting model, with regard to simulation run-times, has limited the extent and detail of the studies performed in this thesis. With increased computational resources, a number of beneficial studies could be conducted using the framework developed here. This includes the assessment of a broader range of microstructures, contact sizes and loading conditions, including more direct comparison with microstructure-sensitive experimental fretting results, to more comprehensively characterise the combined strain-gradient and statistical microstructural effects on fatigue crack initiation in fretting.

8.3 References

- [1] O. J. McCarthy, J. P. McGarry, and S. B. Leen, “Microstructure-sensitive prediction and experimental validation of fretting fatigue,” *Wear*, vol. 305, no. 1–2, pp. 100–114, 2013.
- [2] J. R. Mayeur and D. L. McDowell, “A three-dimensional crystal plasticity model for duplex Ti-6Al-4V,” *Int. J. Plast.*, vol. 23, no. 9, pp. 1457–1485, 2007.
- [3] O. J. McCarthy, J. P. McGarry, and S. B. Leen, “Micro-mechanical modelling of fretting fatigue crack initiation and wear in Ti-6Al-4V,” *Int. J. Fatigue*, 2013.
- [4] Sinead O’Halloran, “Experimental Characterisation, Computational Modelling and Design Tool Development for Fretting Fatigue and Wear in Flexible Marine Risers,” PhD Thesis, NUI Galway, 2017.
- [5] D. M. Mulvihill, M. E. Kartal, D. Nowell, and D. A. Hills, “An elastic–plastic asperity interaction model for sliding friction,” *Tribol. Int.*, vol. 44, no. 12, pp. 1679–1694, 2011.

[6] V. V. C. Wan, D. W. MacLachlan, and F. P. E. Dunne, “Integrated experiment and modelling of microstructurally-sensitive crack growth,” *Int. J. Fatigue*, vol. 91, pp. 110–123, 2016.

[7] F. Farukh, L. G. Zhao, R. Jiang, P. Reed, D. Proppentner, and B. A. Shollock, “Realistic microstructure-based modelling of cyclic deformation and crack growth using crystal plasticity,” *Comput. Mater. Sci.*, vol. 111, pp. 395–405, 2016.

Appendix A Fretting Fatigue Testing and Heat Treatment

A1 Fretting Fatigue Testing

The bridge-type fretting arrangement designed by McCarthy [16] is employed for fretting fatigue testing of the rod material. A diagram of the rig is provided in Fig. 9.1, where a normal load is applied to two cylindrical fretting pads on each side of the fatigue specimen. A proving ring mechanism is used to provide a clamping load to the fretting pads through threaded loading screws. Ball bearings are used to ensure uniform load transfer from the screws to the fretting pad supports. Cylindrical pins are fitted between the pad supports and the fretting pads to eliminate 3-point bending effects, and thus ensure a uniform transfer of normal load to each pad.

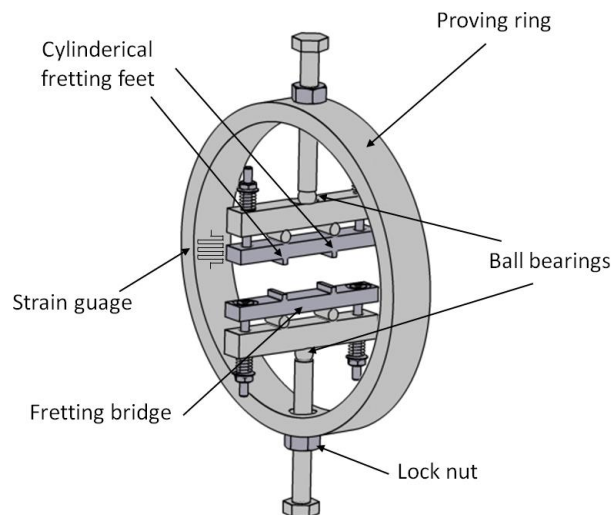


Figure A.1. Schematic of proving ring and fretting bridge set-up.

A load-strain curve has been generated by McCarthy [16] to determine the relationship between circumferential strain on the proving ring surface and applied normal load on the pads, as shown in Fig 9.2. Strain gauges are therefore applied to the surface of the proving ring, in order to achieve the desired normal load for tests.

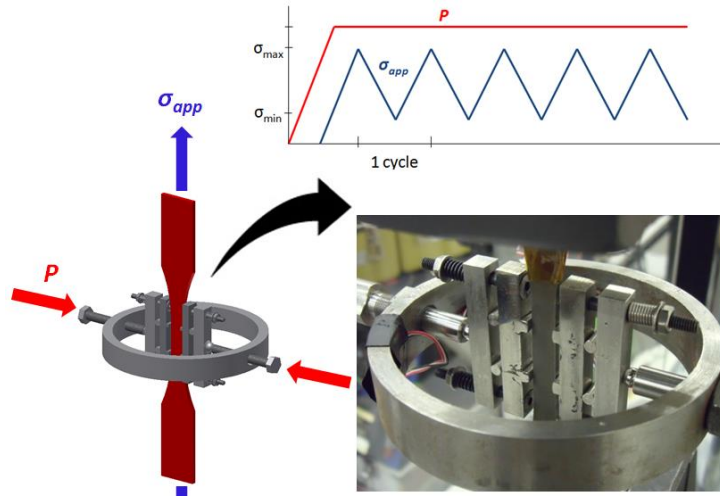


Figure A.2. Schematic full fretting fatigue rig and pads applied to dog-bone fatigue specimen.

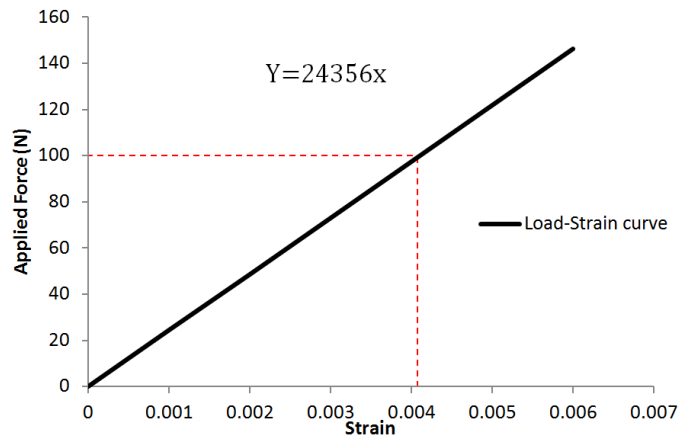


Figure A.3. Relationship between circumferential strain on the proving ring and applied normal load.

A drawing of the dog bone fatigue specimens and fretting pads are given in Fig. 9.4. The pads are machined to a radius of 6 mm. The fatigue specimens were redesigned due to

the constraints imposed by the as-received material. The new design adheres to the ASTM standards for dog bone fatigue specimens.

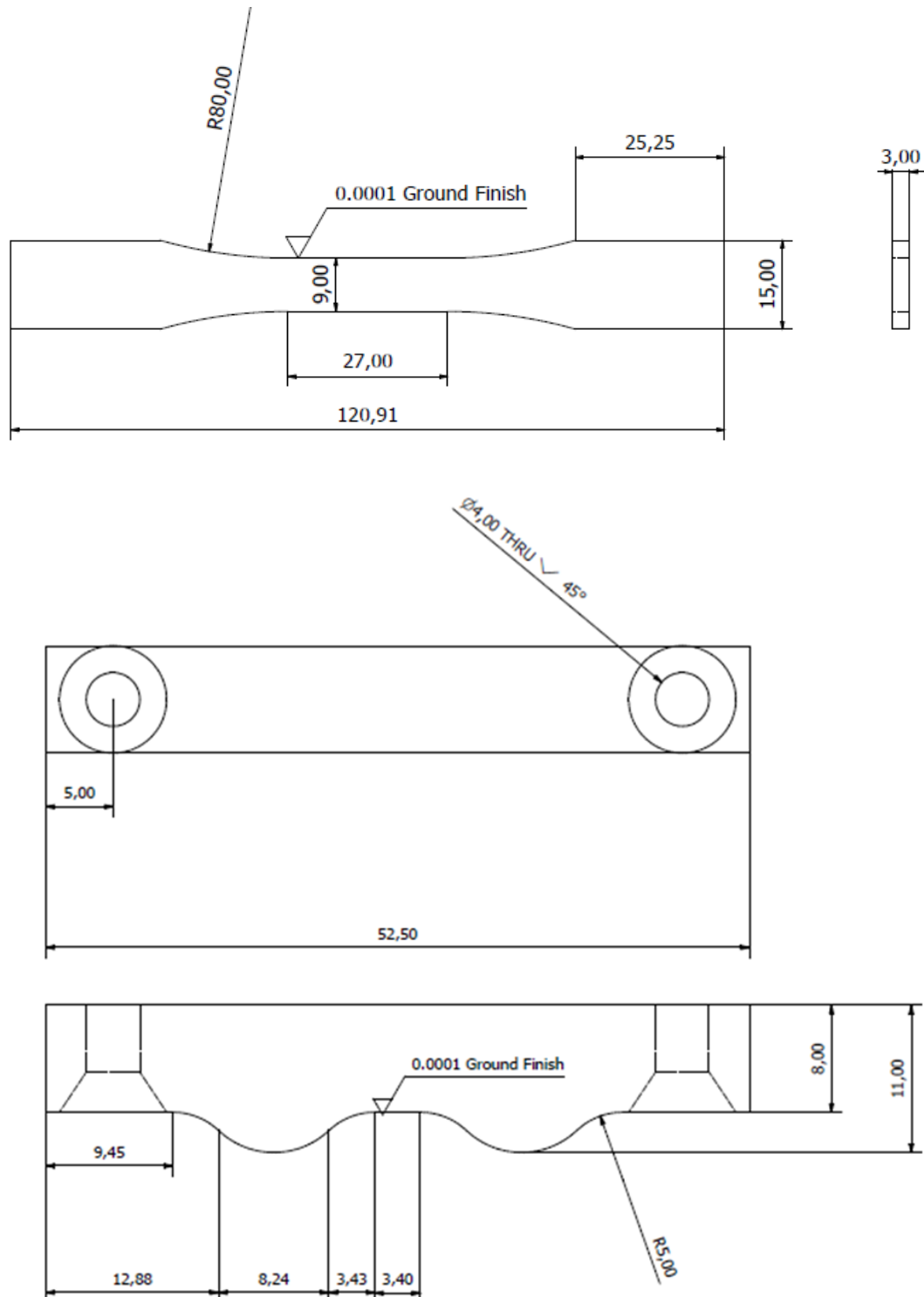


Figure A.4. Drawings of (a) redesigned fatigue specimen, and (b) fretting pad.

A2 Heat Treatment

In order to study the effect of grain size on fretting fatigue, a heat treatment process is developed to obtain a microstructure with large grains of ferrite and pearlite. The rod material undergoes an annealing process, whereby the material is heated above a critical temperature and cooled slowly to increase the average grain size. The material is first placed in a furnace and heated to 950 °C, a temperature considerably above the austenisation temperature A_3 shown in Fig 3.20. As the material is heated above A_3 , a phase transformation to austenite grains occurs. Further temperature increase above A_3 results in coarser austenite grains, which upon slow cooling in the furnace, produces coarse ferrite and pearlite grains. A heat treatment procedure has been iteratively developed here to increase the average grain size from 11 μm to 23 μm , as shown schematically in Fig. 3.21.

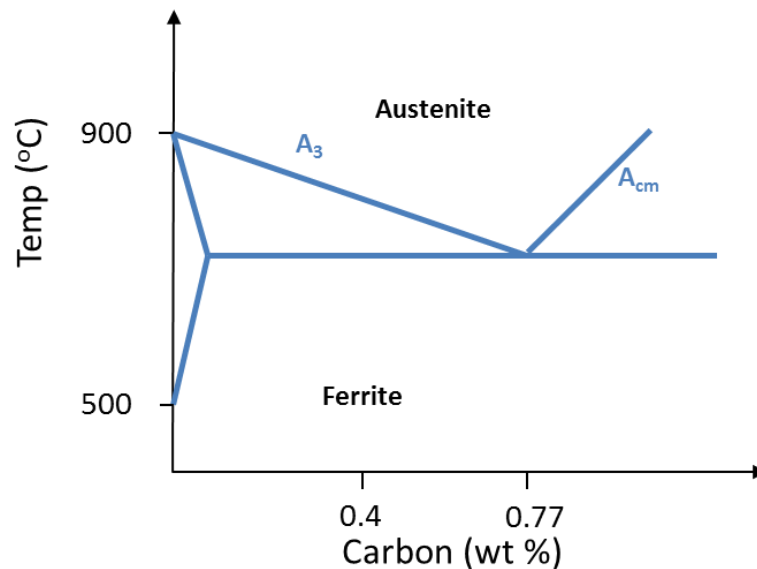


Figure A.5. Phase diagram for steel. The material is heated above A_3 to achieve grain growth.

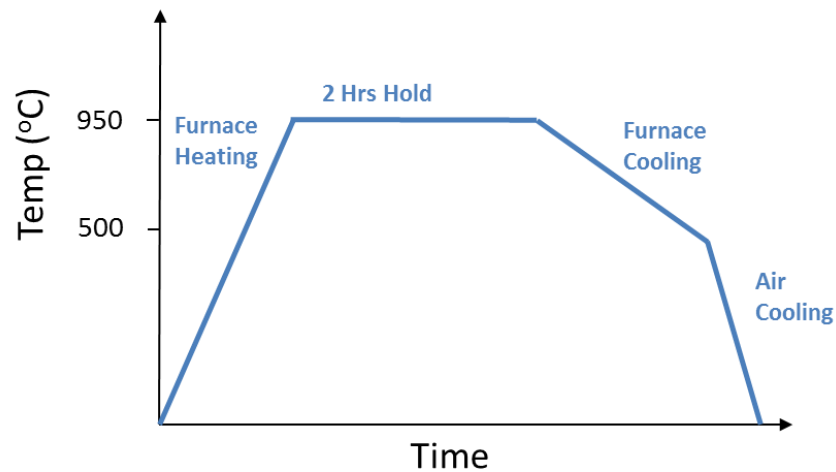


Figure A.6. Schematic of heat treatment procedure developed for grain growth.

The effect of the heat treatment procedure is shown in Fig. 3.22. It can be seen that the microstructure has changed considerable has occurred. A comparison of the ferrite grain area distributions is shown in Fig. 3.23. This histogram reflects the presence of some considerably larger grains in the heat treated microstructure compared to the as-received microstructure.

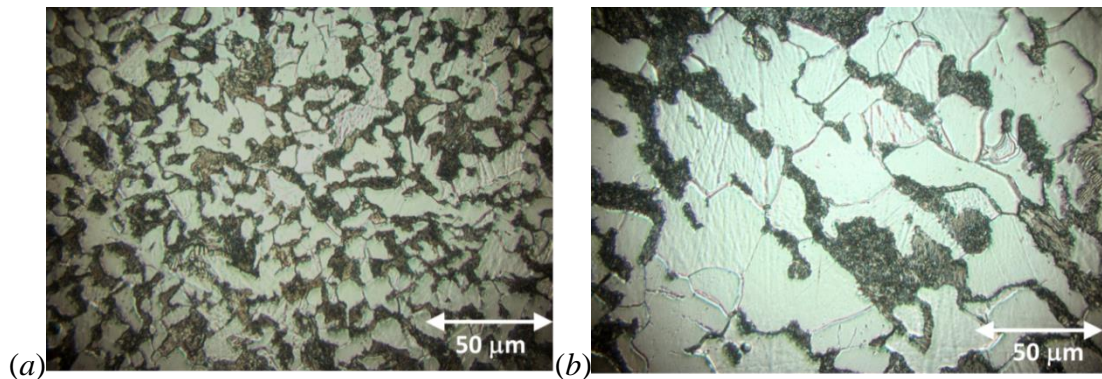


Figure A.7. A comparison of the as-received rod microstructure and heat treated microstructure.

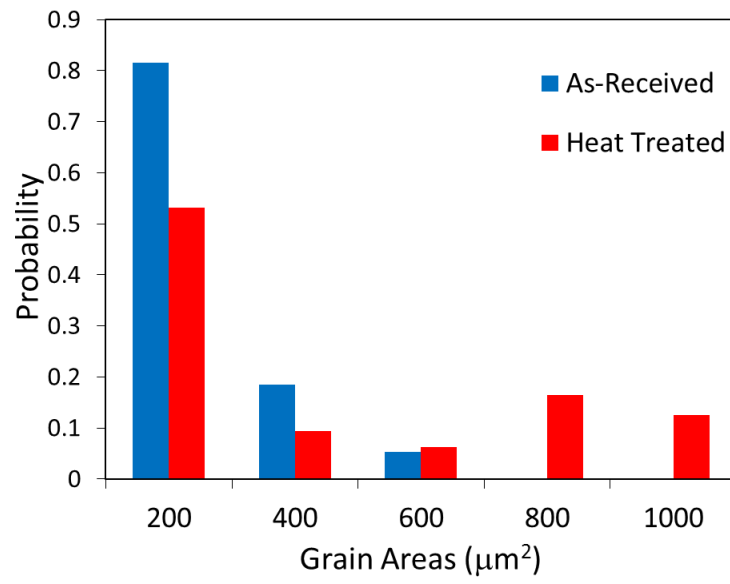


Figure A.8. Grain area distributions for the as-received and heat treated riser steel material.

Appendix B Preliminary 2D Microstructure-Sensitive Fretting Study

B.1 Overview

A 2D CPFE Fretting model methodology was developed to study the influence of microstructure on fretting crack initiation. This initial 2D study allowed the importance of the statistical variation of microstructure to be assessed with relatively simpler modelling techniques and significantly shorter computation run-times compared to 3D modelling.

B.2 Unit Cell Model

A 2D periodic unit cell microstructure model was first developed to compare the simulated cyclic material response with corresponding experimental data. The Huang UMAT (introduced in Chapter 4) was employed to describe the constitutive behaviour of the CoCr material with the identified parameters of Sweeney[1]. Figure B. 1 shows a comparison of the simulated stabilised hysteresis loops with stabilised experimentally measured loops. It can be seen that the 2D model exhibits a harder material response. This is due to the additional constraints in the third dimension, which inhibits crystal slip on particular slip systems, resulting in higher stress. This is to be expected for the 2D model as the material constants employed were calibrated for a 3D model. However, the aim of this preliminary study is purely qualitative, in order to justify the progression to a significantly more complex 3D CPFE study.

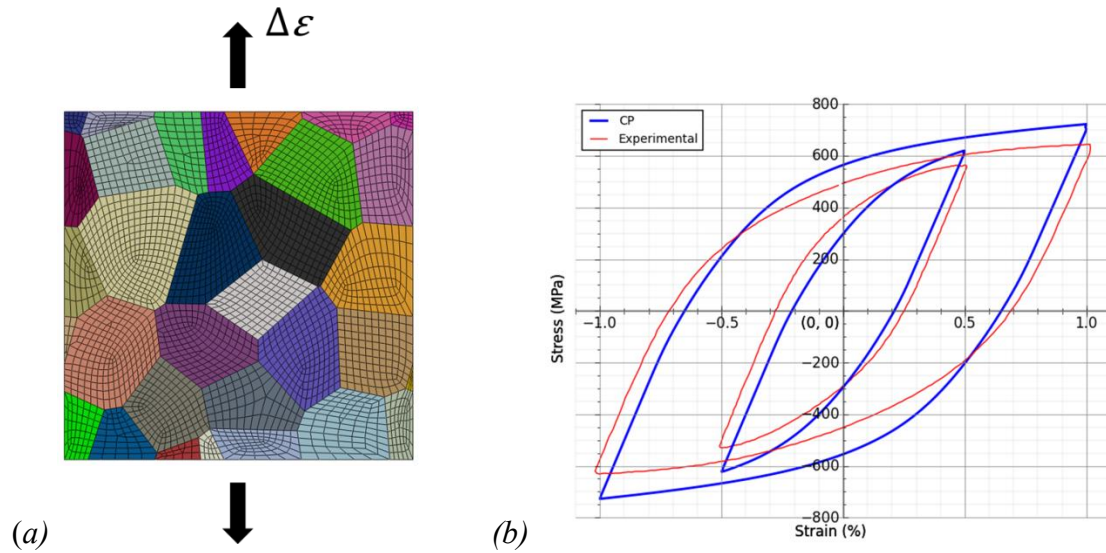


Figure B.1. (a) 2D unit cell microstructure model indicating applied strain and (b) comparison of experimentally measured and CPFE predicted stabilised hysteresis loops for CoCr.

B.3 2D Fretting Model

A 2D cylinder-on-flat frictional contact model was developed to incorporate the CoCr microstructure geometry and CP material model in the contact zones. The model consists of two parts; the cylinder, and the flat. Each part is divided into three regions in order to rapidly refine the mesh towards the contact zone. Only the most refined mesh region, in the contact zone, is assigned the CPFE material parameters. The remaining regions are assigned a J2 plasticity material model to reduce computation expense. Three microstructure realisations are analysed in this study, each with an average grain size of $32 \mu\text{m}$. Figure B.2 shows a schematic of the 2D fretting model and the three microstructures analysed.

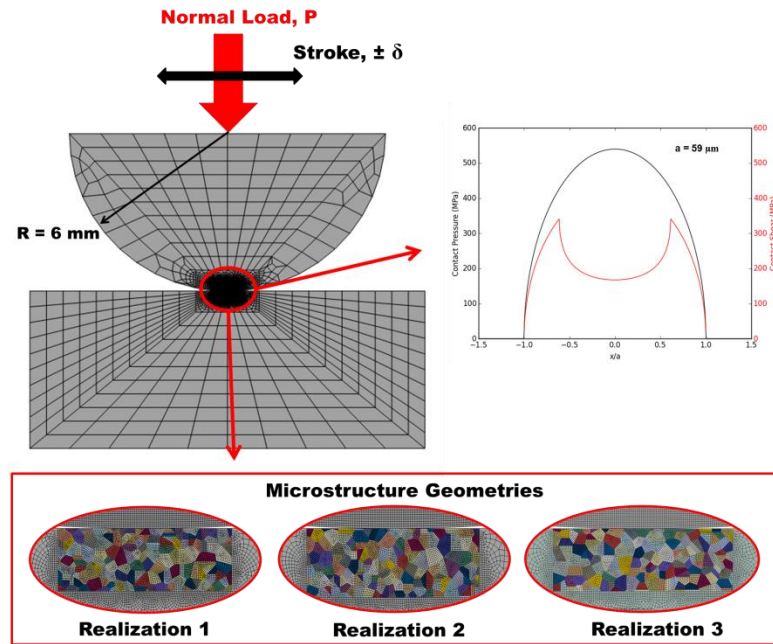


Figure B.2. Schematic of fretting model and 3 microstructure realisations analysed.

A coefficient of friction of 0.6 and a normal load of 50 N/mm are chosen as constant loading conditions. Two applied relative slip amplitudes Δ of 1.95 μm and 1.4 μm are applied to the model, as shown in Fig. B.3. Each simulation is run for 3 fretting cycles in order to achieve a stabilised value of p_{cyc} and thus calculate the number of cycles to crack initiation, as described in Chapter 4.

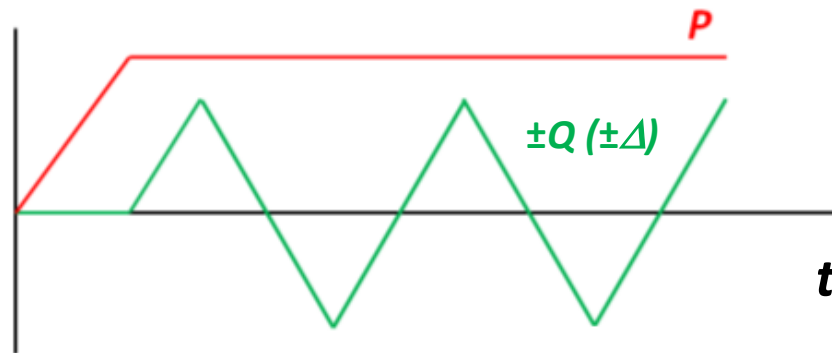


Figure B.3. Loading history showing constant normal load and cyclic tangential load.

Figure B.4 shows the predicted number of cycles to crack initiation for each microstructure realisation across two applied relative slips. It can be seen that a difference of over 20% in N_i is predicted across the three realisations. It is emphasised that these three models are nominally identical, in terms of component-scale geometry and loading conditions. It is only the statistical variation in microstructure that is different. Therefore, this significant effect is purely due to the microstructure morphology and crystallographic orientation in the contact zone. As a result, it was decided to further study the effect of microstructure, and the relationship between contact size and microstructure, using a 3D modelling approach in order to create more realistic finite element models.

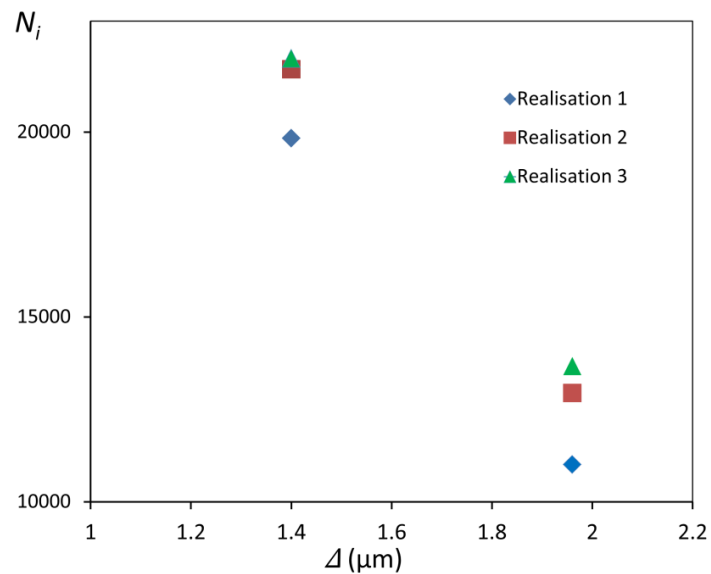


Figure B.4. Preliminary 2D study results showing the sensitivity of N_i to microstructure.

Appendix C Asperity Modelling

C.1 Overview

In this appendix, the methods developed for asperity modelling is presented. The aim of this work was to, for the first time, incorporate a length-scale dependent CP into a FE model of an individual asperity in order to investigate the role of crystal orientation and GND density on COF.

C.2 Methodology

A profilometer was used to measure the surface of pressure armour wire material. A surface profile is presented in fig. C.1. From this data, a FE geometry of an idealised asperity was created, as shown in fig. C.2. The model consists of an upper rigid asperity and a lower 3D elastic-plastic asperity. The lower asperity is modelled with the physically based CPFE material model described in Chapter 2. In the simulation, the upper asperity is displaced in the x direction to ‘plough’ through the lower asperity. During this process, energy is required for plastic deformation of the lower asperity, which contributed to the COF of the material.

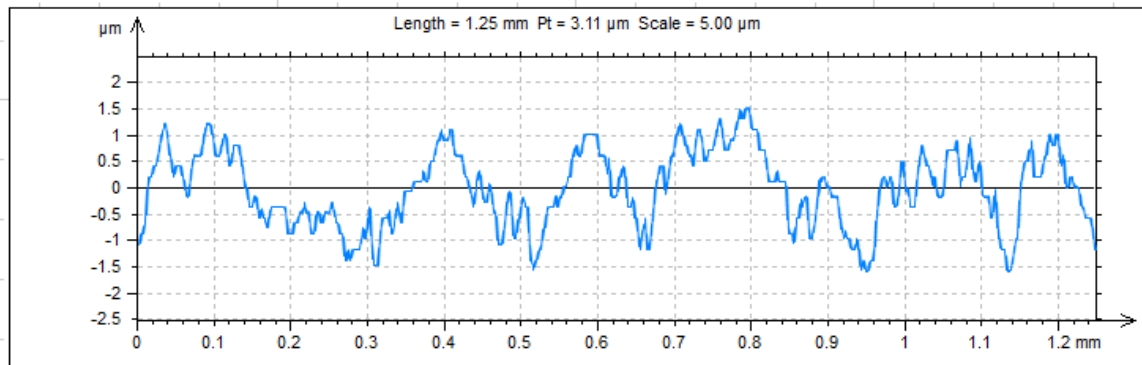


Figure C.1. Profile of pressure armour surface

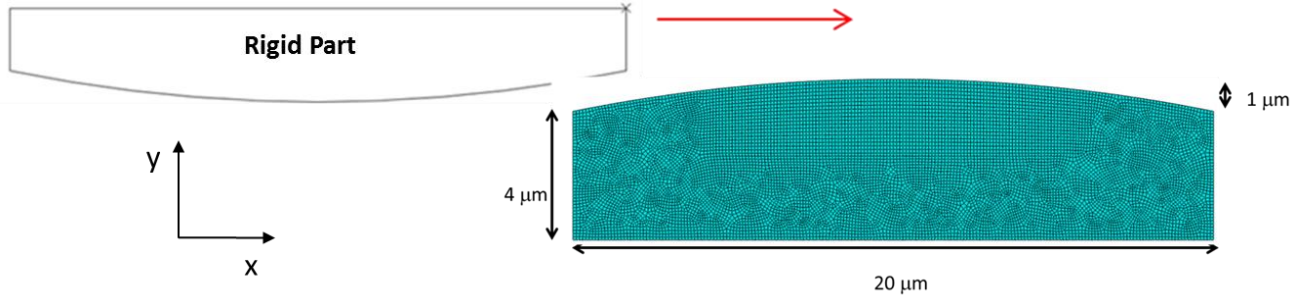


Figure C.2. FE model of idealised asperity based on measured surface profile.

C.3 Results and Discussion

Due to high levels of deformation, the simulations aborted at an early stage due to convergence issues of the FE solution. The last frame in the analysis is given in fig. C.3. Similar previous work by Mulvihill employed an explicit FE formulation for asperity ‘ploughing’ models. It is possible that this will solve the computation problem encountered here. However, for user defined material subroutine the conversion from implicit to explicit requires the current UMAT to be converted to a VUMAT. This is considered to be beyond the scope of the present work.

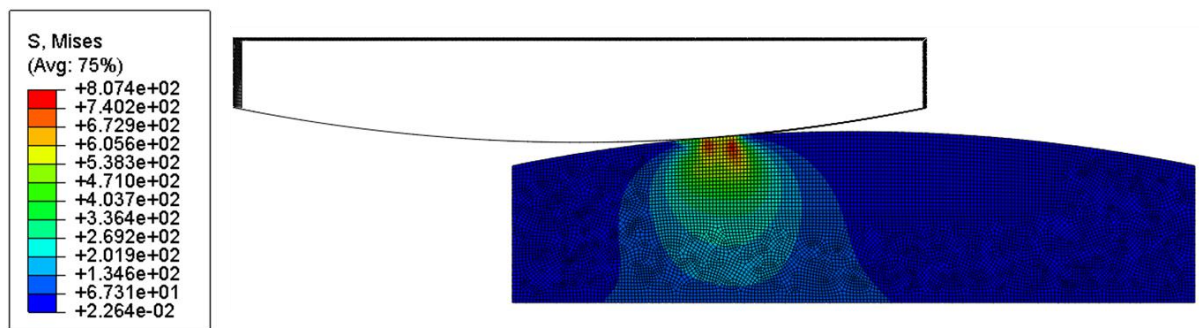


Figure C.3. Last frame in the analysis of the CP asperity model.

Appendix D Mesh Sensitivity Studies

D.1 Ti Unit Cell Model

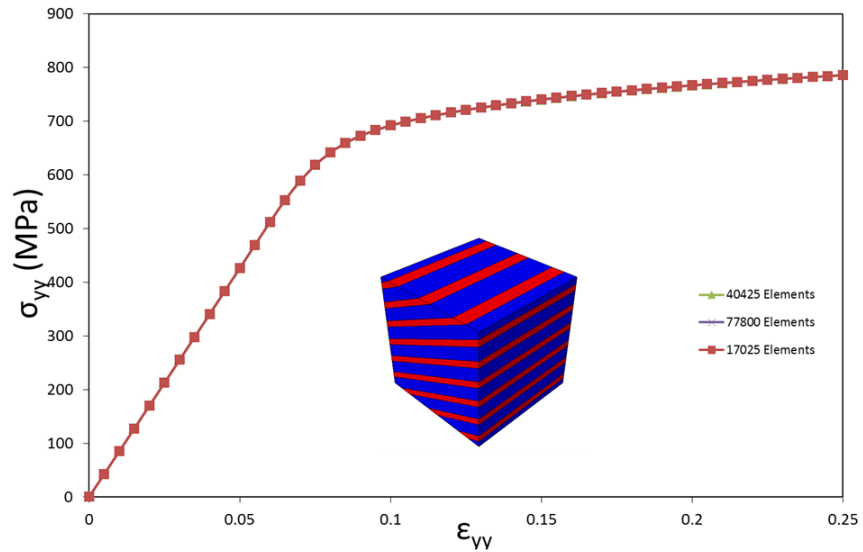


Figure D.1. α - β unit cell microstructure mesh sensitivity.

8.4 D.2 Ti Dwell Model – Pure Alpha Microstructure

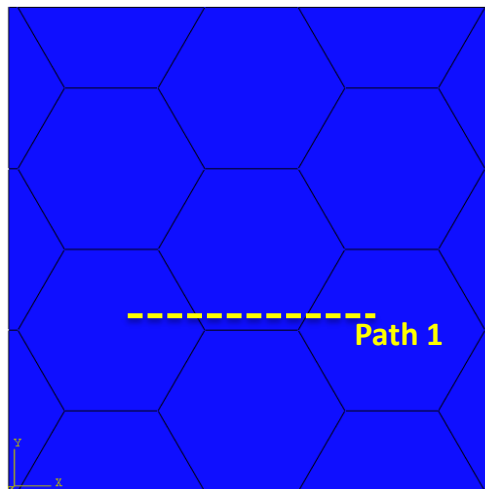


Figure D.2. Pure alpha -Ti dwell model with indicated path for mesh sensitivity.

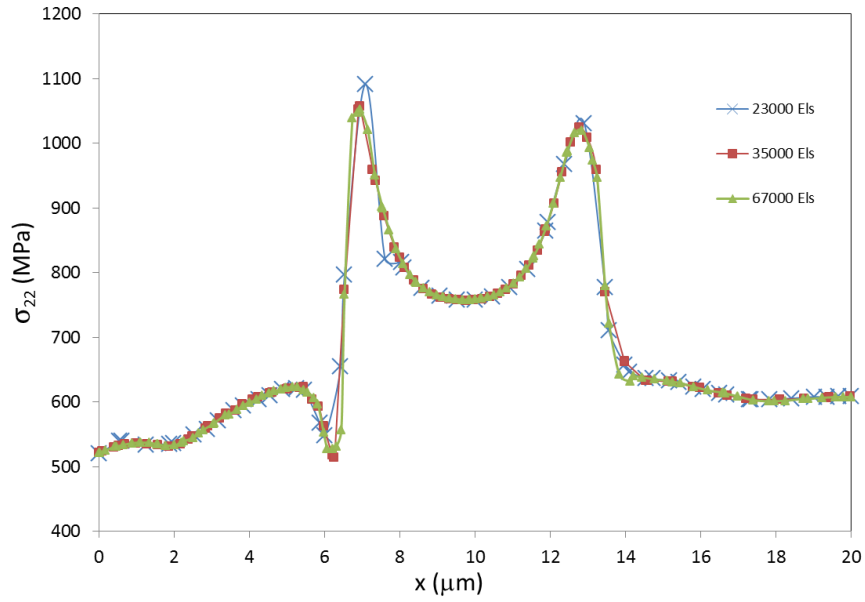


Figure D.3. Post-dwell stress distributions along Path 1 for three mesh densities.

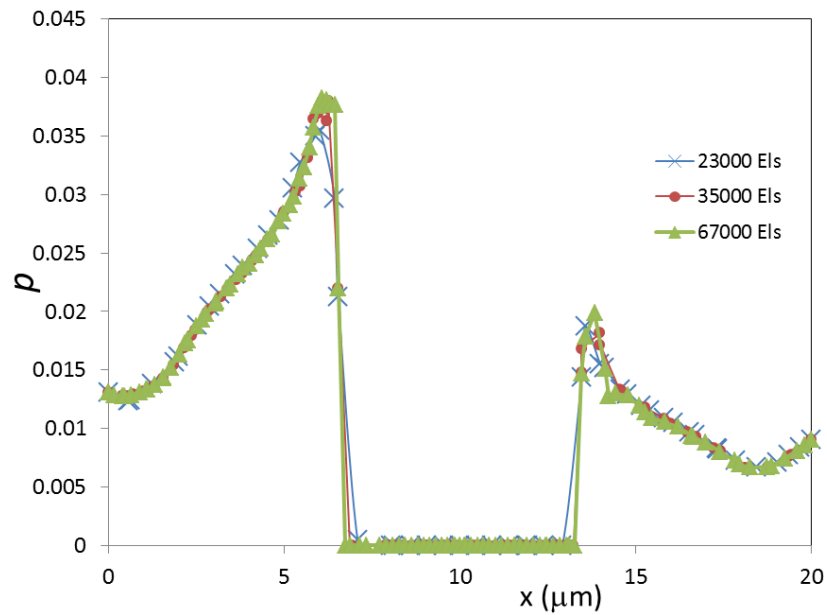


Figure D.4. Post-dwell accumulated plastic strain distributions along Path 1 for three mesh densities.

8.5 D.3 Ti Dwell Model –Alpha-Beta Microstructure

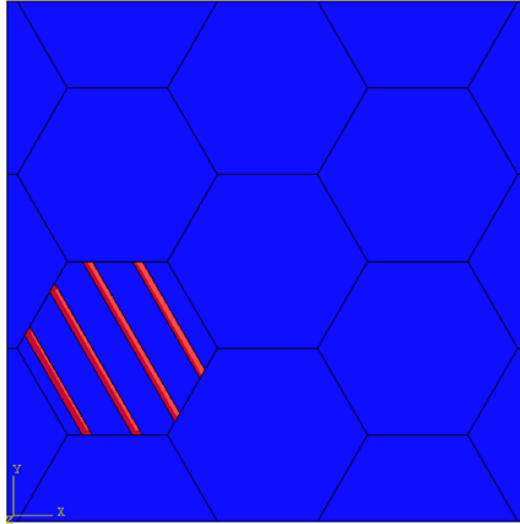


Figure D.5. Alpha-Beta Ti dwell model with indicated path for mesh sensitivity.

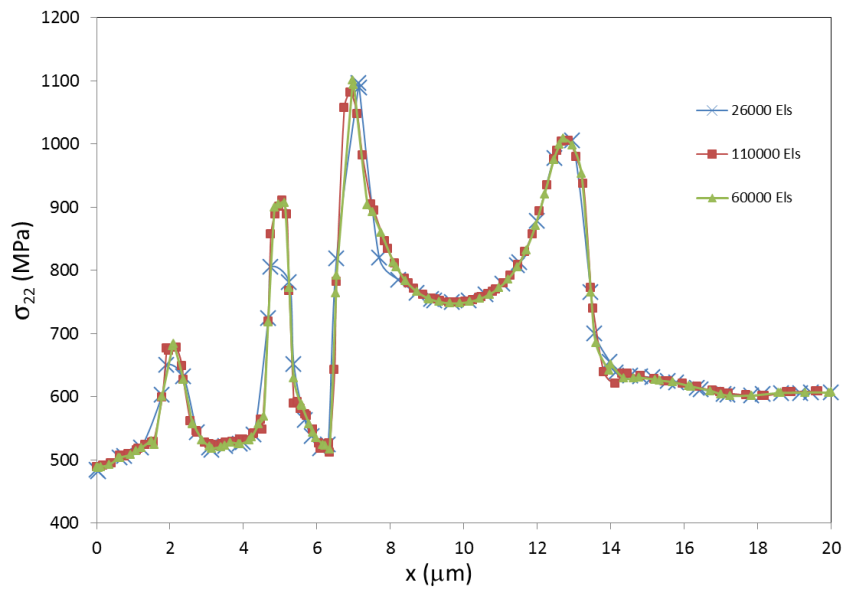


Figure D.6. Post-dwell stress distributions along Path 1 for three mesh densities.

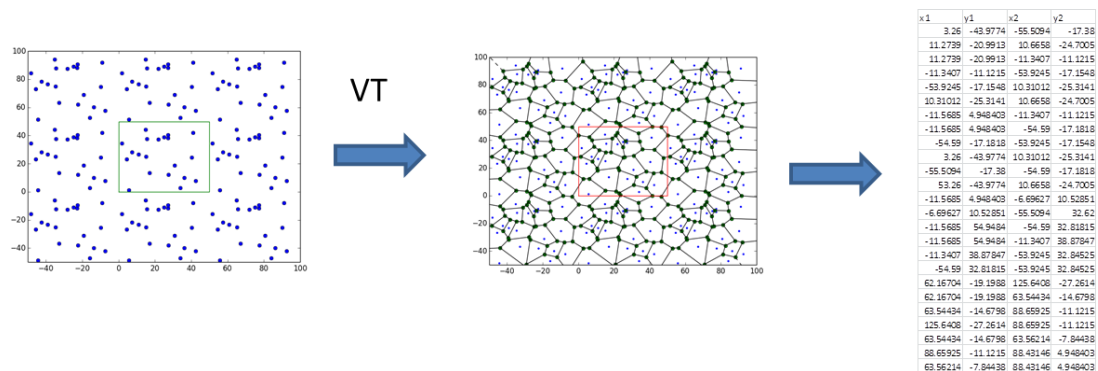
Appendix E Python Scripts

E.1 Overview

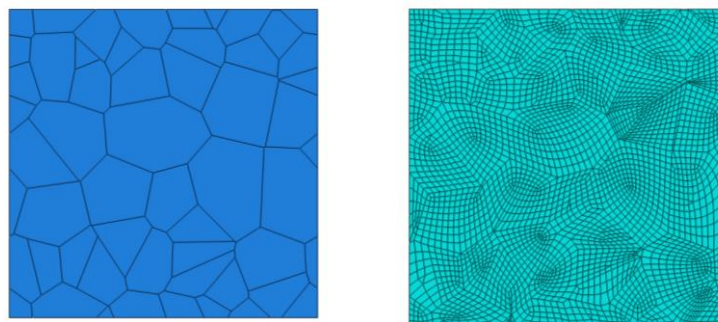
In this thesis, a number of Python scripts were written to automate processes such as ABAQUS pre-processing and post-processing, FE model generation and image processing. In the interest of saving space only the 2D microstructure model generation scripts are included here.

E.2 2D Microstructure Model Generation

- Run Veronoi Tessellation Python code “VT-MicroStructure Generation” to get a set of points for each Voronoi edge.



- Run ABAQUS script “Microstructure Model” to partition a part using the above points and automatically mesh the part.



- Run Python code “InputFileMods” to apply periodic boundary conditions (constraint equations) and insert UMAT data cards.


```

31. averageGrainArea=Cell_area/nuclei
32. #randomly generate nuclei
33. for i in range(0,nuclei):
34.     x=round(random.uniform(0,xlimit),2) #2 decimal places
35.     y=round(random.uniform(0,ylimit),2)
36.     xvals.append(x)
37.     yvals.append(y)
38.     i=i+1
39.
40. #create 3x3 cells for periodicity
41. #east cell
42. for j in range(0,nuclei):
43.     eastcellx=xvals[j]+xlimit
44.     eastcelly=yvals[j]
45.     xvals.append(eastcellx)
46.     yvals.append(eastcelly)
47. #northcell
48. for j in range(0,nuclei):
49.     northcellx=xvals[j]
50.     northcelly=yvals[j]+ylimit
51.     xvals.append(northcellx)
52.     yvals.append(northcelly)
53. #southcell
54. for j in range(0,nuclei):
55.     southcellx=xvals[j]
56.     southcelly=yvals[j]-ylimit
57.     xvals.append(southcellx)
58.     yvals.append(southcelly)
59. #westcell
60. for j in range(0,nuclei):
61.     westcellx=xvals[j]-xlimit
62.     westcelly=yvals[j]
63.     xvals.append(westcellx)
64.     yvals.append(westcelly)
65. #northeast cell
66. for j in range(0,nuclei):
67.     Neastcellx=xvals[j]+xlimit
68.     Neastcelly=yvals[j]+ylimit
69.     xvals.append(Neastcellx)
70.     yvals.append(Neastcelly)
71. #southeast cell
72. for j in range(0,nuclei):
73.     Seastcellx=xvals[j]+xlimit
74.     Seastcelly=yvals[j]-ylimit

```

```

75.     xvals.append(Seastcellx)
76.     yvals.append(Seastcelly)
77. #southwestcell
78. for j in range(0,nuclei):
79.     Swestcellx=xvals[j]-xlimit
80.     Swestcelly=yvals[j]-ylimit
81.     xvals.append(Swestcellx)
82.     yvals.append(Swestcelly)
83. #northwestcell
84. for j in range(0,nuclei):
85.     Nwestcellx=xvals[j]-xlimit
86.     Nwestcelly=yvals[j]+ylimit
87.     xvals.append(Nwestcellx)
88.     yvals.append(Nwestcelly)
89. #concatenate x and y values
90. for i in range(0,len(xvals)):
91.     p=[xvals[i],yvals[i]]
92.     Points.append(p)
93.
94.
95. #plot points
96. plt.figure(0)
97. plt.plot(xvals,yvals, 'o')
98. plt.title('3x3 celll of randomly generated points')
99. points=Points
100.     # compute Voronoi tessellation
101.     vor = Voronoi(points)
102.     # plot
103.     voronoi_plot_2d(vor)
104.     plt.title('Voronoi Diagram')
105.     #plot cell boundary
106.     plt.plot([0,xlimit,xlimit,0,0],[0,0,ylimit,ylimit,0])
107.     plt.xlim(-xlimit,2*xlimit)
108.     plt.ylim(-ylimit,2*ylimit)
109.     ## colorize
110.     #for region in vor.regions:
111.     #    if not -1 in region:
112.     #        polygon = [vor.vertices[i] for i in region]
113.     #        plt.fill(*zip(*polygon))
114.     #
115.     #plt.show()
116.     GBpoints=vor.vertices
117.
118.

```

```

119. #####
    ###
120. #plot voronoi edges -
    the code below sorts the voronoi vertices into each edge
121. #this can easily be implemented into the sketch command in abaqus
122. #####
    ###
123. #open file for writing each line to file (each line contains 2 points to cre
    ate voronoi edge)
124. linefilex1 = open("VTedgesx1.out", "w")
125. linefiley1 = open("VTedgesy1.out", "w")
126. linefilex2 = open("VTedgesx2.out", "w")
127. linefiley2 = open("VTedgesy2.out", "w")
128. Lines=[]
129. i=1
130. X1=[]
131. X2=[]
132. Y1=[]
133. Y2=[]
134. for vpair in vor.ridge_vertices:
135.     if vpair[0] >= 0 and vpair[1] >= 0: # if both indices are greater than z
        ero, the Veronoi point is real (Inside specified cell)
136.         v0 = vor.vertices[vpair[0]] # xcoord1,ycoord1
137.         v1 = vor.vertices[vpair[1]] # xcoord2,ycoord2
138.         l=[v0,v1]
139.         Lines.append(l)
140.         #individual points to be written to file line by line
141.         x1=v0[0]
142.         y1=v0[1]
143.         x2=v1[0]
144.         y2=v1[1]
145.         # Draw lines to confirm the output matches the original voronoi diag
        ram.
146.         plt.figure(2)
147.         plt.plot([x1, x2], [y1, y2], 'k', linewidth=2)
148.         plt.title('Processed data for Abaqus Sklatching')
149.         #plot cell boundary
150.         plt.plot([0,xlimit,xlimit,0,0],[0,0,ylimit,ylimit,0])
151.         plt.xlim(-xlimit,2*xlimit)
152.         plt.ylim(-ylimit,2*ylimit)
153.         i=i+1 # just for counting
154.         X1.append(x1)
155.         Y1.append(y1)
156.         X2.append(x2)

```

```

157.         Y2.append(y2)
158.
159.     print (len(X1),len(X2),len(Y1),len(Y2))
160.
161.     #write to file
162.     for x in range(0,len(X1)):
163.         linefilex1.write("%f\n" % (X1[x]))
164.         linefiley1.write("%f\n" % (Y1[x]))
165.         linefilex2.write("%f\n" % (X2[x]))
166.         linefiley2.write("%f\n" % (Y2[x]))
167.
168.     linefilex1.close()
169.     linefilex2.close()
170.     linefiley1.close()
171.     linefiley2.close()
172.     print 'average grain area is:',averageGrainArea

```

```

1. # -*- coding: utf-8 -*-
2. """
3. Created on Tue Nov 25 15:47:41 2014
4.
5. @author: 10344913
6. """
7.
8. # -*- coding: utf-8 -*-
9. """
10. Created on Fri Nov 21 17:03:04 2014
11.
12. @author: 10344913
13. """
14.
15. from abaqus import *
16. from abaqusConstants import *
17. import pdb
18. import numpy
19. import part
20. import material
21. import section

```

```

22. import assembly
23. import step
24. import load
25. import mesh
26. import regionToolset
27. import job
28. import visualization
29. import amplitude
30.
31. backwardCompatibility.setValues(includeDeprecated=True,
32.                                reportDeprecated=False)
33.
34. # Create a model.
35.
36. myModel = mdb.Model(name='Grains2')
37.
38. # Create a new viewport in which to display the model
39. # and the results of the analysis.
40.
41. myViewport = session.Viewport(name='Grains',
42.                               origin=(5, 5), width=200, height=250)
43.
44. #####
45. #Part
46. #####
47. #Specify Rectangular Coords for reference
48. Point1x=0.
49. Point1y=0.
50. Point2x=50.
51. Point2y=50.
52. # Create a sketch of microstructure - to be used later for partitioning.
53. mySketch = myModel.ConstrainedSketch(name='Grains',sheetSize=250.)
54. #load file - create an array for each coord of two point line
55. f1=open("VTedgesx1.out",'r')
56. f2=open("VTedgesy1.out",'r')
57. f3=open("VTedgesx2.out",'r')
58. f4=open("VTedgesy2.out",'r')
59. x1=numpy.genfromtxt("VTedgesx1.out")
60. y1=numpy.genfromtxt("VTedgesy1.out")
61. x2=numpy.genfromtxt("VTedgesx2.out")
62. y2=numpy.genfromtxt("VTedgesy2.out")
63. f1.close()
64. f2.close()
65. f3.close()

```

```

66. f4.close()
67. # Create the line for each edge of the voronoi diagram.
68. for i in range(0,len(x1)):
69.     mySketch.Line(point1=(x1[i], y1[i]), point2=(x2[i],y2[i]))
70. #Create a sketch of part to be partitioned
71. # Create the rectangle.
72. mySketch2 = myModel.ConstrainedSketch(name='Cell',sheetSize=250.)
73. mySketch2.rectangle(point1=(Point1x,Point1y), point2=(Point2x,Point2y))
74. #mySketch3= myModel.ConstrainedSketch(name='3Cell',sheetSize=250.)
75. #mySketch3.rectangle(point1=(-50,-50), point2=(100,100))
76. #trim grain sketch so only 1 cell of nine contains a microstructure
77. #?
78. ## Create a 2-dimensional, deformable part.
79. mypart = myModel.Part(name='threeCell', dimensionality=TWO_D_PLANAR, type=DEFORMABLE_BODY)
80. #Import sketch to make part
81. mypart.BaseShell(sketch=mySketch2)
82. #get face to partition
83. f=mypart.faces[0]
84. e=mypart.edges[0:3]
85. #Partition cell using sketch of grains
86. mypart.PartitionFaceBySketch(faces=f,sketch=mySketch)
87. ##create region to be used for section assignment and meshing
88. #myregion = regionToolset.Region(side1Edges=e)
89. #####
90. #Property
91. #####
92. #create a material
93. mymaterial=myModel.Material(name='Steel')
94. #Elastic
95. E=200E3
96. v=0.3
97. elasticProperties = (E, v)
98. mymaterial.Elastic(table=(elasticProperties,))
99. #create section
100.     mySection = myModel.HomogeneousSolidSection(name='microstructureSection', material='Steel',thickness=1)
101.     #assign section to part
102.     myregion=(mypart.faces, )
103.     ##-----
104.     mypart.SectionAssignment(offset=0.0, offsetField='', offsetType=MIDDLE_SURFACE, region=myregion, sectionName='microstructureSection')
105.
106.

```

```

107.
108. #####
109.     ###
110.     #Assembly
111. #####
112.     ###
113.     # Create a part instance.
114.
115.     myAssembly = myModel.rootAssembly
116.     myInstance = myAssembly.Instance(name='MicroStructureInstance',
117.         part=mypart, dependent=OFF)
118. #####
119.     ###
120.     #Step
121. #####
122.     ###
123.     # Create a step. The time period of the static step is 1.0,
124.     # and the initial incrementation is 0.1; the step is created
125.     # after the initial step.
126.
127.     myModel.StaticStep(name='Step-1', previous='Initial',
128.         timePeriod=1.0, initialInc=0.02, maxInc=1,
129.         description='Step 1', maxNumInc=10000, nlgeom=ON)
130. #####
131.     ###
132.     #Amplitude
133.     myModel.EquallySpacedAmplitude(name='Amp1', fixedInterval=0.5, data=(0.0,1.0
134.         ,0.0,-1.0,0.0,1.0,0.0,-1.0,0.0,1.0,0.0,-1.0,0.0,1.0,0.0,-1.0,0.0,1.0,0.0,-
135.         1.0,0.0,1.0,0.0,-1.0,0.0))
136. #####
137.     ###
138.     #Load and BCs
139. #####
140.     ###
141.     #find edges coordinates
142.
143.     l=0
144.     LeftEndEdges=[]
145.     LeftEndFaces=[]
146.     for v in range(1,Point2y): # 0.5 used so first edge of other side isnt chose
147.         n

```

```

140.         endEdgeCoords=(Point1x,v,0.0)
141.         endEdge=myInstance.edges.findAt((endEdgeCoords,))
142.         endFace=myInstance.faces.findAt((endEdgeCoords,))
143.         LeftEndEdges.append(endEdge)
144.         LeftEndFaces.append(endFace)
145.         l=0
146.         RightEndEdges=[]
147.         RightEndFaces=[]
148.         for v in range(1,Point2y): # 0.5 used so first edge of other side isnt chose
n
149.             endEdgeCoords=(Point2x,v,0.0)
150.             endEdge=myInstance.edges.findAt((endEdgeCoords,))
151.             endFace=myInstance.faces.findAt((endEdgeCoords,))
152.             RightEndEdges.append(endEdge)
153.             RightEndFaces.append(endFace)
154.             l=0
155.             BottomEndEdges=[]
156.             BottomEndFaces=[]
157.             for v in range(1,Point2x): # 0.5 used so first edge of other side isnt chose
n
158.                 endEdgeCoords=(v,Point1y,0.0)
159.                 endEdge=myInstance.edges.findAt((endEdgeCoords,))
160.                 endFace=myInstance.faces.findAt((endEdgeCoords,))
161.                 BottomEndEdges.append(endEdge)
162.                 BottomEndFaces.append(endFace)
163.                 l=0
164.                 TopEndEdges=[]
165.                 TopEndFaces=[]
166.                 for v in range(1,Point2x): # 0.5 used so first edge of other side isnt chose
n
167.                     endEdgeCoords=(v,Point2y,0.0)
168.                     endEdge=myInstance.edges.findAt((endEdgeCoords,))
169.                     endFace=myInstance.faces.findAt((endEdgeCoords,))
170.                     TopEndEdges.append(endEdge)
171.                     TopEndFaces.append(endFace)
172.                 #...and create Set of nodes at each free edge
173.                 LeftFreeEdge=myAssembly.Set(name='LeftEndEdge',edges=LeftEndEdges)
174.                 RightFreeEdge=myAssembly.Set(name='RightEndEdge',edges=RightEndEdges)
175.                 BottomFreeEdge=myAssembly.Set(name='BottomEndEdge',edges=BottomEndEdges)
176.                 TopFreeEdge=myAssembly.Set(name='TopEndEdge',edges=TopEndEdges)
177.                 #####
###
178.                 #Mesh

```

```

179. #####
    ###
180. #create region(with sequence) to apply mesh controls
181. vertregion=myInstance.faces[0:len(myInstance.faces)]
182. print ('no. of faces:', len(myInstance.faces))
183. myAssembly.setMeshControls(elemShape=QUAD_DOMINATED, regions=vertregion, tec
    hnique=STRUCTURED)
184. elemType = mesh.ElemType(elemCode=CPE4R, elemLibrary=STANDARD)
185. myregion=(myInstance.faces, )
186. myAssembly.setElementType(regions=myregion, elemTypes=(elemType,))
187. # Seed the part instance.
188. #Specify edges(with sequence) to apply mesh controls (if using 'seed edge by
    number')
189. edgeRegion=myInstance.edges[0:len(myInstance.edges)]
190. print ('no. of edges',len(myInstance.edges))
191. #apply global seed
192. myAssembly.seedPartInstance(regions=(myInstance,), size=1)
193. ##assign a fixed number of elements/nodes on each edge -
    for the application of periodic boundary conditions
194. for b in range(0,len(RightEndEdges)):
195.     myAssembly.seedEdgeByNumber(edges=RightEndEdges[b], number=5, constraint
        =FIXED)
196. for b in range(0,len(LeftEndEdges)):
197.     myAssembly.seedEdgeByNumber(edges=LeftEndEdges[b], number=5, constraint=
        FIXED)
198. for b in range(0,len(BottomEndEdges)):
199.     myAssembly.seedEdgeByNumber(edges=BottomEndEdges[b], number=5, constrain
        t=FIXED)
200. for b in range(0,len(TopEndEdges)):
201.     myAssembly.seedEdgeByNumber(edges=TopEndEdges[b], number=5, constraint=F
        IXED)
202. # Mesh the part instance.
203. myAssembly.generateMesh(regions=(myInstance,))
204. # Display the meshed part.
205. myViewport.assemblyDisplay.setValues(mesh=ON)
206. myViewport.assemblyDisplay.meshOptions.setValues(meshTechnique=ON)
207. myViewport.setValues(displayedObject=myAssembly)
208. #print number of objects in free edge sets to confirm node numbers are equal
209. checkVal1=len(LeftFreeEdge.nodes) #FYI - how to get no. of nodes in a set
210. checkVal2=len(RightFreeEdge.nodes)
211. checkVal3=len(TopFreeEdge.nodes)
212. checkVal4=len(BottomFreeEdge.nodes)
213. if checkVal1-checkVal2==0 and checkVal3-checkVal4==0 :

```

```

214.         print 'Equal number of nodes at free ends'
215.     else:
216.         print 'Mesh not suitable for periodic BCs'
217.
218.     ##Create reference point
219.     #myAssembly.ReferencePoint(point=(0.0,0.0,0.0))
220.
221.     #####
222.     ###
223.     #Commands for crystal plasticity implementation
224.     #####
225.     ###
226.     #create an element set for each grain
227.     for k in range(0,(len(myInstance.faces))):
228.         myAssembly.Set(name='Grain-'+str(k+1),faces=myInstance.faces[k:k+1])
229.     #create job to gather input file
230.     jobName = 'UnitCell'
231.     myJob = mdb.Job(name=jobName, model='Grains2',
232.         description='CP calibration Model')
233.     #-----Submit Job-----
234.     ## Wait for the job to complete.
235.     #myJob.submit()
236.     #myJob.waitForCompletion()
237.     #-----
238.     --
239.     #-----INPUT FILE MODIFICATIONS-----
240.     --
241.     #####
242.     ####
243.     #Left free edge node data
244.     LeftNodeLabels=[]
245.     LeftNodeCoords = []
246.     LeftNodeData=[]
247.     for n in LeftFreeEdge.nodes:
248.         Label=n.label
249.         coord = myAssembly.getCoordinates(n)
250.         LeftNodeCoords.append(coord)
251.         LeftNodeLabels.append(Label)
252.         NodeData=(Label,coord)
253.         LeftNodeData.append(NodeData)
254.     #Right free edge node data
255.     RightNodeLabels=[]
256.     RightNodeCoords = []

```

```

253.     RightNodeData=[]
254.     for n in RightFreeEdge.nodes:
255.         Label=n.label
256.         coord = myAssembly.getCoordinates(n)
257.         RightNodeCoords.append(coord)
258.         RightNodeLabels.append(Label)
259.         NodeData=(Label,coord)
260.         RightNodeData.append(NodeData)
261.     #Top free edge node data
262.     TopNodeLabels=[]
263.     TopNodeCoords = []
264.     TopNodeData=[]
265.     for n in TopFreeEdge.nodes:
266.         Label=n.label
267.         coord = myAssembly.getCoordinates(n)
268.         TopNodeCoords.append(coord)
269.         TopNodeLabels.append(Label)
270.         NodeData=(Label,coord)
271.         TopNodeData.append(NodeData)
272.     #Bottom free edge node data
273.     BottomNodeLabels=[]
274.     BottomNodeCoords = []
275.     BottomNodeData=[]
276.     for n in BottomFreeEdge.nodes:
277.         Label=n.label
278.         coord = myAssembly.getCoordinates(n)
279.         BottomNodeCoords.append(coord)
280.         BottomNodeLabels.append(Label)
281.         NodeData=(Label,coord)
282.         BottomNodeData.append(NodeData)
283.
284.
285.     #-----Create Input File-----
286.     ##write input file
287.     mdb.jobs['UnitCell'].writeInput()
288.     print 'Input File Generated'
289.
290.     # Open the output database and display a
291.     ## default contour plot.
292.     #myOdb = visualization.openOdb(path=jobName + '.odb')
293.     #myViewport.setValues(displayedObject=myOdb)
294.     #myViewport.odbDisplay.display.setValues(plotState=CONTOURS_ON_DEF)
295.     #myViewport.odbDisplay.commonOptions.setValues(renderStyle=FILLED)
296.

```

```

297.     #output values
298.     #number of elements in model
299.     numElements=len(myInstance.elements)
300.     numGrains=len(myInstance.faces)
301.     outfile=open("Outputs.txt", 'w')
302.     outfile.write("%s\n %g\n %g\n %g\n %g\n %g\n " % (numGrains,Point1x,Point2x,P
oint1y,Point2y,numElements))
303.     file.close(outfile)
304.
305.     #Get area of a grain(face)
306.     GrainFile=open("GrainAreas.txt", "w")
307.     AREAS=[]
308.     for i in range(0, (numGrains)):
309.         area=myspart.faces[i].getSize()
310.         AREAS.append(area)
311.         GrainFile.write("%8f\n " % (area))
312.     GrainFile.close()

```

```

1. # -*- coding: utf-8 -*-
2. """
3. Created on Mon Dec 01 11:33:09 2014
4.
5. @author: 10344913
6. """
7. from sys import argv
8. import numpy as np
9. import scipy
10. import pylab
11. import random
12. from time import sleep
13. import decimal
14. import matplotlib.pyplot as plt
15. InputFile='UnitCell.inp'
16. #####
17. #BOUNDARY CONDITIONS - INPUT FILE MODIFICATIONS
18. #####
19. #input parameters from abaqus script
20. Parameters=np.genfromtxt("Outputs.txt")
21. #Cell dimensions
22. Xmin=Parameters[1]
23. Xmax=Parameters[2]

```

```

24. Ymin=Parameters[3]
25. Ymax=Parameters[4]
26. numElements=int(Parameters[5])
27. NumGrains=int(Parameters[0])
28. #Open input file and extract node data only)
29. Data=open(InputFile,'r')
30. f=file.read(Data)
31. file.close(Data)
32. err=0 #need this error counter to account for each line before*node
33. endIndex=0
34. for x in range(0,len(f)):
35.     if f[x]=='\n':
36.         err=err+1
37.         if f[x]=='o' and f[x-1]=='N' and f[x-2]=='*':
38.             startIndex=x+err+5
39.             y=err
40.         if f[x]=='e' and f[x-1]=='l' and f[x-2]=='E' and f[x-3]=='*':
41.             endIndex=x-3+y
42.         if endIndex>0:
43.             break
44. with open(InputFile) as fin:
45.     fin.seek(startIndex)
46.     data = fin.read(endIndex- startIndex)
47.
48. nodefile=open("nodefile.out",'w')
49. nodefile.write("%s" % data)
50. nodefile.close()
51. file.close(Data)
52.
53.
54. import csv
55. Rows=[]
56. with open('nodefile.out', 'r') as f:
57.     reader = csv.reader(f, dialect='excel', delimiter=',')
58.     for row in reader:
59.         # print row
60.         Rows.append(row)
61. NodeLabels=[]
62. Xcoords=[]
63. Ycoords=[]
64. for x in range(0,len(Rows)):
65.     label=int(Rows[x][0])
66.     xcoord=float(Rows[x][1])
67.     ycoord=float(Rows[x][2])

```

```

68.     NodeLabels.append(label)
69.     Xcoords.append(xcoord)
70.     Ycoords.append(ycoord)
71.
72. #find nodes at free edges
73. LFEycoords=[]
74. LFEnodes=[]
75. RFEycoords=[]
76. RFEnodes=[]
77. BFEnodes=[]
78. BFExcoords=[]
79. TFEnodes=[]
80. TFExcoords=[]
81. #n should possibly be n-1
82. for n in range (0,len(NodeLabels)):
83.     if Xcoords[n]==Xmin:
84.         node=NodeLabels[n]
85.         coord=Ycoords[n]
86.         LFEnodes.append(node)
87.         LFEycoords.append(coord)
88.     if Xcoords[n]==Xmax: #Should be limit of cell referencing previous file
89.         node1=NodeLabels[n]
90.         coord=Ycoords[n]
91.         RFEnodes.append(node1)
92.         RFEycoords.append(coord)
93.     if Ycoords[n]==Ymin: #Should be limit of cell referencing previous file
94.         node2=NodeLabels[n]
95.         coord=Xcoords[n]
96.         BFEnodes.append(node2)
97.         BFExcoords.append(coord)
98.     if Ycoords[n]==Ymax: #Should be limit of cell referencing previous file
99.         node3=NodeLabels[n]
100.        coord=Xcoords[n]
101.        TFEnodes.append(node3)
102.        TFExcoords.append(coord)
103.    print 'No. of nodes on left free edge:\n', len(LFEnodes)
104.    print 'No. of nodes on right free edge:\n', len(RFEnodes)
105.    print 'No. of nodes on top free edge:\n', len(TFEnodes)
106.    print 'No. of nodes on bottom free edge:\n', len(BFEnodes)
107.    #check for equal number of nodes on opposite free edges
108.    if len(LFEnodes)- len(RFEnodes)==0 and len(BFEnodes)-len(TFEnodes)==0:
109.        print '\nElement mesh is suitable for periodic BCs\n'
110.    else:

```

```

111.         print '***** WARNING *****\nElement mesh is NOT suitable for pe
           riodic BCs'
112.         #organise nodes in ascending order
113.         #Sort left free edge
114.         sLFEycoords=sorted(LFEycoords)
115.         sLFEnodes=[]
116.         for y in range(0,len(sLFEycoords)):
117.             for j in range(0,len(LFEycoords)):
118.                 if sLFEycoords[y] == LFEycoords[j]:
119.                     node=LFEnodes[j]
120.                     sLFEnodes.append(node)
121.         LFEnodes=sLFEnodes #sorted in ascending order
122.         LFEycoords=sLFEycoords
123.         #Sort right free edge
124.         sRFEycoords=sorted(RFEycoords)
125.         sRFEnodes=[]
126.         for y in range(0,len(sRFEycoords)):
127.             for j in range(0,len(RFEycoords)):
128.                 if sRFEycoords[y] == RFEycoords[j]:
129.                     node=RFEnodes[j]
130.                     sRFEnodes.append(node)
131.         RFEnodes=sRFEnodes #sorted in ascending order
132.         RFEycoords=sRFEycoords
133.         #Sort top free edge
134.         sTFExcoords=sorted(TFExcoords)
135.         sTFEnodes=[]
136.         for y in range(0,len(sTFExcoords)):
137.             for j in range(0,len(TFExcoords)):
138.                 if sTFExcoords[y] == TFExcoords[j]:
139.                     node=TFEnodes[j]
140.                     sTFEnodes.append(node)
141.         TFEnodes=sTFEnodes #sorted in ascending order
142.         TFExcoords=sTFExcoords
143.         #Sort bottom free edge
144.         sBFExcoords=sorted(BFExcoords)
145.         sBFEnodes=[]
146.         for y in range(0,len(sBFExcoords)):
147.             for j in range(0,len(BFExcoords)):
148.                 if sBFExcoords[y] == BFExcoords[j]:
149.                     node=BFEnodes[j]
150.                     sBFEnodes.append(node)
151.         BFEnodes=sBFEnodes #sorted in ascending order
152.         BFExcoords=sBFExcoords
153.

```

```

154.
155.
156.     #find corner nodes
157.     for x in range(0,len(NodeLabels)):
158.         if Xcoords[x]==Xmin and Ycoords[x]==Ymin:
159.             BLnode=NodeLabels[x]
160.         if Xcoords[x]==Xmin and Ycoords[x]==Ymax:
161.             TLnode=NodeLabels[x]
162.         if Xcoords[x]==Xmax and Ycoords[x]==Ymax:
163.             TRnode=NodeLabels[x]
164.         if Xcoords[x]==Xmax and Ycoords[x]==Ymin:
165.             BRnode=NodeLabels[x]
166.     print 'Bottom left node: ', BLnode
167.     print 'Top left node: ', TLnode
168.     print 'Top right node: ', TRnode
169.     print 'Bottom right node: ', BRnode
170.
171.
172.     ##Input file modifications for Periodic Boundary Conditions
173.     #Ensure the left and right sides do not rotate with respect to each other
174.     LRtextstring=""
175.     for k in range(1,len(RFEnodes)-1): #neglect corner nodes
176.         text='*EQUATION\n3\n    %s,1,1,    %s,1,-1,    %s,1,-
177.         1\n' %(RFEnodes[k],BRnode,LFEnodes[k])
178.         LRtextstring+=str(text) # concatenate strings
179.     #print LRtextstring
180.     #Ensure the top and bottom sides do not rotate with respect to each other
181.     BTtextstring=""
182.     for k in range(1,len(TFEnodes)-1): #neglect corner nodes
183.         text='*EQUATION\n3\n    %s,2,1,    %s,2,-1,    %s,2,-
184.         1\n' %(TFEnodes[k],TLnode,BFEnodes[k])
185.         BTtextstring+=str(text) # concatenate strings
186.     #print BTtextstring
187.     #Ensure left and right sides deform equally in the y direction (no shear)
188.     LRYtextstring=""
189.     for k in range(1,len(RFEnodes)):
190.         text='*EQUATION\n2\n    %s,2,1,    %s,2,-
191.         1\n' %(RFEnodes[k],LFEnodes[k])
192.         LRYtextstring+=str(text) # concatenate strings
193.     #print LRYtextstring
194.     #Ensure top and bottom sides deform equally in the x direction (no shear)
195.     TBxtextstring=""
196.     for k in range(1,len(TFEnodes)):

```

```

194.         text='*EQUATION\n2\n      %s,1,1,      %s,1,-
        1\n' %(TFEnodes[k],BFEnodes[k])
195.         TBxtextstring+=str(text) # concatenate strings
196.         #print TBxtextstring
197.         #Ensure corner nodes displace evenly in respective directions
198.         CornerBoundary1text='*EQUATION\n 2\n      %s,2,1,      %s,2,-
        1\n' %(TRnode,TLnode)
199.         CornerBoundary2text='*EQUATION\n 2\n      %s,1,1,      %s,1,-
        1\n' %(TRnode,BRnode)
200.         #Displacement BCs
201.         BRSET=('SET%s') %BRnode
202.         BLSET=('SET%s') %BLnode
203.         TRSET=('SET%s') %TRnode
204.         TLSET=('SET%s') %TLnode
205.         #Pin BL node and fix TL node in x dircection and fix BR node in y direction
206.         BC1=' ** BOUNDARY CONDITIONS \n *Boundary\n %s,1,2\n %s,1,1\n %s,2,2\n' %(BL
        SET,TLSET,BRSET)
207.         #Create set for application of cyclic displacement
208.         SetforBCs='*Nset, nset=Ref, instance=MicroStructureInstance \n %s,\n*Nset, n
        set=%s, instance=MicroStructureInstance \n %s,\n*Nset, nset=%s, instance=MicroStruc
        tureInstance \n %s,\n*Nset, nset=%s, instance=MicroStructureInstance \n %s,\n' %(BR
        node,BLSET,BLnode,TLSET,TLnode,BRSET,BRnode)
209.         SetforAllgrains='*Elset, elset=ALLgrains,instance=MicroStructureInstance , g
        enerate\n 1, %s, 1 \n' %(numElements)
210.         #Concatenate into one text string
211.         INPmods=""
212.         Seq=(LRtextstring,BTtextstring,LRYtextstring,TBxtextstring)
213.         INPmods=INPmods.join(Seq)
214.         #print INPmods
215.         #edit input file
216.         Data=open(InputFile,'r+')
217.         f=file.read(Data)
218.         err=0
219.         for x in range(0,len(f)):
220.             if f[x]=='\n':
221.                 err=err+1
222.                 if f[x]=='I' and f[x-1]==' ' and f[x-2]=='d' and f[x-3]=='n' and f[x-
                    4]=='E' and f[x-5]=='*':
223.                     y=err
224.                     StartIndex=x-5+y
225.                 with open(InputFile, "r+") as f:
226.                     f.seek(StartIndex)
227.                     data = f.read()

```

```

228.     f.close()
229.     with open(InputFile, "r+") as f:
230.         old = f.read() # read everything in the file
231.         f.seek(StartIndex) # rewind
232.         f.write(INPmods + data) # write the new line before
233.     f.close()
234.     file.close(Data)
235.     #Cyclic displacement
236.     CycDisp='*Boundary, Amplitude=Amp1\nRef, 1, 1, 0.5\n'
237.     #edit INP file
238.     Data=open(InputFile,'r+')
239.     f=file.read(Data)
240.     err=0
241.     for x in range(0,len(f)):
242.         if f[x]=='\n':
243.             err=err+1
244.             if f[x]=='S' and f[x-1]==' ' and f[x-2]=='d' and f[x-3]=='n' and f[x-
245.                 4]=='E' and f[x-5]=='*':
246.                 y=err
247.                 StartIndex=x-5+y
248.             with open(InputFile, "r+") as f:
249.                 f.seek(StartIndex)
250.                 data = f.read()
251.             f.close()
252.             with open(InputFile, "r+") as f:
253.                 old = f.read() # read everything in the file
254.                 f.seek(StartIndex) # rewind
255.                 f.write(CycDisp + BC1+ data) # write the new line before
256.             f.close()
257.             #edit inp file
258.             file.close(Data)
259.             Data=open(InputFile,'r+')
260.             f=file.read(Data)
261.             err=0
262.             for x in range(0,len(f)):
263.                 if f[x]=='\n':
264.                     err=err+1
265.                     if f[x]=='A' and f[x-1]==' ' and f[x-2]=='d' and f[x-3]=='n' and f[x-
266.                         4]=='E' and f[x-5]=='*':
267.                             y=err
268.                             StartIndex=x-5+y
269.                     with open(InputFile, "r+") as f:
270.                         f.seek(StartIndex)
271.                         data = f.read()

```

```

270.     f.close()
271.     with open(InputFile, "r+") as f:
272.         old = f.read() # read everything in the file
273.         f.seek(StartIndex) # rewind
274.         f.write(SetforBCs + SetforAllgrains + data) # write the new line before

275.     f.close()
276.     file.close(Data)
277.     #####
278.     ####
279.     ##USER MATERIAL - INPUT FILE MODIFICATIONS
280.     #####
281.     #
282.     ##Insert Data Cards
283.     #
284.     ANGLES=[]
285.     RANDB3=[]
286.     print '*****\n\n\n\n\n\nPlease wait while editing file.....\n\n'

287.     j=0
288.     while j <= NumGrains-1:
289.         # random orientations
290.         randA1=random.randint(-1000, 1000)
291.         randA2=random.randint(-1000, 1000)
292.         randA3=random.randint(-1000, 1000)
293.         randB1=random.randint(-1000, 1000)
294.         randB2=random.randint(-1000, 1000)
295.         randB3=randA3
296.         angle=0
297.         #find angle between 2 vectors
298.         counter=0
299.         while angle>1.572367123 or angle<1.56922553: #higher and lower allowed a
ngles
300.             randB3=random.randint(-1000, 1000)
301.             dotprod=randA1*randB1+randA2*randB2+randA3*randB3
302.             magA=pow(randA1,2)+(pow(randA2,2))+(pow(randA3,2))
303.             magA=sqrt(magA)
304.             magB=pow(randB1,2)+(pow(randB2,2))+(pow(randB3,2))
305.             magB=sqrt(magB)
306.             angle=math.acos(dotprod/(magA*magB))
307.             counter=counter+1

```

```

308.         if counter==1000:
309.             break
310.         if angle>1.572367123 or angle<1.56922553:
311.             continue
312.             j=j
313.         else:
314.             j=j+1
315.
316.         #         print (angle, randB3)
317.
318.         #         sleep(0.3)
319.         RANDB3.append(randB3)
320.         print 'Random orientation for grain %s complete' %(j)
321.         ANGLES.append(angle)
322.
323.         DataCards=""
324.         m='*Material, name=GRAIN%s\n*DEPVAR\n 164,\n' % (j)
325.         mat='*USER MATERIAL, CONSTANTS=168, UNSYMM\n'
326.         ElasticModulii1=' 200000.,    0.3,    0.,    0.,    0.,    0.,
0.,    0.\n'
327.         ElasticModulii2=' 0.,    0.,    0.,    0.,    0.,    0.,
0.,    0.\n'
328.         ElasticModulii3=' 0.,    0.,    0.,    0.,    0.,    0.,
0.,    0.\n'
329.         PotAcSlipSys='1.,    0.,    0.,    0.,    0.,    0.,    0.,
0.\n'
330.         NormandSlipDir1=' 1.,    1.,    1.,    1.,    1.,    0.,
0.,    0.\n'
331.         NormandSlipDir2=' 0.,    0.,    0.,    0.,    0.,    0.,
0.,    0.\n'
332.         NormandSlipDir3=' 0.,    0.,    0.,    0.,    0.,    0.,
0.,    0.\n'
333.         InitialOrientation1='%s    ,    %s,    %s,    1.00000    ,    0.00000
,    0.00000\n' %(randA1, randA2, randA3)
334.         InitialOrientation2='%s    ,    %s,    %s,    0.00000    ,    0.00000
,    1.00000\n' %(randB1, randB2, randB3)
335.         RateDep1='100.,    0.002,    0.,    0.,    0.,    0.,    0.,
0.\n'
336.         RateDep2=' 0.,    0.,    0.,    0.,    0.,    0.,    0.,
0.\n'
337.         RateDep3=' 0.,    0.,    0.,    0.,    0.,    0.,    0.,
0.\n'
338.         IsoHard='30.,    104.,    90.,    0.,    0.,    0.,    0.,    0.
\n'

```

```

339.         X1=' 1.,      1.,      0.,      0.,      0.,      0.,      0.,      0.\n
      ,
340.         X2=' 0.,      0.,      0.,      0.,      0.,      0.,      0.,      0.\n
      n'
341.         X3=' 0.,      0.,      0.,      0.,      0.,      0.,      0.,      0.\n
      n'
342.         X4=' 0.,      0.,      0.,      0.,      0.,      0.,      0.,      0.\n
      n'
343.         X5=' 0.,      0.,      0.,      0.,      0.,      0.,      0.,      0.\n
      n'
344.         IntProps='0.5,      1.,      0.,      0.,      0.,      0.,      0.,
      0.\n'
345.         NewtRaps=' 1.,      10.,      1e-
      05,      0.,      0.,      0.,      0.,      0.\n'
346.         KinHard=' 15836.,      74.,      0.,      0.,      0.,      0.,      0.,
      0.\n'
347.         Seq=(m,mat,ElasticModulii1,ElasticModulii2,ElasticModulii3,PotAcSlipSys,
      NormandSlipDir1,NormandSlipDir2,NormandSlipDir3,InitialOrientation1,InitialOrientat
      ion2,RateDep1,RateDep2,
348.             RateDep3,IsoHard,X1,X2,X3,X4,X5,IntProps,NewtRaps,KinHard)
349.         DataCards=DataCards.join(Seq)
350.         #edit inp file
351.         if j==1:
352.             Data=open(InputFile,'r+')
353.             f=file.read(Data)
354.             err=0
355.             #Find location in file to dump Data
356.             for x in range(0,len(f)):
357.                 if f[x]=='\n':
358.                     err=err+1
359.                     if f[x]==',' and f[x-1]=='p' and f[x-2]=='e' and f[x-
      3]=='t' and f[x-4]=='S' and f[x-5]=='*':
360.                         y=err
361.                         StartIndex=x-5+y # location to add new data
362.                         Data=open(InputFile,'r+')
363.                         f=file.read(Data)
364.                         err=0
365.                         #find new location to resume file(in this case after elastic materia
      l definition)
366.                         #ie. save the end of the file to a string and append at a later stag
      e after new data has been added
367.                         for x in range(0,len(f)):
368.                             if f[x]=='\n':

```

```

369.             err=err+1
370.             if f[x]=='r' and f[x-1]=='e' and f[x-2]=='t' and f[x-
371.                 3]=='a' and f[x-4]=='M' and f[x-5]=='*':
372.                 y=err
373.                 newStartIndex=x-
374.                     5+y # location to start saving temporarily removed data
375.                 with open(InputFile, "r+") as f:
376.                     f.seek(StartIndex)
377.                     data = f.read()
378.                     f.close()
379.                     file.close(Data)
380.                 with open(InputFile, "r+") as f:
381.                     old = f.read() # read everything in the file
382.                     f.seek(newStartIndex) # rewind
383.                     f.write(DataCards + data) # write the new line before
384.                     f.close()
385.                     file.close(Data)
386.             else:
387.                 ##
388.                 Data=open(InputFile,'r+')
389.                 f=file.read(Data)
390.                 err=0
391.                 for x in range(0,len(f)):
392.                     if f[x]=='\n':
393.                         err=err+1
394.                         if f[x]==',' and f[x-1]=='p' and f[x-2]=='e' and f[x-
395.                             3]=='t' and f[x-4]=='S' and f[x-5]=='*':
396.                             y=err
397.                             StartIndex=x-5+y
398.                             Data=open(InputFile,'r+')
399.                             f=file.read(Data)
400.                             err=0
401.                             for x in range(0,len(f)):
402.                                 if f[x]=='\n':
403.                                     err=err+1
404.                                     if f[x]==',' and f[x-1]=='p' and f[x-2]=='e' and f[x-
405.                                         3]=='t' and f[x-4]=='S' and f[x-5]=='*':
406.                                             y=err
407.                                             newStartIndex=x-5+y
408.                                             with open(InputFile, "r+") as f:
409.                                                 f.seek(StartIndex)
410.                                                 data = f.read()
411.                                                 f.close()

```

```

409.         file.close(Data)
410.         with open(InputFile, "r+") as f:
411.             old = f.read() # read everything in the file
412.             f.seek(newStartIndex) # rewind
413.             f.write(DataCards + data) # write the new line before
414.         f.close()
415.         file.close(Data)
416.
417.     #Create Section for each grain
418.     #Locations
419.     Data=open(InputFile,'r+')
420.     f=file.read(Data)
421.     err=0
422.     StartIndex=0
423.     #Remove original section definition
424.     for x in range(0,len(f)):
425.         if f[x]=='\n':
426.             err=err+1
427.             if f[x]=='T' and f[x-1]=='A' and f[x-2]=='U' and f[x-3]=='Q' and f[x-
428.                 4]=='E' and f[x-5]=='*':
429.                 y=err
430.                 StartIndex=x-5+y # location to add new data
431.                 if StartIndex>0:
432.                     break
433.             err=0
434.             for x in range(0,len(f)):
435.                 if f[x]=='\n':
436.                     err=err+1
437.                     if f[x]=='d' and f[x-1]=='i' and f[x-2]=='l' and f[x-3]=='o' and f[x-
438.                         4]=='S' and f[x-5]=='*':
439.                             y=err
440.                             newStartIndex=x-
441.                                 5+y # location to start saving temporarily removed data
442.                             with open(InputFile, "r+") as f:
443.                                 f.seek(StartIndex)
444.                                 data = f.read()
445.                                 f.close()
446.                                 file.close(Data)
447.
448.                             #edit inp file
449.                             # dummy needed as the data does not fully overwrite original text -
450.                                 extra spaces are needed to 'wipe-out' all existing text
451.                             dummy=""
452.                             for d in range(0,10*(abs(StartIndex-newStartIndex))):

```

```

449.         dum=(' ')
450.         dummy+=dum
451.         #print d
452.
453.         with open(InputFile, "r+") as fid:
454.             old = fid.read() # read everything in the file
455.             fid.seek(newStartIndex) # rewind
456.             fid.write(data+dummy) # write the new line before
457.         fid.close()
458.         ##Write new section data for each grain
459.         for i in range(1,NumGrains+1):
460.             section=('*Solid Section, elset=Grain-
461.                 %s, material=GRAIN%s\n*Hourglass Stiffness\n 385,,\n') % (i,i)
462.             Data=open(InputFile,'r+')
463.             f=file.read(Data)
464.             err=0
465.             file.close(Data)
466.             newStartIndex=0
467.             for x in range(0,len(f)):
468.                 if f[x]=='\n':
469.                     err=err+1
470.                     if f[x]=='T' and f[x-1]=='A' and f[x-2]=='U' and f[x-
471.                         3]=='Q' and f[x-4]=='E' and f[x-5]=='*':
472.                         y=err
473.                         newStartIndex=x-5+y
474.                         if newStartIndex>0: #write section data before first *equation
475.                             break
476.             with open(InputFile, "r+") as f:
477.                 old = f.read() # read everything in the file
478.                 f.seek(newStartIndex) # rewind
479.                 f.write(section+data) # write the new line before
480.             f.close()
481.             file.close(Data)
482.
483.         ##move the *end instance keyword to below grain sets.
484.         Data=open(InputFile,'r+')
485.         f=file.read(Data)
486.         err=0
487.         StartIndex=0
488.         #Remove Keyword
489.         for x in range(0,len(f)):
490.             if f[x]=='\n':
491.                 err=err+1

```

```

490.         if f[x]=='I' and f[x-1]==' ' and f[x-2]=='d' and f[x-3]=='n' and f[x-
           4]=='E' and f[x-5]=='*':
491.             y=err
492.             StartIndex=x+10+y # location to add new data
493.             if StartIndex>0:
494.                 break
495.             err=0
496.             for x in range(0,len(f)):
497.                 if f[x]=='\n':
498.                     err=err+1
499.                 if f[x]=='I' and f[x-1]==' ' and f[x-2]=='d' and f[x-3]=='n' and f[x-
           4]=='E' and f[x-5]=='*':
500.                     y=err
501.                     newStartIndex=x-
           5+y # location to start saving temporarily removed data
502.                     with open(InputFile, "r+") as f:
503.                         f.seek(StartIndex)
504.                         data = f.read()
505.                         f.close()
506.                         file.close(Data)
507.                         with open(InputFile, "r+") as f:
508.                             old = f.read() # read everything in the file
509.                             f.seek(newStartIndex) # rewind
510.                             f.write(data+dummy) # write the new line before
511.                         f.close()
512.                         file.close(Data)
513.                         #Add Keyword
514.                         Data=open(InputFile, 'r+')
515.                         f=file.read(Data)
516.                         err=0
517.                         StartIndex=0
518.                         for x in range(0,len(f)):
519.                             if f[x]=='\n':
520.                                 err=err+1
521.                             if f[x]=='e' and f[x-1]=='L' and f[x-2]=='=' and f[x-3]=='t' and f[x-
           4]=='e' and f[x-5]=='s'and f[x-6]=='n':
522.                                 y=err
523.                                 StartIndex=x-13+y # location to add new data
524.                                 if StartIndex>0:
525.                                     break
526.                                 err=0
527.                                 for x in range(0,len(f)):
528.                                     if f[x]=='\n':
529.                                         err=err+1

```

